

# Thermal transport at the quantum scale

**Inauguraldissertation**

zur  
Erlangung der Würde eines Doktors der Philosophie  
vorgelegt der  
Philosophisch-Naturwissenschaftlichen Fakultät  
der Universität Basel

VON

**Andrea Gemma**

Basel, 2022

Genehmigt von der Philosophisch-Naturwissenschaftlichen Fakultät  
auf Antrag von  
Dr. Bernd Gotsmann  
Prof. Dr. Michel Calame  
Prof. Dr. András Halbritter

Basel, 16.11.2021

Prof. Dr. Marcel Mayor  
Dekan

## **Widmung**

Dieser Arbeit widme ich meiner Freundin Carla für ihre ständige und geduldige Unterstützung und meiner Familie für ihr unerschütterliches Vertrauen.

Dedico questo lavoro alla mia ragazza Carla per il suo costante e paziente sostegno, e alla mia famiglia per la loro incrollabile fiducia in me.

*The noblest pleasure is the joy of understanding.*

Leonardo da Vinci (1452-1519)

# Contents

<b>1</b>	<b>Introduction</b>	<b>1</b>
<b>2</b>	<b>Theoretical background</b>	<b>5</b>
2.1	Charge transport . . . . .	5
2.1.1	Electrical conductance in Quantum Point Contacts . . . . .	8
2.1.2	Electrical conductance in Single Molecule Junctions . . . . .	10
2.2	Electronic thermal transport and Thermoelectricity . . . . .	14
2.3	Phonon transport . . . . .	15
2.4	Perspective: Phonon thermal transport through quantum channels and molecules . . . . .	16
2.4.1	Abstract . . . . .	17
2.4.2	Quantized and quantum thermal transport . . . . .	17
2.4.3	Experimental evidence for heat conductance quantization . . . . .	19
2.4.4	Heat transport through molecules . . . . .	21
2.4.5	Outlook and conclusions . . . . .	27
<b>3</b>	<b>Experimental Methods &amp; Instruments</b>	<b>31</b>
3.1	Working Principle . . . . .	31
3.1.1	Introduction . . . . .	31
3.1.2	Thermal STM-Break Junction . . . . .	32
3.1.3	Data acquisition and remote operation control . . . . .	33
3.1.4	Sensing circuits and Mathematical model . . . . .	35
3.2	Experimental Setup . . . . .	41
3.2.1	Noise Free Lab . . . . .	41
3.2.2	Room Temperature Setup . . . . .	44
3.2.3	Variable Temperature Setup . . . . .	45
3.3	Ultra-stable dry cryostat for variable temperature Break Junction (HIBERNUM) . . . . .	48
3.3.1	Abstract . . . . .	48
3.3.2	Intro . . . . .	48
3.3.3	Description of the setup . . . . .	50
3.3.4	Characterization of vibrational noise and its effects . . . . .	53
3.3.5	Break-Junction operation . . . . .	55
3.3.6	Outlook and conclusion . . . . .	56
3.3.7	Annex: Optical access . . . . .	56
3.3.8	Annex: Noise performance . . . . .	57
3.4	MEMS Sensor . . . . .	58
3.4.1	Design . . . . .	59
3.4.2	Fabrication process . . . . .	66
3.4.3	MEMS characterization and thermometer calibration . . . . .	68

3.5	Sample Preparation . . . . .	74
3.5.1	Cleaning steps . . . . .	74
3.5.2	Functionalization . . . . .	74
3.5.3	Mounting . . . . .	75
3.5.4	Tip etching . . . . .	75
3.6	Results on Quantum Point Contacts . . . . .	76
3.6.1	Experimental verification of Wiedemann-Franz law at room temperature . . . . .	77
<b>4</b>	<b>Results on Single Molecule Junctions</b>	<b>79</b>
4.1	Thermal Transport through Single-Molecule Junctions . . . . .	79
4.1.1	Abstract . . . . .	80
4.1.2	Introduction . . . . .	80
4.1.3	Methods . . . . .	81
4.1.4	Results and Discussion . . . . .	83
4.1.5	Conclusion . . . . .	91
4.2	Thermoelectric properties of Single-Molecule Junctions . . . . .	92
4.2.1	Abstract . . . . .	93
4.2.2	Introduction . . . . .	93
4.2.3	Experimental . . . . .	95
4.2.4	Results and Discussion . . . . .	96
4.2.5	Conclusion . . . . .	104
4.3	Complete thermoelectric characterization of OPE3-Anthracene . . . . .	105
<b>5</b>	<b>Machine learning tools for the analysis of single molecules</b>	<b>107</b>
5.1	Clustering tool . . . . .	107
5.1.1	Motivation . . . . .	107
5.1.2	Clustering principles . . . . .	109
5.2	Results . . . . .	111
5.2.1	OPE3-tetramethyl . . . . .	112
5.2.2	OPE3-dimer-C <sub>1</sub> & OPE3-dimer-C <sub>10</sub> . . . . .	116
5.2.3	para-pcp3 . . . . .	121
5.2.4	Conclusions & Outlook . . . . .	126
<b>6</b>	<b>Towards applications</b>	<b>129</b>
6.1	A roadmap for molecular thermoelectricity . . . . .	129
6.1.1	Abstract . . . . .	129
6.1.2	Introduction . . . . .	130
6.1.3	The Roadmap: 8 technological milestones . . . . .	131
6.1.4	Technological use cases . . . . .	134
6.1.5	Conclusions . . . . .	136
<b>7</b>	<b>Conclusion and Outlook</b>	<b>139</b>
	<b>Bibliography</b>	<b>143</b>
	<b>Author Contributions</b>	<b>159</b>

**Acknowledgements**

**161**



# 1 Introduction

---

The aim of this thesis is to add new experimental insights to the knowledge of thermal transport physics at the scale of single atoms and molecules, where quantum effects become apparent. In particular a new instrument and measurement protocol to study heat transport at the nanoscale will be introduced, and the key experimental results on single molecules will be presented and compared to the outcomes of the latest theoretical predictions. Finally, possible technological perspectives and future directions of the fields will be reviewed and commented.

**The Quantum Scale.** In the last decades, scientists all over the world have designed a plethora of different physical systems with dimensions smaller than few nanometers, in order to find answers to crucial questions: *How can we take full advantage of the quantum nature of matter? What is the typical scale of a quantum system and in which regime it can be operated? Can we control and engineer quantum devices? How are charges and energy transported within the quantum picture?* Some common examples of quantum-scale systems studied to answer those questions are classical and artificial atoms [1–4], Josephson junctions [5, 6], quantum point contacts (QPC) [7, 8] and single molecule junctions [9–11]. Many of them have been proposed to be used in novel technologies such as single electron transistors (SET), single photon sources, second harmonic generators, innovative solar cells and lasers [12–15]. In particular, Josephson junctions are already at the basis of present quantum computers [16–18], while natural and artificial atoms are mainly studied as alternative implementations for quantum bits (qubits)[2, 19]. QPCs and single molecules, instead, probably represent nowadays the most interesting systems for studying transport physics at reduced dimensions, thanks to their relative easy fabrication and broad chemical tunability [20–23].

**Thermal transport.** All of the quantum systems described above are already well known in terms of electrical properties, but much less is known in terms of their thermal properties and energy transport mechanism. Despite thermal engineering represents today the bottleneck for many technologies [24], and it has been widely recognized as one of the main limiting factors for the performances of nanoscale electronics devices [25, 26], measurements of heat conduction in quantum objects have remained elusive. This is mostly due to the lack of suitable experimental techniques. For instance, measuring thermal resistances is much more challenging than the electrical counter-part. One of the main reason is that the thermal conductivities of available materials extend over only 6 orders of magnitudes, while electrical conductivities cross more than 26. From this follows that the only good thermal insulator is essentially vacuum (if neglecting the contribution of radiation) and that standard electrical techniques as the 4-probe

measurement are not possible in thermal transport experiments. However, being able to engineer the thermal properties of materials would enable or improve many different technologies, from thermoelectric energy conversion to solid-state cooling, and this motivates the continuous research in the field.

Historically, the first theoretical description of thermal transport was provided in the early 1800s by the french physicist and mathematician Jean Baptiste Joseph Fourier. The law that brings his name states that the heat current density ( $J_q$ ) (i.e. the rate of heat transfer) is proportional to the temperature gradient ( $\nabla T$ ), as expressed by:

$$J_q = -\kappa \nabla T \quad (1.1)$$

where the coefficient  $\kappa$  is known as the thermal conductivity.  $\kappa$  is often treated as a constant, although this is not always true. First, it varies with temperature, even though for some common materials variation can be small over a significant range of temperatures [27]. Second, in anisotropic materials, the thermal conductivity typically changes with orientation and it can be represented by a second-order tensor. Third, in non-uniform materials,  $\kappa$  varies with the spatial location. Different models have been proposed to predict the thermal conductivity of a material. Among the most common, the one from Debye uses the concept of a gas of particles in a box to express, with simple kinetic theory, the thermal conductivity in terms of specific heat, velocity, and mean free path of specific quasi-particle called *phonons*, i.e. collective, periodic excitation in a lattice of atoms <sup>1</sup>. Although, in most solids heat conduction is actually mediated by phonons, several other actors take part to the thermal transport picture, like electrons, photons and even magnons [28–30]. Later, more precise and complete models have been developed, mostly based on a modified Boltzmann equation [31–33].

In recent years, for the obvious reason of being relevant to the miniaturization in the electronic industry, a lot of research has been carried out on microscopic systems, including thermal transport [34, 35]. At low dimensions, some notions very familiar at macroscopic scale, like the distribution function of both coordinate and momentum used in the Boltzmann equation, may not be valid anymore. Even the Fourier's law must be modified at the nanoscale. Indeed, equation 1.1 implies diffusive energy transfer and relies on the definition of local heat flux and temperature field, which are not well defined concepts at the atomic scale, and assume local equilibrium in the system [36–38]. For this reason, to characterize the heat transport properties of single atoms and molecules comprised between two electrodes, a better option is to use the thermal conductance

$$G_{th} = \frac{\dot{Q}}{\Delta T} \quad (1.2)$$

where  $\dot{Q}$  is the heat flow rate and  $\Delta T$  the temperature difference between the leads.

At this scale, also quantum effects become important, and classical equations must be replaced by something more fundamental [31]. Among the different possibility, one is to derive a quantum version of the Boltzmann equation [39, 40]. Another option is to use molecular dynamics (MD) [38, 41, 42], where the thermal conductivity can be computed thanks to the Green-Kubo functions, when the system is in equilibrium, or through a

---

<sup>1</sup>Phonons can be thought as quantized sound waves, in analogy to photons that are quantized light waves.

---

direct computation of the thermal current in nonequilibrium situations [31]. However, since MD is a method based on purely classical physics, quantum effects cannot be fully taken into account. Thus, the results obtained from MD are valid in the high temperature regime, where carriers obey Boltzmann statistics.

In a more simplified picture, when the linear regime (small  $\Delta T$ ) occurs, harmonic approximations can be used to describe the force fields involved, and, if the carriers mean free path is larger than the system size, phonon transport can be expressed in terms of ballistic and elastic interactions, within the Landauer formalism (see section 2.3). In this simplified particle-like picture, for example, the thermal conductance of a molecular junction,  $k_{ph}$ , is proportional to the transmission probability of the phonons  $T_{ph}(\omega)$ , travelling through it. The phonon transmission  $T_{ph}(\omega)$  is typically derived in terms of Green's function for single particle in combination with the mean field Hamiltonian of the system calculated with Density Functional Theory (DFT), from which the dynamical matrix describing the harmonic response is obtained. Within this method all inelastic processes are assumed to occur only in the leads and the force interactions between the atoms in the junction are calculated within the harmonic approximation. The main advantage of this ab-initio method is its intrinsically quantum nature, thus making it suitable to study quantum interference processes [14, 7, 12]. However, being a one-particle description, the interactions among different carriers (e.g. phonon-phonon, electron-phonon) cannot be taken into account. Furthermore, because inelastic processes are supposed to take place only in the leads, the temperature distribution inside the system is assumed to be homogeneous and non-linear phenomena, like rectification or memory effects cannot be included.

Despite the lacking of experimental data, numerous theoretical studies have been produced, predicting novel effects such as quantum phonon interference [43, 44], thermal rectification [45] and large efficiency for thermoelectric conversion [46]. The majority of those effects, however, still need to be verified experimentally. With the methods and instruments developed in this work, we aim to provide novel experimental verifications for some of those predictions, and to prompt the development of additional theoretical frameworks to support eventual, unexpected data, arising from the experiments.

As per title, this thesis presents strategies and tools for measuring the thermal transport properties of atomic and molecular junctions at the quantum scale, from the building of a new experimental setup, to the measurement protocols and results.

## Outline of the thesis

In Chapter 2, the theoretical framework for the physical phenomena investigated along this thesis is given, with a particular focus on phonon transport. The chapter also includes a theoretical perspective article, prepared for submission to the Applied Physics Review journal. In Chapter 3, a new instrument for the measurement of thermal transport at different temperatures is described. The results validating its performance are presented in the form of a contributed article, already submitted to the Review of Scientific Instruments journal. In the same chapter, also the mathematical model, the measurement protocol and sensor design, with detailed fabrication steps are given. At the end of the same chapter, the applied methods for sample preparation are

also explained. In Chapter 4, the results for the characterization of single molecules are presented within two publications in the ACS Nano Letters and Nanoscale journals. Results about single molecules were also analysed by means of new clustering tools based on machine learning algorithm, and presented in Chapter 5. In Chapter 6 possible applications are envisioned, with a technological roadmap highlighting the necessary step to eventually transition molecular thermoelectricity from research labs into the market. The roadmap is currently in press for the Nature Nanotechnology journal. In Chapter 7 a summary of the thesis is given and possible future research directions discussed.

# 2 Theoretical background

In this chapter, the theoretical background related to charge and phonon conduction at the quantum scale will be presented. First, charge transport in quantum point contacts and molecular junctions will be introduced, together with the break-junction technique. Secondly, basic notions of thermoelectricity and energy-filtering capabilities of molecules will be delineated. Finally, phonon transport in nanoscale systems will be described within the Landauer formalism, presenting the concepts of thermal conductance quantization and phonon transmission, with a particular focus on molecular junctions.

## 2.1 Charge transport

Different transport regimes can take place according to the size of the system under study. In everyday life, when we deal with macroscopic conductors, their electrical conductance can be calculated from the notorious Ohm's law:

$$G = \sigma \frac{A}{L} \quad (2.1)$$

where  $A$  represents the cross-section area of the conductor perpendicular to the current direction,  $L$  the conductor length parallel to the current direction and  $\sigma$  its conductivity, that depends only on material properties. This formula is valid only in case of *diffusive transport* and assumes a homogeneous current distribution inside the conductor. Interestingly, when the size of the conductor goes below certain boundaries, Ohm's law doesn't hold anymore, and the quantum wave-character of electrons comes into play. Figure 2.1 shows a schematic of the two major transport regimes and characteristic lengths, when transitioning from the macro- to the quantum scale.

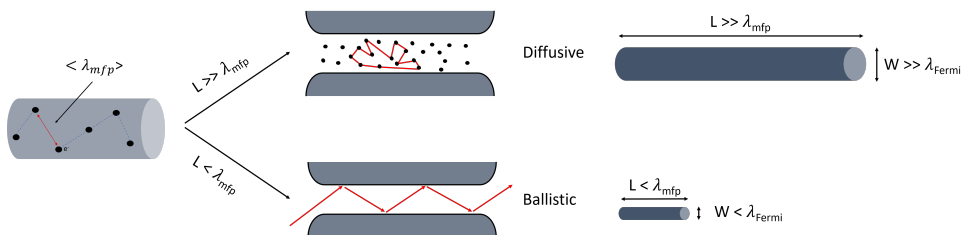


**Figure 2.1** Different transport regimes according to the sample dimension  $L$  and the electron mean free path  $\lambda_{mfp}$ .

To distinguish among the different transport regimes, two main characteristic lengths must be taken into consideration:

- The electron mean free path  $\lambda_{mfp}$ : average distance that an electron can travel before losing its initial momentum. In most of the cases, it corresponds to the distance between two successive scattering events.
- The Fermi wavelength  $\lambda_F$ : De Broglie wavelength of the electrons, at the Fermi energy, participating to the conduction.

There is also another important length parameter that comes into play when dealing with electron interference phenomena: the phase-coherence length  $\lambda_\phi$ . This corresponds to the average distance for which the electron preserves its initial phase.

When the size of the system is lower than the electron mean free path, charge transport becomes ballistic. Additionally if one of the system's dimensions is equal or smaller than the Fermi wavelength  $\lambda_F$ , confinement effects occur. Atomic filaments formed during break junction experiments are quantum one-dimensional ballistic systems, as their typical diameter, of about few atoms, is on the order of the Fermi wavelength of the electrodes material ( $\lambda_F \sim 0.5$  nm in metals [47]), while their length, that can go up to few nm (see sec. 3.3.5), is much below the electron mean free path (10-100 nm) at room temperature [47, 48]. For this reason they are also called Quantum Point Contacts (QPCs). Usually, in QPCs, charge transport is described with the help of the Landauer-Büttiker formalism, introduced first by Rolf Landauer in 1957 [49] and then generalized some years later for multiple probes by Markus Büttiker [50]. Their formula connects the electrical properties of a mesoscopic conductor to the transmission probability coefficients of the propagating quantum modes (i.e. electron wavefunctions).

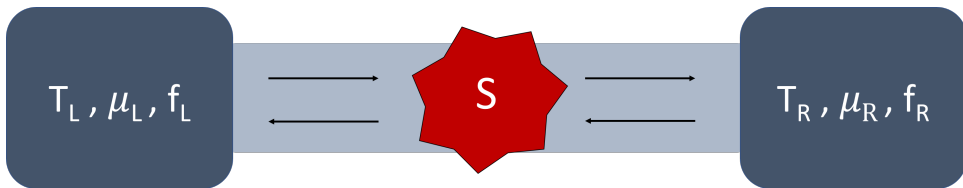


**Figure 2.2** Schematic representation of 1D ballistic channel with a scattering center S. Being transport ballistic through the system, electrons can elastically scatter at S. Here,  $\mu$  is the chemical potential<sup>1</sup>, T is the temperature of the leads, while f is the Fermi distribution.

Let us consider a 1-dimensional ballistic channel along x-direction, with its extremities connected to macroscopic leads acting as electron reservoirs. The channel contains a scatterer S, i.e. a non-uniformity which can cause electrons to scatter, Figure 2.2. As the electrons are confined along the other directions, their energy spectrum results quantized. The resulting dispersion relation is:

$$E_n(k_x) = \varepsilon_n + \frac{\hbar^2 k_x^2}{2m^*} \quad (2.2)$$

<sup>1</sup>Often in literature as well as in this work, the chemical potential  $\mu$  and the Fermi energy  $E_F$  are used as synonyms. Despite the distinction is not relevant for the purposes of this thesis, we note that this is formally true only when  $T = 0$  K. In the following, both terms will be used interchangeably.

where  $\hbar$  is the reduced Planck constant,  $m^*$  is the effective mass of the electron and the integer  $n$  is the principal quantum number. In the reciprocal space this translates into  $n$ -parabolic sub-bands, whose vertices are at  $\varepsilon_n$  for integer values of  $n$ . Since electrons can move along  $x$ , while are confined along  $y$  and  $z$ , their corresponding wave-functions  $\Psi_n$  can be written as the product of a propagating plane-wave in the  $x$ -direction times a transverse wave-function  $\chi_n(y, z)$ , obtained as solutions of the Schrödinger equation for a 1-dimensional wire:

$$\Psi_n \propto e^{\pm ik_x x} \cdot \chi_n(y, z) \quad (2.3)$$

To wit, those are the (only) propagating modes travelling through the 1D conductor, i.e. the *available* conduction channels. According to the position of the Fermi energy, electrons can occupy one or more sub-bands. If  $T_L = T_R$  and a positive voltage difference is applied to the right reservoir, electrons will flow from left to right, since  $\mu_R < \mu_L$ . The contribution to the electrical current  $I$ , for a single conductive channel of length smaller than  $\lambda_{mfp}$ , can then be written as:

$$I = -\frac{e}{\pi} \int_{-\infty}^{\infty} \tau(k) \rho(k) v(k) (f(E_k, \mu_L) - f(E_k, \mu_R)) dk \quad (2.4)$$

where  $\tau(k)$  is the transmission probability involving the scattering at S,  $\rho(k)$  is the density of states in 1 dimension,  $v(k)$  the electron velocity and  $f(E_k, \mu)$  the Fermi distribution. It is possible to demonstrate [51] that the electron density of states as function of energy, for a given direction, is equal to:

$$\rho(E) = \frac{4}{h} \cdot \frac{1}{v(E)} \quad (2.5)$$

Thus, moving into the energy domain, equation 2.4 translates to:

$$I = -\frac{2e}{h} \int_0^{\infty} \tau(E) (f(E, \mu_L) - f(E, \mu_R)) dE \quad (2.6)$$

where the factor 2 accounts for spin-degeneracy. This equation is very general and applies broadly. The specific properties of the system under study (represented by the scatterer) are all contained in the transmission function  $\tau(E)$ , that can be theoretically calculated with ab-initio methods based on Density Functional Theory (DFT) in combination with tight-binding models or Green's function scattering theory [21, 52]. Let's now assume to study a perfect 1D conductor ( $\tau(E) = 1$ ) at  $T = 0$  K. At this temperature, the Fermi distribution is a step function equal to 1 for  $E < \mu$  and 0 otherwise. Therefore the difference ( $f(E, \mu_L) - f(E, \mu_R)$ ) is equal to 1 for energies  $\mu_R < E < \mu_L$  and it is null outside the interval<sup>2</sup>. Eq.2.6 then simplifies to:

$$I = -\frac{2e}{h} \int_{\mu_R}^{\mu_L} dE = -\frac{2e}{h} \cdot (\mu_L - \mu_R) \quad (2.7)$$

<sup>2</sup>For temperature  $T \neq 0$  K, the difference  $f(E, \mu_L) - f(E, \mu_R)$  can still be approximated as a delta function if the applied voltage is small in the scale of  $k_B T$

Being the chemical potential difference proportional to the voltage difference through the electron charge, i.e.  $(\mu_L - \mu_R) = -e(V_R - V_L)$ , the contribution of a single channel to the electrical current becomes:

$$I = \frac{2e^2}{h} \cdot (V_R - V_L) = G \cdot (V_R - V_L) \quad (2.8)$$

This means that, in the ballistic regime, the conductance of a perfect single electron channel is constant and equal to the quantum of electrical conductance  $G_0 = \frac{2e^2}{h} \simeq 77.5 \mu S$ , that corresponds to a quantized resistance of  $R_0 = \frac{h}{2e^2} \simeq 12.9 k\Omega$ .

In case the number of available perfect channels  $N$  is larger than 1, the total conductance  $G$  will be equal to the sum of all the  $N$  single-channel contributions  $G_0$ , that is:

$$G = N \cdot \frac{2e^2}{h} = N \cdot G_0 \quad (2.9)$$

This formula is a special case of the Landauer-Büttiker formalism, where all the conductive channels show perfect transmission. For a more general formulation, the role of the scatterer must be taken into account, by considering that some electrons have a non-null probability to be backscattered or lose energy. In this case we get:

$$G = \frac{2e^2}{h} \sum_{i,j}^N T_{ij} \quad (2.10)$$

where  $T_{ij}$  represents the transmission probability for an electron to go from the  $i_{th}$  mode of the left reservoir to the  $j_{th}$  mode of the right reservoir [47, 49, 50].

### 2.1.1 Electrical conductance in Quantum Point Contacts

There are two major strategies to control the number of electronic channels available for conduction. The first one consists in shifting the Fermi energy of the system  $E_F$  by applying a gate voltage. The second one changes the spacing between energy subbands by precisely tuning the size of the system. Several demonstrations of conductance quantization have been reported for different materials, but not all of them at room temperature. In fact, the energy splitting among the different channels depends on the Fermi wavelength  $\lambda_F$ , in accord with the following formula:

$$\Delta E = \frac{\pi^2 \hbar^2}{2m^* \lambda_F} \quad (2.11)$$

For semiconductor materials  $\lambda_F$  can be on the order of several tens of nanometers, resulting in an energy splitting of only few meV. At  $T = 300$  K, the average thermal energy  $K_B T$  is  $\sim 26$  meV, larger than the spacing between the modes. For this reason, in those materials, conductance quantization is only observable at cryogenic temperatures [8, 53]. Differently, for metals  $\lambda_F$  is much smaller ( $\sim 1$  nm) and the resulting  $\Delta E$  is on the order of  $\sim 1$  eV. So for atomic size metallic systems, conductance quantization can be observed even at room temperature [54, 55].

In order to control precisely the size of the metallic contacts two techniques has been exploited successfully, namely the Mechanically Controlled Break Junction (MCBJ) [56, 57] and the Scanning Tunnelling Microscope-Break Junction (STM-BJ) [47, 57]. Since the latter is the technique employed to perform most of the experiments in this thesis, the theoretical basis will be provided in the following section while the actual implementation, adapted for thermal studies, will be given in section 3.1.

### STM Break Junction for QPC

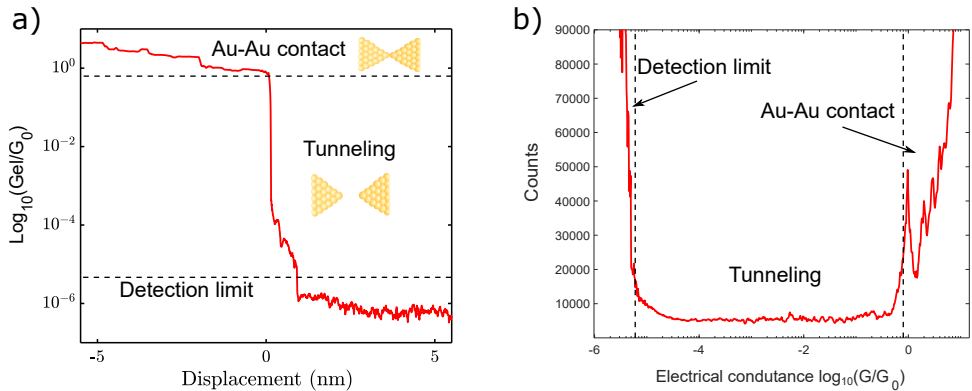


**Figure 2.3** Charge transport through gold quantum point contact. a) Example of single opening trace. The origin for the x-axis is set at the breaking of the last atom contact. b) 1D electrical histograms built from more than 1700 opening traces showing peaks at multiples of the electrical conductance quantum  $G_0$ . In both charts the three conductance regions (contact, tunnelling, detection limit) are indicated.

The STM-Break Junction technique is based on the repeated creation and breaking of the contact between the tip of a scanning tunnelling microscope and a second metallic electrode. This technique has been exploited since the the nineties to study the electrical conductance of atomic point contacts of gold and other different metals [47, 54, 58]. A measurement of the electrical conductance as function of the distance between the two electrodes performed during the creation of the contact is called *closing trace*, while a measurement done during the breaking of the same contact is called *opening trace*. Fig. 2.3 a) shows a typical break junction measurement for an opening trace between two gold electrodes recorded at small bias ( $<90$  mV, with a series resistor of 100 k $\Omega$ ). Since the signal varies by several orders of magnitude along a trace, it is typically plotted on a logarithmic scale and normalized by the conductance quantum  $G_0$ . In general a closing trace stops when a contact of few  $G_0$  is observed. Then, the relative opening trace starts, the contact is broken and the conductance decreases in a typical step-like fashion due to quantization. When the size of the contact reduces below 3 atoms, the quantization steps (or plateaus) visible in the conductance traces, can be related to the number of atoms connecting the tip to the second electrode. If the system is mechanically stable enough, just before entering into the tunnelling regime, a plateau

at  $1 G_0$  is typically observed, indicating the formation of a single atom contact. Indeed, in case of pure gold (Au), a single atom corresponds to one electron channel available for conduction with perfect electron transmission ( $\tau = 1$ ). This characteristic of gold is now well understood and it has been confirmed both experimentally and theoretically by several independent groups [47]. In particular at low temperatures, long ( $> 0.3$  nm)  $1 G_0$  plateaus can be observed, corresponding to the formation of single-atom chains [59–61] (see also section 3.3). Due to the mechanical re-arrangement of the junction and the different configuration it can assume, it is common and good practice to build one dimensional (1D) electrical histograms of few thousands traces to obtain enough statistics to infer relevant information about the charge transport properties, as shown in Fig. 2.3 b). When fully in contact ( $G > 1 G_0$ ), sharp peaks at multiples of the quantum of conductance  $G_0$  may appear, indicating the accessibility of an integer number of electronic channels and confirming the hallmark of quantization. In fact, peaks not located at multiple of  $G_0$  are usually associated to the plastic deformation of the junction and not to conductance quantization. In gold contacts, conductance quantization typically occurs up to  $3G_0$  [62].

### 2.1.2 Electrical conductance in Single Molecule Junctions

Within the field of molecular electronics, charge transport through molecular junctions has been thoroughly studied in the last 20 years. As a result, several books and reviews are now available in the literature describing the different aspects of conduction through single molecules [20, 57, 63–65]. In an energy diagram, an isolated molecule can be imagined as a quantum dot, featuring discrete energy levels and a characteristic HOMO-LUMO gap (i.e. a gap between the Highest Occupied Molecular Orbital and the Lowest Unoccupied Molecular Orbital). When a molecule is contacted by two electrodes and a junction is formed, due to a hybridization process of its orbitals, the discrete levels of the molecule are broadened by the coupling with the metal electrodes [64], as schematically shown in Fig. 2.4.

The stronger the coupling with the electrodes, the larger the broadening of the energy levels, and so the probability to inject charges into the molecule. Besides, a charge transfer from the molecule to the metal electrodes (or vice versa) is needed in order to reach an equilibrium state (constant Fermi level) inside the junction, with the additional charging energy introducing a shift in the levels. The electrical conductance  $G_{el}$  of a molecular junction can be derived from the Landauer formula for current (eq. 2.6). The transmission function  $\tau(E)$  appearing in the formula can be calculated with Non Equilibrium Green's Function (NEGF) methods applied to the Hamiltonian of the junction, whose fundamental electronic state can be calculated by means of Density Functional Theory (DFT) [52]. The position of the peaks in the transmission function corresponds to the energies of the molecular orbitals, and their width is proportional to the coupling strength with the electrodes. If the energy of the electrons travelling through the contacts is equal to one of the molecular orbitals, then resonant tunnelling occurs. Unfortunately the requirements to get resonant tunnelling are hard to achieve without proper electrical gating of the junction. The Fermi energy of the metal-molecule-metal system in fact, generally lies inside the HOMO-LUMO gap, and the so called *off-resonant elastic tunnelling* represents the main mechanism for charge transport in short molecules ( $< 3$  nm). For longer molecules instead, tunnelling mediated transport becomes negligible

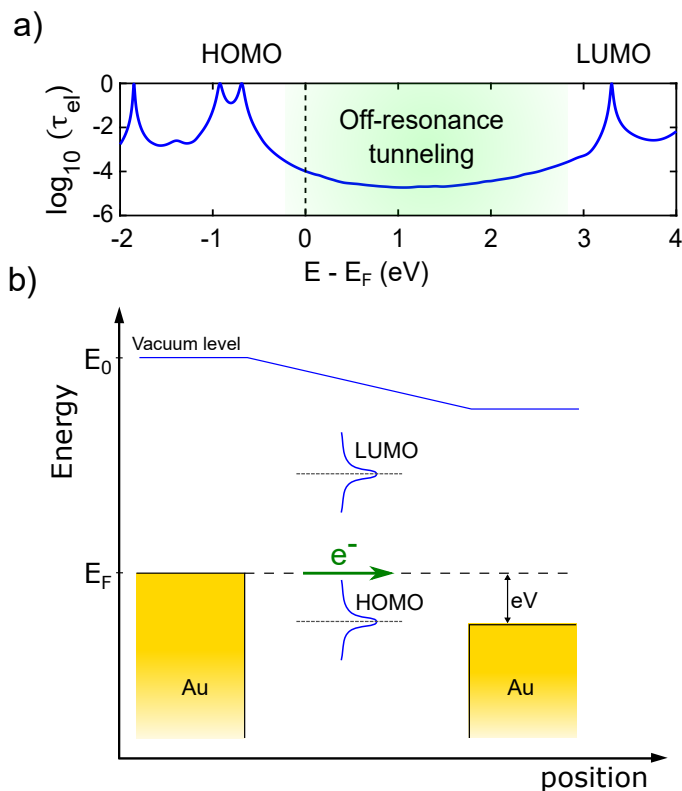


**Figure 2.4** Charge transport mechanism through a single molecule. a) An example of electronic transmission function ( $\tau_{el}$ ) through a HOMO-dominated single molecule junction. The origin of the energy scale has been shifted to the predicted Fermi energy of the junction  $E_F$ . b) Energy diagram of a single molecule junction between two gold leads. A positive voltage  $V$  has been applied to the right electrode. The HOMO and LUMO molecular energy levels are broadened because of the electrodes coupling.

and a different mechanism called *inelastic hopping* kicks in, in which electron transport is mediated by thermal lattice vibrations [66]. Therefore, the position of the Fermi energy determines the charge transport properties of the molecular junction. In case of small bias voltage the difference between the Fermi distributions of the leads can be approximated as a delta function. Hence, the electrical conductance of the junction can be calculated from 2.6 as:

$$G = \frac{2e^2}{h} \tau(E_F) \quad (2.12)$$

where  $\tau(E_F)$  is the value of the transmission function at the Fermi energy. Usually, the position of the Fermi energy in the junction is not known and cannot be exactly located with DFT methods. This gives rise to a possible bad agreement on the precise value of  $G_{el}$  between theory and experiments and it is a well-known limitation of DFT methods. Another important role in influencing the charge transport properties of molecular junctions is played by the anchoring groups (atomic groups binding to the metal electrodes), that determine if the junction is HOMO or LUMO conducting (i.e.  $E_F$  closer to the HOMO or LUMO respectively). For example sulphur based binding groups generally show a HOMO conducting behaviour, with holes entrusted for charge transport, while pyridine-based anchoring groups are LUMO conducting [67, 68]. This behaviour will also influence the sign of the Seebeck coefficient, as described in the future section 2.2.

### STM Break Junction for Single Molecule

Also in the case of single molecules, charge transport has been extensively studied with break-junction techniques [57]. The main benefit of this technique is to be experimentally easy to implement and that can be exploited in completely different environments from solvents at room temperature [69] to ultra-high-vacuum at cryogenic temperatures [70]. In a standard molecular STM-BJ measurement, molecules are deposited on a metallic surface (usually gold) to form a scattered layer. The STM tip is then used to trap molecules while repeatedly forming and breaking the electrical contact with the substrate electrode. While opening the metallic junction, in fact, there is a certain probability to catch a single molecule between the two electrodes. The constant tunnelling current flowing through the molecule gives a very different signature with respect to normal tunnelling through the empty gap, allowing for the identification of a single molecule in the junction. Figure 2.5 a) shows a typical opening trace ( $G_{el}$  vs. tip separation) exhibiting a roughly constant current plateau, that is the typical signature of the sliding motion of the molecule in between the two gold electrodes [71].

To extract the most probable conductance of the molecule, 1D electrical histograms are built out of few thousands opening traces. Molecular signature appears as a broad peak below  $1 G_0$  in the histogram, see Fig. 2.5 d). Compared to the case of bare Au-Au junctions, Figure 2.3 didn't show any particular feature in the tunnelling regime. A second important tool for the study of molecular break junction signals, is the 2D histogram of the electrical conductance  $G_{el}$  versus displacement, Figure 2.5 e). In order to build this kind of histograms, the origin of the displacement axis for each opening trace is rescaled according to the breaking point of the Au-Au contact (end of the  $1 G_0$  plateau), so that traces with different lengths can be analysed together. In this way, the Au-Au contact will appear in the negative side of the displacement axis, while the

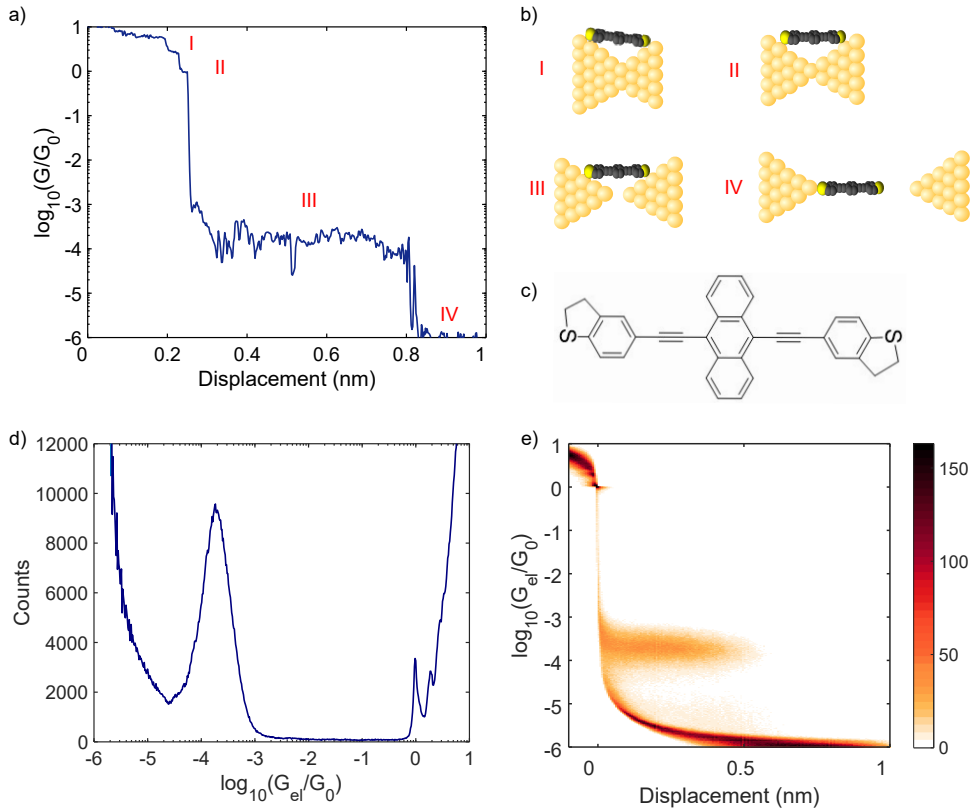


**Figure 2.5** STM Break Junction of a single molecule. a) Example of a single molecule break junction opening trace, featuring a conductance plateau around  $1 \times 10^{-4} G_0$  for the OPE3-Anthracene molecule. The constant current plateau is an indication for the formation of a molecular junction. b) Schematic representation of the sliding of a molecule inside the junction. c) Structural formula of the Anthracene molecule. d) 1D electrical histogram built with 5000 traces displaying an apparent molecular peak around  $2 \times 10^{-4} G_0$ . e) 2D histogram of electrical vs. distance curves, demonstrating that most of the opening traces exhibits a molecular conductance plateaus between  $1 \times 10^{-3}$  and  $1 \times 10^{-4} G_0$ . Data in the figure have been obtained in collaboration with N.Mosso.

molecular regime in the positive one. Results are usually displayed as 2D histograms since they make easier to recognize artefacts and unpredicted variations of the tip-surface contact. In fact, peaks in the 1D electrical histograms can be misleading and arise from contaminated spurious opening traces, which could hinder the identification of the characteristic molecular signature.

## 2.2 Electronic thermal transport and Thermoelectricity

Within the Landauer formalism is also possible to describe the electronic contribution to the thermal transport for atomic and molecular junctions [52]. In a linear regime, the current  $I$  and heat flux  $\dot{Q}$  are related to the temperature difference  $\Delta T$  and the voltage difference  $\Delta V$  by the following mutual relations [72, 73]:

$$\begin{pmatrix} I \\ \dot{Q} \end{pmatrix} = \begin{pmatrix} G & L \\ M & K \end{pmatrix} \begin{pmatrix} \Delta V \\ \Delta T \end{pmatrix} \quad (2.13)$$

The Seebeck coefficient  $S$  is then defined as:

$$S = \left( \frac{\Delta V}{\Delta T} \right)_{I=0} = -L/G \quad (2.14)$$

and the thermal conductance  $k$ :

$$k = - \left( \frac{\dot{Q}}{\Delta T} \right)_{I=0} = -K - S^2 G T \quad (2.15)$$

where the minus sign in the definition of the thermal conductance takes into account the heat flux direction.

In this framework, those coefficients depend on the transmission function  $\tau(E)$  in the form:

$$G = -\frac{2e^2}{h} \int_0^{+\infty} dE \frac{\partial f}{\partial E} \tau(E) \quad (2.16)$$

$$L = -\frac{2e^2}{h} \frac{k_B}{e} \int_0^{+\infty} dE \frac{\partial f}{\partial E} \tau(E) (E - E_F) / k_B T \quad (2.17)$$

$$\frac{K}{T} = \frac{2e^2}{h} \left( \frac{k_B}{e} \right)^2 \int_0^{+\infty} dE \frac{\partial f}{\partial E} \tau(E) [(E - E_F) / k_B T]^2 \quad (2.18)$$

where  $k_B$  is the Boltzmann constant. If the transmission function  $\tau(E)$  varies slowly around the Fermi energy  $E_F$  on the scale of  $k_B T$ , these integrals can be simplified with the Sommerfeld expansion. We get:

$$K \approx -\frac{2e^2}{h} T L_0 \tau(E_F) \quad (2.19)$$

$$G \approx \frac{2e^2}{h} \tau(E_F) \quad (2.20)$$

with  $T$  being the temperature of the system and  $L_0 = \frac{k_B \pi^2}{3e} = 2.44 \text{ V}^2/\text{K}^2$  the Lorenz number. It follows that, if  $S^2 \ll L_0$  the electronic contribution to the thermal conductance is proportional to the electrical conductance via the so called Wiedemann-Franz law:

$$k_{el} \approx L_0 T G \quad (2.21)$$

Eventually, the Seebeck coefficient  $S$  is then proportional to the slope of the transmission function  $\tau(E)$  via:

$$S \approx -L_0 e T \left( \frac{d \ln(\tau(E))}{dE} \right) \quad (2.22)$$

Those equations predict that in metallic contact, the electronic contribution to the thermal conductance will be proportional to the electrical conductance, as the transmission function  $\tau(E)$  is mostly flat around  $E_F$ . However, it is important to remember that this approximation does not include the phonon contribution to the thermal conductance, and that in case of molecular junctions, is valid only if the Fermi energy is far from the resonances.

## 2.3 Phonon transport

Similar to the case of charge transport, the Landauer-Buttiker formalism can also be applied to sample of small dimensions to describe thermal transport in terms of *phonons* flowing through a quantized number of transmission channels [74–76]. To take into account the fact that those channels are often not ideal and thus carriers have a non-null probability to be scattered or lose energy, a transmission factor ( $\tau \leq 1$ ) must be introduced. To derive the conductance formula for phononic transport inside a molecule between two reservoirs, we can start from the definition of the heat flow rate  $\dot{Q}$ :

$$\dot{Q} = \frac{1}{2\pi} \sum_m \int_0^\infty dk \hbar \omega_m(k) v_m(k) (n_R - n_L) \tau_m(k) \quad (2.23)$$

here  $\dot{Q}$  is the sum over all phonon frequencies  $\omega$  for all phonon modes  $m$ , and  $n_{R,L}(\omega, T)$  is the Bose-Einstein distribution function for phonons in the right (R) and left (L) reservoir.  $\tau(\omega)$  is the transmission coefficient indicating the probability of a phonon to be transmitted through the molecule. Since the phonon velocity  $v_m(k) = \partial \omega_m / \partial k$  and the 1D density of states  $\rho_m(k) = \partial k / \partial \omega_m$  cancel each other out, we can write eq. 2.23 as:

$$\dot{Q} = \frac{1}{2\pi} \sum_m \int_{\omega_m(0)}^\infty d\omega \hbar \omega [n_R(\omega) - n_L(\omega)] \tau_m(\omega) \quad (2.24)$$

The thermal conductance between the two reservoirs  $g = \dot{Q} / \Delta T$  is obtained in the linear response regime assuming that a small temperature difference  $\Delta T$  is applied on the system. This allows for writing  $[n_R(\omega) - n_L(\omega)] \approx \Delta T \frac{\partial n(\omega, T)}{\partial T}$ , hence we get:

$$g = \frac{1}{2\pi} \sum_m \int_0^\infty d\omega \hbar \omega \frac{\partial n(\omega, T)}{\partial T} \tau_m(\omega) \quad (2.25)$$

Thereby, if the transmission probability  $\tau$  is unity, the above integral depends only on temperature, and for each channel  $m$  we find:

$$g_0 = \frac{\pi^2 k_B^2 T}{3h} \quad (2.26)$$

Here,  $k_B$  is the Boltzmann's constant and  $T$  the absolute temperature. For imperfect channels, eq. 2.26 becomes:

$$g = g_0 \sum_m \tau_m \quad (2.27)$$

In the past, given the challenges in measuring tiny heat flux, thermal properties of organic molecules have been studied mostly theoretically [77–79]. The very few experimental studies investigated the average properties of self assembled monolayers (SAMs) where, however, the uncertainty on the number of molecule contacted represents one of the biggest source of error [80]. For this reason in the last decade a lot of researchers focused on performing experiments at the single molecule level, with two independent groups succeeding in measuring for the first time the thermal conductance of single molecules [23, 81]. Given the new experimental capabilities, in the next section the future directions and applications of phonon engineering in quantum channels will be discussed, walking the reader through the main theoretical and experimental milestones that have characterized, so far, phononic transport at the atomic and molecular scale.

## 2.4 Perspective: Phonon thermal transport through quantum channels and molecules

This chapter is based on a preliminary version of an article that the author of this thesis, together with Dr. Bernd Gotsmann and Prof. Dvira Sagal, is preparing for submission to the Applied Physics Review journal.

### Quantum phonon transport through channels and molecules - a perspective

Bernd Gotsmann and Andrea Gemma<sup>\*</sup>

*IBM Research - Zurich, Säumerstrasse 4, 8803 Rüschlikon, Switzerland.*

Dvira Segal

*Department of Chemistry and Centre for Quantum Information and Quantum Control,  
University of Toronto, 80 Saint George St., Toronto, Ontario, M5S 3H6, Canada and*

*Department of Physics, 60 Saint George St., University of Toronto, Toronto, Ontario, Canada M5S 1A7*

**AUTHOR CONTRIBUTIONS:** BG conceived the paper and wrote the main structure. AG contributed to the sections involving electronic thermal transport and experiments on quantum point contact and single molecules. AG also prepared the figures. DS wrote the section about the theoretical insights into conductance quantization, that however has not been included in the following.

### 2.4.1 Abstract

Phonon transport is the dominant mechanism of thermal conduction in most solids and has been studied for decades. A good understanding on many transport regimes in micro- and nanostructures could be established, including ballistic and diffusive transport, mode softening, or band structure engineering in phononic crystals. On the other hand, the limit of quantized transport and the engineering of single transport channels is much less explored, due to the challenges in reaching the necessary experimental sensitivity and control during the experiments. Recently, however, heat transport measurements through quantum channels and single molecules have become available at room temperature using break junction techniques. These techniques are well established in the molecular electronics community and have recently been expanded to the measurement of heat transport on the single-molecule level. Given the latest results, it is now inviting to address the rather unexplored area of molecular phonon-engineering, focusing both on theoretical prediction and experimental open questions.

### 2.4.2 Quantized and quantum thermal transport

In this perspective, we discuss thermal transport mediated by phonons in quantum channels, at the atomic and at the molecular scale. To explore the richness of transport physics in general, it has proven useful to study transport on various length scales and explore low-dimensional geometries. Small contacts or wires, for example, have been used to explore charge, heat or mass transport. Phonon transport through contacts is already a well-known way to explore fundamental transport properties (see for example [82–88]). A contact between two bodies, such as a mechanical contact between a tip and a surface, can be experimentally scaled to small dimensions such that different characteristic length scales and thereby transport regimes can be tested. For example, the transition from diffusive to ballistic transport of charge or heat carriers has been studied by reaching contact diameters below the mean-free path of carriers [87]. Similarly, transport in one-dimensional structures such as wires undergoes characteristic changes when transitioning between these two transport regimes [88].

Reducing the sample dimensions even further leads to quantization effects, a transport regime well studied for charge transport and much less explored for heat transport. At those relatively small lengths, the Landauer-Buttiker picture of transport is very popular, expressing the transport in terms of conductance through quantized transport channels. If the channels are perfect (i.e. if it is possible to assume perfectly adiabatic contact between the thermal reservoirs and the sample), one finds:

$$g_0 = \frac{\pi^2 k_B^2 T}{3h} \quad (2.28)$$

for each channel.

In a more general case of  $m$  imperfect channels, one expresses

$$g = g_0 \sum_m \tau_m \quad (2.29)$$

with a suitable effective transmission coefficient  $\tau_m$ . The number of transmission channels in crystalline solids at sufficiently low temperature is four, including two transversal, one longitudinal and one twisting mode [29].

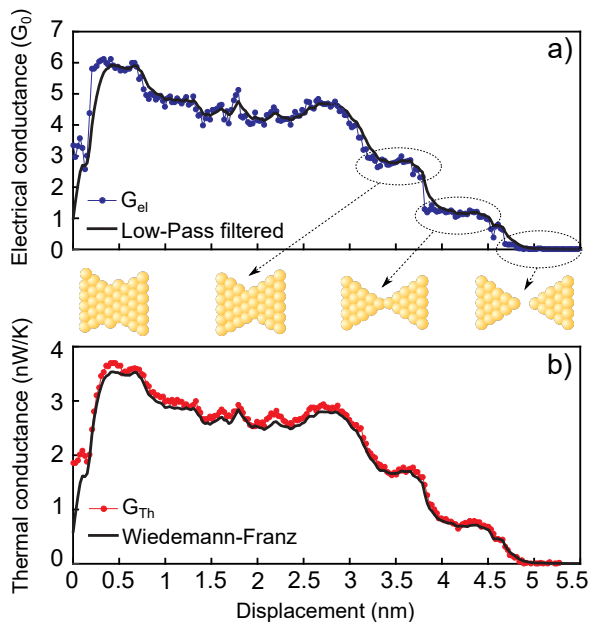


**Figure 2.6** Electrical and thermal conductance signal during a break-junction experiment. Here a gold-contact is gradually broken at room temperature through the displacement of an actuator. a) The electrical conductance values are clustered around multiples of the conductance quantum, which can be correlated with the thinning of gold wire down to a single atom diameter (center row). b) The simultaneously-measured thermal conductance exhibits quantization with multiples of the thermal conductance quantum. Image from [22]

### 2.4.3 Experimental evidence for heat conductance quantization

The observation of quantized heat transport based on phonons has only rarely been claimed. One important reason for this may be the small magnitude:  $g_0$  is only  $\sim 600$  pW/K at 300 K, and  $\sim 20$  pW/K at 10 K. To estimate below which constriction's diameter quantization can be expected, one should consider the characteristic dimension of a phonon wave packet through the thermal wavelength  $\lambda_{th} = hc/k_B T$  [29], where  $c$  is the phonon velocity. At room temperature this can nearly reach atomic dimensions. The highly original landmark paper of Schwab *et al.* [89] has observed a minimum of  $g_0$  for four channels in nano-constrictions of  $< 200$  nm in silicon nitride, when T was lowered to below 1 K. These findings, however, were not experimentally reproduced. Quantized thermal transport was invoked in so-called nano-asperities of contacts with atomic roughness to explain the large pressure-dependence of heat transport in nano-contacts [90]. However, the indications are somewhat indirect and remain controversial [91, 92].

A recent, and very careful study by Tavakoli *et al.* [93] tackled the problem also using micro-fabricated constrictions in silicon nitride. Similar to the study of Schwab *et al.* [89], the shape of the constriction was chosen to form an impedance matching [74], a prerequisite of achieving ideal transmission ( $\tau = 1$ ) in microscale devices. (This impedance matching is similar and analogous to matching acoustic mismatch between sound in 3D air and the speaker of a hi-fi sound system). However, quantization effect through reaching a minimum constant conductance of  $N \cdot g_0$  for lowering T was not observed by Tavakoli *et al.*. Instead, the conductance reduced further, which was interpreted as imperfect transmission, in accordance to theoretical predictions [94]. It therefore remains to be shown to what extent the quantization of heat transport can be viewed as universal in phonon transport of nanowire systems or can merely be viewed as a theoretical upper limit.

#### Quantized heat transport through single-atom contacts: electronic contribution

A somewhat special case for the measurement of quantized transport are so-called quantum point contacts (QPCs) [95, 96]. QPCs are narrow constrictions between two wide conducting regions. One example is the constriction between electrically conducting regions in two-dimensional conductors. For sufficiently narrow constrictions, transport through such constrictions is quantized in electrical and thermal conductance signals [96]. Experimentally easily accessible is a special kind of QPCs, in which the narrow constriction is formed through slow and gradual breaking of a mechanical contact of ductile metals, i.e. so-called break junction experiments. In charge transport, quantized electrical conductance can be routinely observed in such QPCs. The ability to form single-atom junctions using break-junction techniques has led to the observation of electrical conductance quantization in gold and several other metals. A particular benefit in studying break-junction QPCs is the ease to make an atomically-thin constriction, which exhibits quantization effects up to room temperature. It is conceptually simple and can be easily reproduced. Such QPC are also referred to as atomic junctions.

Quantized heat transport in atomic junctions of gold was recently measured by one of the authors and team [22, 97], see Figure 2.6, and independently reproduced by Cui *et al.* [92]. Both studies used micro-fabricated heater-sensors, operated in vacuum at room

temperature. The approach is based on the well-established break-junction technique, in which a mechanical contact between a gold tip and gold surface is slowly broken such that conductance steps can be observed in the electrical signal. For this a break-junction experiment was set up with one of the electrodes being situated on heater/sensor element capable of reaching sub-nW/K sensitivity to thermal conductance, when biased to a few tens of K with respect to the other electrode, a tip remaining at room temperature. During the experiment, the gold tip was repeatedly pushed into and out of contact with a gold electrode on the MEMS sensor, which was heated to above ambient temperature. The resulting small change of temperature measured in the MEMS sensor at constant heating power is then detected and used to calculate the thermal conductance of the junction by subtracting the much larger conductance of the MEMS supporting beams. Figure 2.7 shows the experimental arrangement with tip and MEMS heater/sensor, operated in vacuum. The results showed conductance quantization in parallel with the electrical conductance quantization, see Figure 2.6. Within the measurement uncertainty (of below 20%), the Wiedemann Franz relationship is confirmed. This implies that heat is almost entirely carried by electronic excitations and phonon transport plays a minor role. This is expected because the experiments were performed at room temperature, and therefore far above the Debye temperature and the realm of applicability of the above 'derivation' of quantized thermal transport. Furthermore, it is consistent with the notion that the electron scattering processes involved are conventional in that they scatter energy and momentum alike. Numerical simulations and analytical estimations are in agreement with the experimental data.

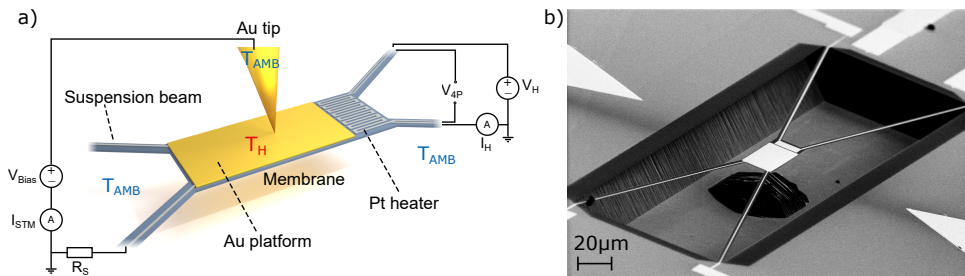


**Figure 2.7** (a) Schematic of the experimental arrangement measuring quantized electronic heat transport (not to scale): A silicon nitride MEMS platform comprises both a platinum thin film heater/sensor and a gold electrode. It is operated in vacuum using DC electronics circuits to measure electrical conductance (left) and thermal conductance (right). (b) Scanning electron micrograph of the heater sensor used in previous studies [22, 23, 97]. The picture is taken from an angled view, which may be misleading. The length of the four beams is around 250 microns, the membrane thickness is 150 nm. With these dimensions, a thermal resistance of  $2 \times 10^7$  K/W was achieved.

### Quantized heat transport of phonons: A Challenge

An open question is whether quantized transport of the phonon contribution would be observable in QPCs at lower temperatures [98], i.e. below the Debye temperature of

gold, at which three or four phononic transport channels would have to be added to the electronic ones. An experimental study of this regime would require sensitivities on the order of 1 pW/K, which is certainly a challenge. It is not readily clear how much the phonons would contribute to heat transport in QPCs at low temperatures. In contrast to electronic QPCs, phonons are sensitive to an impedance mismatch formed by the spatially varying diameter of the constriction on the atomic scale, as was already predicted using classical molecular dynamics simulations [99], compare also Panzer *et al.* [100]. Atomistic quantum mechanical transport calculations in break-junction geometries predict negligible phonon contribution at room temperature [98, 101] in agreement with the aforementioned experiments. At reduced temperatures, however, below the Debye temperature of the bulk metals, the phonon contribution is predicted to appear [98], albeit staying well below the quantization value. The somewhat idealized system of an atomic QPC appears ideal to relate experimental to theoretical transmission factors.

### 2.4.4 Heat transport through molecules

A natural next step from considering single, quantized channels of transporting heat via phonons is to modify that transport channel, add functionality, and link the transport channel to local degrees of freedom inside the channel. To this end, probably the most tangible approach is the use of molecular systems. Heat transport through organic molecules is a fascinating area of research, as it combines unresolved conceptual questions with slowly increasing availability of experimental data.

To begin with, one needs to distinguish between thermal transport in organic materials such as amorphous polymers and fibers from molecular junctions, the latter considered here. In amorphous polymers [102], heat transfer is mainly limited by energy transfer between the interlaced molecular groups through relatively weak van der Waals interactions or electrostatic bonds. Therefore, although thermal transport along a single chain, i.e. intra-molecular transport, can be large and ballistic [102–104], in amorphous media we typically find diffusive transport and low thermal conductivity. In contrast, in a molecular junction setup, when one or more molecules are individually bonded to two solid electrodes (or thermal reservoirs), heat transport can be quantum coherent, meaning that it can be described by coherent quantum mechanical waves [23, 105]. (Many people find the notion useful, in which the waves move as quasi-particles in a ballistic fashion, applying a Landauer approach based on a scattering picture). In either case, thermal transport in/along organic molecules is typically dominated by the phonon contribution while charge transport can be largely neglected. Exceptions comprise carbon-based structures derived from fullerenes, graphene or nanotubes.

#### Experimental studies

**Ensemble-based method.** Turning first to the status of experimental methods to measure thermal transport across molecular junctions, one should distinguish between ensemble-based methods [80, 103, 106–109] and recent work using single molecules [23, 81]. Ensemble based methods typically use self-assembled monolayers (SAMs) sandwiched between two electrodes [106] or one solid electrode and a liquid counter electrode [109, 110]. These samples can then be studied using optical techniques, of which time-domain thermorefectance has been particularly successful [106]. However,

the fabrication of such sandwiched structures is challenging, because defects and imperfections of the surfaces can influence the transport strongly. Ideally, atomically flat surfaces and rather perfect films are required over macroscopic areas. A typical uncertainty for transport measurements of SAMs is therefore the percentage of molecules of a film that are actually contacted (typically chemisorbed) to both electrodes. For example, a careful study by Majumdar *et al.* [80] estimated that by only about 50%. Despite these inherent difficulties, there are beautiful measurements with high reproducibility studying the effect of molecular length and bonding strength on the transport (see more details below). To address the limitation of defects on the interpretation, a small ensemble (tens to hundreds of molecules) has been studied using the contact of a tip of a scanning thermal microscope to a SAM. A study [111], however, while showing the potential of the method, reported systematic errors larger than observed for optical studies. Nevertheless, the community is watching with interest new tip-based studies, for example at Lancaster University.

**Single-molecule measurement** A second limitation of using SAMs, relevant to this study, is that only a small group of molecules actually form well-defined molecular layers, typically involving simple molecules such as alkane chains, while relevant current questions are related to more complicated molecular designs. This motivates the use of single molecule junctions. For this however, the ability to contact individual molecules has to be combined with sensitive heat flux measurements to reach a sensitivity to detect the conductance of a single molecule on the order of a few tens of pW/K. Based on the aforementioned experiments on single-atom junctions, two groups have recently succeeded to measure heat transport across single molecules [23, 81]. Both groups have used essentially the same approach, by combining a break-junction method based on a scanning tunnelling microscope (STM) with a heater/sensor microfabricated using MEMS (micro electro-mechanical system) technology. The method combines charge and heat transport measurements, and the well-understood charge transport properties of single molecules serve to probe the integrity of single-molecule junctions. The first demonstration of heat transport on the single molecule level utilized molecules that are well known from previous charge and thermal transport studies. Oligo(phenylene-ethynylene) (OPE3) is probably the best characterized molecule in electrical break junctions to date [23], and alkane chains [23, 81] have been used in numerous experimental and theoretical studies on thermal transport through SAMs. The two studies [23, 81] agree on the value of the latter, a first validation of the methodology. The results, shown in figure 2.8 (f), compare well to simulation results [23, 112], if one assumes coherent phonon transport across the junction and confirms the negligible contribution of heat transport by charge carriers. Therefore, experiments could already confirm or falsify certain assumptions coming from the theoretical studies.

### Theoretical description of molecular junction

There is already a large number of studies offering theoretical prediction of heat transport across molecular junctions. Looking from a bird's eye view, we first notice that the size of the problem of heat transfer is challenging, because is inherently multiscale. Phonons contributing to room temperature heat transport have phonon wavelengths and mean free paths ranging from atomic dimensions to several microns. On the other

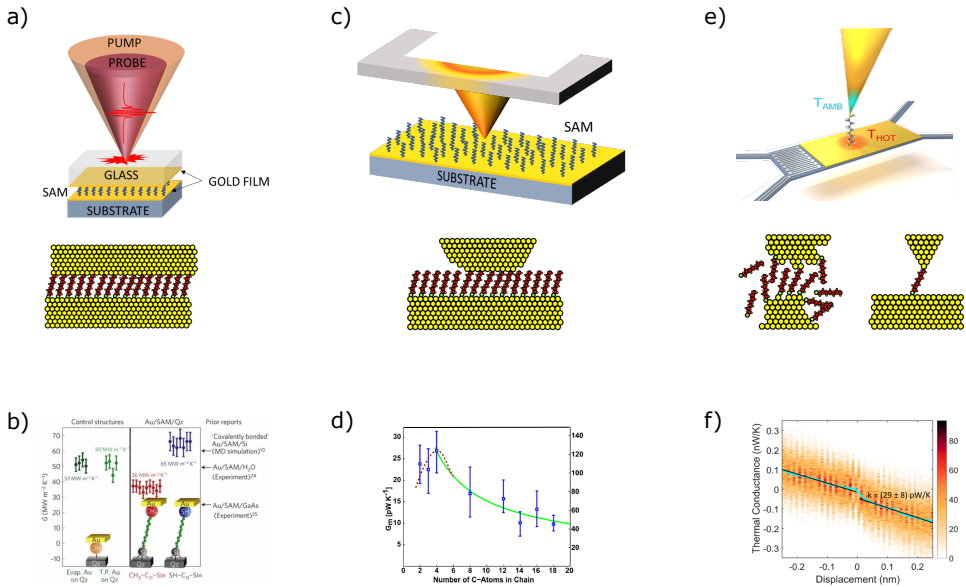


**Figure 2.8** Schematic and examples of different experimental approaches to the measurement of heat transport across molecular junctions of alkanes. Pump-probe techniques using self-assembled monolayers (a) have been successful for systematically studying the role of end-groups (binding groups) between molecules and electrodes/reservoirs (b). (From Losego *et al.* [106]). Scanning thermal microscopy (c) remains a niche technique so far. An example (d) shows the studied length-dependence of alkane chains studied [111]. We note that more recent measurements [81] do not agree with these findings. Single molecule techniques (e) using break-junction techniques or scanning tunnelling microscopy (shown here in a realistic and idealized arrangement) have been able to measure thermal transport through octanedithiol [23] (f).

hand, the calculation of phonon properties on the atomic scale are much less prone than excited electronic states to systematic errors of first-principle methods like density functional theory (DFT), which result in difficulties in predicting electronic conductance of molecular junctions.

There are several methods applied to the problem of phononic heat transport along molecules. There are examples for both classical molecular dynamics [78, 80, 113, 114] and quantum mechanical calculations [35, 43, 105, 115–120] including density functional theory and with nonequilibrium greens functions [23, 101, 121]. It is found in almost all studies, that heat transport is coherent along small molecules of up to a few nanometers in length. Therefore, the simple picture of an (energy-dependent) scattering coefficient in a Landauer transport picture is well justified. Otherwise one may revert to classical molecular dynamics, which can cover also diffusive transport, but is bound to the classical limit.

### **Nature of phonon transport along molecules**

Some of the main conclusions on the mechanisms of phonon transport in molecular junctions, based on ongoing theoretical and experimental studies are:

(1) Several studies indicate that it is dangerous to apply simple estimations that have proven useful for bulk solids. In particular, by applying kinetic theory to phonon gases, the thermal conductivity should be proportional to the phonon group velocity (as well as heat capacity and mean free path). This implies that stiffer bonds along a molecule, which should lead to higher phonon velocities, would lead to better thermal conductance of a junction. This is not the case and we learn that one needs to take into account the phonon density of states in relevant energy ranges, which is rich for both stiff and soft chains.

(2) Coherent transport dominates phonon conduction in relatively short and uniform molecules. This applies, for example, to the aforementioned experimental studies of single molecule transport [23, 81], and is well supported by simulations (see above). One of the direct implications is the length-dependence of thermal transport, saturating (in accord with ballistic transport) for long chains.

(3) Sensitivity to the coupling strength of the molecular-electrode bond has been observed using time-domain thermo-reflectance (TDTR) experiments (see [106] as an example) and it was predicted early on using various methods [105, 113]. In the studied examples of small and simple molecules like alkane chains, the effect of binding to the reservoirs appears to be stronger than variations of the molecular length, in accord with coherent-ballistic conduction mechanism.

(4) Beyond coherent-ballistic transport, anomalous or diffusional heat transport was exemplified in pump-probe (donor-acceptor type) experiments as well as at the meso- and microscale, see e.g. [122], yet not in molecular junctions of nanoscale length, see point (2).

(5) Apart from strong differences for chemically- versus van der Waals-bonded molecules, the differences in thermal conductance between different molecules are relatively small, both in experimental and simulation data. The differences roughly stay within the range of a few to a few tens of pW/K for simple and short molecules as studied in the context of molecular electronics. (Larger differences appear for bucky balls or very long molecules, of course.) The intuitive reason is the fact that the bosonic nature of phonon

transport implies integrating over a large range of phonon frequencies, over which the density of vibrational states of molecular junctions are similar on average.

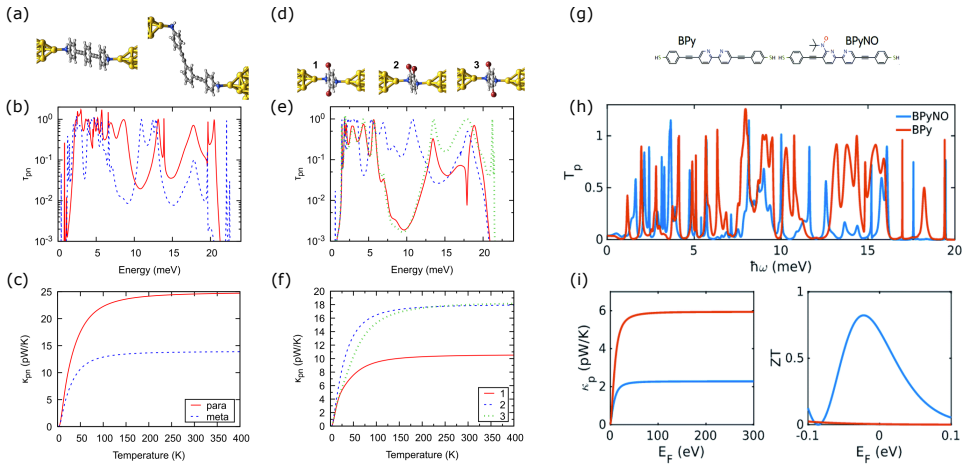


**Figure 2.9** Examples for phonon engineering predicted from transport calculations of single-molecule junctions. (a) Quantum interference leads to a suppression of phonon conductance of the meta-connected OPE3 molecule compared to the symmetric para configuration [44]. The energy-dependent transmission coefficients and the temperature-dependent thermal conductance are shown in (b) and (c). (d) Replacing hydrogen atoms on a benzenediamine molecule by the much heavier bromine, leads to transmission coefficients (e) strongly dependent on which pair of hydrogen atoms was replaced [121]. This leads to strongly varying thermal conductance (f). (g) Also a single but more complex side group can have a strong effects as shown here for bipyridine connected to thiobenzene anchor groups [123]. Again, a contrast in transmission coefficient (h) leads to a difference in the magnitude of thermal conductance (i). The predicted thermoelectric figure of merit (ZT) is also shown. Figures (a)-(f) adapted from [121] and (g)-(i) from [123].

### Open questions on molecular thermal transport

In conjunction with ongoing developments, there are significant open questions and research opportunities in the field of heat transport along molecular junctions. These relate both to conceptual understanding and abstraction, as well as to possibilities of phonon engineering to increase or reduce thermal conductance. In the following we list questions already addressed using theory but not yet verified through experiments, which, given recent experimental progress, should be possible to assess in the near future.

(1) Similarly to what has been discussed in the molecular electronics community for charge transport, phonon transport could also display quantum interference effects [44, 121]. Figure 2.9 (a) gives an example, based on the popular backbone of oligo(phenyleneethynylene) (OPE3), in which phonon transmission around the central aromatic ring has two paths leading to destructive phonon interference in the meta configuration. In the

para configuration, in contrast, there is no difference in path-length, and therefore no destructive interference. Through destructive interferences, a reduction of conductivity by about a factor of two is predicted.

(2) Another proposed mean to reduce thermal conductance is the attachment of pendant side groups to molecules [121, 123–125]. Local vibrational states can induce resonances in transport reminiscent of Fano resonances, which are prominent in different fields of transport. According to predictions, a single side-group can reduce the thermal conductance of a molecular junction by a factor of up to three, see (figure 2.9 (d-f)) for an example based on side-groups in benzenediamine. Another example for the predicted influence of pendant side groups is given in figure 2.9 (g-i), in which a single side group reduces strongly the conductance of bipyridine connected to thiobenzene anchor groups [123]. This example shows that extremely low thermal conductance at room temperature of only a few pW/K may be reached even for relatively short molecule junctions and with proper chemical binding to metal electrodes. Such a control, and suppression of thermal conductance has potential applications in thermoelectric energy conversion or for the use of junctions as thermodynamic machines in general.

(3) **Harnessing anharmonic interactions towards functional devices.** Anharmonic effects are expected to be important in flexible molecules made of weakly-connected and distinct components, where raising the temperature induces, for example, bond weakening, torsional motion and conformational changes. Asymmetric molecular junctions with prominent anharmonic couplings can support an anisotropic heat flow (diode) effect; predictions include [45, 118, 126, 127]. The realization of molecular thermal rectification would be a valuable contribution for two reasons. First, there are some predictions or demonstrations of thermal diode behaviour [128–133], but mostly with only modest rectification, in particular when compared to electrical diodes. Therefore, current technological applications are mostly limited to opening and closing mechanical contacts and thereby switching thermal conductance. Truly passive and scalable thermal diodes could be an asset for thermal management. Second, a thermal diode would be an excellent example of true phonon engineering.

(4) Identifying and creating molecular junctions that display quantum thermal transport beyond coherent-ballistic behaviour remains an open challenge. While meso- and micro-scale junctions show the onset of anomalous and normal diffusive transport, it is not clear yet what range of transport regimes can molecular junctions support, beyond coherent transport. While we do not expect diffusive transport to develop at the nanoscale, complex mechanisms may arise due to atomic heterogeneity and disorder, allowing phonon localization and thus the suppression (or more generally, control) of thermal conductance.

(5) **Effect of the environment.** In most experimental situations and certainly in anticipated technological applications, a molecule will not be isolated but surrounded by solvent, residues, or other molecules. There is a significant experimental challenge to create a clean and defined experimental environment, even when using nominally-perfect molecular SAMs [134]. Molecular dynamics simulations indicate a clear influence [80] when using alkane SAMs. Conceptually, there is a question whether lateral coherence is large enough to cover two neighbouring molecules. More importantly, however, this is closely related to defects and technological efforts around the integration of molecular films.

(6) Beyond passive control of thermal conductance by modifying the molecular structure, active control by means of mechanical forces, electric fields and light excitation is yet to be explored. Particularly exciting is the prospect of building on advances in molecular electronics, and using electric current to induce mechanical forces thus control vibrational heat flow at the atomic scale [135].

### 2.4.5 Outlook and conclusions

Atomic contacts, quantum point contacts (QPCs) and single molecular junctions in general may appear far away from any technological relevance at first sight. However, the research on tribology has shown clearly that interfaces between solids with roughness oftentimes employ distributed atomic contacts [136] as displayed in Fig. 2.10. That this has profound implications on the pressure dependence of thermal contacts has already been hypothesized [137]. Research on thermal QPCs therefore will contribute to a bottom-up picture of thermal boundary conductance or thermal contact resistance. Such interface effects are predominant on the sub-micron scales already for reasons of classical scaling. For the construction and verification of models of thermal contacts, the independent measurement of heat transport in point contacts is needed. An improved understanding of phonon scattering in atomic-scale structures will also feed into the engineering of novel devices. For example, memristive devices as used today for neuromorphic computing, can exhibit current carrying filaments with atomic diameters. Research on nanoscale phonon transport is anticipated to have technological impact in

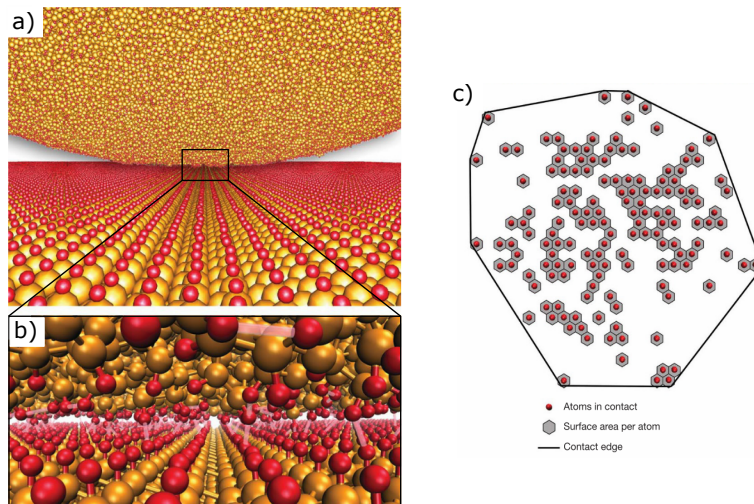


**Figure 2.10** Atomic simulations of mechanical contacts a)-b), show that the distribution of pressure c) is distributed over few and oftentimes separated single atom contacts between the two bodies [136].

the quest for thermal processes at high efficiency, particularly for reducing self-heating of densely packed nanodevices on modern computer chips. In general, the contrast be-

tween good and bad thermal conductors (of about four orders of magnitude) is rather small compared to the control and variability of electrical conductance, spanning over more than 30 orders of magnitude. Thermal engineering is therefore an increasingly important topic. On the molecular level, this is already being done empirically by comparing e.g. different polymer materials. The technological community would welcome novel ideas that help with the trade-off between mechanical, processing and thermal properties. Whether junction geometries will be applied widely is less clear, given the few examples used today, e.g. in some sensor implementations. An exciting prospect for

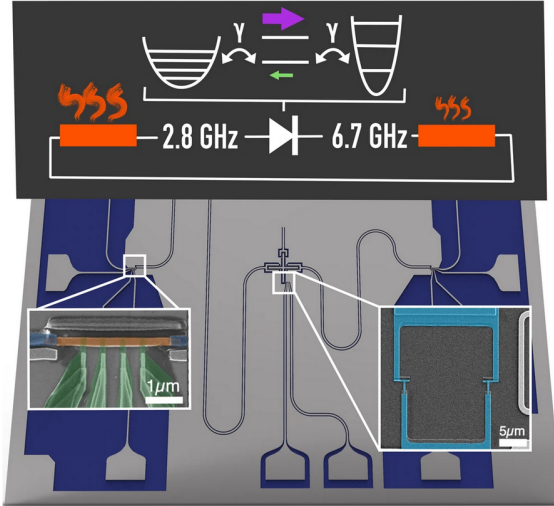


**Figure 2.11** Heat diode realized in a superconducting circuit. The system consists of a centrally located superconducting qubit coupled to two superconducting waveguide resonators of different frequencies, which themselves are coupled to resistors (thermal baths) [138]. The top diagram displays a simple model of the resonator-qubit-resonator system.

the field of phonon transport is the growing cross fertilization between different physical platforms, nanostructures and molecular junctions, optomechanical devices [139] and superconducting circuit quantum electrodynamics [140] (with studies of photonic heat transport for the latter). Open question and predictions listed above, e.g. on the realization of a thermal diode by utilizing the vibrational anharmonicity can be tested in such highly controlled, engineered devices. Fig. 2.11 presents a quantum heat diode based on a superconducting circuit [138] utilizing principles first proposed in Ref. [45], albeit in the context of phonon heat transport through molecular junctions. Once theoretical predictions on the passive and active control of quantum heat transport are tested and established in such engineered devices, an exciting prospect is to utilize the enormous diversity of materials, nanostructures and molecules to build and enrich the functionality of quantum phonon transport systems.

In conclusion, studies of phonon transport through quantum conductance channels is a lively field of research. Pioneering original experiments now open research questions

2.4 Perspective: Phonon thermal transport through quantum channels and molecules

of fundamental interest and significant technological potential.



# 3 Experimental Methods & Instruments

---

In this chapter the working principle, the lab and the different instruments and sensors used to perform the experiments are described in detail. The chapter is split in the following way: in the first section (3.1) the experimental technique and the mathematical model employed are presented; in the second section (3.2) the two measuring setups are introduced, with the variable temperature instrument HIBERNUM being described accurately in the third section (3.2.3). The fourth section reports the design, fabrication and calibration steps of the different generations of the micro-electro-mechanical-system (MEMS) used in the experiments. In the fifth section (3.5), sample and tip preparation are presented, starting from the necessary cleaning steps applied before any measurement, and then turning to the chemical functionalization of the MEMS with organic molecules. The fabrication of gold STM tips by electrochemical etching is detail at the end of the same chapter. Finally, the correct functioning of the new HIBERNUM setup is assessed by measuring the Wiedemann-Franz relationship for quantum point contacts (QPCs) at room temperature (sec. 3.6).

## 3.1 Working Principle

### 3.1.1 Introduction

Today, the Break Junction technique is an already well established method, that has allowed in the last decades the measurement of charge transport through single atoms and molecules [61, 63, 64, 141, 142]. Only recently, however, thanks to the enormous progress in the field, it has been possible to probe their thermal and thermoelectric properties as well [23, 81, 143, 144]. The basic idea of a Break Junction (BJ) experiment, as stated in section 2.1.1, is to gradually form an electrical connection between two metallic reservoirs and then slowly break it until only a single atom (or a monoatomic filament) bridges the two electrodes and then eventually breaks. This can be achieved by mechanically stretching a wire deposited onto a bending substrate (MCBJ) [56, 57], or by bringing into and out of contact the tip of a Scanning Tunnelling Microscope (STM) with an electrical conductive substrate (STM-BJ, see section 2.1.1). Indeed, since its invention in 1981 by Gerd Binnig and Heinrich Rohrer (at IBM Zurich) [145], the STM, in addition to the imaging capabilities, has offered to the many researchers around the world a natural way to manipulate precisely atomic filaments and single molecules [146–148].

As described in section 2.1.1, if the diameter of the filament connecting the two electrodes reduces below the electronic wavelength, a *Quantum Point Contact* (QPC) is

formed and the electrical conductance assumes quantized values. After the breaking of the last atom connection, sub-nm gaps can be maintained between the two electrodes, where single molecules can be trapped in and measured. The next section will introduce a modified version of the STM-Break Junction technique, able to measure not only the electrical conductance ( $G_{el}$ ), but also the thermal conductance ( $G_{th}$ ) and the Seebeck coefficient ( $S$ ) of QPCs and single molecules.

Due to the mechanical re-arrangement of the junction during the thinning-down process and the different configurations that a molecule can assume when binding to the electrodes, it is necessary to collect a large statistics in order to probe the most recurrent properties of the junction [149]. Such results will be presented for QPCs and single molecules at the end of this chapter and in the next one, respectively.

3

### 3.1.2 Thermal STM-Break Junction

To go beyond the measurement of only charge transport and be able to probe heat transport at the quantum scale, we combined the STM-BJ technique with a highly thermally insulated heat flux sensor. The sensor is based on a suspended Micro-Electro Mechanical System (MEMS) with an integrated micro-heater, Figure 3.1

The experiments are performed in high vacuum ( $1 \times 10^{-6}$  -  $1 \times 10^{-7}$ ) mbar, either at room or variable temperature with one of the two custom-built STM setups located in the IBM Noise Free Labs [151]. By measuring the electrical conductance of the tip-MEMS contact it is possible to detect the presence of a single atom or a single molecule in the junction. The electrical conductance represents, in fact, the reference signal and it is used to gather information about the structure of the QPC/molecular junctions [152]. The MEMS consists of 4 silicon nitride (SiNx) beams suspending a central platform, which features a Pt micro-heater, to control and monitor the temperature, and a metallic pad, to form electrical contacts with the STM tip. A further description of the MEMS will be given in section 3.4. Thermal equilibrium can be assumed between the pad and the heater, thanks to larger thermal resistance of the suspension beams. To measure the thermal conductance of the junction, the MEMS is heated up to a temperature  $T_H$  by applying a constant voltage to the Pt-heater and then the heat flux towards the tip is measured, while forming and breaking the contact. When the tip touches the platform, heat can travel out both via the suspending beams and the tip-sample junction 3.1d. The resulting thermal conductance is then equal to:

$$G_{TOT} = G_{MEMS} + G_J = \frac{\dot{Q}}{\Delta T_1} \quad (3.1)$$

where  $\dot{Q}$  is the power provided by Joule dissipation at the heater and  $\Delta T$  is the resulting temperature difference. Following to contact breaking, heat can only be transported to the substrate through the suspending beams of the MEMS, as it happens before contact formation. In this case we get:

$$G_{MEMS} = \frac{\dot{Q}}{\Delta T_2} \quad (3.2)$$

The thermal conductance of the junction is then obtained by subtracting the value of  $G_{MEMS}$ , measured after the breaking, to the total conductance  $G_{TOT}$  measured previously with the tip still in contact.

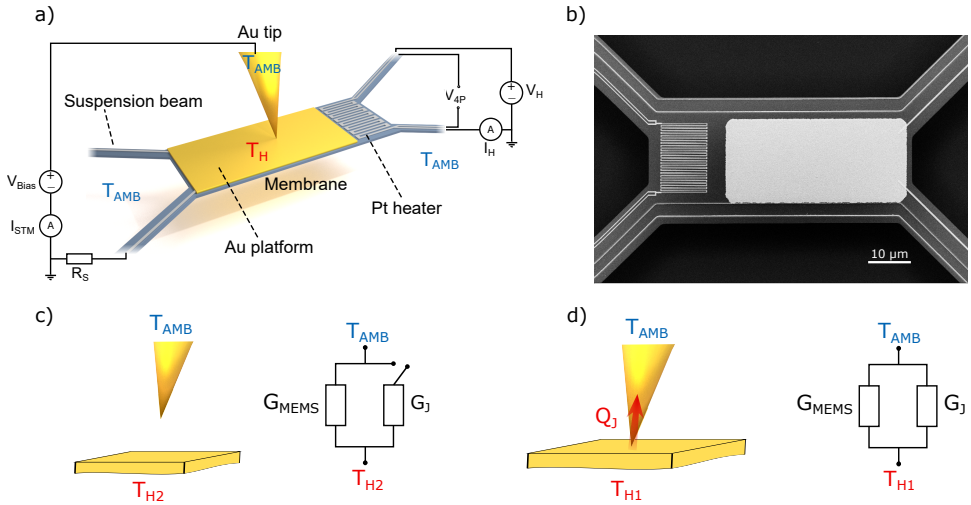


**Figure 3.1** a) Schematic diagram of the experiment, adapted from [150]. To monitor the temperature  $T_H$  of the gold electrode, the four-probe voltage,  $V_{4P}$ , and the heater current,  $I_H$ , are measured. Simultaneous measurement of the tunneling current,  $I_{STM}$ , allows us to extract the electrical conductance of the junction. An external resistor  $R_s$  limits the current. b) Scanning electron micrograph of a typical MEMS used in this work. c) Prior to contact formation, the membrane is heated to  $T_{H1}$ . The total thermal conductance of the system is given only by the contribution of the suspension beams of the MEMS. d) After contact formation, the temperature of the membrane decreases to  $T_{H2}$ , because of the additional heat path. The total thermal conductance is now given by the sum of the thermal conductance of the MEMS ( $G_{MEMS}$ ) and that of the tip-MEMS junction ( $G_j$ )

To get enough statistics, this procedure is usually repeated few 1000s of times, as in a standard break-junction experiment. In other words, to capture the thermal conductance of the junction  $G_J$ , a reference value must be subtracted, that in the simplest case, corresponds to the thermal conductance of the device,  $G_{MEMS}$ . This implies that the amplitude of the measured temperature drop depends on the ratio between  $G_J$  and  $G_{MEMS}$ . Thus, to maximize the signal to noise ratio, the MEMS sensors should feature a thermal resistance as close as possible to  $G_J$ . In fact, by using an electronic analogy, the two conductances  $G_J$  and  $G_{MEMS}$ , form a parallel, being the tip and the substrate at the same temperature. Decreasing the thermal conductance of the MEMS to a value close to  $G_J$  means to make the suspending beams thinner and/or longer. On the other hand, to precisely control the gradual breaking of the junction, the MEMS is required to be mechanically stiff, posing a severe trade-off between stiffness and temperature sensitivity. Typical values are:  $G_J \sim \text{pW/K}$ ,  $G_{MEMS} \sim 10 \text{ nW/K}$  and effective stiffness  $\sim 10 \text{ N/m}$

### 3.1.3 Data acquisition and remote operation control

The measurement unit designated for controlling the experiment and acquiring raw signals is the ADwin Pro II from Jäger Messtechnik. A schematic of the whole system is depicted in Fig. 3.2. The Adwin unit features an internal processing unit with 300 MHz clock rate, 768 kB local memory and 256 MB RAM, which allows floating point operations with 40-bit resolution. It is a high-performance, versatile system that can be customized with different functional modules, e.g. Analog, Digital and Multi-I/O modules. Our version hosts an analog 8-channels differential input card, with ADC resolution of 18-bits and a conversion time of 2 ms, an analog output card, with 16-bit resolution and a settling time of 3 ms, and a digital card with 32 inputs/outputs. The dynamic range of both input and output analog cards is  $\pm 10\text{V}$ . The internal processing unit of the Adwin Pro II, programmable within the proprietary programming environment (ADbasic), offers the possibility to handle multiple programs at the same time with very accurate timing and priority assignment.

The ADwin system is used as voltage source for the thermal and electrical sensing circuits described in section 3.1.4, to collect analog raw data, and to control the open loop piezoscanner via a low noise, high voltage amplifier (ANC250 from Attocube). The positioning of the coarse piezo-elements is instead performed by a separate control unit (ANC150 from Attocube) directly connected to the computer, but the selection of the coarse axis is managed by the Adwin digital card. The analog inputs of the ADwin are connected to the output of a Low Noise / High Stability I to V converter (SP983c from Basel Precision Instrument) to read the STM current, and to two differential amplifiers (SR640 Programmable Filters from Stanford Research) for the heater resistance and current. In order to perform a measurement, a specific routine is loaded onto the ADwin processor and data are read/written by a Matlab<sup>®</sup> interface. The main benefit of using this combined approach ADwin+Matlab is the possibility to run fast and accurate measurements independently from computer load and possible crashes. It also offers the possibility to remote control the setup. In fact all the instruments and tools, except for the I to V converter, have been integrated in the Matlab interface and can be easily controlled from outside the lab by means of several graphical user interfaces (GUIs), Fig.3.3. Compared to the previously reported version [150], a cryogenic temperature

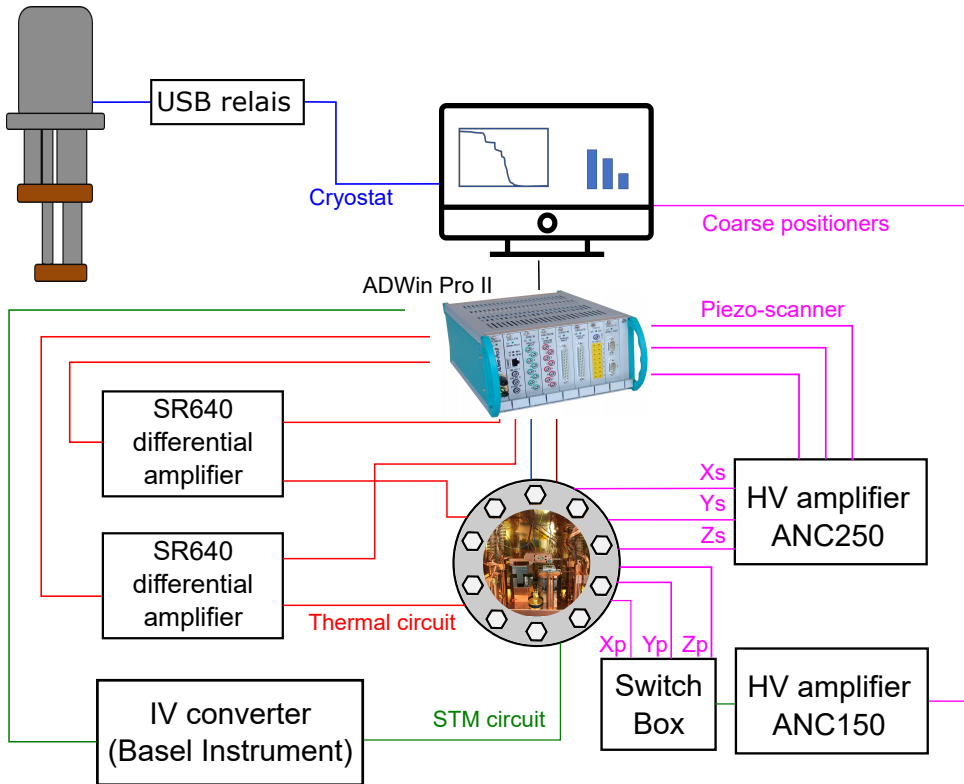


**Figure 3.2** Schematic view of the data acquisition and control system. The red circuit is used to measure the 4-probe resistance of the heater element integrated on the MEMS and the dissipated electrical power. The green circuit is used to measure the tunnelling current between the STM tip and the MEMS platform. The magenta circuit controls the piezoelectric scanner through the high-voltage amplifier ANC250 and the coarse positioners through the ANC150 control unit, while the blue circuit controls the operation of the cryostat.

controller (LSCI-MODEL 335 from Lakeshore) has been integrated in the controlling system, together with an USB-relay (Yoctopuce) to turn ON/OFF the cryocooler.

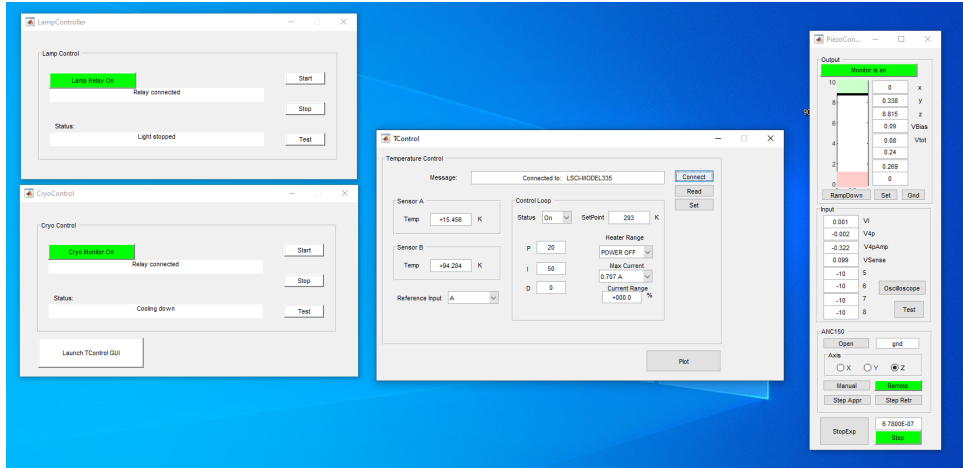


Figure 3.3 Example of interfaces to control remotely the setup.

### 3.1.4 Sensing circuits and Mathematical model

The mathematical model used to derive the electrical and thermal conductance was already developed by B. Gotsmann and N. Mosso. Calculation of the Seebeck coefficient and adaptations for the variable temperature measurements were developed by the Author with the help of B. Gotsmann.

#### STM circuit

In order to calculate the electrical conductance of the junction  $R_J$ , we use the electrical circuit shown in Fig. 3.4.

A small constant bias  $V_{Bias} \leq 90\text{mV}$  is applied to the tip over a series resistor  $R_S$ , and the current between the tip and the MEMS platform is measured by means of the IV converter, Fig. 3.4. We get:

$$R_J = \frac{V_b}{I_{STM}} = \frac{V_b \cdot A}{V_{STM} - V_{off}} - R_b - R_S \quad (3.3)$$

$V_{off}$  being the amplifier offset measured at open circuit and  $A$  its gain.  $R_b$  is evaluated by connecting the bias voltage to the platinum line running along the second beam, instead of the tip and measuring the 2-point resistance. Typical values range from 5 to 15 k $\Omega$  depending on the specific design of the MEMS and on the cleaning procedure that can decrease the thickness of the metallic lines. The external series resistance  $R_S$  helps to shunt the current when a large, low-resistance contact is formed with the tip, avoiding any damage to the MEMS.  $R_S$  permits also the dynamic range of the amplifier

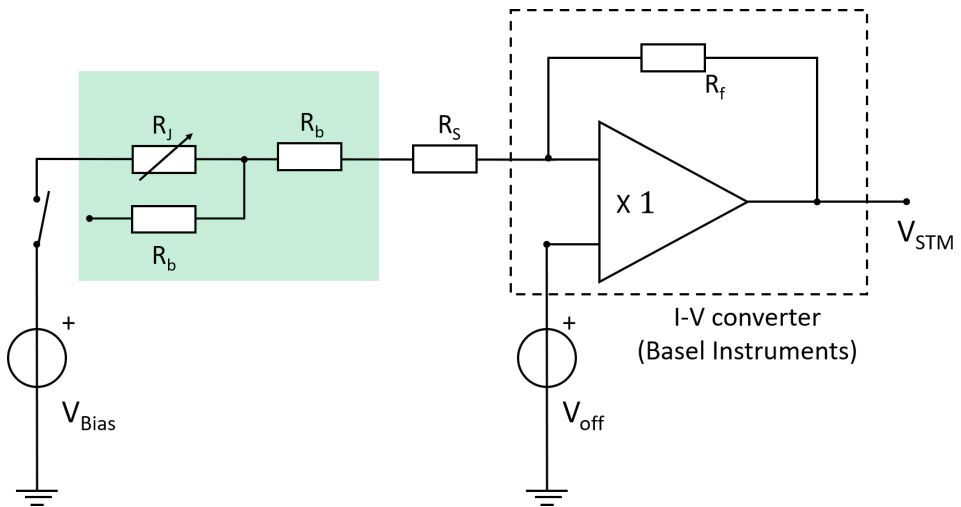


**Figure 3.4** Schematic of the electric circuit used to measure the electrical conductance of the junction.  $R_J$  is the junction electrical resistance between Tip and MEMS;  $R_b$  is the resistance of the platinum line running along the beam and  $R_S$  the external series resistance used to limit the STM current. The amplifier is a current to voltage I-V converter, whose gain is given by the feedback resistor  $R_f$ .  $V_{Bias}$  and  $V_{STM}$  are the voltage output and input of the data acquisition system, respectively. The shaded region represents the part of the circuit in vacuum.

to be increased without switching the gain, allowing measurements of resistance over different order of magnitude (from 1 k $\Omega$  to 10 G $\Omega$ ) as normally required by STM-Break junction experiments. The value of  $R_S$  is usually set to 100 k $\Omega$ .

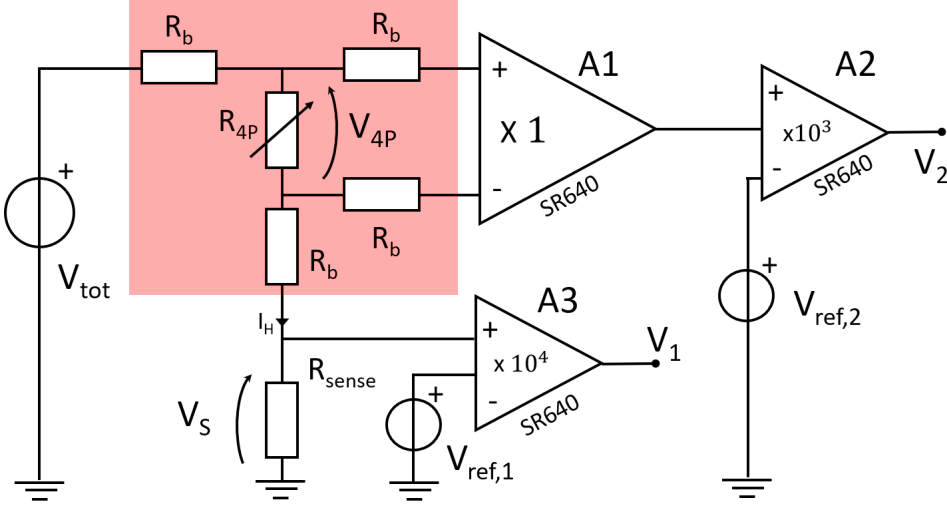


**Figure 3.5** Schematic of the electric circuit used to measure the thermal conductance of the junction.  $R_{4P}$  is the (4-probe)resistance of the heater,  $R_b$  is the resistance of the metal line along the beam,  $R_S$  is the series resistor.  $V_{tot}$  is the voltage bias for the heater.  $V_{ref,1}$  and  $V_{ref,2}$  are voltage outputs of the ADWin used to increase the dynamic range of the differential amplifiers indicated with gains A1, A2 and A3.  $V_1$  and  $V_2$  are the two signals recorded.

### Thermal circuit

Figure 3.5 shows a simplified schematic of the thermal circuit involved in our STM-Break Junction measurement. To extract the thermal conductance of single atoms/molecules, we start by measuring the 4-probe voltage  $V_{4P}$  and the current  $I_h$  across the heater. From the measured signals  $V_1$  and  $V_2$  we get:

$$V_{4P} = \frac{1}{A_1} \cdot \left( \frac{V_2 - V_{2off}}{A_2} + V_{ref2} \right) \quad (3.4)$$

$$I_H = \frac{V_S}{R_S} = \frac{1}{R_S} \cdot \frac{V_1 - V_{1off}}{A_3} + V_{ref1} \quad (3.5)$$

with  $V_{1off}$  and  $V_{2off}$  being the voltage offset at the output of the amplifiers, measured at  $V_{tot} = 0$ . The 4-probe resistance  $R_{4P} = V_{4P}/I_h$  can now be calculated and used to extract the temperature  $T$  of the heater by using:

$$T - T_{amb} = \frac{1}{\alpha} \cdot \frac{R_{4P} - R_{4Pamb}}{R_{4Pamb}} \quad (3.6)$$

where  $\alpha$  is the temperature coefficient of resistance (TCR) of the Platinum thin-film heater and  $R_{AP_{amb}}$  the electrical resistance of the heater at ambient temperature  $T_{amb}$ . The total power  $P$  provided to the central platform, through the MEMS heater, can be defined as

$$P = R_h I_h^2 + r_u R_b I_h^2 \quad (3.7)$$

in fact there are two contribution to the total power: the first term stands for the contribution of the integrated heater ( $R_h I_h^2$ ), while the second one represents the additional contribution of the suspended portion of the two metal lines carrying the current to the heater (each line contributing with  $\frac{1}{2} \cdot r_u R_b I_h^2$ ). It is possible to demonstrate that only half of the total electrical power developed across the beams actually increases the MEMS temperature. The other half is in fact dissipated directly into the silicon substrate [150]. Furthermore, since only the section of the line that is indeed suspended has to be taken into account, being the rest well coupled to the substrate, a correction factor  $r_u$  must be introduced. Thus,  $r_u$  represents the fraction of electrical resistance of the underetched portion of the beam, Figure 3.6.

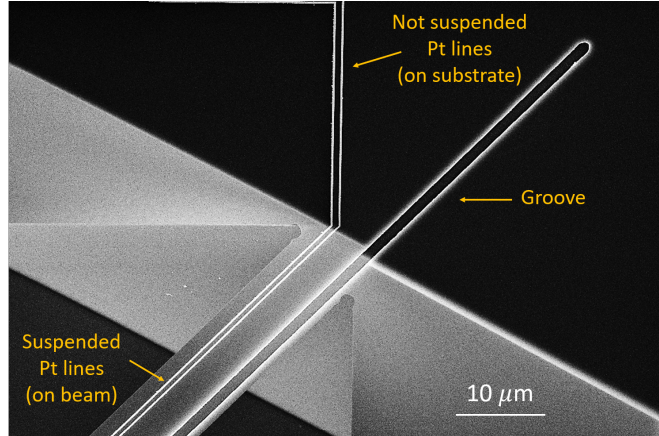


**Figure 3.6** SEM micrograph indicating the suspended portion of the metallic lines (on beam) and the part that is actually not underetched (on substrate).

Typically  $r_u \sim 85\%$  and can be directly deduced from the design layout, as it depends only on geometrical factors.

$R_b$  is extracted then from the value of the 2-probe resistance

$$R_{2P} = V_{tot}/I_h = R_{AP} + 2R_b \quad (3.8)$$

The main interest in using a configuration with two differential amplifiers consist on having the option to set high gains ( $A_2$  and  $A_3$ )  $\geq 60dB$  by subtracting the reference voltages  $V_{ref1}$  and  $V_{ref2}$  and so focus only on the small changes around the resistance and current values. Now, it is possible to use equations 3.2 and 3.1 to calculate the thermal conductance of the device and the junction, respectively.

### Thermoelectric circuit

A schematic of the circuit used to measure the thermoelectric properties of the junction is drawn in Fig.3.7a. When a temperature difference is applied, the current flowing across the junction can have two contributions:

$$I = -GV_{Bias} + GS\Delta T \quad (3.9)$$

where  $G$  is the electrical conductance of the junction and  $S$  the Seebeck coefficient, also called thermopower (see Section 2.2). The first term is due to the electrical bias applied to the junction, while the second term  $I_{Seeb} = GS\Delta T$ , is proportional to the applied temperature difference  $\Delta T$  through the Seebeck coefficient, Fig.3.7. To extract experimentally the thermopower of the junction,  $V_{Bias}$  can be set to 0, so that the first term in 3.9 is null. For each temperature difference  $\Delta T_i$  applied to the junction, the thermoelectric voltage  $V_{Seeb}$  is calculated by dividing the thermoelectric current for the junction electrical conductance:

$$V_{Seeb} = \frac{I_{Seeb}}{G} = S \cdot \Delta T \quad (3.10)$$

At this point, by plotting the thermovoltage  $V_{Seeb}$  as function of the different  $\Delta T_i$ , is possible to extract  $S$  as the slope of the linear fit, see Fig. 3.7b.

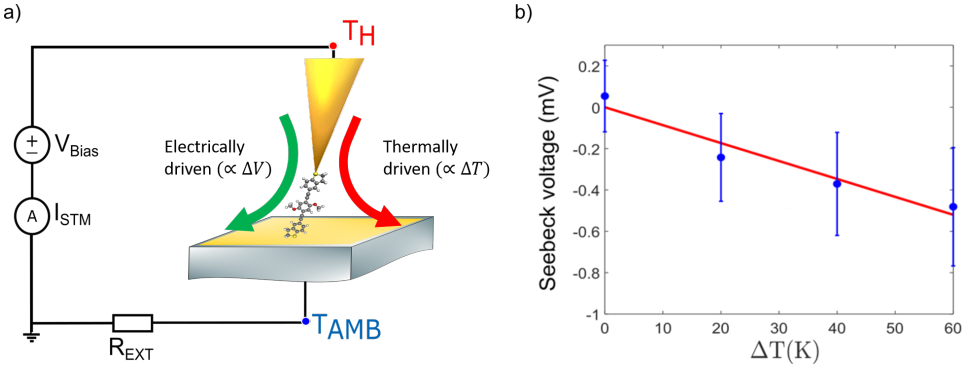


**Figure 3.7** Schematic of a molecular junction under an applied electrical bias  $V_{Bias}$  and temperature difference  $\Delta T$

### Correction to the mathematical model

All the models and circuits presented above provide a first introduction to the sensing methods used to measure the electrical, thermal and thermoelectric properties of break-junctions. But several adjustments are needed to be able to reach the required sensitivity and correct for experimental errors and non-idealities.

Starting from the STM electrical circuit, we note that when using an IV converter (i.e. a feedback ammeter) the series resistance  $R_S$  should be higher than the feedback resistor providing the gain  $A$  to the amplifier [153]. In fact voltage offsets and noise

at the input of the IV converter are amplified by the ratio  $A/R_S$ . In our experiment  $A = 1 \times 10^7$  and  $R_S = 100 \text{ k}\Omega$ , meaning that, when metallic contacts ( $R_J \leq 12.9 \text{ k}\Omega$ ) are formed, the bias voltage  $V_{Bias}$  must be corrected by a voltage  $V_C$ , which takes into account the small errors on the bias voltage  $V_{Bias}$  and internal offsets of the IV converter. In this way the junction resistance  $R_J$  becomes:

$$R_J = \frac{(V_{Bias} - V_C) \cdot A}{V_{STM} - V_{off}} - R_b - R_S \quad (3.11)$$

To characterize  $V_C$ ,  $R_J$  was substituted with resistors calibrated earlier and covering the whole target resistance range ( $\sim 1 \text{ k}\Omega - 10 \text{ G}\Omega$ ) [150].

A second correction factor involves the beam resistance  $R_b$ . Indeed the metal line running over the beam is made of platinum and its resistance varies with the average temperature of the beam itself. Being  $r_u$  the suspended part of the beam that is not thermalized, and  $\alpha$  the temperature coefficient of resistance, we get:

$$R_b = r_u R_{b,amb} \left(1 + \alpha \frac{\Delta T}{2}\right) + (1 - r_u) R_{b,amb} \quad (3.12)$$

where  $\frac{\Delta T}{2}$  is the average temperature drop on the beam, and  $\Delta T$  the one at the heater.

Looking at the thermal circuit, the  $1 \text{ M}\Omega$  input resistance of the differential amplifiers (SR640 Stanford Research) is only  $\sim 20$  times larger than the 2P-resistance of the heater ( $\sim 50 \text{ k}\Omega$ ). This doesn't allow to neglect the currents flowing into the beams connected to A1, but it can be corrected by introducing the input impedances of the amplifiers in Fig. 3.5 and re-calculating the actual currents flowing in each beam. Without this correction the value of the heater and beam resistances are overestimated by roughly 1%.

Another factor that must be taken into account, deals with the calculation of the exact power provided to the MEMS. For  $I_{STM} \neq 0$ , additional heat is generated across the junction resistance  $R_J$  and the series resistance of the beam  $R_b$ . To compensate for this effect, the extra heat generated in the STM circuit is calculated:

$$P_{STM} = \frac{1}{2} R_J I_{STM}^2 + \frac{1}{2} r_u R_b I_{STM}^2 \quad (3.13)$$

This value is then added to the power provided by the heater (3.13) and it is particularly relevant at low temperature. The second term is equal to the one already used for the contribution of the heater lines, but for STM measurement only one metal line is involved, contributing  $\frac{1}{2} r_u R_b I_{STM}^2$  (compare eq. 3.7). The first term instead, refers to the assumption that in QPCs or molecular junctions the power is symmetrically dissipated ( $\times \frac{1}{2}$ ) in both electrodes, tip and MEMS. It was demonstrated that in 1-dimensional systems which can be described within the Landauer formalism, there is a direct link between the transmission function  $\tau(E)$  of the junction and the power dissipation [154–156]. Precisely, if  $\tau(E)$  changes slowly around the Fermi energy ( $E_F$ ) then the power is dissipated equally in the two electrodes, as in the case of homogeneous QPCs. On the other hand, for molecular junction (or heterogeneous<sup>1</sup> QPCs) this assumption is not

<sup>1</sup>heterogeneous here means a junction made by two different metals as electrodes.

valid anymore and Peltier effects come into play, making the dissipation asymmetric. The level of asymmetry is firmly related to the slope of  $\tau(E)$  at  $E_F$  and thus to the Seebeck coefficient. Hence, equation 3.13 can be directly used in case of homogeneous metallic QPCs, but for molecular junctions the degree of asymmetry has to be estimated case to case from the reported or measured values of their Seebeck coefficients. Note that usually, because of the high resistance involved in molecular junctions and the small voltage applied ( $<100$  mV), these effects are essentially negligible.

For what concerns the thermoelectric measurements there are two main sources of non-idealities. The first one consist in the DC-offset present at the input of the IV converter when  $V_{Bias} = 0$ . This can be easily compensated by measuring the open circuit signal at the input of the converter, and by checking that its value stays constant before and after each measurement. The second one is given by the thermoelectric voltage arising across the copper lead connecting the Au-tip, due to the uncompensated temperature gradient, see Fig.3.8. This systematic error can be subtracted during the data analysis.

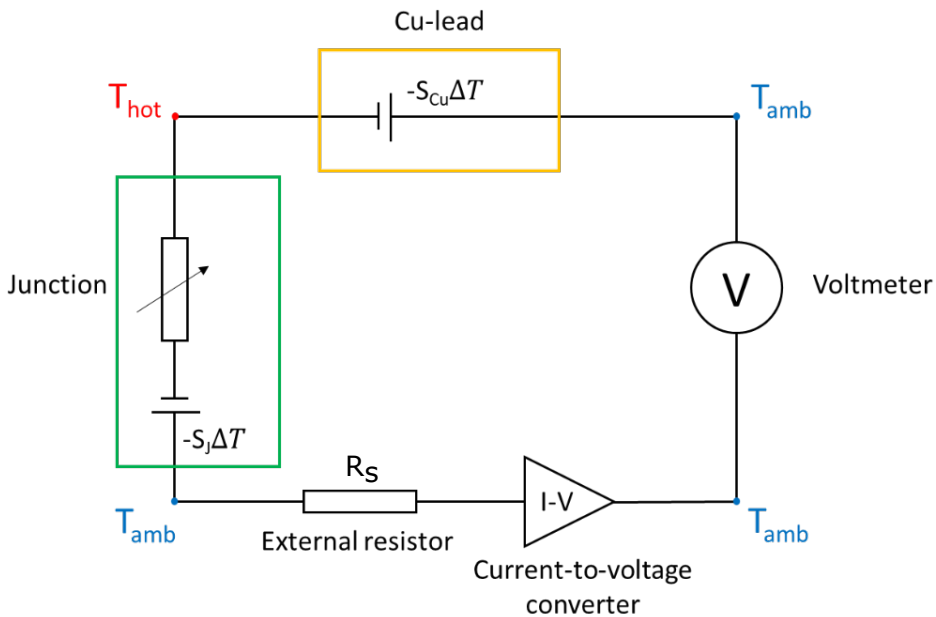


**Figure 3.8** Electrical circuit (as in 3.4) and equivalent thermal circuit, when  $V_{bias}$  is set to zero. The junction (marked in green) is electrically equivalent to a conductance  $G$  and a thermovoltage (battery) in series. It is also necessary to include the thermovoltage that develops across the connecting copper lead (marked in yellow), due to the uncompensated temperature gradient. Adapted from supplementary information of [143].

## 3.2 Experimental Setup

In the first part of this section a small description of the ultra low noise laboratory hosting the experiments is given. Following that, the two STM-based setups used for Break Junction experiments will be presented. The first one is devoted to room-temperature measurements of thermal, electrical and thermoelectric properties of single atoms and molecules. It has been developed by N. Mosso and B. Gotsmann and for that will be only described briefly in paragraph 3.2.2. For more details refer to [150]. The second setup, instead, is devoted to variable-temperature measurements of heat and charge transport in single atoms and molecules, in the range between 12 K and 400 K. This new setup, also referred as HIBERNUM, has been designed and developed from scratch by the Author of the thesis, with valuable help from A. Zulji and B. Gotsmann, 3.2.3.

3

### 3.2.1 Noise Free Lab

Our experiments are located inside one of the IBM Noise Free Labs in the basement of the Binnig and Rohrer Nanotechnology center, right outside Zurich [151]. The design of the laboratory aims to screen simultaneously all the disturbances relevant for a nanotechnology experiment, namely, vibrations, AC and DC magnetic fields, temperature, humidity and sound. Figure 3.9 shows a cross-section of the lab.

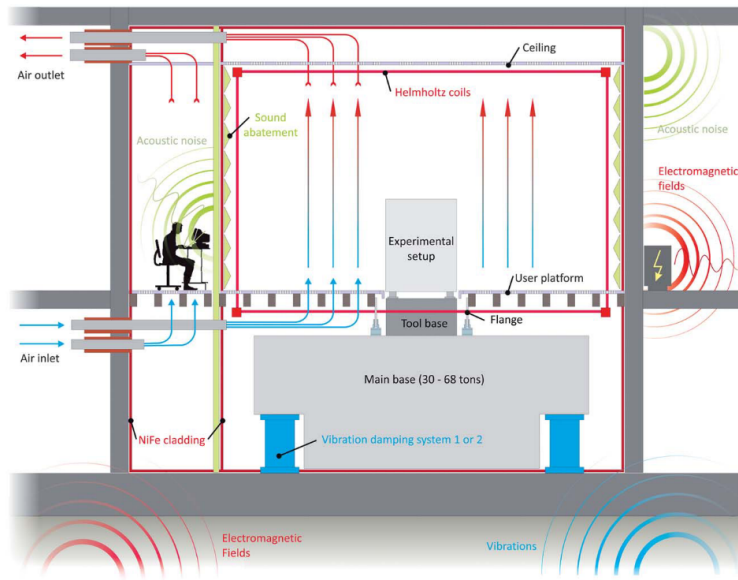


**Figure 3.9** Cross-sectional view of the lab including operator room and underground installations. From [151]

A Noise-Free-Lab consists of an operator room, from where the researcher can control the setup without disturbing the measurements and an experiment room, where the setup and the sensitive electronic equipments are placed. Next to the lab there are

two additional side rooms, in which the noisy equipments (compressors, pumps, etc...) are installed. An optical table to accommodate for the setup is positioned on top of a large concrete block of 30 or 68 tons to passively damp the high frequency mechanical vibrations (above 5 Hz). The concrete slab is further suspended on a combination of air springs and air cushions to allow for active compensation of the residual vibrations. With this solution, vibrations of less than 300 nm/s at 1 Hz and less than 10 nm/s above 100 Hz were achieved. The air flow coming from the conditioning system was designed to not excite the optical table and the concrete block. The temperature is maintained constant within  $\pm 0.01$  °C and the humidity within  $\pm 2\%$ . Foamy sound-absorbing panels decorate the walls of the experiment room to absorb the acoustic noise generated inside and outside of the lab. A magnetic layer made of conducting NiFe sheets (80% Ni, 20% Fe), that passively shields from medium and low frequency electromagnetic fields (100 Hz – 100 kHz), coats the door, walls and ceiling. An additional aluminum layer is welded to the magnetic one to form a Faraday cage. Furthermore, three Helmholtz coils to actively compensate for variations in the DC magnetic field are installed inside the room. In term of performances, AC-electromagnetic peaks are contained below 0.3 nT and DC variations are within  $\pm 15$  nT. The benefits of working in such a lab, especially in terms of mechanical stability, will be discussed in more details in Section 3.2.3. As side remark, we note that in spite of the risk to increase the acoustical and electromagnetic noise, most of the electronic instruments (differential amplifiers, IV converter and ADWin) are installed inside the experiment room, close to the setup, to minimize the pick-up noise induced by long coaxial cables.

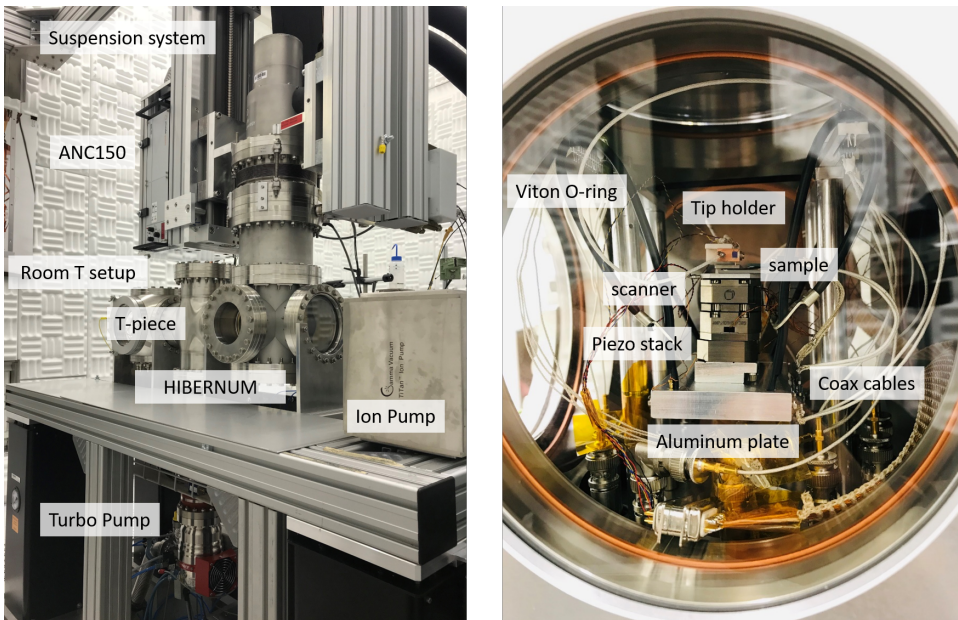


**Figure 3.10** Room temperature setup as used in [23, 97, 143]. The HIBERNUM setup will be described in Sec. 3.3.

### 3.2.2 Room Temperature Setup

The development of the room temperature setup, was initiated by B. Gotsmann and then finalized by N. Mosso. The original version is described in [150]. The setup was then modified by the author, with the help of F. Hurtak, to be integrated in a more complex variable temperature configuration (3.2.3). The room temperature chamber is placed on the leftmost part of the setup, see Fig.3.10, and features 6 openings connected via CF160 flanges. A quick access door on the front allows for sample loading and tip exchange. All the vacuum parts, apart from the door, are UHV compatible. Pressure sensors are positioned at the back of the chamber. On its side (see Fig.3.10 left) a T-piece connects it to the turbo pump (HiPace<sup>®</sup> 300 from Pfeiffer Vacuum, bottom) and to the variable temperature arrangement HIBERNUM (right). Inside (Fig.3.10 right), the sample holder is positioned on top of a stack of piezoelectric elements consisting of 2 positioners (Attocube ANPx101) for the coarse motion in-plane and the open loop xyz-scanner (Attocube ANSxyz100) for STM operation. The sample holder is composed of a stainless steel base plate on top of which a custom-layout probecard (from SQC AG) is mounted. The holder is then attached magnetically to the piezo-scanner thanks to an intermediate plate, screwed on the scanner itself, which contains few tiny but strong permanent magnets. The copper tip holder, instead, is placed behind the sample on top of the z-positioner for the coarse out-of-plane motion (Attocube ANPz101). The lower piezoelectric elements are screwed on an aluminum base plate, which is suspended via 4 Viton<sup>®</sup> O-rings. The location of the aluminum plate inside the setup is adjusted at short distance from the front door ( $\sim$  cm), to enable optical access and navigation of the tip via a simple stereo-microscope. Finally, to trade off between the electronic noise level and the mechanical vibrations reaching the sample stage, short coaxial cables first go from the probecard to an intermediate series of pins, which are anchored onto the aluminum baseplate and then connected to the feedthroughs via floppier coaxial cables.

### 3.2.3 Variable Temperature Setup

To clearly separate and characterize all the different effects and contributions occurring in transport physics it is often necessary to vary the temperature of the experiment over a wide range, from above ambient to cryogenic temperatures. In thermal experiments in fact, temperature plays the same role as the voltage bias in electric measurements, varying which allows to probe different operating regimes and specific transport mechanisms. For example, at room temperature, the well-known Wiedemann-Franz law (WF) states the proportionality between the electrical and thermal conductance of a metal. It can be expressed as:

$$\frac{\kappa}{\sigma \cdot T} = L_0 = \text{const} \quad (3.14)$$

where  $\kappa$  is the thermal conductivity,  $\sigma$  the electrical conductivity and  $L_0 = \frac{\pi^2 k_B^2}{3e^2} = 2.44 \times 10^{-8} \text{ W}\Omega\text{K}^{-2}$  the Lorenz number. Despite being largely approximate, i.e. neglecting phonon contributions, electronic corrections, and inelastic scattering, it is found to be remarkably robust in ordinary metals, where heat is mainly transported by electrons. Eq. 3.14 can then be re-written more accurately as:

$$L_0 = \frac{\kappa_{el}}{\sigma T} \quad (3.15)$$

where  $\kappa_{el}$  is only the electronic contribution to the thermal conductivity. The importance of the Wiedemann-Franz law is due to the fact that it manifests the intimate and indissoluble connection between charge and heat transport inside metal-like materials at room temperature. But if one looks at the whole picture and considers both the electronic and phononic contribution to the thermal conductivity,  $\kappa = \kappa_{el} + \kappa_{ph}$ , then eq. 3.15 can be re-written in more general terms as:

$$L(x) = \left(1 + \frac{\kappa_{ph}}{\kappa_{el}}\right) L_{el}(x) \quad (3.16)$$

where  $x$  = temperature, size, electrical bias, etc... The ratio  $L(x)/L_0$  represents the deviation from the Wiedemann-Franz law. Significant deviations from  $L_0$  imply a decoupling between the electronic and heat transport [98]. This is essential e.g. for thermoelectricity, where:

$$ZT = \frac{S^2 \sigma \nearrow}{\kappa \searrow} \quad (3.17)$$

here  $S$  is the Seebeck coefficient and  $ZT$  the dimensionless thermoelectric figure-of-merit, expressing the ability of a material to convert heat into electric power.<sup>2</sup> The arrows in equation 3.17 show the increase( $\nearrow$ ) or decrease( $\searrow$ ) needed to improve the thermoelectric performance of the material. Unfortunately, as already seen in eq. 3.14, the two conductances cannot be varied in opposite direction, unless a deviation occurs. Recently, it has been proven that by reducing at room temperature the size of the metallic electrodes below to just a single atom didn't bring to any observable violation of WF [22, 98]. Another interesting way to probe possible deviations is by changing the temperature (i.e.  $x = T$ ). In this case we get:

$$L(T) = \left(1 + \frac{\kappa_{ph}}{\kappa_{el}}\right) L_{el}(T) \quad (3.18)$$

At low  $T$ , in fact, the ratio  $\frac{\kappa_{ph}}{\kappa_{el}}$  is supposed to increase, because of the relative larger contribution of the phononic part to the thermal conductivity below the Debye temperature of the material, see Fig.3.11.

In the following section (3.3), a new setup allowing for variable temperature measurement of single atom junction, from 12 K to 400 K, will be described in details and results on WF will be presented in section 3.6.

---

<sup>2</sup>In literature is possible to find two definitions for the thermoelectric figure of merit: the *material*  $ZT$  (also called  $zT$  and directly linked to the material properties [157]), where  $S(T), \sigma(T), \kappa(T)$  are functions of temperature; and the *device*  $ZT$ , calculated from the formula for maximum efficiency, where one assumes 1-dimensional transport, constant  $S, \sigma, \kappa$  and perfect match between n-type and p-type materials [157]. In this thesis we always refer to  $ZT$  as the *material-ZT*.

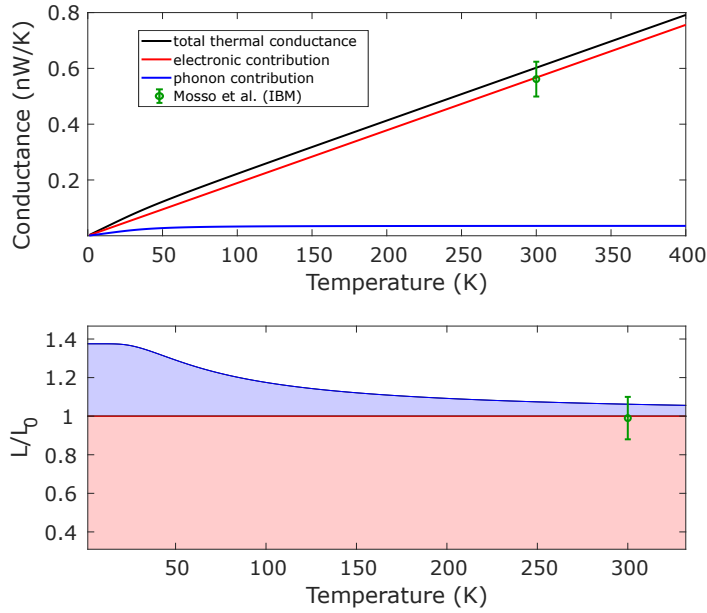


**Figure 3.11** Top: temperature dependence of the different contributions to the thermal conductance. The green dot refers to [22]. Bottom: Deviation of the Lorentz number  $L(T)$  from  $L_0$  as function of temperature in single atom contacts, assuming Wiedemann-Franz and phononic contribution, with a fixed transmission function  $T(E)$ .

## 3.3 Ultra-stable dry cryostat for variable temperature Break Junction (HIBERNUM)

This chapter has been submitted for publication in July 2021 to Review of Scientific Instruments. The text, figures and references have been re-formatted in the style of this thesis.

3

# Ultra-stable dry cryostat for variable temperature STM-Break Junction

Andrea Gemma<sup>1</sup>, Anel Zulji<sup>1</sup>, Femke Hurtak<sup>1</sup>, Shadi Fatayer<sup>1</sup>, Achim Kittel<sup>2</sup>, Michel Calame<sup>3,4</sup> and Bernd Gotsmann<sup>1</sup>

<sup>1</sup> IBM Research – Zurich, 8803 Rueschlikon, Switzerland

<sup>2</sup> Institute of Physics, University of Oldenburg, D-26111 Oldenburg, Germany

<sup>3</sup> Empa, Swiss Federal Laboratories for Materials Science and Technology, 8600 Dübendorf, Switzerland

<sup>4</sup> Department of Physics, University of Basel, 4056 Basel, Switzerland

**AUTHOR CONTRIBUTION:** AG and BG designed the setup with some initial input from AK. AG, AZ, FH and BG built the setup. AG performed the measurements and analysed them with input from BG, MC and SF. AG and BG wrote the manuscript with inputs from all co-authors.

### 3.3.1 Abstract

We present the design of a variable temperature setup that uses a pulse tube cryocooler to perform break-junction experiments at variable temperature ranging from 12 K to room temperature. The use of pulse tube coolers is advantageous because they are easy to use, can be highly automatized and avoid wasting of the cryogenic fluids. This is the reason why dry cryostats are conquering more and more fields in cryogenic physics. However, the main drawback is the level of vibration that can be up to several micrometers at the cold-head. The vibrations make operation of scanning probe-based microscopes challenging. We implemented vibration-damping techniques that allow to reduce the vibration level reaching down to 12 pm. With these adaptations, we show the possibility to perform break junction measurements in a cryogenic environment and keep in place atomic chains of few nanometers between the two electrodes.

### 3.3.2 Intro

Transport measurements of heat and charge at atomic and molecular scales have benefited tremendously from scanning probe microscopy and related techniques. For exam-

ple, to probe quantum transport properties, break junction (BJ) experiments based on scanning tunneling microscopy (STM) have become a major working horse to characterize atomic and molecular junctions. In STM-BJs, two electrodes, the metal tip and the metal surface, are brought in contact and then slowly separated. In this way it is possible to slowly thin down their contact to the atomic level and pull out from the substrate a single atom or even linear chains of atoms, that can be then studied in terms of their physical properties. In break junctions, quantization effects are routinely used as models to study electrical, thermal and mechanical properties down to the atomic scale at different temperatures [22, 23, 143, 148, 158]. Because of a clear quantum nature and their atomic size, those junctions are often referred as “quantum point contacts” (QPCs). Transport physics involves various effects, ranging from hopping to tunneling, quantum interference, magnetic correlations, etc. To clearly separate and characterize these effects, it is often necessary to vary the temperature of the experiment over a wide range, from above room temperature to cryogenic temperatures. Bath cryostat setups allowing variable temperature operation consume considerable amounts of liquid helium, which is both costly and demanding for the operator. Pulse tube coolers (PTCs), in contrast, recycle helium in a closed-cycle operation. PTCs require less handling, are most cost-efficient and can be remotely controlled compared to standard wet refrigerators. On the other hand, even though they can be built without moving parts at low temperatures, the main drawback with Pulse Tubes is indeed the level of vibration, that in most cases is about several micrometers at the cold end. The formation and study of QPCs by STM-Break Junction techniques require a significant level of mechanical stability (below  $1\text{\AA}$ ), that is in contrast with the vibration levels of PTCs, for which micrometer level amplitudes are considered already ambitious [159, 160]. A level prohibitive in case of sensitive techniques, like scanning probes. The reason is that pulse tubes rely on a periodic compression of the working gas, usually helium, inside the refrigerator. The periodic change in pressure causes a periodic elastic deformation (“breathing”) of the tubes inside the cryostat, that results in mechanical oscillations at the cold end. To address the issue, mechanical decoupling schemes have been proposed, in which the cold end of the pulse tube is thermally coupled to the experimental site (such as the STM head) through compliant springs, minimizing mechanical interaction [161–163]. A completely different approach is the employment of two pulse tube units that are  $180^\circ$  out of phase with each other to self-cancel the amplitude of the low-frequency oscillations [164]. More sophisticated solutions rather rely on the combination of passive damping methods with active feedback control either directly at the experimental site, e.g. feedback loop in a AFM system [162], or simply at the cold-head stage [165, 166].

Here we report on the construction of a variable temperature setup that uses a Pulse Tube refrigerator to reliably perform STM-Break Junction experiments at vibration levels in the picometer regime by solely using passive damping techniques, with a minimum working temperature of 12 K. The proposed design can be combined with conventional mechanical shielding such as optical tables or concrete slabs (like in the present case).

### 3.3.3 Description of the setup

#### Setup

The overall schematic of the laboratory and the instrument is shown in Fig.3.12. The setup involves vibration reduction measures at different scales. First, it is important to physically decouple the noisy mechanical parts, i.e. the pulse-tube cooler and the helium pressure valves, from the sensitive parts, i.e. the microscope stage, that is housed inside the vacuum chamber. This oftentimes necessitates considering the floor of the setup carrying the vacuum chamber as a sensitive part of the setup, from which pulse tube should be decoupled. In the present case, the setup is located inside one of the IBM *Noise Free Labs* to guarantee a superior isolation from the main sources of mechanical and electromagnetic noise through the floor[151]. Of particular interest, in this case, is the vibration isolation, see Fig. 3.12a. The laboratory floor is split in two segments. The first one is a heavy slab of around 30 t of concrete, that is mechanically decoupled from the rest of the environment and suspended on active-controlled air pistons. The concrete slab is used as tool base for the experiment. The second segment instead, is a wooden platform surrounding the concrete slab and attached to the inner walls of the laboratory, with no mechanical link to the concrete block. The wooden platform is walkable by the users and permits to control the experiment without any interference from close distance. The main idea driving the whole design is to mechanically decouple the Pulse Tube Cooler (PTD4200, TransMIT GmbH) from the microscope head, while preserving a good thermal link between the two. In order to do that, first, the rotary valve is physically separated from the cryocooler head and mounted on a suspended aluminum frame (Fig. 1, (1)). A sound-absorbing material (ArmaSound) was used to cover the rotary valve and helium-supplying lines to reduce mechanical and acoustical noise. Second, the cryocooler itself is suspended to a transversal aluminum crossbar attached to the sidewalls of the laboratory (2). The suspension is realized through a linear guide system (Igus, (3)) that connects the cryocooler flange to the aluminum crossbar and allows to change the height of the cryocooler with respect to the vacuum chamber where it will be inserted for the experiment. The vacuum chamber, instead, sits on an optical table (4) standing on the isolated concrete slab (5). Upon insertion, the only mechanical link connecting the cryocooler flange to the vacuum chamber is a flexible stainless-steel bellow (6), that provides a first stage of damping. Right below the bellow there is a flange for the electrical feedthroughs (7) and then a supporting flange to which an aluminum shield (9) is hung by means of low thermal conductivity glass-fiber rods (8) ( $\varnothing = 6$  mm,  $k_{th} \simeq 0.7$  W/(m·K)). The aluminum shields are gold plated using electroplating to increase reflectivity. The shield is thermally connected to the first stage of the cryocooler, at 50 K, through flexible copper braids (OFHC grade,  $k_{th} \simeq 395$  W/(m·K), thickness = 2 mm). Inside the shield, a first copper platform is attached to the inner part of the shield through another set of the same glass-fiber rods. The copper platform is then thermally linked to the second stage of the pulse tube cooler, at 4 K, by means of a second series of copper braids like the ones above. This stage is used to thermalize all the wires (24x silver-plated copper twisted pair (34-AWG) plus 4x copper single wires (24-AWG)) before reaching the experiment. Then, a second copper platform (11), situated below the first one, holds the microscope head and it is mechanically suspended to the upper platform via a combination of stiff rods and

### 3.3 Ultra-stable dry cryostat for variable temperature Break Junction (*HIBERNUM*)

custom made Be-Cu springs (10) (spring constant  $\sim 150$  N/m). In order to provide an optimal thermal link, a copper strip (thickness = 0.5 mm), shaped as a floppy spiral, goes around each spring, connecting the two stiff rods (10). At the scanning stage (11), a sample carrier (FerroVac SHOMECE13) is placed on a stack of piezoelectric elements consisting of 2 positioners (Attocube ANPx101) for the coarse motion in the XY-plane and one open loop xyz-scanner (Attocube ANSxyz100) to guarantee sub-nm resolution during STM-break junction measurements. The thermalization of the sample carrier is guaranteed by the attachment of an additional copper wire to the scanning stage. Finally, to allow for a variable operating temperature of the microscope, a heater (50  $\Omega$  resistor, (12)) is attached to the bottom of the scanning copper stage and regulated via a temperature controller (Lakeshore 335).

3

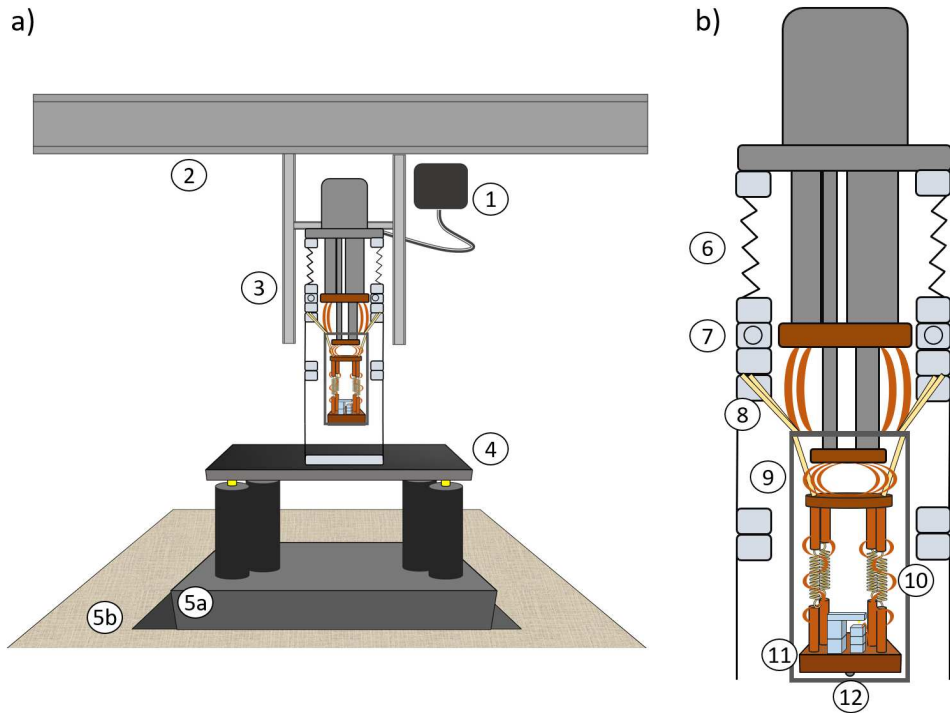


**Figure 3.12** Schematic drawing of Variable Temperature STM-Break Junction Setup. 1) Rotary valve separated from the rest of the cryogenic setup; 2) aluminum crossbar; 3) linear guide system; 4) optical table; 5) concrete slab (5a) and walkable wooden frame (5b); 6) edge-welded bellow; 7) feedthrough flange; 8) glass-fiber rods; 9) aluminum radiation shield; 10) springs and copper floppy spirals; 11) scanning stage; 12) heater for variable temperature operation.

### Cooling operation

The system is designed to reach a temperature of 12 K, mainly limited by the thermal conduction of the cabling involved and the thermal coupling of the shield to the first cooling stage. However, in the selection of the cooler, the low level of vibration has been preferred over cooling capabilities. In the case under consideration, the anticipated experiments are also rather slow. Therefore, a large copper mass could be used to avoid thermal fluctuations, leading in return to relatively long cool down times. Usually, a minimum temperature of 12 K is steadily reached after 9 h of cooling from room temperature.

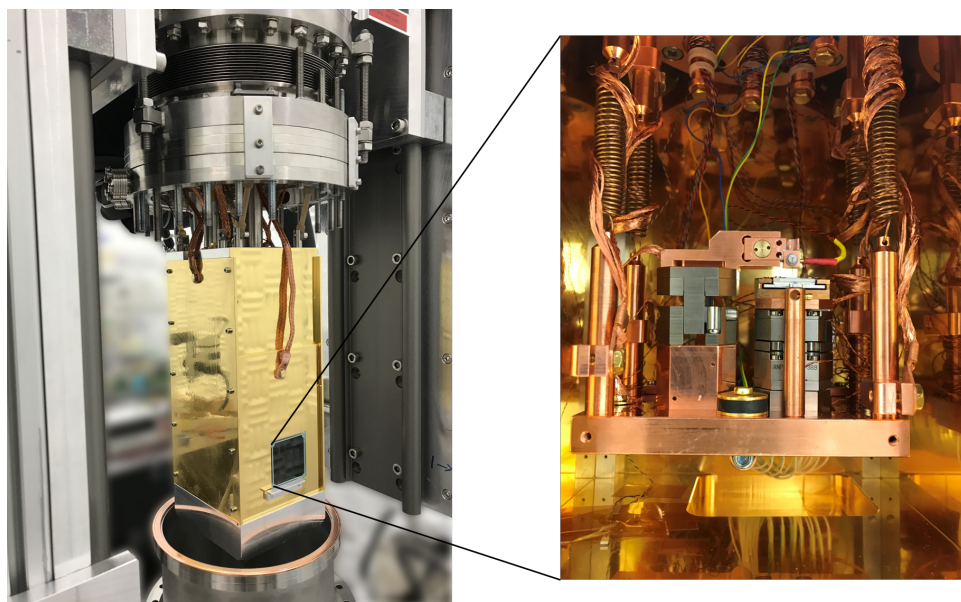


**Figure 3.13** Picture of the setup with thermal radiation shield. In the box, a close view of the scanning stage suspended via Be-Cu springs.

### Characterization methods

**Vibration.** Within the system, there is interest to measure the vibration levels at two locations, at the second stage of the PTC, and at the STM head, to probe the relative motion of the tip with respect to a sample surface. The vibration levels at the PTC are measured using accelerometers (Bruel and Kjaer, Type 4506-B-003) mounted directly to the second stage. Measurements were recorded at room temperature directly after starting the PTC operation. The measured power spectrum of vibration was then numerically integrated twice to calculate the displacement spectrum, over a 20 Hz bandwidth, see Fig.3.14a). To measure the vibration amplitudes in the microscope head we make use of the strong distance dependence of a tunneling current between the STM tip and surface. To this end, we use a gold STM tip and 150 nm-thick gold layer deposited

on a silicon chip. The tip is chemically etched from a 250  $\mu\text{m}$  pure gold wire (Goodfellow AU005140), then rinsed in DI water and isopropanol and finally dried under nitrogen flow. The gold surface of the chip is cleaned by flame annealing, wire-bonded to a chip carrier and then loaded into the vacuum chamber. The net displacement between the tip and the sample is calculated inverting the equation:

$$I(z) \propto I_0 e^{-2kz} \quad (3.19)$$

where  $z$  is the distance between the two electrodes, while  $k$  is the inverse decay length specific to the material. As  $k$  is sensitive to the exact work function of the sample and tip, we measure  $m = 2k$  each time before and after performing a new measurement of vibration. Measured values of  $m$  range from 0.1  $\text{\AA}^{-1}$  to 0.8  $\text{\AA}^{-1}$ . A schematic of the measurement technique is depicted in Fig.3.15a). The amplifier used is a low noise current-to-voltage converter (SP983c from Basel Precision Instruments) with a gain of  $1 \times 10^7$  V/A. The acquisition time interval is set to 10 sec with a sampling time of 1 ms, so that the accessible frequency range spans from 0.1 Hz to 500 Hz. In this way all frequencies relevant to STM-BJ operation, including the low frequencies typical of Pulse Tube oscillation of 1-2 Hz, can be probed.

**Break Junction measurements.** Break junction traces are acquired right after vibration measurements, by approaching the tip of the microscope into contact with the counter electrode (closing trace) and slowly retracting it apart (opening trace). The closing trace stops when a conductance of  $G_{el} = I_{stm}/V_{Bias} = 10G_0$  is reached. Here  $G_0 = \frac{2e^2}{h} = 7.75 \times 10^{-5} S$  is the quantum of electrical conductance. The speed for both approach and retraction from the surface is set to 7 nm/s

### 3.3.4 Characterization of vibrational noise and its effects

#### Vibration of the cryocooler

For comparison Fig.3.14 displays measurement of the vibration level of the second stage of the PTC during operation of the PTC and in the idle stage. Fig.3.14a) shows the rms-displacement spectrum for the  $z$ -axis over a 20 Hz bandwidth. A peak around  $\sim 1.2$  Hz, signature of the Pulse Tube Cooler, is clearly visible, together with higher frequency harmonics. In Fig.3.14b, the mechanical oscillations recorded by the accelerometer are plotted over a 3 seconds period. For this plot, the low-frequency drift visible in Fig.3.14a was removed using a high-pass filter to visualize better the vibration level induced by the operation of the PTC. The peak amplitude of the signal vs. time is equal to  $\pm 72.6 \mu\text{m}$  and the rms-amplitude to 35.6  $\mu\text{m}$ .

#### Net displacement

Next, we turn to measurements of the vibration inside the microscope head. A schematic of the measurement technique is depicted in Fig.3.15a). For the measurements we chose a temperature of 45 K after a week of cooling operation, which represents a typical experimental scenario. A vibration trace of 10 sec, with RMS-value as low as 11.8 pm could be recorded and is presented in Fig.3.15b). We note that vibration levels vary throughout the day but were never worse than 65 pm, see SI. Those levels

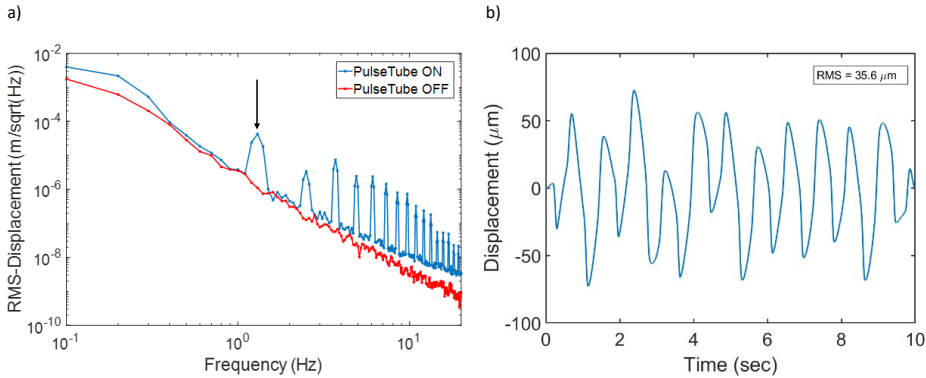


**Figure 3.14** Vibration specifications of the Pulse Tube cooler measured at the second stage: a) RMS spectrum (the black arrow indicates the main frequency of vibration at 1.2 Hz); b) Amplitude of displacement at 1.2 Hz.

are manageable for scanning probe measurements and compare well to other systems using PTCs cryocoolers for sensitive measurements. Our system has vibration levels lower than other dry-cryostat setups using single stage damping techniques, that feature rms-values of 65 pm or higher [161, 162], and it is in the same range of vibrations of other setups utilizing more sophisticated multi-stage methods, showing a cumulated displacement of 60 pm over almost a 10 kHz bandwidth [163]. We suppose that the reason for such high stability and small net displacement between tip and sample, can be attributed, in part, to the stillness of the lab and to the mechanical decoupling of the cold head from the rest of the setup, but mainly to the series combination of springs, acting as a “low-pass” filter for vibrations, and the “high-pass” filter, due to the rigid connection of the tip holder and sample carrier to the scanning stage.

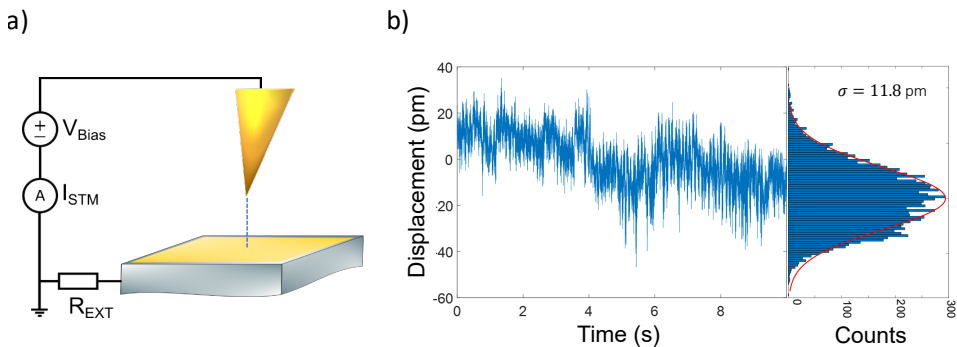


**Figure 3.15** a) Schematic for the measurement of the net tip-surface displacement; b) raw displacement trace, including low frequency drift, from STM current recorded over an acquisition period of 10s and its relative RMS-value ( $\sigma$ ).

### 3.3.5 Break-Junction operation

To demonstrate the capability of the instrument to operate during break-junction experiments at variable temperature, we performed a break junction experiment at 45 K. During the experiment the tip is repeatedly brought into (closing trace) and out of contact (opening trace) with the sample. The electrical conductance measured during such break-junction events demonstrates the hallmark of quantization steps and the thinning down of the junction down to single-atom diameters. An important criterion for the usability of good transport measurements is the temporal stability of the junction. Ideally a junction plateau (the conductance being on a defined and narrow range of values) is long enough in time (or pulling distance) to enable detailed measurements [23, 97].

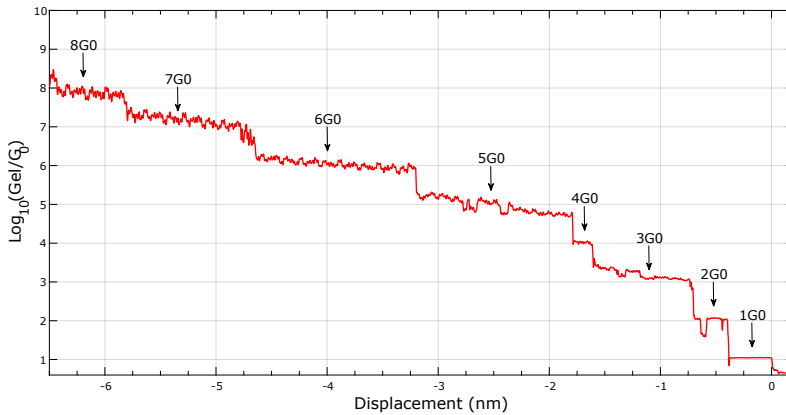


**Figure 3.16** Opening trace of a break junction measurement at 45 K

Because of the great stability of the system, the quantization of the electrical conductance is observable up to  $8 G_0$ , see Fig.3.16. Indeed, each quantization step represents the number of atoms (or monoatomic filaments) bridging the two electrodes, each one carrying a single quantum of electrical conductance  $G_0$ . To check for spurious events we performed 2300 measurements and combined them in a 1D histogram, see Fig.3.17a). More than 90% of the traces (2127 out of 2300) show a plateau of at least 5 datapoints in the range  $[0.9 ; 1.1] G_0$ . For those selected traces we calculate the length of the plateau at  $1G_0$ , showing how the stability of the system allows for the formation of long single-atom filaments up to several Ångstrom in length, with a good percentage of traces ( $\sim 25\%$ ) going above 1 nm, Fig.3.17b). We note that this distance suggests pulling atomic chains. To estimate the number of atoms in such chains, reported values for the radius of a gold atom, varying from  $1.35 \text{ \AA}$  to  $1.96 \text{ \AA}$  [167–169], can be considered, together with a stretched Au-Au bond distance around  $3.6 \text{ \AA}$  [60]. Fig. 3.17b) doesn't show obvious peaks at exact multiples of the aforesaid values, but ultimately illustrates the possibility to uphold nanometric, single-atom wires.

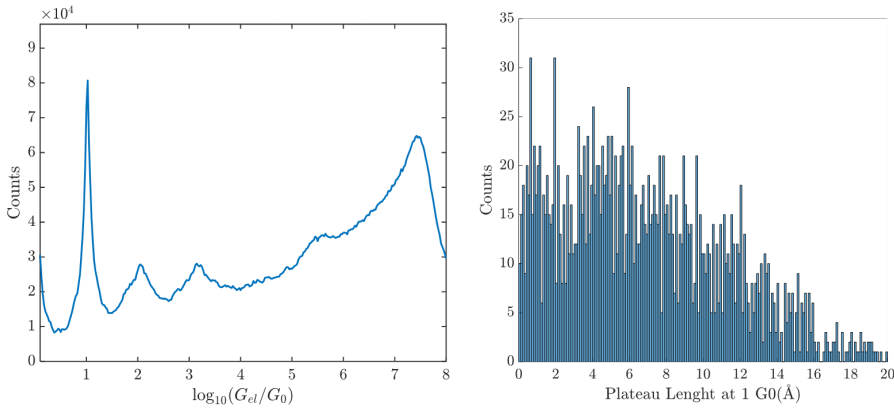


**Figure 3.17** 1D histograms showing a) peaks at multiples of the electrical conductance quantum  $G_0$ , and b) length of the plateaus at  $1G_0$

### 3.3.6 Outlook and conclusion

We have designed a system which can passively reduce the vibrations of a pulse tube cryocooler below 65  $\mu\text{m}$ . We show that in optimal conditions of the lab the system can achieve a level of vibration as low as 11.8  $\mu\text{m}$ . This allows for measurement of break junctions at variable temperature with a pulse tube cryostat. Compared to previously reported systems, the present setup reaches competitive vibration levels with a single stage damping system and without the need for more elaborated damping solutions such as cascaded mass-spring systems. Further improvement appears possible using, for example, an eddy-current damper installed between the bottom of the experiment stage and the shield to further reduce vibrations. Possible improvements for reaching lower temperature consist in using more resistive wires for lines that don't carry the signal (piezos, temperature sensors, ...) and/or reducing the diameter of the same. However, with the current modifications we already reached a level of vibrations that allows to run break junction experiment with sub-Å mechanical noise at variable temperatures and extract, from a gold surface, single-atom filaments stretching over more than 1 nm before rupture. We hope that the description of our STM Break-Junction experiment in a pulse tube-driven cryostat, can also help designing other cryogenic setups, especially with the present trend towards dry systems in cryogenics.

### 3.3.7 Annex: Optical access

During the first operation of the instrument an issue was immediately clear. The larger dimension of the vacuum chamber compared to the room-T setup induced a larger distance ( $>200\text{mm}$ ) between the sample and the optical microscope used for positioning the tip above the MEMS. Such a long distance made the previous microscope unusable, forcing a re-design of the whole optical arrangement. For this reason we tested different combinations of long-distance lenses and digital cameras, but none of them was capable, at 200 mm distance, to precisely resolve the central platform of the MEMS ( $\sim 20\mu\text{m}$ ).

To solve the problem, we decided to reduce the optical working distance by installing a re-entrant viewport in the front part of the setup. This allowed using a more standard long-distance 7:1 zoom lens (OPTEM) in combination with a digital industrial camera (pixel size  $1.55 \times 1.55 \mu\text{m}$ , HAYEAR 4K UDH HY-5299). Improvements in the optical resolution can be seen in Figure 3.18

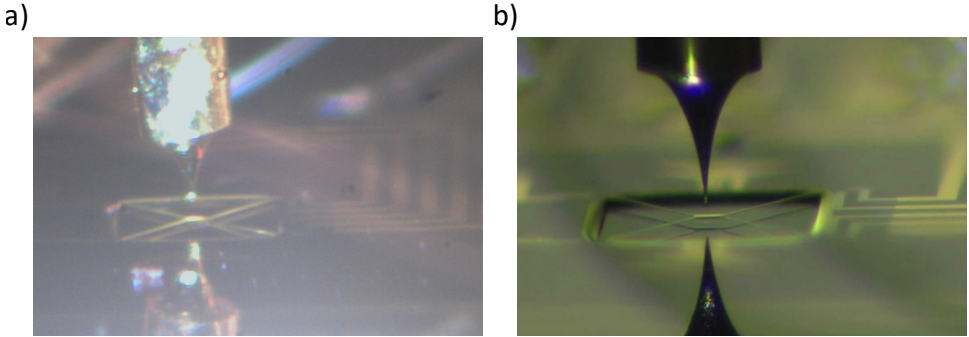


**Figure 3.18** Images of tip and MEMS a) before and b) after the installation of the new optical arrangement.

### 3.3.8 Annex: Noise performance

The noise on the STM circuit has been characterized in open loop configuration (i.e. without the tip being in contact). By using the low-noise I-V converter from Basel Precision Instruments (SP983c), which features an automatic offset compensation and a dynamic range of  $\pm 10$  V, we obtain a noise floor  $\leq 1 \times 10^{-6} G_0$ . Figure 3.19 shows the effect of temperature on the STM noise. The fact that the noise doesn't change considerably between 293 K and 15 K indicates that the major contribution comes from the electronics at ambient temperature (IV converter, ADWin system, cables).

The noise on the thermal conductance signal has been optimized by carefully tuning all the elements in the thermal circuit, with particular attention to the two differential amplifiers SR640 (Stanford Research). After the subtraction of suitable offsets provided by the ADwin system, both the heater voltage ( $V_H$ ) and current ( $I_H$ ) are amplified with a gain of  $\times 1000$ . In this way is possible to increase the gain of the two amplifiers to measure the small heater resistance changes ( $\Delta R \sim \Omega$ ) induced by the heat flowing out through the junction, and at the same time to compensate for the large resistance variation occurring upon setting a different temperature to the heater ( $\Delta R \sim k\Omega$ ), or by changing the setup base temperature via the cryostat ( $\Delta R \sim 50\%$ ). Figure 3.20 shows the thermal conductance noise for different temperatures. Compared to the previous setup [150], a new electronic peak related to the cryostat operation is present, but the overall noise floor has remained unchanged. By integrating the signal for at least 30 ms at 15 K, the noise level reduces to  $\sim 11$  pW/K. In the same bandwidth we get a sensitivity of  $T = 9$  mK,  $R = 0.5 \Omega$  (over  $\sim 17$  k $\Omega$ ) and heat flux  $P = 8.5$  pW in the same bandwidth. Those numbers compare well with literature, but the improvement expected by operating the device at reduced temperature was not apparent. This,

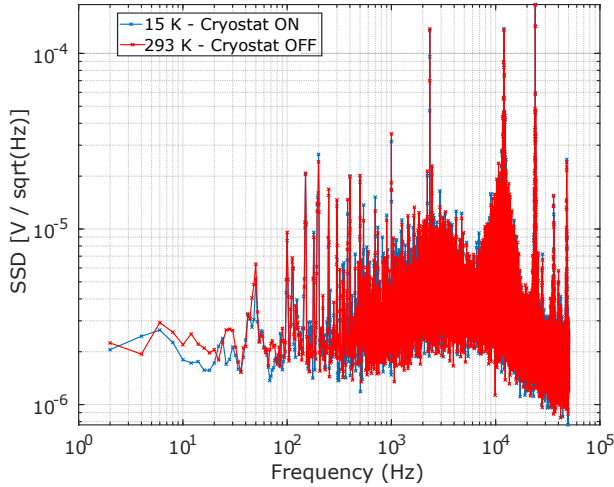


**Figure 3.19** Electrical noise on the STM circuit. Red trace refers to noise measurement at ambient temperature and cryostat off, while the blue trace is measured at 15 K, during cryostat operation.

together with results in Figure 3.19, suggests again that the main source of noise in the setup comes mostly from the cables and amplifiers at room temperature. At the moment we don't use any lock-in/AC technique, that would possibly result in a higher sensitivity, below 1 mK [170]. However, the induced temperature fluctuations on the compliant MEMS structure would negatively affect the mechanical behaviour of the junction, with a resulting strong decrease in bandwidth, making break junction measurements really arduous [150]. Future tests with lock-in techniques will confirm this thesis or shed a new light on the possible resolution limits of the setup.

### 3.4 MEMS Sensor

To measure tiny thermal signals, like the ones flowing through QPCs and single molecules, a fundamental requirement is to have sensors with very low thermal coupling to the environment, so that small heat fluxes can induce a measurable temperature change. This is a common situation in thermal science: differently from electrical conductivity where there are more than 26 orders of magnitude between a good insulator (e.g. fused quartz, electrical resistivity  $> 1 \times 10^{18} \Omega\text{m}$ ) and a good conductor (e.g. silver, electrical resistivity  $16 \times 10^{-9} \Omega\text{m}$ ), in case of thermal conductivity the range narrows down to only 5 orders between one of the best thermal insulator (e.g. silica aerogels with  $k \sim 0.01 \text{ W}/(\text{mK})$ ) and one of the best thermal conductor (diamond with  $k \sim 2200 \text{ W}/(\text{mK})$ ). To overcome this issue, people often use vacuum as main way to guarantee thermal insulation, by suspending the device under test. For this reason suspended micro-electro-mechanical structures (MEMS) have been widely used for many different thermal applications, from

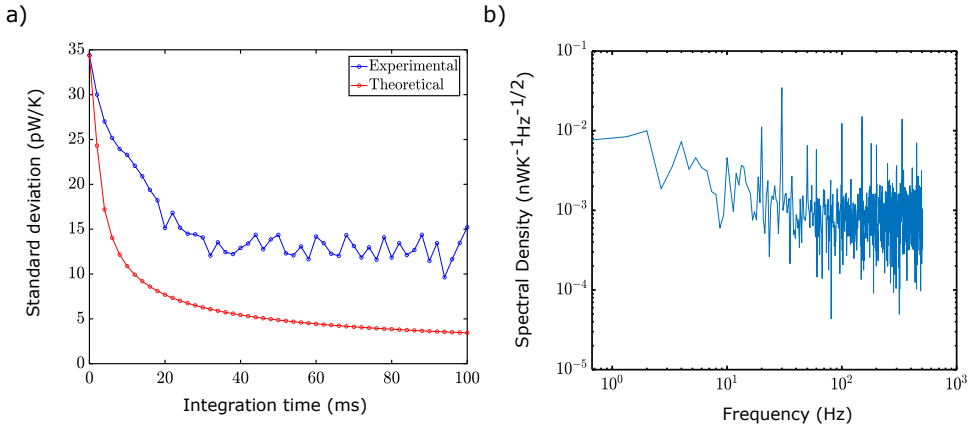


**Figure 3.20** Standard deviation and spectral density of the thermal conductance measured at  $T = 15$  K. a) Standard deviation of the thermal conductance at different integration times (blue) and expected theoretical trend for white noise only. b) Spectral density of the thermal conductance measured with a sampling time of 1 ms.

industry (production of bolometers and thermal cameras [171–173]) to research (thermal properties of nanomaterials [174–177], phonon conduction [89] and near field heat transfer [178]). In our case, we use a suspended MEMS with an integrated heater/sensor and a high thermal resistance ( $> 1 \times 10^7$  K/W) to measure signals on the order of pW/K. Because of the dynamic nature of Break Junction experiments, where the tip is continuously brought into and out of contact with the suspended platform, the mechanical stiffness also plays an important role. The two requirements, i.e. high thermal resistance and sufficient stiffness, are at odds with each other and a trade-off between them must be found to achieve an optimal MEMS design.

### 3.4.1 Design

The previous generation of the MEMS featured a thermal sensitivity of  $\sim 13$  pW/K and an electrical noise level of  $\sim 1 \times 10^{-6} G_0$  [150]. Those specifications allowed for the measurement in [22] and 4. During this thesis, improvements on the design were developed to solve two major issues of the previous generation, namely the rather low perpendicular mechanical stiffness ( $< 1$  N/m), and the difficult optical examination of the platform due to the large working distance of the camera. In the past, a trick used to circumvent the first problem was to use the larger in plane stiffness of the platform ( $\sim 500$  N/m) by approaching/retracting the tip with an angle  $< 90^\circ$  with respect to the MEMS surface. Typical values for moving angle were between  $20^\circ$  and  $40^\circ$  and the resulting stiffness around  $\sim 10$  N/m, as explained in [22, 23, 150].

To solve the stiffness, a first approach problem was to increase the number of beams suspending the platform, see Fig.3.21a). An interesting follow-up, to reduce twisting modes, consisted in connecting the middle point of every beams in a sort of *spider-net*, Fig.3.21b). In fact each middle point is at the same temperature, and linking all

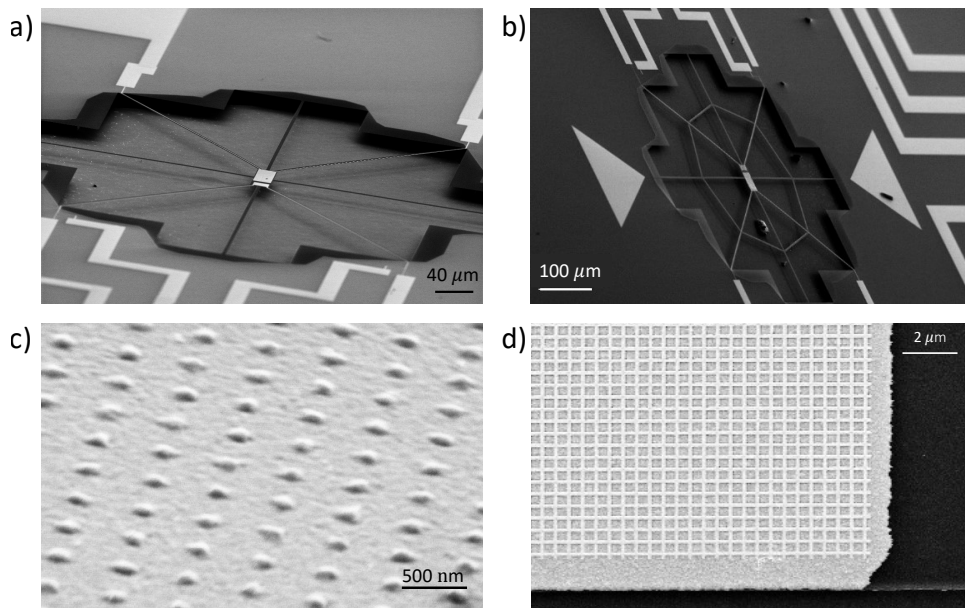


**Figure 3.21** Reinforced MEMS design: a) structure with 4 additional supporting beams; b) structure with supporting *spider-net*; c-d) micrographs showing patterning of the gold platform surface, to avoid stiction in structures a) and b), respectively.

of them together doesn't decrease the overall thermal resistance. However both the solutions utilizing additional beams didn't provide a good trade-off, with the decrease in thermal resistance not compensated by a significant increase in stiffness.

Another problem that was faced during the same fabrication run, was to reduce stiction between the tip and the sensor surface. For this reason a micrometer roughness was patterned in the gold surface consisting of differently shaped bumps or a grid (Fig.3.21c-d)). This allows for the local formation of lateral junctions between the tip and the side of a bump.

With the next generation of sensors we tackled the stiffness issue by designing a new version of the sensor that could feature an increased stiffness but maintaining a similar level of thermal sensitivity. To estimate the thermal resistance ( or equivalently the thermal conductance of the platform ) we can use the Fourier's law for thermal conduction:

$$G_{th} = \kappa_{th} \frac{A}{L} \quad (3.20)$$

where  $\kappa_{th}$  is the thermal conductivity typical of the material, L and A=w·t the length and cross-section respectively, Figure 3.22. According to 3.20, to minimize  $G_{th}$  we must design long supporting beams with a small cross-section and choose a material with low thermal conductivity. For our sensors the selected material is silicon nitride (SiNx), with typical thermal conductivity of 3-4 W/(m·K) [72, 73] and a Young modulus  $E \sim 260$  GPa[74] for thin films. In terms of geometry, the length of the beams L remains the main design parameter since the width w of the beams is constrained to  $4\mu\text{m}$  by the resolution of the optical lithography ( $\sim 2\mu\text{m}$ ) and to compensate for possible misplacing of the metallic lines on top. A thickness of 150nm has been optimized for the release process and it is usually not varied. Additional attention must be paid to the thermal conductance coming from the Pt lines used to contact the heater and the gold platform. Thin films of Pt have a thermal conductivity of  $\sim 30$  W/(m·K) at room temperature. Therefore, to keep their contribution to the overall thermal conductance below 10%, metallic lines are designed with a thickness of 25 nm and width varying from 100 to 200 nm. With typical values of length ranging from L= 250  $\mu\text{m}$  to L= 500  $\mu\text{m}$  we reached a measured thermal conductance  $G_{mems}$  between 4 and  $2 \times 10^{-8}$  W/K at room temperature and around  $3 \times 10^{-9}$  W/K at 15 K. Usually, because of a greater mechanical stability and easier tip-landing, the beams length L = 250  $\mu\text{m}$  is preferred.

To model the mechanical stiffness of the MEMS is instead quite challenging. It depends in fact on many different parameters that are usually not easily accessible and that change with the operating temperature. A list of such parameters would include the post-fabrication stress between the layers, the torsional and flexural bending modes, the thermal stress caused by the different thermal expansion coefficient of the SiNx and the metallic layers. However, to have a rough idea of the out-of-plane stiffness, we can use the equation derived for double-clamped beams under stress within the linear elastic continuum theory [75, 76]

$$k_{\perp} = 16 \frac{Ewt^3}{L^3} + \frac{2A\sigma wt}{5L} \quad (3.21)$$

where  $E$  is the Young's modulus and  $\sigma$  represents the tensile uniaxial stress along the silicon nitride beams.

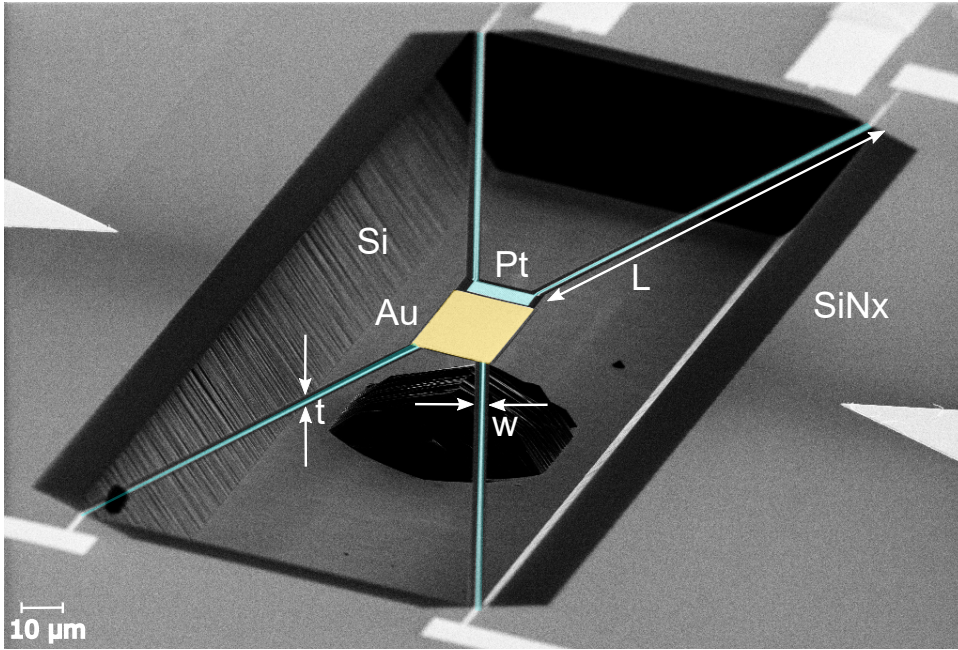


**Figure 3.22** False-color SEM micrograph of a typical MEMS structure.  $L$  is the length,  $w$  the width and  $t$  the thickness of the silicon nitride beams. The yellow color highlights the gold platform, while the light blue the platinum heater and lines. Adapted from [150]

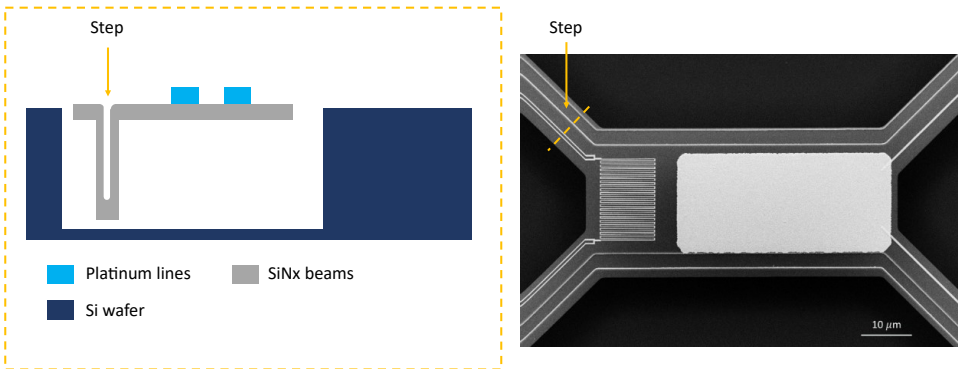


**Figure 3.23** Schematic (left) and SEM micrograph (right) of a new MEMS generation, introducing a step along the beam thickness to increase stiffness of the suspended membrane.

By looking at equation 3.20 is clearly visible that to get a low thermal conductivity, the cross section of the suspending beams must be reduced, while their length increased. From 3.21, on the other hand, follows that to increase the stiffness thicker beams are required. A way to combine the two equation is presented in figure 3.23. The T-shape of the beams aims to increase the thickness of the beam without changing drastically the cross-sectional area, with the new equivalent thickness given by the height of the step in the SiNx layer. Typical values for the step height are between 0.5 and 1.5  $\mu\text{m}$ , with different solutions currently being tested. The new structures required the design of an additional optical mask for the definition of the new beam layout, and a precise and uniform deposition of the SiNx layer. Together with the new design, a novel approach strategy for the tip has been developed and it is described in figure 3.27. The possibility to now operate the measurement with a  $90^\circ$  angle between tip and sample, thanks to the new, reinforced design, is confirmed by Fig. 3.24, where a 1D histogram collects more than 1700 traces showing quantization plateaus at 1,2,3 and 4  $G_0$ , validating the ability of the system to modulate the size and number of atoms in the junction. In fact, to gradually break contacts down to a single atom without mechanical backlash requires the MEMS having a stiffness larger than the one of the gold-gold bond ( $\sim 1 \text{ N/m}$ ).

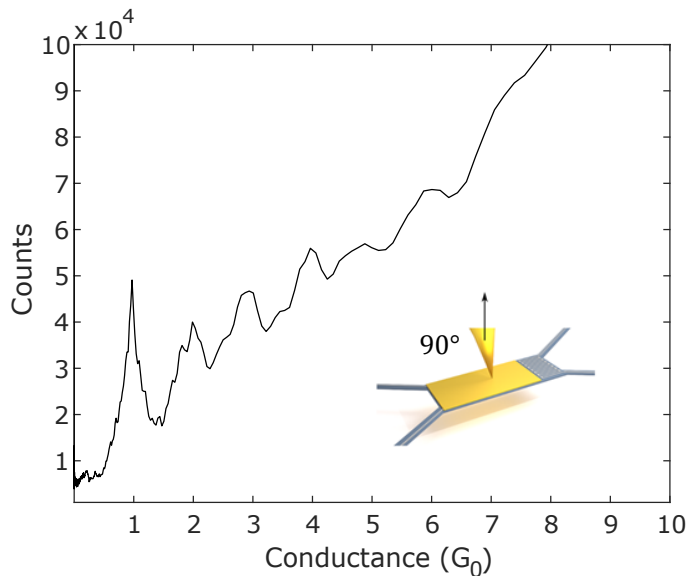


**Figure 3.24** 1D Histogram collecting more than 1700 break-junction traces showing stable plateaus at multiples of the quantum of electrical conductance  $1G_0$ .

Another key consideration about the design of the MEMS sensor is the assumption of homogeneous temperature across the platform. This is valid only if the thermal resistance of the beams is much larger than the one between the Pt-heater and the platform itself. In fact, the heat, spreading from the MEMS-heater towards the silicon substrate, sees on one side a thermal resistance of  $R_{th} = 2R_{beam}$ , while on the opposite

side a series of 2 thermal resistances  $R_{th} = R_{plat} + 2R_{beam}$ . Hence, the temperature difference over the platform can be calculated as

$$\Delta T_{plat} = R_{plat}/(R_{plat} + 2R_{beam}) \times \Delta T \quad (3.22)$$

where  $\Delta T$  is the temperature difference between the heater and the substrate. If we assume a thermal conductivity of gold  $k_{Au} = 125 \text{ W/mK}$  [150] and neglect the boundary thermal resistance between gold and silicon nitride, we obtain  $R_{plat} = 3 \text{ to } 4.5 \times 10^5 \text{ K/W}$ . With a typical beam thermal resistance  $R_{beam} = 9 \times 10^7 \text{ K/W}$ , we get  $\Delta T_{plat}/\Delta T < 1\%$ , small enough to safely consider the central platform in thermal equilibrium with the heater.

Looking at the dynamic response of the system, the reaction time of the temperature measurement needs to be fast enough to follow the breaking events. This can be described by a thermal time constant  $\tau = R_{mems}C_{mems}$ , where  $R_{mems}$  is the thermal resistance of the MEMS and  $C_{mems}$  the effective heat capacity. To optimize  $\tau$ , MEMS platforms with different dimensions have been devised, with the lower limit given by the size required to optically align the tip onto the MEMS. The smallest fabricated MEMS platforms are  $62 \mu\text{m} \times 17 \mu\text{m}$  including heater and gold platform, with a time constant around  $\tau \sim 20 \text{ ms}$  [150]. We note that at low temperature  $C_{mems}$  drops significantly, allowing the design of larger MEMS structures without sacrificing the reaction time.

### Design for improved optical resolution

To improve the positioning of the MEMS under the tip during the approach phase, some modifications were implemented also at the MEMS level. To mitigate for the poor optical resolution due to the limited depth of view of the optical unit, we changed the orientation of the platform to have the longer axis aligned with the direction where the resolution is lower (y-axis), see Fig 3.25

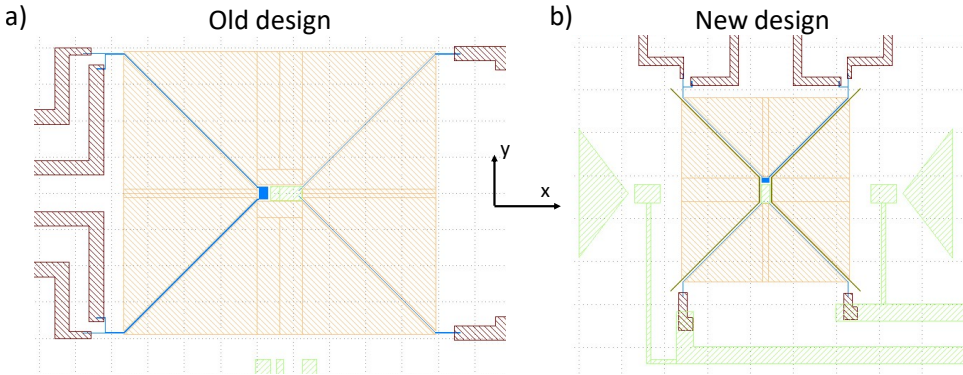


**Figure 3.25** a) MEMS design used in previous studies [22, 23]; b) new design with  $90^\circ$  rotation. The colors in figure indicate the different optical masks required for the patterning of the relative layer: orange for SiNx, green for gold, blue and red stripes for fine and coarse platinum layers, respectively.

In this way the user benefits of an increase probability to land directly on the platform on the first try, reducing drastically the approaching time and the number of attempts needed, that could damage and/or dirty either the tip or the MEMS in case of wrong landing, see fig. 3.26. A second modification consists in the presence of two alignment pads, connected to the STM lines and visible in Fig.3.25b) at the left and right side of the platform. Those pads serve as first landing sites to check electrical connection, but also to align the tip with the platform. In fact along the y-axis they have the same size of the suspended platform, so that, once aligned, the movements required to bring the tip above the platform are only along the x-axis. The new approaching procedure is depicted in Fig.3.27

3

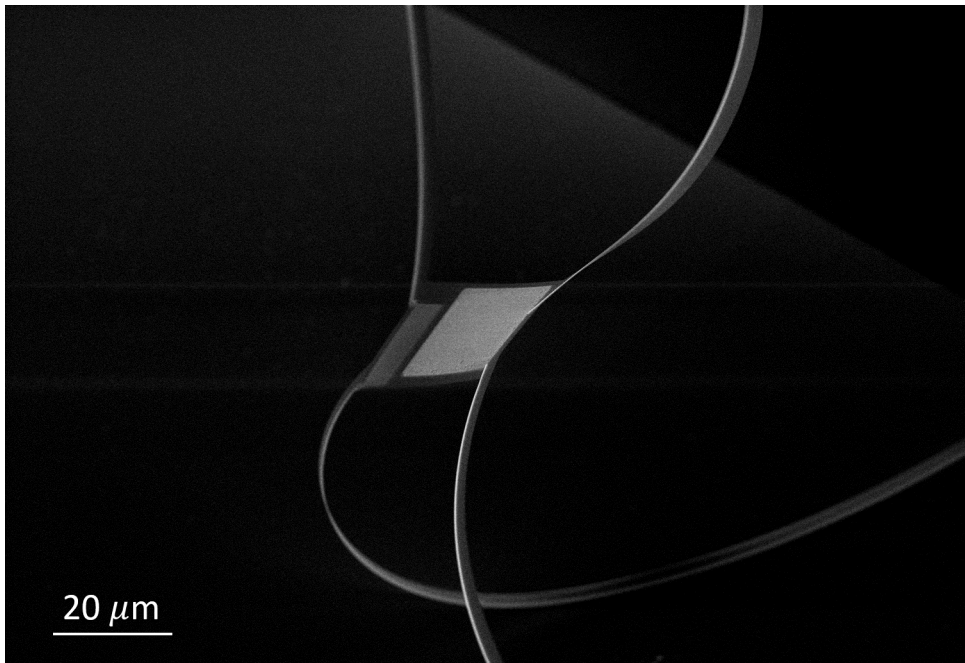


**Figure 3.26** MEMS damaged during a wrong landing onto one of the beams.

### On the materials selection

We selected silicon nitride ( $\text{SiN}_x$ ) to fabricate the supporting structure of the MEMS, platinum (Pt) for the heater/ thermometer and gold (Au) as platform electrode to perform STM-BJ measurement.  $\text{SiN}_x$  offers, in our case, a good combination of large Young modulus (260 GPa) and low thermal conductivity, making it ideal for optimizing the trade-off between mechanical stiffness and thermal sensitivity. Thanks to the uniform deposition achievable by low-power chemical vapor deposition (LPCVD) process, high quality films can be produce with minimum stress. This makes  $\text{SiN}_x$  one of the most popular materials to build suspended membranes on silicon. Platinum, instead, is

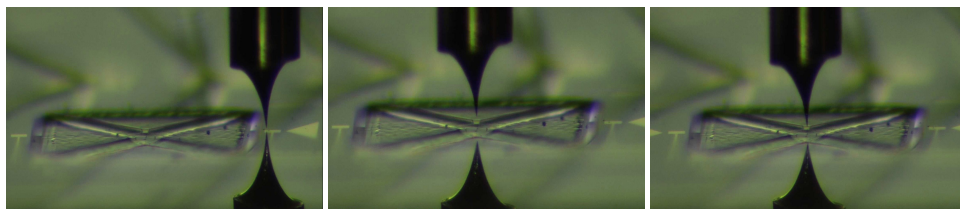


**Figure 3.27** Alignment protocol shown using the same long distance camera as described in section 3.3.7. Left: as first step the tip is aligned on top of the gold pad having the same size of the membrane along y-axis. Contact can be verified by STM measurement. Center: after the tip has been aligned in the y-direction, it is moved on top of the suspended platform. Right: a computer-guided approach routine lets the tip slowly land on the membrane.

one of the most used metals for fabricating precision thermometers (as the commercial standards Pt-100 and Pt-1000), because of its resistance linearity over a wide range of temperatures, its inertness and durability. Another important aspect is the capability to sustain large current densities (up to  $1 \times 10^7$  A/cm<sup>2</sup> [79]) before electro-migration failure. The reason for which Gold was selected as platform electrode is mainly because of its affinity to different molecules and anchoring groups. It also shows a relative simple electronic configuration that makes it one of the most understood and well studied material with the STM-BJ technique in terms of conductance quantization[27, 15], atomic chain manipulation [26, 15] and formation of molecular junctions [31]. However, in literature, other metals like palladium[81], silver [82, 83], nickel [84, 85] or even graphene [86, 87] are currently studied as alternative electrode materials for molecular electronics applications.

### 3.4.2 Fabrication process

For the fabrication of the MEMS devices we started from the process already established by our colleague Ute Drechsler in our IBM cleanroom at the Binnig and Rohrer Nanotechnology center. During the PhD different generation of MEMS structures were designed and tested. In Figure 3.28 the last version of the fabrication process is shown.

In its most complete version, the process consists of 4 lithographic steps: 2 electron-beam lithography (EBL) and 2 optical lithography, see Fig.3.28. The first part of the fabrication (1-4 in Fig.3.28) is carried out in collaboration with the Technical Research Centre of Finland (VTT). In VTT's cleanroom, trenches for the beams steps with a depth varying from 1  $\mu$ m to 1.5  $\mu$ m are defined into the Si substrate by EBL (1-2), subsequently etched (3) and coated with 150 nm low-stress LPCVD SiN<sub>x</sub> (4). Next steps are carried out in the cleanroom at IBM Research Lab in Rüschlikon. A first step of metallization (5) consists in the deposition of 25 nm of Pt with 2 nm of Cr as adhesion layer. Then we pattern the Pt layer with another step of e-beam lithography to fabricate the heater and the suspended metal lines (6) that are etched by an Ion Milling process (7). Before the release, we perform a second metallization step (8) with 75 nm of Au to define the platform electrode and the contact pads by using optical

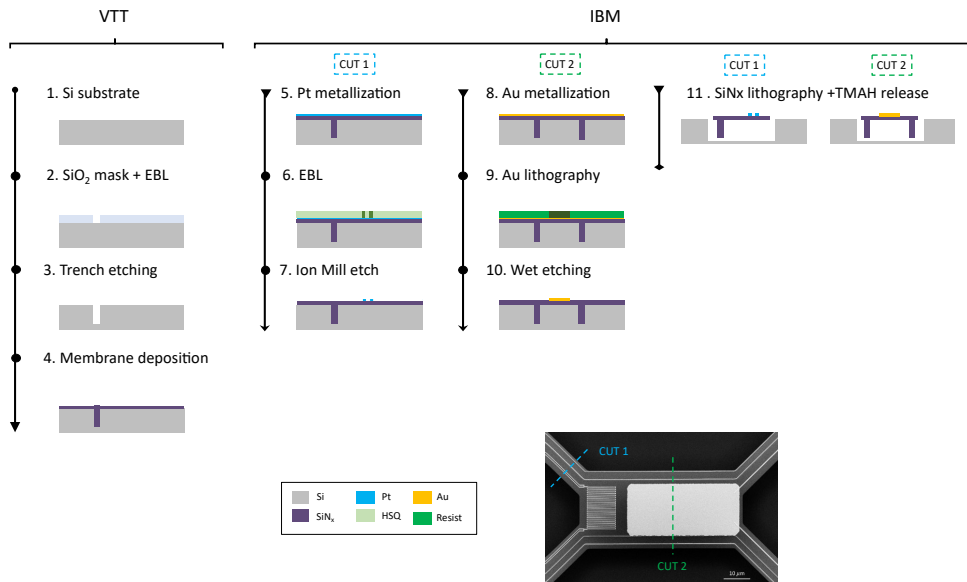


**Figure 3.28** Fabrication process of the MEMS structure with beam steps for improved mechanical stiffness. CUT 1 shows the cross-section for the new T-shape beam, featuring a larger effective height. CUT 2 shows the cross-section perpendicular to the short edges of the membrane. Step 1-4, performed at VTT, are common to the whole wafer and are used to pattern the substrate before the definition of the beams and the central platform. Steps from 5 to 7 are used to delineate the beams layout, while steps from 8 to 10 outline the central platform. Finally, step 11 is used to pattern the SiNx layer and suspend the beams and the platform altogether.

lithography in combination with wet etch process (9-10). Finally, we perform an optical lithography step to define and release the MEMS by underetching the SiN<sub>x</sub> layer in tetramethylammonium hydroxide (25% concentration for 30 min at 80 °C). To clean from the etchant and safely suspend the MEMS, we remove the solvent from the previous step by immersing the wafer in isopropanol, which is then quickly dried to avoid stiction with an N<sub>2</sub>-gun on top of a hotplate. The resulting MEMS are then cleaned before any measurement via a combination of O<sub>2</sub> plasma (400W, 5min) and a further gentle Ion Milling step (150 mA, 20 s). The resulting structures consist of (typically) four SiN<sub>x</sub> beams of lengths ranging from 250 μm to 500 μm, according to the design, a thickness of  $t = 150$  nm (as defined by the SiN<sub>x</sub> layer) and width  $w = 4$  μm. Usually, the Pt lines connecting to the heater element have widths between 100 and 200 nm, while the STM lines to the Au platform are designed with a larger width of about 400 nm to lower their electrical resistance.

Figure 3.29 shows a MEMS perfectly fabricated a) and two images were the process failed because of a not successful release b) or optical misalignment during fabrication c).

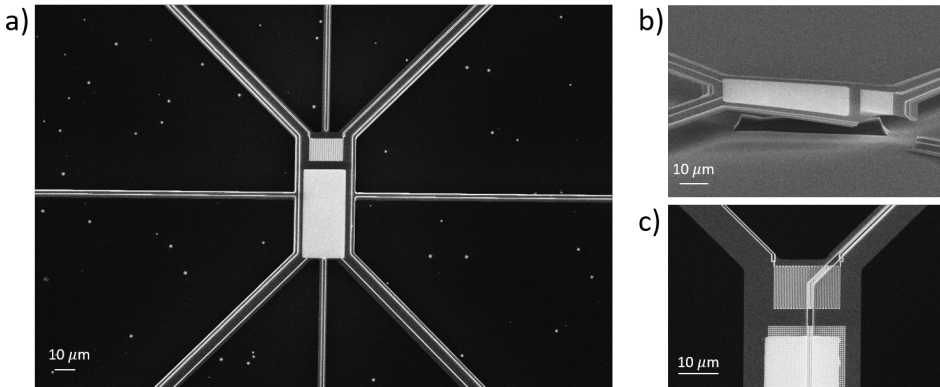


**Figure 3.29** a) MEMS device after successful fabrication. b) Broken device due to failed under etching of the suspended membrane. c) Example of optical misalignment during fabrication.

### 3.4.3 MEMS characterization and thermometer calibration

The calibration procedure and the thermal characterization steps follow the ones described in [150]. Corrections for the cryogenic regime were implemented by Femke Hurtak during her master thesis project at IBM Research [179], under the supervision of B. Gotsmann and myself.

Before starting any new measurement, it is necessary to precisely calibrate the electrical and thermal properties of the MEMS. The essential parameters are the electrical resistance of the Pt lines connecting the gold platform for the STM, and the heater resistance  $R_H$  and its thermal coefficient of resistivity  $\alpha$  for the temperature measurement.

**Electrical characterization** First of all, we characterize the STM electrical circuit. To obtain the value for the STM beams resistance we can measure the device directly inside our setup, by letting a current flow through the two Pt lines connecting the gold platform and then plotting the current-to-voltage characteristic, see Figure 3.30. The inverse of the slope of such a curve will provide a measurement of  $R_{beam} = \frac{1}{2} \times R_{STM}$ , with the series resistance in front of the IV converter ( $R_s = 1 \times 10^5 \Omega$ ) already taken into account, see Figure 3.4.

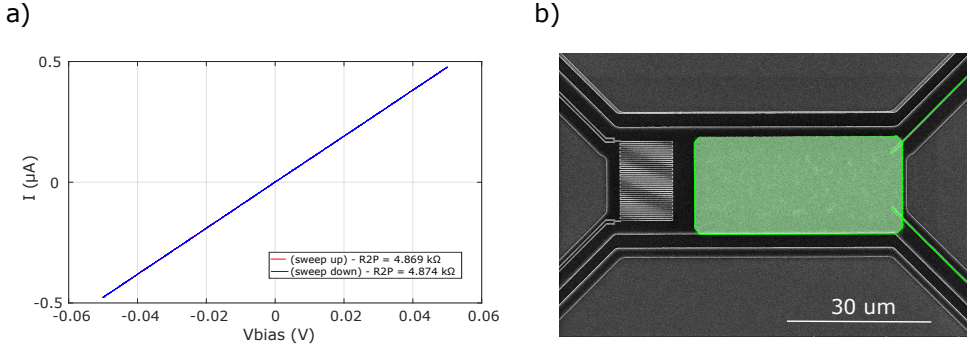


**Figure 3.30** a) Current to voltage (IV) curve recorded through the STM circuit at 15 K. R2P indicates the 2-probe resistance of the series beam+platform+beam. b) Scanning electron micrograph of MEMS structure with STM circuit highlighted in green.

**Thermal characterization.** To be able to anticipate the behaviour of the heater at low temperatures and use it as a sensitive thermometer, a more precise knowledge of the heater resistance vs. temperature  $R_H(T)$  is necessary. The calibration of the thermometer is performed in a commercial tool (Dynacool by Quantum Design) usually on two different devices coming from the same wafer, with the same heater but different beams design (to have similar  $R_{4H}$  but different  $G_{th,dev}$ ). We start the calibration by monitoring the behaviour of the electrical resistance  $R_{4H}$  as a function of temperature, with a probing current small enough such that no self-heating occurs. Results are shown in figure 3.31, labelled as 'Raw data'. We can distinguish three different temperature ranges labelled as low ([4; 80] K), intermediate ([40; 120] K) and high ([80; 350] K). An overlap of approximately 40 K, has been set between adjacent ranges to avoid gaps in the crossing regions. This is possible thanks to the smoothness of the signal when transitioning from a range to another.

For each range we can define a peculiar model:

- Low Temperature([4; 80] K): As we can see from the leftmost graph of Figure 3.31 the resistance profile is approximately constant at very low temperature ( $\lesssim 20$ K), as typical for metals where defect scattering dominates [51]. At higher temperature ([15; 60] K) the resistance curve can be fitted with a high order polynomial with contributions from electron-electron scattering ( $R_H \propto T^2$ ), and possible Umklapp electron-phonon scattering [180].

- Intermediate Temperature([40; 120] K): In the intermediate temperature range an almost perfect linear relationship between  $R_H$  and T can be observed, despite the range is well below the Debye temperature of platinum ( $\Theta_D = 234\text{K}$ ). The behaviour of the curve can be explained as a transition linear region between a convex curve at lower temperatures and a slightly concave curve at higher temperatures.
- High Temperature: In this region the curve is mostly linear, with a small second order correction. For  $T \gg \Theta_D = 234\text{K}$  we observe a linear dependence of the resistance vs. temperature, as one would expect when the resistivity is dominated by electron-phonon scattering at high temperature. The transition through a high order polynomial dependence, with  $R_H \propto T$  when  $T \gg \Theta_D$  to  $R_H \propto T^5$  when  $T \ll \Theta_D$ , could then explain the observed small concavity of the correction. [CHECK!!]

3

**Thermometer calibration** Because of the different fitting regimes due to diverse kind of scattering that take place in the platinum heater when varying the temperature, there is no straightforward analytic equation to describe the dependence of  $R_H(T)$ . Also, there is a requirement of simplicity coming from the fact that the formula  $R_H(T)$  must be inverted to use the Pt-heater as thermometer. For this reason a maximum order of  $n=2$  has been selected for the polynomial fit in all the three temperature ranges, with a relative error on  $R_H$  being less than 1%. Starting from the well known Callendar-Van Dusen equation [70] for platinum at room temperature and by using linear Taylor expansion, we can write the following equations for  $R_H(T)$ :

$$R_H(T) = R_H(T_0) \times [1 + \alpha(T_0)(T - T_0)] \quad (3.23)$$

$$R_H(T) = R_H(T_0) \times [1 + \alpha(T_0)(T - T_0) + \beta(T_0)(T - T_0)^2] \quad (3.24)$$

where  $T_0$  is a reference temperature (that can be different from  $T=0$  °C) and  $R_H(T_0)$  the electrical resistance of the heater at  $T_0$ . In our setup,  $T_0$  is the operating temperature given by the cryostat. For different devices coming from the same wafer, we assume that the coefficients  $\alpha$  (and  $\beta$ ) don't vary from device to device, since they depend only on the shape and quality of the Pt thin film. This means that, just one calibration procedure performed on one or two devices (as in figure 3.31) is needed to calibrate all the devices sharing the same design and coming from the same wafer to be calibrated. Then, to start a new measurement with a device, the only thing needed is to determine  $R_H(T_0)$  from an IV measurement at the cryostat temperature  $T_0$ , see Fig. 3.32. This practically translates into the following steps:

1. For each wafer and each design we take a device and we perform the calibration as in figure 3.31, obtaining  $\alpha$  (and  $\beta$  for second order);
2. before starting a new experiment we measure the temperature of the cryostat  $T_0$  and  $R_H(T_0)$ . Depending on the value of  $T_0$  we chose the suited model, selecting the range that gives more temperature span in case of ambiguity.
3. to use the heater as thermometer we calculate the temperature difference by inverting eq.3.23 (or eq.3.24).

According to the degree of the polynomial fit, we get:

$$\Delta T = \frac{\Delta R}{R_0 \cdot \alpha(T_0)} \quad (3.25)$$

$$\Delta T = \frac{-\alpha(T_0) + \sqrt{\alpha^2(T_0) + 4\beta(T_0) \cdot \Delta R/R_0}}{2\beta(T_0)} \quad (3.26)$$

The solution to the second order fit is well determined, as the MEMS can only be heated up by the heater, meaning that  $\Delta R$  and  $\Delta T$  can only assume strictly positive values.

**Thermal conductance.** To measure the thermal conductance of the MEMS device as function of temperature  $G_{th,dev}(T)$ , for each target temperature we run four-probe IV measurements at large bias, so that self-heating is visible. We combine the IV curves with low-power resistance measurements in four-probe and two-probe configurations in order to determine the electrical resistance of the beams  $R_b$  and heater resistance  $R_H$ , as explained in sec.3.1.4). A typical IV curve is shown in Figure 3.32. We can distinguish two regions: linear at low bias and non-linear (self-heating) at high bias. From the first order fit of the linear region we get the resistance, and thus the temperature. Then for each point in the non-linear regime we compute the ratio:

$$R_P = \frac{V_P}{I_P} \quad (3.27)$$

From the obtained values we deduce the temperature increase on the platform  $\Delta T_P$ , as well as the effective power:

$$P_H = V_H \cdot I_H + \frac{1}{2} \cdot 2 \cdot R_b(T_0) \cdot I_H^2 \quad (3.28)$$

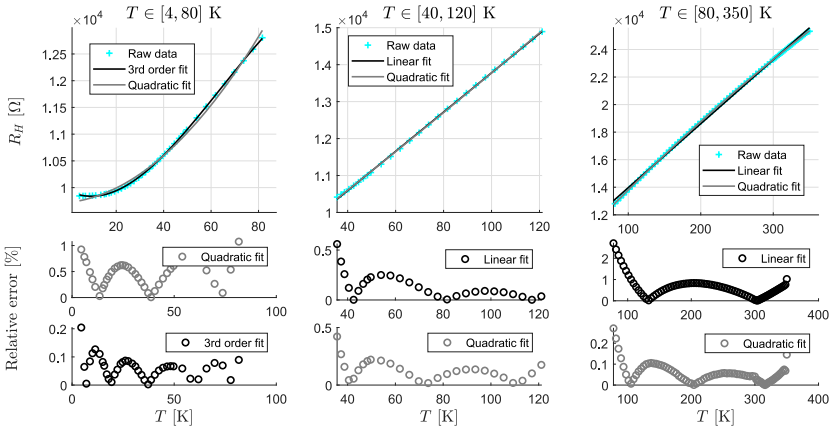
where the first term stands for the contribution of the integrated heater ( $V_H \cdot I_H$ ), while the second one represents the additional contribution of the two metal lines carrying the current to the heater (each line contributing with  $\frac{1}{2} \cdot R_b I_h^2$ ).

Then from the ratio between the effective power  $P_H$  and the temperature difference  $\Delta T_P$  it easily follows:

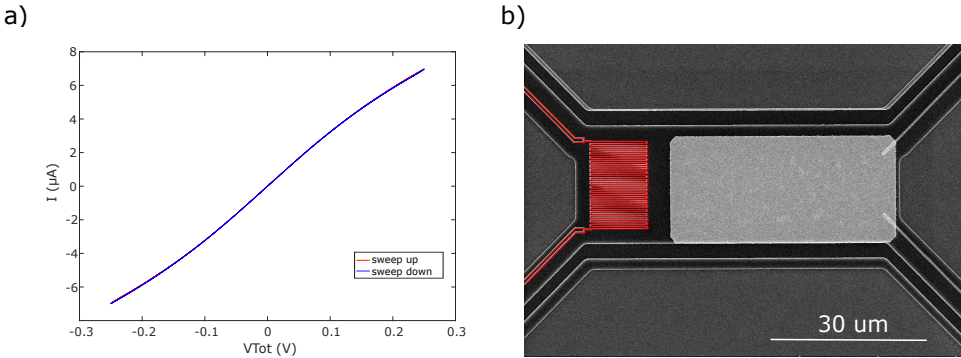
$$G_{th,dev} = \frac{P_H}{\Delta T_P} = \frac{1}{R_{th,dev}} \quad (3.29)$$

Figure 3.33 shows a typical  $\Delta T_P(P_H)$  curve. The inverse of the slope gives the  $G_{th,dev}$  of the MEMS.

**Thermal time constant** The thermal time constant of the MEMS device  $\tau_{dev}$  indicates the minimum amount of time required to the Pt thermometer to equilibrate with the rest of the device. All signals that are faster than the time constant (or response time)  $\tau_{dev}$  are low-pass filtered, as can be predicted by a lumped capacitance model. Assuming that in vacuum our suspended platform is a 'thermally thin' object (the ratio  $R_{th,plat}/R_{th,beam} \simeq 0.005$ ) we can calculate  $\tau_{dev} = R_{th}C_{th}$ , where  $C_{th}$  is the heat capacity of the MEMS platform. To experimentally estimate the thermal time



**Figure 3.31** Electrical resistance of the heater  $R_H$  as a function of temperature. The curve is divided in three overlapping temperature ranges. Each curve is modelled with polynomial fits. Left: at low temperatures, a third order fit is accurate within 0.2%, but a quadratic fit allows already to reach relative errors below 1%; Middle: at intermediate temperatures, a linear fit is accurate up to 0.5%. Right: at high temperatures, a quadratic fit gives a relative error below 0.3%. Adapted from [179]



**Figure 3.32** a) Current to voltage (IV) curve recorded through the thermal circuit at 15 K. b) MEMS structure with thermal circuit highlighted in red.

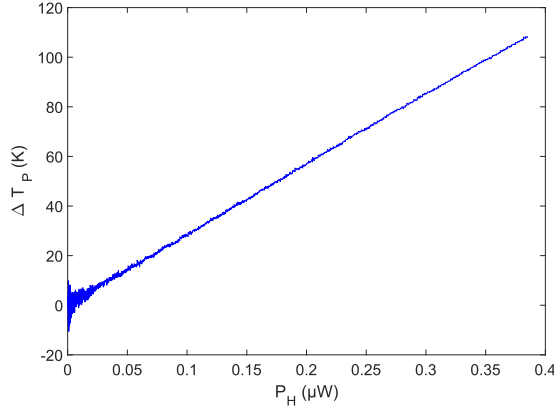


**Figure 3.33** a) Temperature difference as function of ramping up power for positive voltage (and current), recorded at 15 K. The slope is a measurement of  $R_{th,dev}$ . For simplicity, the symmetrical negative voltage range and ramping down curve are not shown.

constant, we have two methods. With the first one, we apply a voltage step to the heater in vacuum, provoking a fast transition of the input power, and measuring the transient in resistance change.  $\tau_{dev}$  can then be extracted by fitting the resistance  $R_H$  vs. time, with the low-pass filter response of an equivalent electrical RC-circuit

$$R(t) = Ae^{-t/\tau} + R_{inf}$$

where  $R_{inf}$  is the value at the saturation after the transient.

The second method instead uses two successive calibration-IV curves (with increasing and decreasing power, respectively). If we plot the resistance ( $R_H = V/I$ ) as a function of the heater power ( $P = I \cdot V$ ) we observe a hysteresis of constant width in the graph. This is again coherent with the fact that our system can be modelled as a first order RC. By measuring the horizontal offset in the central part of the  $R_H(P)$  graph, i.e. in the stationary part, away from the turning-points, we can deduce the reaction time of the device, by translating the power offset into time offset via the speed of the power ramping. In order to minimize the time constant, different design with a smaller platform (and so smaller  $C_{th}$ ) have been tested, with a minimum size limited by the optical access to the MEMS. For this reason, the smallest tested platform allowing for a quick and safe tip alignment is  $17 \times 62 \mu\text{m}$  with a time constant  $\tau_{dev} = 19 \text{ ms}$  at room temperature[150]. Because at lower temperatures, thermal capacitance gets smaller, also larger pad ( $62 \times 67 \mu\text{m}$ ) have been devised in order to facilitate the tip approach, but to date their thermal time constant has not been tested yet. The fact that the thermal signal is not as fast as the electrical one (that is only limited by the bandwidth of the I-V converter) induces a time delay in the observed events between the electrical conductance trace and the corresponding thermal one. This is taken into account in the analysis when comparing the two signals, by applying a LP-filter with appropriate

$\tau = \tau_{dev}$  to the electrical trace. On the experimental side, the delay translates into the need of keeping the atomic or molecular junction stable for at least one time constant, in order to measure an accurate thermal conductance signal.

## 3.5 Sample Preparation

3

To be measured, a sample requires some preparation steps that will be discussed in the following sections, starting from the cleaning of the platform electrode surface, to the deposition of organic molecules. Furthermore, the fabrication process, needed to realize a good tip suited for STM-Break junction measurements, will be discussed in section 3.5.4

### 3.5.1 Cleaning steps

Measuring the transport properties of quantum point contacts and single molecules with STM-BJ requires clean metal surfaces. However, the idea of 'cleanliness' can be very different from a research field to another one. For example in surface science, a typical cleaning process may consist of several sputtering cycles with noble gases (He, Ar,...) followed by an annealing step at high temperature ( $>500^{\circ}\text{C}$ ) to retrieve an atomically flat surface of the electrodes. In case of imaging/measurement of molecules, those are usually deposited in-situ by thermal evaporation or electro-spray deposition. Besides, those experiments are typically conducted in UHV and at cryogenic temperature to always keep the system under controlled conditions [181, 182]. In case of Break Junction experiments, cleaning conditions are a bit more relaxed, in fact a discrete number of different experimental conditions have been used in literature especially to study charge transport in QPCs and single molecule junctions, from UHV [39, 103] to solution [37, 104] and even ambient conditions [105, 106]. In any case, the cleanliness of the electrodes has to be adequate to enable deposition of molecules and a clear breaking process of the junction. Our procedure starts by dicing the chip from the main wafer. Then a first electrical test, to determine whether there are short-cuts, broken connections or resistances out from the expected range, is performed. In case of anomalies we proceed to an optical inspection under the optical microscope. After the testing procedure, devices are cleaned with a combination of  $\text{O}_2$  plasma exposure (400 W, 5 min) and Ion Milling with an  $\text{Ar}^+$  gun (150 mA, 20 s). After the cleaning, devices are again tested to verify if they survive the process and to check the increase in electrical resistance due to the thinning down of the films occurring during the ion sputtering.

### 3.5.2 Functionalization

Once the devices are cleaned, they can be deposited with the molecules under study. The deposition is done by dip coating, i.e. the whole chip is immersed in a molecular solution containing a variable mixture of ethanol (EtOH) and dichloromethane (DCM) as a solvent. Afterwards, the chip is rinsed in a bath of the same solvent mixture to remove any not-bound molecule, and quickly dried under nitrogen flow to avoid stiction of the suspended membrane. By varying the molecular concentration in the solution and the deposition time, it is possible to control the amount of molecules at the MEMS

surface. Different molecules are in general bonded to the surface via different anchoring groups, that may require a slight modification of the deposition concentration/time. Typically, we use solutions with concentrations of 0.1 to 1 mM and deposition times between few seconds to 2 hours.

### 3.5.3 Mounting

When the device is functionalized the only step missing is the sample mounting inside the vacuum chamber. To do that, we first attach the chip to a sample holder by means of a drop of silver paste or high-vacuum grease. Once in position, the chip is then wire bonded to the electrical lines patterned in the holder. Finally the sample is connected to the rest of the experiment chamber by pressing the holder against the conductive spring-loaded pins inside the vacuum receiver. A device ready to be tested is shown In Figure 3.34

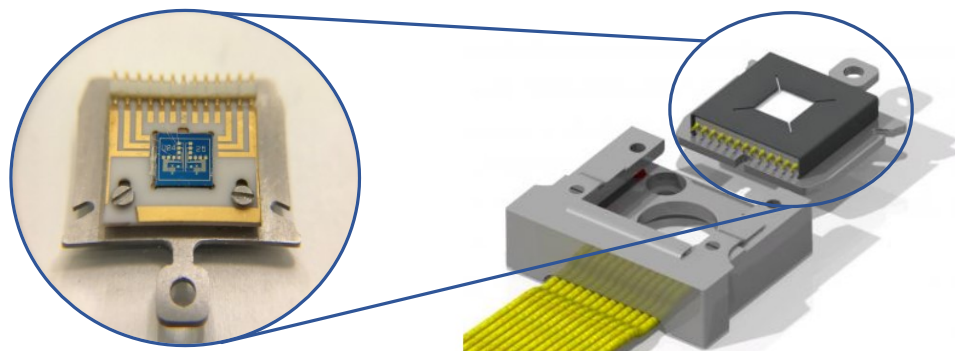


**Figure 3.34** A device cleaned, deposited, bonded and ready to be measured (left). The sample holder drawing (right) refers to the adopted commercial solution from Ferrovac AG.

### 3.5.4 Tip etching

Figure 3.35 shows a schematic of the electrochemical etching setup used for the fabrication of the STM-BJ tips. The complete process has been adapted from Boyle et al. [183] by N. Mosso and A. Prasmusinto [97, 150]. A small piece of gold wire ( $\varnothing = 0.25$  mm, 99.99+% purity, GoodFellow) is dipped by  $\sim 1$  mm in a 2 M solution of  $\text{CaCl}_2$ . A 8 V peak-to-peak alternating voltage (300 Hz) with a positive 4.5 V DC offset is then applied between the Au wire (1<sup>st</sup> electrode) and a 99.99+% pure graphite rod (2<sup>nd</sup> electrode), also immersed in the solution. While etching, the current flowing in the electrochemical cell is monitored by measuring the voltage  $V_{etch}$  dropping over a small series resistance  $R_S = 50 \Omega$ . The process is finished when no current is observable between the two electrodes. In this way tip with radius of about 20 to 50 nm can be fabricated in a single etching step. The final step consists in rinsing the tip in DI water to remove residues formed during the process. The full recipe proceeds as follow:

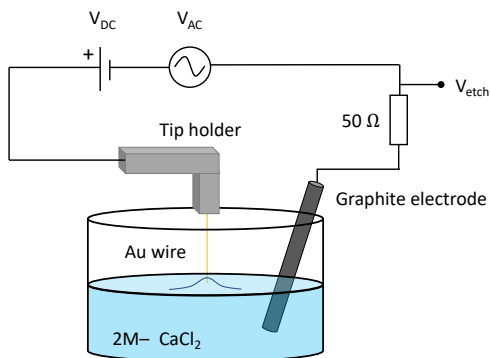


**Figure 3.35** Schematic of the etching setup used to fabricate STM-BJ gold tips.

1. cut about 1 cm of 0.25 mm gold wire and fix it to the tip holder;
2. (optional) flame anneal the tip of the wire for 1-2 s using a flame torch until a gold sphere forms at the tip (this allows for a smoother tip surface with visible crystalline planes);
3. (optional) coat the apex (1-2 mm) with varnish, to protect it during the etching as in a drop-off method.
4. immerse the electrically connected graphite rod inside the electrolyte solution;
5. dip the wire by about 1-2 mm into the electrolyte (make sure that the coated portion of the wire is fully immersed into the solution);
6. apply an AC voltage  $V = 8$  V peak-to-peak at 300 Hz with a DC offset of 4.5 V. The etching takes about 1-2 min;
7. rinse the tip in deionized water;
8. dry tip with  $N_2$  gun.

The main benefit of this process is that tips are fabricated with a good yield (80%) in a relatively short time, without the necessity for a feedback circuit to stop the current at the end of the etching procedure.

### 3.6 Results on Quantum Point Contacts

This section aims at testing whether our new variable temperature setup could reproduce two already confirmed predictions: the exact quantization of the electrical conductance in mono-atomic gold junctions, and the validity of the Wiedemann-Franz law at room temperature, as reported in [22, 92]. The experimental results presented in the following were obtained in collaboration with Femke Hurtak, during her master thesis project at IBM Research [179], under the supervision of B. Gotsmann and myself.

### 3.6.1 Experimental verification of Wiedemann-Franz law at room temperature

To test the new setup, we recorded the electrical ( $G_{el}$ ) and thermal ( $DG_{th}$ ) conductance of gold quantum point contacts at room temperature and high vacuum ( $1 \times 10^{-6}$  mbar). A temperature bias of 20 K was set between the MEMS and the tip, producing an effective temperature variation on the MEMS of about 3 K during breaking events. Results are presented in figures 3.36.

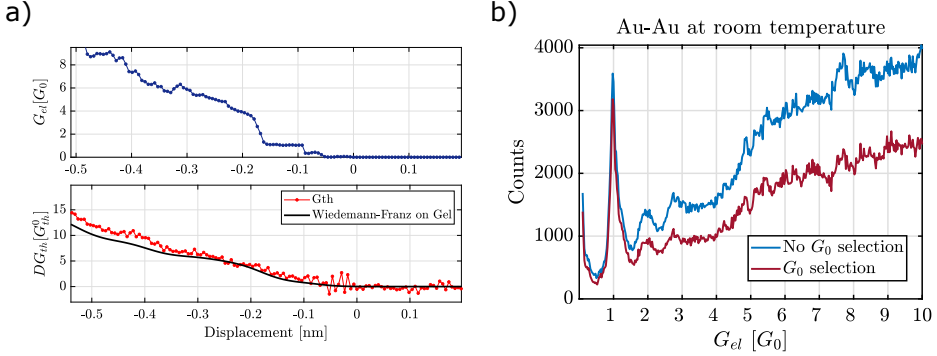


**Figure 3.36** Au-Au break junctions experiments at room temperature. Adapted from [179]. a) Single retraction trace with the electrical conductance  $G_{el}$  vs. displacement on the top, and the thermal conductance  $DG_{th}$  (red) vs. displacement on the bottom. The black line indicates the electronic thermal conductance obtained by applying Wiedemann-Franz to  $G_{el}$ . b) 1D histogram of  $G_{el}$  obtained by averaging 1800 retraction measurements. The curve labelled ' $G_0$  selection' was drawn after selecting only traces showing a plateau of more than 5 points in the range  $G_{el} \in [0.5, 1.5] \cdot G_0$ .

For this study, 2300 break-junction traces have been measured, out of which 1800 were considered to be physically relevant, and 825 displayed a plateau (of at least 5 datapoints) at  $G_0$ . We note that  $\sim 30\%$  of the retraction traces show a plateau at  $G_{el} = G_0$ . In Fig. 3.36 b), the peaks at multiples of  $G_0$  show the quantization of the electrical conductance. These peaks are robust against trace-selection in the  $G_0$  region: including or not the traces that don't display a plateau in the range  $G_{el} \in [0.5, 1.5] \cdot G_0$ , doesn't shift the position of the peaks. This confirms that the over fitting due to data selection is actually limited.

Figure 3.36a) shows a single trace with good agreement between the electrical conductance ( $G_{el}$ ) and the junction thermal conductance ( $DG_{th}$ ), as stated by the Wiedemann-Franz law. The relation between  $DG_{th}$  and  $G_{el}$  is further analysed in figure 3.37. The results confirm the validity of the Wiedemann-Franz law in quantum point contacts with a large peak at  $L = L_0$ , as expected from theory. By looking at the quantization of  $G_{el}$ , Fig. 3.36b) and the observation of the Wiedemann-Franz law, Fig. 3.37 b), we have strong evidence that the setup works as per design at room temperature. Additionally,  $L/L_0$  and  $G_{el}/G_0$  now show peaks exactly at 1, simultaneously. This is an improvement compared to previous measurements [22], where the authors found a slightly shifted elec-

trical signal, with peaks at  $\sim 0.4 \cdot G_0$  and  $\sim 1.3 \cdot G_0$ , attributed to contamination by CO molecules. At the moment is hard to tell if the improvement comes from a better cleaning procedure or because of a higher accuracy in the electrical measurements. On the other hand, the spread of the thermal signal is now  $\sim 4\times$  higher than in [22], which could initially compromise the measurements at low temperature. The increased spread of the thermal data is visible in the histogram of Fig. 3.37 a) and from the width of the  $L$  curve in Fig. 3.37b).

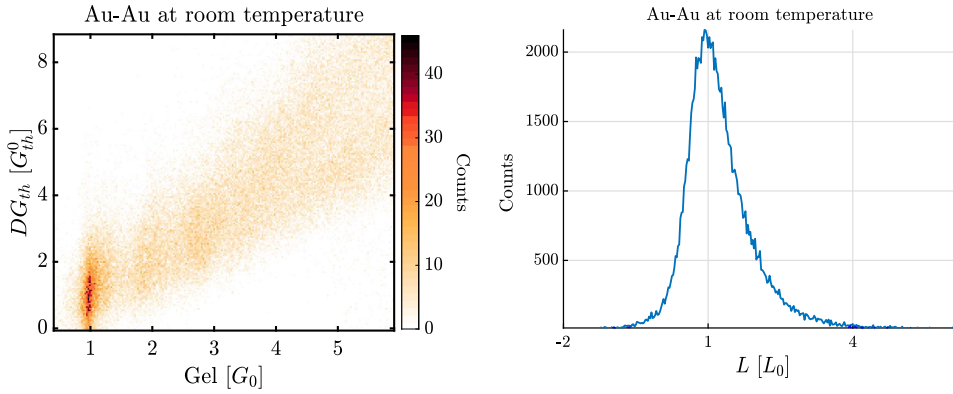


**Figure 3.37** Au-Au junctions at room temperature. Data from 1800 retraction traces. Left: 2D histogram of  $DG_{th}$  versus  $G_{el}$ . Right: 1D histogram of the Lorentz ratio calculated from raw signals in the range where  $G_{el} \in [0.9, 3] \cdot G_0$ . The few negative points of  $L$  are outliers due to an ill-defined parasitic device conductance  $G_{th,dev}$  for some traces, and should be disregarded.

# 4 Results on Single Molecule Junctions

---

In the following, the main results on single molecules are shown. At the beginning of the chapter, the first ever measurements of the thermal conductance at the single molecule level are presented for two selected molecules, namely the oligo(phenyleneethynylene) (OPE3) and octan-dithiol (ODT). In the second part instead, results on the thermoelectric properties of three OPE3-derivatives are given. Finally, in the last part of the chapter, a full experimental thermoelectric characterization of the OPE3-Anthracene molecule is provided, together with the calculation of its thermoelectric figure of merit  $ZT$ .

## 4.1 Thermal Transport through Single-Molecule Junctions<sup>1</sup>

This chapter has been published in 2019 in the September issue of the ACS Nano Letters Journal. The text, figures and references have been re-formatted in the style of this thesis. Supporting Information available online:

[https://pubs.acs.org/doi/suppl/10.1021/acs.nanolett.9b02089/suppl\\_file](https://pubs.acs.org/doi/suppl/10.1021/acs.nanolett.9b02089/suppl_file)

NANO LETTERS

Cite This: *Nano Lett.* 2019, 19, 7614–7622

Letter

[pubs.acs.org/NanoLett](https://pubs.acs.org/NanoLett)

### Thermal Transport through Single-Molecule Junctions

Nico Mosso,<sup>†</sup> Hatef Sadeghi,<sup>\*,‡,§</sup> Andrea Gemma,<sup>†</sup> Sara Sangtarash,<sup>‡,§</sup> Ute Drechsler,<sup>†</sup> Colin Lambert,<sup>§</sup> and Bernd Gotsmann<sup>\*,†</sup>

<sup>†</sup>IBM Research–Zurich, Rueschlikon 8803, Switzerland

<sup>‡</sup>School of Engineering, University of Warwick, Coventry CV4 7AL, United Kingdom

<sup>§</sup>Physics Department, Lancaster University, Lancaster LA1 4YB, United Kingdom

**AUTHOR CONTRIBUTIONS:** NM led the experiment. AG measured the ODT samples. NM carried out the data analysis with inputs from BG and AG. HS developed the theory with help from SS. UD fabricated the measuring devices. NM wrote the manuscript with contributions from all the co-authors.

<sup>1</sup>Adapted with permission from Ref.[23]. Copyright (2021) American Chemical Society.

### 4.1.1 Abstract

Molecular junctions exhibit a rich and tunable set of thermal transport phenomena. However, the predicted high thermoelectric efficiencies, phonon quantum interference effects, rectification, and nonlinear heat transport properties of organic molecules are yet to be verified because suitable experimental techniques have been missing. Here, by combining the break junction technique with suspended heat-flux sensors with picowatt per Kelvin sensitivity, we measured the thermal and electrical conductance of single organic molecules at room temperature simultaneously. We used this method to study the thermal transport properties of two model systems, namely, dithiol-oligo(phenylene ethynylene) and octane dithiol junctions with gold electrodes. In agreement with our density functional theory and phase-coherent transport calculations, we show that heat transport across these systems is governed by the phonon mismatch between the molecules and the metallic electrodes. This work represents the first measurement of thermal transport through single molecules and opens new opportunities for studying heat management at the nanoscale level.

4

### 4.1.2 Introduction

Heat transport through molecular systems takes place through a wealth of transport mechanisms. When the heat is carried by vibrations, these include ballistic and hopping transport, phonon interference[44, 113, 184], rectification [45] and localization [105], and extend beyond equilibrium-based thermodynamic transport [185]. Molecular junctions represent an ideal platform to probe quantum transport phenomena at the nanoscale, and investigation of charge transport in these systems have led to numerous fundamental discoveries in the last 20 years [63]. Tuning the thermal properties of such molecular devices would underpin numerous technologies based on heat management at the nanoscale. However, the thermal characterization of molecular junctions has not been experimentally accessible yet. Both experimental and theoretical analyses of molecular heat transport face severe challenges. To simulate phononic heat transport in molecular junctions, different length scales of heat carrying phonons have to be taken into account, ranging from Ångströms to microns at ambient temperature. Molecular dynamics simulations have been utilised in the classical or high temperature limit to identify the role of binding groups and interference effects [113]. More recently, significant progress was made describing junctions as Landauer systems with an energy-dependent phonon transmission coefficient calculated using Green's functions and density functional theory [105, 184, 186], or approaches beyond the harmonic approximation [185]. The Green's function method has also been employed to compute the electronic contribution to heat transport. However, numerous predictions of interference phenomena [43, 125, 184] and non-linear effects [45] await experimental verification. The thermal conductance of a single molecular junction is typically well below a thermal conductance quantum (284 pW/K at room temperature) and therefore difficult to measure. For example, alkanes chemically bound to two metal thermal reservoirs, have measured and predicted thermal conductance values on the order of tens of picowatts per Kelvin [117, 185]. As these systems form self-assembled monolayers of high quality, they can be measured using spatially averaging methods like time/frequency-domain thermoreflectance [77, 106] or scanning thermal microscopy[111]. However, for most molecular systems, ordered

films cannot readily be made and uncertainties in the actual percentage of molecules bridging the reservoirs still remain[77, 111]. Even though single molecule measurements are prone to difficulties, due to the experimental inaccessibility of the atomic-scale environment of an individual molecular junction, they would enable systematic studies of the relationship between chemical structure and energy transport properties. Indeed recently, experiments using break-junction techniques have been used to probe the thermal conductance of atomic point contacts [22, 92]. Here, for the first time, we demonstrate how a combination of a break junction with a suspended microfabricated heat flux sensor can be used to probe the thermal conductance of molecular junctions. As model molecular systems, we have chosen oligo(phenylene ethynylene)dithiol (OPE3) and octanedithiol (ODT) contacted by gold electrodes. OPE3 is probably the best studied molecule for electrical transport, with widespread agreement reached by different groups for its electrical conductance [67, 187–189], using both mechanically controlled break-junctions[184] (MCBJ) and break junctions based on scanning tunneling microscopes (STM-BJ). However, heat transport through OPE3 with thiolate end groups has neither been studied experimentally nor theoretically. On the other hand, ODT is a member of the alkane family, whose thermal transport properties have been intensively studied both theoretically and experimentally. Nevertheless, the many possible junction configurations recognized in the charge transport experiments [56, 152, 190, 191], make it a challenging system to test the limits of our new method.

### 4.1.3 Methods

A detailed description of the setup is given in Sec.3.2.2. A schematic of it is represented in Fig.4.1a). In order to combine heat and charge transport measurements at the single-molecule level, we devised suspended micro-electro-mechanical systems (MEMS) characterized by a low thermal conductance  $G_{MEMS}$  ranging from  $3.5$  to  $4.5 \times 10^{-8} \text{ W K}^{-1}$ . These devices consist of a central membrane with a Pt heater/thermometer and a gold platform that can be used to form electrical contacts with the tip of a scanning tunneling microscope (STM). The membrane is suspended via four silicon nitride beams, which are usually oriented at  $45^\circ$  with respect to its axis to reduce the torsional degrees of freedom. The MEMS are cleaned by a combination of oxygen plasma and ion milling to remove contaminants postfabrication and retrieve a fresh gold surface. OPE3 or ODT are deposited on the gold platform by immersing the entire MEMS in solutions of dichloromethane or ethanol, respectively, with concentrations ranging from  $0.1$  to  $1 \text{ mM}$  for  $30 \text{ s}$  to  $2 \text{ h}$ . After the deposition, the samples are rinsed several times in clean solvent to eliminate physically adsorbed molecules. For a detailed description of the sample preparation procedure, see the Supporting Information. We would like to stress that depositing molecules from solution poses severe challenges on the cleanliness of the gold surface, but it extends considerably the variety of molecules that can be investigated. All the measurements are performed at room temperature and in high vacuum ( $1 \times 10^{-7} \text{ mbar}$ ) within a custom-built STM, located in a low-noise environment.[151] The experiment consists in performing STM-Break Junction (STM-BJ) measurements with an electrochemically etched gold tip (typical tip radius around  $50 \text{ nm}$ ) on the gold platform of the suspended MEMS. Measuring the electrical conductance  $G_{el}$  upon breaking the tip-MEMS contact allows us to detect the formation of a molecular junction. Prior to contact formation, the membrane is heated to a temperature  $T_H \sim 350 \text{ K}$  by applying

a constant voltage to the Pt-heater, which corresponds to few  $\mu W$  of dissipated power. The temperature  $T_H$  is continuously monitored by measuring the four-probe resistance of the heater and using the previously calibrated temperature coefficient of resistivity  $\alpha = 1.37 \times 10^{-3} \text{ K}^{-1}$ , which is in the expected range for Pt thin films. The thermal conductance  $k_{th}$  of the MEMS is calculated by dividing the total power provided to the heater and the  $\Delta T = T_H - T_{AMB}$  generated with respect to the substrate. When the tip, also at room temperature  $T_{AMB}$ , is brought into contact with the MEMS, the total thermal conductance increases because of the additional heat flux to the tip. The difference between these two values corresponds to the thermal conductance of the contact formed. Fig.4.1b) shows an example of a single opening trace measured by retracting the tip at  $25^\circ$  with respect to the MEMS surface in order to take advantage of the greater in-plane stiffness [22] at a speed of 2 nm/s. Lower angles led to irreproducible results indicating that including roughness the local angle between tip and surface is smaller. We calculate the stiffness normal to the MEMS surface about 0.7 N/m and the in-plane stiffness 540 N/m, resulting in an effective stiffness on the order of 10s of N/m. Note that the plotted thermal conductance includes both the contributions of the MEMS ( $\sim 45 \text{ nW/K}$ ) and the contact with the tip. We can distinguish three different transport regimes within the trace: (I) Au-Au, (II) Au-molecule-Au, (III) Au-tunnelling-Au. During the thinning of an Au-Au point contact (I), the thermal conductance of the junction is proportional to the electrical one, decreasing in a step-like fashion because of the quantized availability of electron channels. Hereby, the last few channel changes coincide with the number of atoms bridging the contacts after rearrangement. Most of the heat is transported by electrons following the Wiedemann-Franz law [22, 192]. Some traces exhibit a second regime (II), in which  $G_{el}$  shows a plateau indicating the formation of a molecular junction [71]. Finally, in the last regime (III), the molecular junction is broken. The thermal conductance of the molecule can then be obtained from the signal change around the breaking point of the junction. A similar plateau might be expected for the thermal conductance in the second regime (II). However, a linear decrease is usually observed versus tip displacement, with slopes ranging between 0.5 and 3 nW/K/nm. This is caused by additional thermal conductance paths around the actual molecular junction. These paths have relatively long-range and can be attributed to three effects. First, even clean gold surfaces can show significant heat transfer of this magnitude due to thermal near-field radiation.<sup>27,28</sup> The magnitude of the near-field contribution is under debate [193, 194]. Second, despite the cleaning processes described above, there may be residues and spurious molecules present on the surface from processing and chemically bound to both surfaces, but they can carry significant heat via the van der Waals bonds [105, 106, 111]; they form a strong mechanical contact between tip and MEMS, with a typical thermal conductance of about 10-30 nW/K that depends on their relative distance. The reproducibility and the slope of the background signal are more important than its magnitude. We note that even in nominally clean experiments [22, 92, 193, 194] in the near-field radiation regime exhibit background slopes between 0.5 and 8 nW/K/nm, similar to the range reported here. Upon retracting the tip, the contact area with the adsorbate layer and the influence of radiation are gradually reduced, giving rise to the thermal background observed in the opening traces. Notably, thermal conductance variations versus tip-surface distance with similar slopes were recently measured in near-field heat transport measurements between nominally clean surfaces

in UHV, even after thorough in situ cleaning procedures. This indicates that the contribution of radiation to the distance-dependent thermal conductance at nm distances cannot be excluded and most likely cannot be avoided experimentally[193, 194]. Under our experimental conditions, the thermal background is stable and does not significantly change during repeated opening and closing of the break-junction contact, remaining approximately linear in the region of analysis described below.

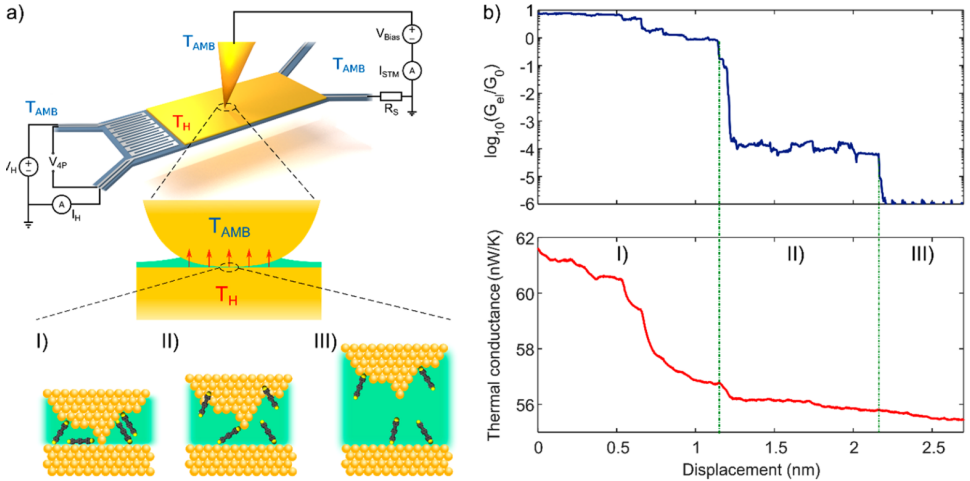


**Figure 4.1** Schematic of the measurement technique. (a) Schematic diagram of the experiment with the different transport regimes I-II-III upon breaking the tip-MEMS contact. The green meniscus represents the thermal contact with adsorbates on the MEMS. The thermal conductance of the junction is obtained by measuring the four-probe resistance of the platinum heater ( $R = V_{AP}/I_H$ ), which is directly related to its temperature  $T_H$ , and the total electrical power dissipated. Simultaneously, the electrical conductance is calculated from the tunnelling current,  $I_{STM}$ , measured at a fixed bias voltage,  $V_{bias}$ . (b) Example of a typical opening trace showing the variation of the electrical conductance of the junction  $G_e$  normalized by the conductance quantum  $G_0 = 2e^2/h$  and the overall thermal conductance of the Tip-MEMS system versus the tip displacement. (I) Au-Au contact. (II) Formation of a single-molecule junction indicated by the electrical conductance plateau. The variation in thermal conductance can be due to a modulation of the contact area with the adsorbates. (III) Breaking of the molecular junction, resulting in a small decrease of the overall thermal conductance, on the scale of a few tens of pW/K.

#### 4.1.4 Results and Discussion

Fig.4.2 illustrates the experimental procedure to extract the thermal conductance of the OPE3 molecule, using the electrical signal to verify the formation of molecular junctions. As in a standard break junction measurement, we collect typically 2000-5000 traces per data set and construct 1D and 2D histograms for the electrical (Fig.4.2a) and thermal

(Fig.4.2b) conductance opening traces. We then rescale the displacement and the thermal conductance axis by shifting their origin to the breaking point of the molecular junction. This means that for every trace that has a defined molecular signature in the electrical signal, we locate the breaking point of the molecular plateau in the electrical conductance trace and use this to rescale the distance and thermal conductance traces. Rescaling here refers only to shifting the origin of the displacement axis to the breaking point of the molecular plateau signal in each curve (no stretching factor was introduced). In the literature [56, 191, 195] such shifts are made with respect to the conductance signal falling below the conductance quantum, i.e., the breaking of the metal-metal contact. In any case, the rescaling helps to accommodate for drift and statistical variations of the breaking process. In this way, we can construct 2D histograms of the thermal conductance versus the displacement and average over the changes occurring in every trace when the junction breaks. To extract the thermal conductance of the molecule, we take the difference of the linear fits of the mean of the thermal background before and after the breaking point, see Figure 4.2b.

The variation of the slopes extracted from the fitting of different data sets appears random and is included in the reported uncertainty. On the small fitting range of few Ångstroms, non-linear fits did not yield better results. On a larger length scale, however, there is no prior assumption on the linearity of the background signal. Applying this method to dithiol-OPE3s, Figure 4.2a,b, we first note that the observed single peak in the electrical conductance histogram at  $2.7 \times 10^{-4} G_0$  (where  $G_0 = 2e^2/h$  is the electrical conductance quantum), is in excellent agreement with several independent reports in different environmental conditions [187, 195, 196] indicating single-molecule OPE3 junctions. The mean of the 2D thermal histogram shows a clear step in the thermal background at the breaking point of the molecular junction ( $d = 0$  nm), Figure 4.2b. The difference at 0 between the linear fits of the mean gives a molecular thermal conductance  $k = (20 \pm 6)$  pW/K. To construct a theoretical description of thermal transport, we use density functional theory (DFT) to obtain the optimized geometry of each junction. We then use the harmonic approximation to calculate forces on each atom in order to study the vibrational properties of the junctions. Using these force matrices, we obtain a dynamical matrix and combine it with the Green's function method to calculate the transmission coefficient  $T_{ph}(\hbar\omega)$  of phase-coherent phonons with energy  $\hbar\omega$  traversing from one electrode to the other. The thermal conductance due to phonons is then obtained from  $T_{ph}(\hbar\omega)$  using a Landauer-like formula [52, 186]. Figure 4.2c shows the phonon transmission coefficient  $T_{ph}$  of OPE3. Due to the low Debye frequency of gold electrodes ( $\sim 20$  meV)[186], phonons with energies higher than 20 meV are filtered (Figure 4.2c) and the phonon thermal conductance for temperatures higher than  $\sim 200$  K (Figure 4.2e) saturates to 19 pW/K in excellent agreement with the experimental data. In order to calculate the electrical properties of the junctions, we combine DFT mean-field Hamiltonians of each junction with the Green's function method to calculate transmission coefficient  $T_{el}(E)$  for electrons traversing from the hot electrode to the cold one (Figure 4.2d) through the molecules. The electron transmission through OPE3 is dominated by their highest occupied molecular orbitals (HOMO) in agreement with previous reports [67]. The electrical conductance is then obtained using the Landauer formula. At low temperatures, the conductance  $G = G_0 T_{el}(E_F)$  where  $E_F$  is the Fermi energy of electrodes [52]. In addition, the room temperature thermal conductance due

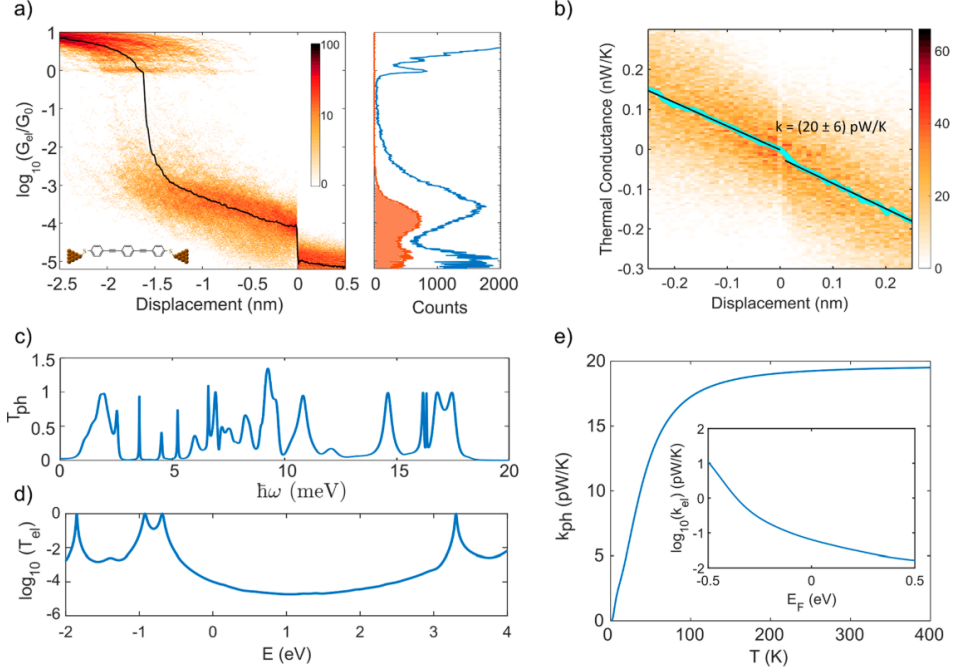


**Figure 4.2** Experimental (a, b) and theoretical (c-e) results for OPE3-dithiol. (a) Electrical 2D and 1D histograms constructed with 411 traces measured at a fixed voltage of 50 mV and a pulling speed  $v = 3$  nm/s at an angle of  $40^\circ$  with respect to the MEMS surface. From the histograms, we can extract the molecular electrical conductance of about  $2.7 \times 10^{-4} G_0$ . The orange 1D histogram indicates the electrical conductance of the junction before breaking, reconstructed from the 2D histogram in the displacement range between -0.5 and 0.2 nm. (b) 2D Thermal conductance histogram for OPE3. The width of the mean line (light blue) includes the total uncertainty of the extracted thermal conductance and shows a clear step around 0 (breaking point of the molecular junction). The black lines represent the linear fits of the mean before and after the step, giving a thermal conductance  $k = (20 \pm 6)$  pW/K. (c) Transmission coefficient  $T_{ph}$  of phonons with energy  $\hbar\omega$ . (d) Transmission coefficient  $T_{el}$  of electrons with energy  $E$ . (e) Calculated thermal conductance  $k_{ph}$  due to phonons versus temperature  $T$ . The inset shows the thermal conductance due to electrons versus the Fermi energy at room temperature.

to electrons can be calculated from the electron transmission  $T_{el}$  as a function of the electrodes Fermi energy  $E_F$ , as shown in the inset of Figure 4.2e. At the DFT predicted Fermi energy ( $E_F = 0$ ), the thermal conductance due to electrons is  $<0.1$  pW/K, which is much smaller than the phonon contribution. In addition, for a wide energy range around  $E_F = 0$ , the contribution of electrons to the total thermal conductance is negligible. The same experimental and theoretical methods were then applied to study the thermal transport properties of ODT (Figure 4.3).

In contrast to OPE3, the junction dynamics of ODT show stronger variation in independent reports. Different conductance values observed are attributed to various binding configurations of the S-Au bond [152, 197] gauche defects [191, 198] and a higher likelihood to observe multiple-molecules in a single junction [56, 199]. Nevertheless, there is some consensus about the frequently observed electrical conductance of  $5 \times 10^{-5} G_0$  relating to the atop-atop configuration of a single stretched ODT the molecule[56]. Most of the histograms show a prominent peak at  $5-7 \times 10^{-5} G_0$ , which we attribute to the atop-atop configuration. With lower probability, we observe plateaus at  $1 \times 10^{-5} G_0$  and at about  $1 \times 10^{-4} G_0$ , in agreement with a recent robust statistical approach [191]. Therefore, to simplify the analysis of the thermal signal, we focus on the atop-atop junction configuration considering molecular traces with plateaus between 2 and  $8 \times 10^{-5} G_0$ . For this junction geometry, we obtain a thermal conductance  $k = (29 \pm 8)$  pW/K. Simulations were based on the atop-atop configuration (inset of Figure 4.3a) resulting in a thermal conductance value of 22 pW/K at room temperature (Figure 4.3e) in reasonable agreement. When the tip is pulled from the electrode surface even with an angle, there may be a backlash because the system has a limited mechanical compliance [22]. This backlash can translate into a modification of the thermal signal due to the distance-dependent thermal background. In what follows, our aim is to demonstrate that the effect of a backlash is not significant in our case. First, for a given stiffness of the MEMS and the stiffness of a molecular bond, the backlash should lead to a certain backlash distance. Then, for different slopes of the thermal background signal, we should have an apparent step in the thermal conductance trace in proportion to the slope of the background signal. To test this, we repeated the experiment for both OPE3 and ODT on the same respective sample on different spots and on different samples (Figure 4.4). We found the slope of the background varying from measurement to measurement within certain limits, while the MEMS stiffness should be approximately constant. Within our uncertainty, we do not observe any significant dependence of the thermal conductance of OPE3 and ODT on the background slope (Figure 4.4). Therefore, we can argue that the backlash cannot be significant. By taking the weighted average of the different data points, we obtain  $k = (23 \pm 5)$  pW/K for OPE3 and  $k = (37 \pm 5)$  pW/K for ODT. We note, the same method was applied to gold-gold junctions leading to the results reported by two independent studies [22, 92]. In particular, we obtain a thermal conductance of 540 pW/K for a single gold atom contact (or atomic chain), which is very close to the value predicted by the Wiedemann-Franz law of 577 pW/K, for one electrical conductance quantum at  $T = 305$  K. A second independent argument that a backlash cannot be responsible for the observed step-change in thermal conductance comes from performing a test using closing traces. The junction formation yield is typically smaller for closing traces. Nevertheless, we were able to collect sufficient traces in the case of ODT with a clear molecular signature. We obtained similar values of thermal conductance

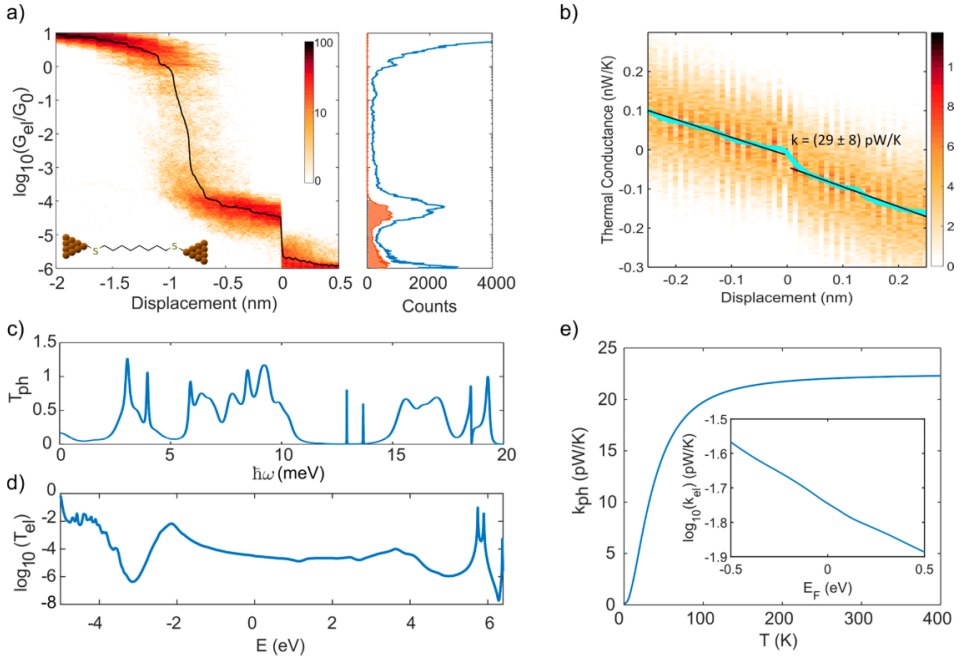


**Figure 4.3** Experimental (a, b) and theoretical (c-e) results for octane-dithiol (ODT). (a) Electrical 2D and 1D histograms constructed with 615 traces measured at a fixed voltage of 90 mV and a pulling speed  $v = 3$  nm/s at an angle of  $40^\circ$  with respect to the MEMS surface. From the histograms, we can extract the most probable molecular electrical conductance of about  $7 \times 10^{-5} G_0$ . Note that the peak shifts to  $5 \times 10^{-5} G_0$  before breaking (orange 1D histogram). (b) 2D Thermal conductance histogram. The width of the mean line (light blue) includes the total uncertainty of the extracted thermal conductance and shows a clear step around 0 (breaking point of the molecular junction), giving a thermal conductance  $k = (29 \pm 8)$  pW/K. (c) Transmission coefficient  $T_{ph}$  of phonons with energy  $\hbar\omega$ . (d) Transmission coefficient  $T_{el}$  of electrons with energy  $E$ . (e) Calculated thermal conductance  $k_{ph}$  due to phonons versus temperature  $T$ . The inset shows the thermal conductance due to electrons versus the Fermi energy at room temperature.

upon forming molecular junctions within closing traces ( $k = 35 \pm 7$  pW/K from 440 traces). The mechanics of a loaded spring is very different for a closing trace, in which a junction can be formed with a much reduced or even insignificant backlash. We estimate that a sensor stiffness of  $>20$  N/m is required to produce this result. Finally, it is well-known that bond breaking is a thermally activated process that can be accelerated exponentially by an applied pulling force. Spontaneous, and therefore backlash-free, bond breaking is favoured if sufficient time is given. Huang et al.[200] reported spontaneous bond breaking of ODT junctions at pulling velocities below 7 nm/s using an STM tip. Nef et al.[201] observed only a minority of breaking processes accompanied by measurable backlash using a sensor of 3-4 N/m pulling at 15 nm/s. Increasing the pulling velocity to 18 and 40 nm/s (with stiffer sensors) finally resulted in appreciable backlash according to other reports [202, 203]. In contrast, our experiments use the pulling speed of 2-3 nm/s. Therefore, we expect no backlash, taking into account these literature items. A further contributing effect to the absence of a backlash is that the non-chemically bound molecules were contributing to the thermal background, which also stabilize the junction mechanically. This, when combined with the contribution of the in-plane stiffness of the MEMS, can lead to an effective stiffness larger than the chemical bonds of the molecular junction. Evidence for this is the fact that we can controllably break a gradually thinning metal-metal contact. The stiffness of an initial multi atom-wide contact is much larger than a single molecular bond. Therefore, either the restoring force reduces significantly with pulling distance, or, otherwise, the contact would directly rupture from a larger contact area instead of going through the gradual changes. In fact, the latter is what we observe, if we perform experiments at a vertical pulling angle with only the smaller normal stiffness of the MEMS. One confirmation that either the spring constant must be larger than  $\sim 10$  N/m or the breaking force must be smaller than 0.1 nN can also be concluded from the fact that the Au-Au contact can be gradually broken. As seen in the individual sample traces, breaking from a  $2 G_0$  or  $3 G_0$  plateau to a  $1 G_0$  plateau can be observed in many traces. If the break force was in the force-driven regime, then the tip would apply a force of 2-3 nN to the 2-3  $G_0$  contact. The backlash after breaking of this would have to be efficient enough to reduce the force to below 1 nN as to not immediately break the  $1 G_0$  bond during the same breaking event. However, the maximum backlash would be the length of stretching of a single atom gold wire, and at room temperature, the average plateau length is below 0.1 nm. In contrast, a spring constant of only 1 N/m combined with a breaking force of 1 nN needs a minimum of 2 nm to relieve a force related to the transition from  $3 G_0$  to  $1 G_0$ . The Supporting Information comprises a detailed discussion on the potential error induced by the backlash issues based on the above arguments. From studies of thermal transport across self-assembled monolayers,<sup>41</sup> we learn that the environment of a molecule can influence its vibrational freedom and therefore the transport characteristic. In break junction experiments, however, the molecule is not in a densely packed configuration such as in self-assembled monolayers. Therefore, the environment has no significant influence on the thermal conductance other than providing a slowly varying background. The expected mobility of unbound molecules and the immobility of molecules bound to one of the electrodes leads us to believe that molecular rearrangement cannot be a source of major influence on the observed step change. The relatively slow measurement (compared to the molecular rearrangements time scale) and statisti-

cal analysis is expected to average out different configurations of surrounding molecules and the probed junction. We not only find good agreement between theory and experimental data but also note that our data agrees with expected bounds from reference data on similar systems. While heat transport of the thiol-bound OPE3 system has not been studied before, there are simulations (based on a similar approach to ours) for Au-OPE3-Au junction using amine anchor groups [204] yielding  $\sim 24$  pW/K, suggesting a very similar bonding strength of the respective anchor groups. Simulations of OPE3 bound to silicon [205] predicting  $\sim 60$  pW/K highlights the role of a higher Debye temperature of Si compared to Au electrodes, which allows higher frequency phonon transport leading to higher thermal conductance. Thermal transport through SAMs of alkanethiols between different materials, in contrast, have been studied using different methods, demonstrating that the thermal conductance is independent of the molecular length with more than 8 C atoms [106, 206, 207]. Interesting phonon filtering effects were instead simulated and probed for shorter chains [111]. Thermal conductance values up to a maximum of 14 pW/K were reported for  $C_{10}S_2$  and  $C_{11}S_2$  with gold electrodes [77, 80], in contrast with the usually higher values predicted by molecular dynamics (MD) simulations ranging between 25 pW/K [77, 117] and 45 pW/K [78, 79]. This discrepancy is attributed to uncertainty in the number of molecules in contact with the electrodes because of roughness. Interestingly, our experimental and theoretical results fit well with the available MD simulations. Another ab initio study [112] predicts  $k = 35$  pW/K for ODT between gold electrodes. We attribute this variation in the predictions and experimental results to the complex behaviour of the molecule in the junction, which includes not only bonding geometries but also the ability of the ODT to form gauche defects. This needs further systematic investigations in future studies. Thermal transport in both OPE3 and ODT is dominated by phonons with negligible contributions from electronic transport channels. The electrical conductance of OPE3 is higher than that of ODT for a wide range of energies around the DFT Fermi energy ( $E_F = 0$ ), as shown in Figures 4.2d and 4.3d. Consequently, the room temperature thermal conductance of ODT due to electrons is lower than that of OPE3 for a wide range of Fermi energies, in agreement with the Wiedemann-Franz law (inset of Figures 4.2 and 4.3e). At the DFT Fermi energy  $E_F = 0$ , the electronic thermal conductance of OPE3 and ODT are 0.07 pW/K and 0.01 pW/K, respectively. Although the electronic contribution to heat transport is found negligible in these systems, it is interesting to discuss, why a deviation from the Wiedemann-Franz law could lead to a more appreciable contribution. The Wiedemann-Franz law holds only when electron transmission coefficient  $T(E)$  is linear in the scale of  $k_B T$ . In both OPE3 and ODT,  $T(E)$  is linear in the scale of  $k_B T$  (25 meV at room temperature) in the vicinity of Fermi energy (Figures 4.2d and 4.3d). Therefore, the Wiedemann-Franz law holds, and  $k_{el} = \alpha T G$ , where  $\alpha$  is the Lorenz number,  $T$  is temperature, and  $G$  is electrical conductance. It is worth to mention that we have chosen two molecular backbones, which by chemical design are different. The OPE3 molecule has double and triple bonds and is very stiff compared to the more compliant and flexible alkane backbone. A stiffer material has in general higher phonon propagation speed (or velocities of sound) leading to larger thermal conductance. However, we observe that ODT is the better thermal conductor. This can be explained within the phonon mismatch picture. The frequencies of heat-carrying phonons in the gold electrodes are relatively low due to the large mass of the gold nuclei. To quantify, we have to remember

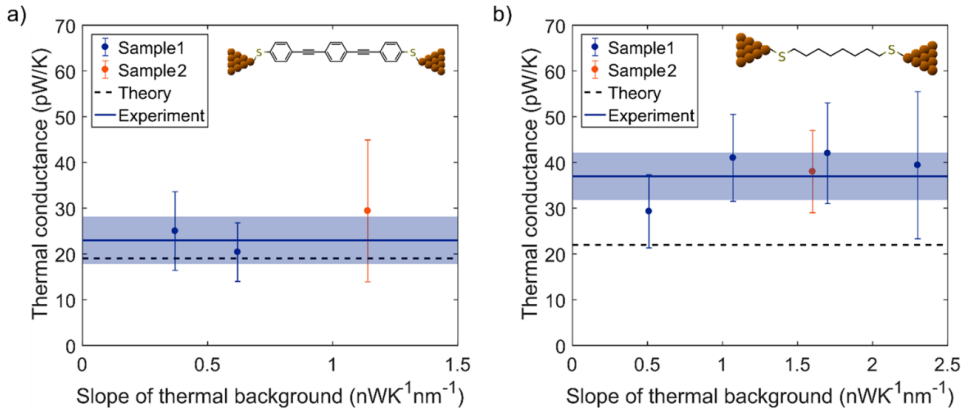


**Figure 4.4** Summary of the experimental results obtained for OPE3 (a) and ODT (b). By performing the weighted average of the different experimental data points for each molecule, we obtain  $k = (23 \pm 5)$  pW/K for OPE3 and  $k = (37 \pm 5)$  pW/K for ODT. The experimental uncertainty is represented by the shaded region around the mean value (blue line). 1D and 2D histograms relative to the data points in panels a and b are provided in the Supporting Information available online here.

that a sum over all phonon frequencies needs to be made to account for all heat transport, which reaches 20 meV. The phonon transmission spectra of Figures 4.2c (OPE3) and 4.3c (ODT) show transmitting modes in this range. The videos in the Supporting Information show the motion of both OPE3 and ODT due to different phononic modes below the Debye frequency of gold. While modes are found in both, the width of the phonon transmission resonances overall is greater in ODT (Figure 4.3c) compared with OPE3 (Figure 4.2c), which implies a higher density of phonon states at the connection point to electrodes in ODT. Nevertheless, the difference in thermal conductance between the two systems is less than a factor of 2 in the experiments. This underpins the more general notion that the variation in thermal conductivity between solid materials is rather limited when compared to the tunability of charge or photon transport in matter. In order to manipulate thermal transport, we, therefore, need to employ strategies based on phonon engineering in molecular systems carefully. These include, for example, placing Fano-resonances in the integration window of frequencies offered by the electrodes to reduce thermal conduction [43, 125]. Furthermore, phonon interference of two conduction paths along a molecule is another interesting candidate mechanism. The proposed mechanisms, in general, rely on a specific transport regime. One of the main aspects of the theoretical description allied here is the phase coherence nature of transport. Through the quantitative agreement between experiment and theory, one of our main results is the confirmation of the phonon transport being phase-coherent along these junctions.

### 4.1.5 Conclusion

We demonstrated the first measurement of the thermal conductance of single-molecule junctions. We applied this method to the two benchmark molecules OPE3 and ODT and found good agreement with our ab initio simulations, based on phase-coherent heat transport at the single-molecule level. Given the versatility of the approach, we expect this work to enable systematic investigations of molecular-scale heat transport, opening new possibilities for engineering materials with tailored thermal transport properties.

## 4.2 Thermoelectric properties of Single-Molecule Junctions<sup>2</sup>

This chapter has been first published on 9th September 2020 in the 12th issue of *Nanoscale*. The text, figures and references have been re-formatted in the style of this thesis. Supporting Information (ESI) available online:

<https://www.rsc.org/suppdata/d0/nr/d0nr04413j>



Nanoscale

PAPER



Cite this: *Nanoscale*, 2020, 12, 18908

### Electronic conductance and thermopower of single-molecule junctions of oligo (phenyleneethynylene) derivatives†

Hervé Dekkiche,<sup>a</sup> Andrea Gemma,<sup>b</sup> Fatemeh Tabatabaei,<sup>c</sup> Andrei S. Batsanov,<sup>id</sup><sup>a</sup> Thomas Niehaus,<sup>id</sup><sup>\*c</sup> Bernd Gotsmann<sup>\*b</sup> and Martin R. Bryce<sup>id</sup><sup>\*\*a</sup>

**AUTHOR CONTRIBUTIONS:** AG performed all the experimental work and data analysis with help from BG. Molecules were synthesized by HD. Theory and simulation by FT, TN and AB. HD and AG wrote the manuscript with contribution from all the other co-authors.

---

<sup>2</sup>Adapted with permission from Ref.[143]. Copyright (2021) The Royal Society of Chemistry.

### 4.2.1 Abstract

We report the synthesis and the single-molecule transport properties of three new oligo(phenylene-ethynylene) (OPE3) derivatives possessing terminal dihydrobenzo[b]-thiophene (DHBT) anchoring groups and various core substituents (phenylene, 2,5-dimethoxy-phenylene and 9,10-anthracenyl). Their electronic conductance and their Seebeck coefficient have been determined using scanning tunnelling microscopy-based break junction (STM-BJ) experiments between gold electrodes. The transport properties of the molecular junctions have been modelled using DFT-based computational methods which reveal a specific binding of the sulfur atom of the DHBT anchor to the electrodes. The experimentally determined Seebeck coefficient varies between  $-7.9$  and  $-11.4 \mu\text{V K}^{-1}$  in the series and the negative sign is consistent with charge transport through the LUMO levels of the molecules.

### 4.2.2 Introduction

Over the last decade molecular-scale electronics has progressed rapidly with increased understanding of the structure-function relationships of devices that comprise a single molecule or assemblies of molecules bridging two metallic electrodes [63, 64, 208]. The interplay of electrical, thermal and thermoelectric transport in molecular junctions is a key aspect in the design and operation of energy conversion devices in the quest for new energy-saving technologies [23, 209–211]. The continuous downsizing of the components used in everyday electronic devices such as computers, smartphones and other screen-based apparatus, is accompanied by an increase of the heating/power ratio. Being able to manage that extra heat would then enable reduced electricity consumption and increased efficiency of the whole system. Therefore, there is keen interest in the thermoelectric properties of conductive materials [212]. However, the thermal characterisation of molecular junctions is a challenging topic [36, 154]. The energy conversion efficiency of a specific thermoelectric material is determined by the figure of merit  $ZT$  given by the ratio

$$ZT = \frac{S^2 \sigma_{electric}}{\sigma_{thermal}} \quad (4.1)$$

where  $S$  is the Seebeck coefficient (or thermopower),  $\sigma_{electric}$  is the electrical conductance, and  $\sigma_{thermal}$  is the thermal conductance. For energy harvesting, a value of  $ZT \geq$

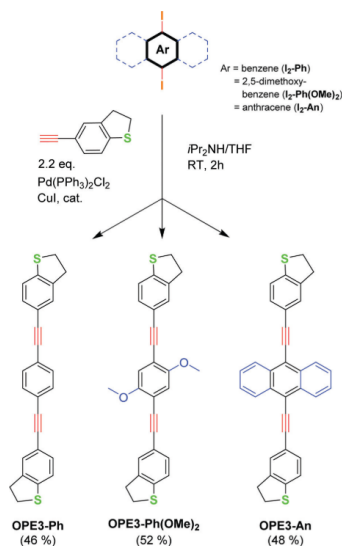


**Figure 4.5** Synthesis of the OPE3 derivatives.

1 is required to be technologically interesting. For cooling applications, a large power factor,  $S^2\sigma_{electric}$ , is needed. To date the best intrinsic efficiency has been obtained for bulk materials, typically metallic (nano)composites [213, 214]. However the drawback of these materials is that they are usually quite expensive and/or necessitate complicated manufacturing processes and therefore cannot easily be employed in small-scale junctions. Recently, the idea of using single molecules in thermoelectric junctions, and more specifically organic molecular wires, has emerged [215]. These molecules possess an appropriately conductive delocalised  $\pi$ -electronic system, they can be produced on a large scale and their properties and dimensions can be finely tuned by chemical synthesis. Importantly, high Seebeck coefficient values have been predicted for some of them, such as  $-56 \mu\text{VK}^{-1}$  for a fullerene pair [216] or the impressive range of  $-280 \mu\text{VK}^{-1}$  to  $230 \mu\text{VK}^{-1}$  for selected metalloporphyrins [217]. Therefore, organic molecules are perfect candidates for applications in thermoelectric devices [218]. The electrical conductance of single molecules is now well understood and can be measured by using various techniques such as Scanning Tunnelling Microscopy (STM) based or mechanically controlled (MC) break-junction (BJ) experiments [219]. On the other hand, the experimental [220] and theoretical characterisation [21] of thermal conductivity in those systems is still in its infancy and only recently thermal conductance of single molecules has been measured experimentally [23, 211]. The measurement of the Seebeck coefficient involves performing BJ experiments at variable temperature bias between the two metal electrodes [209, 220]. The main issue of thermoelectric materials for the use in thermoelectric converters is the low energy conversion efficiency. The requirements for high efficiency, i.e. a high value of ZT, need careful tuning of the material to optimize the mutually related properties: electrical, S and thermal. In addition, there is a need for stable molecular films with high integrity. A prerequisite is the availability of a stable and versatile molecular platform. Such a platform would have favourable anchor groups and the ability to host side-groups. Ideally, these groups would not interfere with the electrical transport and therefore allow reduction of phonon transport [43]. As a first step in this direction, there is need to demonstrate that thermoelectric transport through a promising molecular backbone can be maintained despite chemical modification through anchor points for side-group chemistry. The present work explores the single-molecule conductance and thermoelectric properties of new oligo(phenyleneethynylene) (OPE3) derivatives (3 denotes the number of phenylene rings in the backbone) using STM-BJ experiments. Extensive computational calculations using DFT and DFTB were then performed to support the results obtained. OPE3 derivatives were chosen as they are synthetically-versatile, highly-conjugated, robust molecules and they have been widely studied in molecular electronics [221, 222]. OPE3 systems, in particular, can be conveniently assembled and measured in metal-molecule-metal junctions [189, 223, 224]. The wide agreement between conductance data obtained for OPE3 junctions in different research groups, makes this an excellent candidate for a systematic study on the influence of side and end-groups. We chose the very stable dihydrobenzo[b]thiophene (DHBT) anchor as this group is known to bind efficiently to metal electrodes, with high junction formation probability [68, 225, 226], and without the problems associated with thiol anchors, such as oxidation and formation of metal-thiolate clusters [227]. We demonstrate that these molecules possess the highly versatile structural features that are required for thermal conductance studies.

### 4.2.3 Experimental

#### Synthesis and characterisation of the molecules

Reagents were purchased commercially and used as received unless otherwise stated. THF was dried using an Innovative Technology solvent purification system and stored in ampoules under argon. Thin-layer chromatography (TLC) analysis was carried out using Merck silica gel 60 F254TLC plates and spots were visualised using a UV lamp emitting at 365 or 254 nm. Column chromatography was performed using silica gel 60A (40-63  $\mu\text{m}$ ) purchased from Fluorochem.  $^1\text{H}$  and  $^{13}\text{C}$  NMR spectroscopy was carried out on a Bruker AV400 NMR spectrometer. For  $^1\text{H}$  NMR spectra, chemical shifts are reported relative to the residual solvent peak (7.26 ppm for  $\text{CHCl}_3$ ) and for  $^{13}\text{C}$  NMR spectra, chemical shifts are reported relative to the solvent peak (77.16 ppm for  $\text{CDCl}_3$ ). All NMR spectra were processed using MestReNova V12. ASAP mass spectrometry was carried out using an LCT Premier XE mass spectrometer (Waters Ltd, UK) using TOF detection. X-ray single crystal data were collected on a Bruker 3-circle D8 Venture diffractometer with a Photon100 CMOS detector, using Mo-K $\alpha$  radiation ( $\lambda = 0.71073$  Å) from a I  $\mu\text{S}$ -microsource with focusing mirrors. The crystals were cooled with a Cryostream (Oxford Cryosystems) open-flow  $\text{N}_2$  cryostat. UV-Vis absorption spectra were obtained using a Thermo Scientific Evolution 220 spectrophotometer. 4-Acetylnyl-dihydrobenzo[b]thiophene was prepared according to the procedure described previously [68]. 2,5-dimethoxy-1,4-diodobenzene and 9,10-diidoanthracene were obtained starting from p-methoxyanisole and anthracene using known methods [228, 229]. Detailed experimental procedures for the preparation of the compounds and their characterisation data are provided in the ESI.

#### STM-BJ experiments

Gold tips were prepared by electrochemical etching of gold wires with a diameter of 0.25 mm with 99.99+% purity (GoodFellow) in  $\text{CaCl}_2$ , using the procedure reported by Boyle et al. [183]. A typical tip radius obtained with this etching procedure is 50-100 nm. The counter-electrode consists of a  $5 \times 5 \times 1$  mm chip of silicon, whose top surface has been fully covered with pure sputtered gold. After fabrication, to eventually remove contaminants and recover a fresh gold surface, prior to use, every chip is cleaned either via flame-annealing or with a combination of Oxygen Plasma + Ion Milling. After cleaning the gold substrate, it was then immersed in the solution of the target molecules. Three different solutions were prepared with a concentration  $c = 0.25$  mM to 0.3 mM in a mixture of dichloromethane (DCM) and ethanol (EtOH), 1 : 1 v/v ratio. Samples were immersed for 5 min and then rinsed for 1 min in a fresh mixture of DCM and ethanol. Immediately after rinsing, samples were carefully dried under  $\text{N}_2$  flow in a chemical fume hood. To combine electrical and thermoelectrical measurements the tip of the STM was equipped with two platinum resistors, one acting as heating element and the other acting as a thermometer. The temperature of the system was maintained at the desired value using a temperature controller (Meerstetter TEC 10-91) with an accuracy and stability better than  $0.01^\circ\text{C}$ . All the measurements were performed in vacuum ( $\sim 1 \times 10^{-7}$  mbar) and at room temperature ( $22^\circ\text{C}$ ) with a custom-built STM, located in a low-noise laboratory [151].

## Theoretical calculations

4

Binding energies of OPE3-Ph on Au(111) were computed using Density Functional Theory (DFT) as implemented in the plane wave code Quantum ESPRESSO [230, 231]. We used the Perdew-Burke-Ernzerhof (PBE) exchange-correlation functional [232] and PAW pseudopotentials from the pslibrary 1.0.0. [233]. Energy cutoffs of 70 Ry and 280 Ry were used for the plane wave expansion of wave functions and electron density, respectively. A 4-layer slab model of the  $(5 \times 6)$  surface supercell of Au(111) was relaxed at the  $\Gamma$  point with a convergence criterion of 0.001 a.u. for the forces. The two topmost layers were allowed to move and a vacuum thickness of about 20 Å was applied in the dimension orthogonal to the surface to avoid artificial interactions. The same settings were applied to model the adsorption of OPE3-Ph on the surface. Binding energies  $E_{ads}$  were finally computed as  $E_{ads} = E_{cmp} - E_{mol} - E_{Au(111)}$ , where  $E_{cmp}$  denotes the total energy of the OPE3-Ph-Au(111) complex,  $E_{mol}$  the total energy of OPE3-Ph relaxed in the gas phase (modelled in the same simulation cell as the complex), and  $E_{Au(111)}$  the total energy of the relaxed surface. Electronic transport properties of the OPE3 derivatives were computed using Non-Equilibrium Green's Function Theory based on the Density Functional Based Tight-Binding Method (DFTB) [234–236] as implemented in DFTB+ version 19.1 [237]. DFTB is an approximate DFT method with an appealing cost/accuracy ratio and has been successfully used in a variety of applications in the field of molecular electronics [238–240]. Here we employed the auorg-0-1 Slater-Koster set [241, 242] with orbital dependent Hubbard parameters and used a periodic setup, where the device is replicated perpendicular to the transport direction along the surface. This entails a solution of the Poisson equation under periodic boundary conditions to obtain the charge density in the device region. The actual device model was created in several steps. We first optimised the target molecule attached to two Au<sub>20</sub> clusters in the gas phase using the atomic orbital NWChem code [243]. The calculations were performed with the PBE functional and a 6-31G\* basis set for C, H, S and a lanl2dz\_ecp basis set and corresponding core potentials for Au. The defaults for energy and force convergence were kept. With the help of the simulation environment ASE, [244] the Au<sub>20</sub>-molecule-Au<sub>20</sub> complex was then embedded between two identical Au(111) surfaces, each containing three atomic layers with 30 atoms per layer, to form a full device as shown later in the manuscript in the theory section. Note that in this process the Au-S-C binding angles (found in the gas-phase relaxations) were conserved, such that the molecular tilting with respect to the surface was correctly captured. This device was then coupled to gold electrodes, consisting of three additional gold layers that were periodically replicated in the transport direction.

### 4.2.4 Results and Discussion

The new OPE3 molecules bearing the DHBT anchoring group were synthesised by reacting a corresponding diiodo-aryl derivative with a small excess of 4-acetynyl-benzo[b]thiophene in a two-fold Sonogashira cross-coupling reaction conditions (Fig. 4.5). Starting from 1,4-diiodobenzene, 2,5-dimethoxy-1,4-iodobenzene and 9,10-diiodoanthracene, OPE3-Ph, OPE3-Ph (OMe)<sub>2</sub> and OPE3-An were respectively obtained in about 50% yield. After purification by column chromatography, the compounds were fully characterised by <sup>1</sup>H and <sup>13</sup>C NMR spectroscopy and high-resolution mass spectrometry (HRMS)

(as shown in the ESI). The presence of the DHBT anchoring group in the molecules was notably confirmed by the observation of symmetrical signals in the 7.59-7.18 ppm and 3.44-3.27 ppm windows in the  $^1\text{H}$  NMR spectra, corresponding to the aromatic and  $\text{CH}_2$  protons, respectively [68]. Single crystals suitable for X-ray diffraction analysis were obtained for OPE3-Ph and OPE3-An by slow exchange of methanol and hexane vapours respectively into a  $\text{CH}_2\text{Cl}_2$  solution of the compounds. OPE3-Ph lies at a crystallographic inversion centre. Thus, arene ring A and its axis X are parallel to their equivalents ( $A'$  and  $X'$ ), while inclined to the central ring (Ph) by  $18.7^\circ$  and  $10.7^\circ$  respectively (Fig. 4.6a). OPE3-An has no crystallographic symmetry. Rings A1 and A2 are inclined to the planar anthracene moiety (An) by  $26.9^\circ$  and  $38.4^\circ$ , respectively, their axes X1 and X2 by  $3.3^\circ$  and  $19.5^\circ$ . The A1/A2 dihedral angle is  $21.7^\circ$ , the X1/X2 angle  $22.9^\circ$  (Fig. 4.6b). In both molecules, the heterocycles adopt envelope conformations, with the  $\text{CH}_2$  group adjacent to the S atom, tilting out of this (and the fused arene) ring plane. In OPE3-An, both heterocycles are disordered between two envelope conformations with opposite tilt, in 4:1 and 10:1 ratios. Overall, the OPE3 backbone is essentially planar in each case, suggesting a good  $\pi$ -electron delocalisation in these molecules. Moreover, a highly organised extended network was observed in the case of OPE3-Ph. The molecules stack together and arrange in a 2D fashion, resembling what could be expected for a self-assembled monolayer (SAM) on a surface. In contrast, a dimeric arrangement, rather than continuous stacks, was observed for OPE3-An (see ESI for figures).

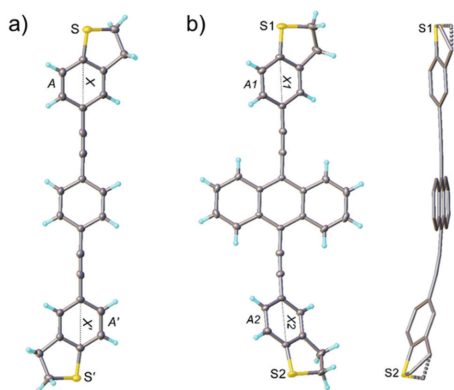


**Figure 4.6** X-ray molecular structures. (a) Projection on the central phenylene plane (Ph) of OPE3-Ph, inversion-related entities are primed, thermal ellipsoids are drawn at 50% probability level and (b) major conformer of OPE3-An, projection on the anthracene (An) plane, and side-view showing the disorder (H atoms omitted).

substrate is maintained at room temperature, while the overall temperature difference,

The electrical conductance and Seebeck coefficient for the three synthesised molecules have been measured via STM Break Junction techniques. The experimental setup is represented schematically in Fig. 4.7a. The chips were coated with the material following the procedure described in the Experimental section. Applying the two cleaning methods (flame annealing or oxygen plasma + ion milling) resulted in comparable, high-quality histograms without obvious signs of contamination, such as seen sometimes at intermediate conductance. The experiment is based on a modified version of the STM-Break Junction technique, where the current between the two electrodes is recorded as a function of the separation distance, at different temperature difference between the electrodes.

A typical experiment runs as follows. First, the temperature bias between the two electrodes is set using the resistive elements present in the tip holder. The

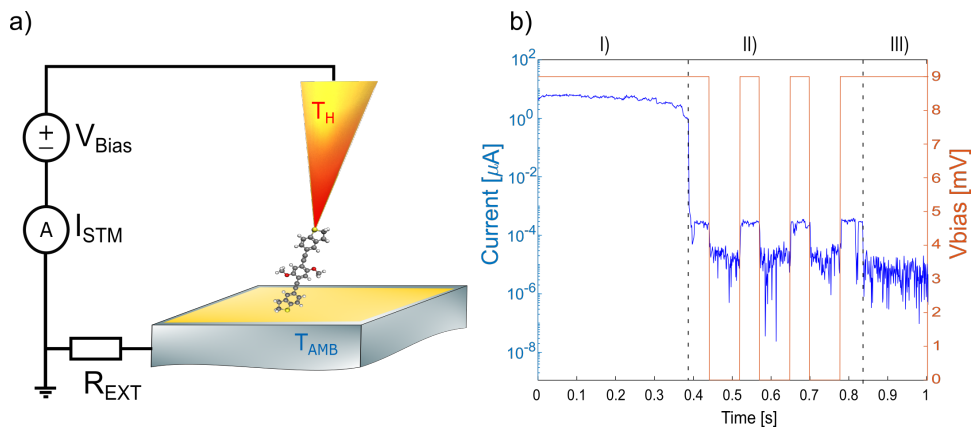


**Figure 4.7** (a) STM break junction setup for the electric and thermoelectric characterization of single molecules; (b) typical example of opening trace:  $I(t)$  and  $V_{bias}(t)$  for a single-molecule junction.

$\Delta T$ , ranges from room temperature up to 60 K. The temperatures in the setup are then allowed to settle to a steady state for more than 1 h at each temperature, before starting a new measurement. After the thermal equilibrium has been reached, the tip is moved closer to the gold substrate where molecules have been deposited (closing trace) with a speed of 5 nm/s. Then, after a good electrical contact has been established ( $>5 G_0$ , where  $G_0$  denotes the electrical conductance quantum), the two electrodes are slowly moved apart (opening trace), at speeds of 3 nm/s. For the sake of simplicity, we will consider only the closing traces, since statistically they show a larger number of molecules trapped in the junction. During the trace the current is measured at constant bias of  $\Delta V = 9$  mV. This is a value over the junction plus a series resistance, that is added in front of the current-to-voltage converter to prevent it from saturation. In fact, the resistance of the junction usually varies from few ohms  $\sim \Omega$ , when the two electrodes are in contact, to  $\sim G\Omega$ , when the electrodes are separated by a single molecule. A typical trace is shown in Fig. 4.7b. Three different regions can be distinguished: (I) At low resistance (1 to  $10 G_0$ ), the conductance is dominated through a metal junction between the gold electrodes (Au-Au). During the thinning down of the Au-Au junction (I), the electrical conductance and consequently the current decreases in a step-like fashion, because of the quantized availability of electron channels in 1D systems. In this framework, the last few channels correspond to the last atoms bridging the contact, down to a single atom, immediately before the rupture [22]. (II) After breaking the metal junction, some opening traces also show a second regime (II), where the electrical current exhibits a plateau with a constant value of current (and therefore a constant value of conductance), implying the formation of a molecular junction (Au-molecule-Au). Since for the OPE3 derivatives, the molecular plateau has been theoretically predicted to have a conductance around  $1 \times 10^{-4} G_0$ , as confirmed by the conductance histograms, we define a molecular region as the interval of conductance between  $1 \times 10^{-3} G_0$  and  $1 \times 10^{-5} G_0$ . In this region the speed of the piezo-scanner is lowered to 1 nm/s. (III)

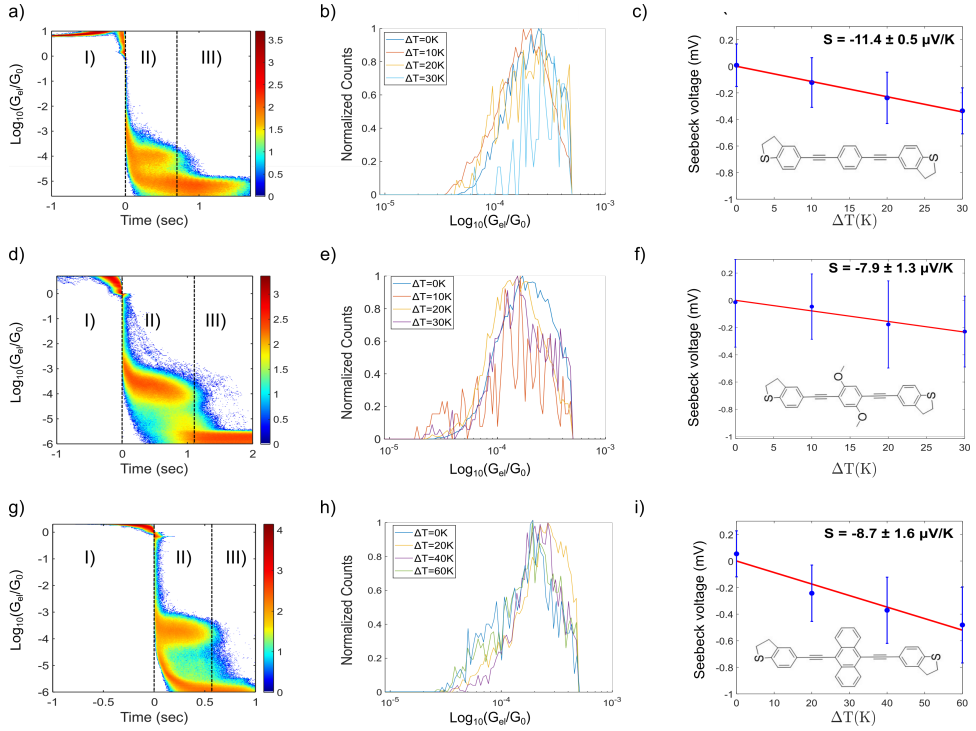


**Figure 4.8** (Break-junction conductance histograms (a, d, and g) with a logarithmic color bar ( $\log(\text{counts})$ ), 1D single-molecule conductance traces obtained as a function of the temperature (b, e and h) and Seebeck voltage vs.  $\Delta T$  graphs (c, f and i) respectively, obtained for OPE3-Ph, OPE3-Ph(OMe)<sub>2</sub> and OPE3-An.

After the molecular junction is broken, a much smaller tunnelling current is measured (Au-tunnelling-Au) and the current signal falls into the noise level of the setup. To measure the Seebeck coefficient, we proceeded as follows. When a molecular plateau is found within the molecular region, the following steps were performed while continuing to retract the tip (i) The conductance  $G_{before}$  of the first 50 points of the plateau is analysed. If the conductance value stays between set thresholds ( $1 \times 10^{-3} G_0 - 1 \times 10^{-5} G_0$ ), then it is assumed a molecular junction is still present; (ii) Then, the bias is turned off for a window of 80 data-points, and the thermoelectrical current  $I_{Seeb}$  is measured; (iii) Subsequently, the bias is restored and the conductance  $G_{after}$  of the following 50 data-points is compared to the value before the switching. If both values of conductance, before and after the bias switching, are found to be within the bounds of the molecular region and  $G_{after} = G_{before} \pm 20\%$ , the switching is repeated until the conditions of  $G_{before}$ ,  $G_{after}$  are not fulfilled anymore. This technique enables the determination of the electrical conductance and thermoelectric current within one single measurement, and therefore for the simultaneous determination of  $G_{el}$  and  $S$  for each molecule. Fig. 4.8 shows the results for the series of three OPE3 derivatives.

The first column shows the 2-dimensional histograms for the electrical conductance at room temperature for the different molecules. The colour bar gives the number of counts in a logarithmic scale. The second column compares the 1-dimensional conductance histograms, obtained during the Seebeck measurements, for four different temperature gradients applied to the junction. Here the maximum of each distribution represents the most probable value of the electrical conductance, during the bias switching, at each given  $\Delta T$ . In the third column the Seebeck voltage is plotted for different values of  $\Delta T$ . The thermovoltage is calculated from the measured thermocurrent using the following equation:

$$\Delta V_{Seebeck} = \frac{I_{V_{bias}}}{G_{avg}} = S\Delta T \quad (4.2)$$

where  $G_{avg}$  is the average between  $G_{before}$  and  $G_{after}$ . The slope of the line fitting the data-points, represents the experimental Seebeck coefficient. Every data-point has been obtained as the average of at least  $\sim 500$  measurements and the error bar of each point indicates the width of the relative distributions. Note, that the measurement noise is smaller than the width of the distribution, which is expected to arise due to variations of the atomic configurations during the experiments. The experiments probe many configurations and are performed on different areas of the sample. The mean value is a measure of the most frequent, and thereby expected to be the most likely, molecular configuration. The measurements are typically repeatable for up to one week, by when signs of degradation are observed, which we assign to oxidation of the molecules. However, the systematic unknown parameters in the experimental configuration add to the difficulties of comparing experimental data with theoretical predictions. For example, in these experiments the Seebeck voltage distribution is large, implying that the chemical potential could be substantially varied among the many different configurations that are probed. All the molecules show a negative Seebeck coefficient, indicating LUMO-dominated conductance. Also, the introduction of the side-groups in OPE3-Ph(OMe)<sub>2</sub> and OPE3-An slightly decreased the absolute value of the Seebeck coefficient compared to OPE3-Ph, while the overall electrical properties were not greatly affected. As a side-remark, for OPE3-An a higher thermal stability is observed, that allowed a doubling of the temperature difference range compared to the other molecules (Fig. 4.8h and i). The mechanical arrangement of a molecular junction can be thermally unstable, which is visible at higher temperatures through a reduced yield of measuring a molecular plateau in individual opening traces. Such thermal instability of the junction will leave the molecule intact and is different from thermal decomposition of the molecules, which is found to be higher than 250°C in measurements of the molecular crystals. To support the experimental results, first principles calculations were performed as detailed in the method section. The metal-molecule binding configuration is not directly accessible in the measurements and will also strongly depend on the electrode distance. We therefore investigated the binding of OPE3-Ph to ideal gold surfaces without adatoms and defects. This allows us to get a first impression of the relevant binding motifs that should also be of relevance for the rough surfaces in break junctions. Geometry relaxations have been performed for OPE-Ph attached to the Au(111) surface using periodic plane wave DFT calculations. The sulfur atom of the DHBT anchoring group was positioned at the top, bridge, fcc and hcp positions of the surface. Configurations that differ by rotations

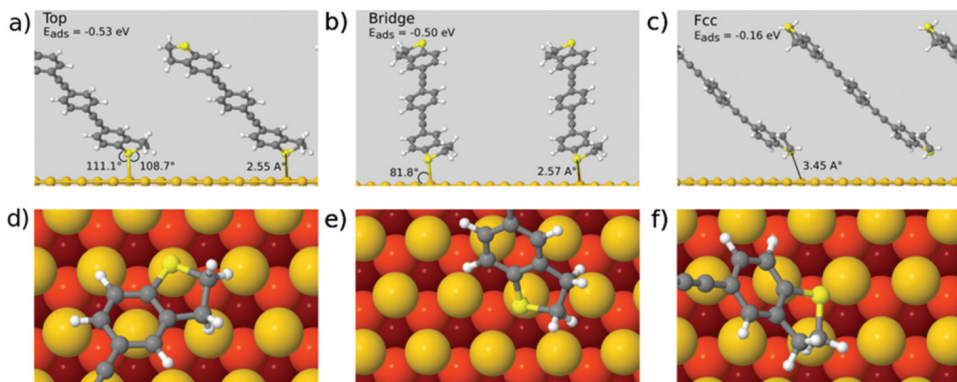


**Figure 4.9** Optimal binding configurations of OPE3-Ph on Au(111) from periodic DFT simulations. (a)–(c) Side views for top, bridge and fcc initial structures, (d)–(f) same structures viewed from the top (darker colour of Au atoms indicates larger distance to the surface). Bond angles are shown for covalently bonded configurations.

of the molecular backbone around the surface normal have not been considered. This task remains for a later and more complete study. The size of the periodic unit cell was chosen such that the distance between molecular images is around 9 Å, so that a low surface coverage is effectively simulated.

As shown in Fig. 4.9 the most stable binding configuration is the top position with an Au-S bond length of 2.55 Å. The bonding angles indicate a pyramidalisation of sulfur, consistent with a dative bond where one of the S lone pairs interacts with Au d-orbitals. We also found stable conformations in which the OPE3 backbone is oriented perpendicular to the surface (see ESI). These are 1.1–1.4 eV higher in energy than the tilted conformers and will not be discussed in detail. The adsorption energy of  $E_{ads} = -0.51$  eV for the most stable conformer shows that the DHBT group provides an effective anchor. Moreno-Garcia and coworkers [68] investigated the binding energy of several aurophilic functional groups. Specifically, they looked at cyano (CN), amino (NH<sub>2</sub>), thiol (SH), 4-pyridyl (PY) and the present DHBT and found the energetical ordering NH<sub>2</sub> < DHBT ≈ CN ≈ PY < SH, where NH<sub>2</sub> denotes the least stable anchor group. Although the OPE3 molecular wire was coupled to an Au pyramid in the Moreno-Garcia study, the reported binding energy of  $E_{ads} = -0.41$  eV is close to our result for the top position. Considering the other configurations in Fig. 4.9, we find that binding into hollow sites of the Au(111) surface is not likely: the hcp starting structure relaxes into a top configuration (and is therefore not shown), while the fcc structure shows a low adsorption energy of  $E_{ads} = -0.16$  eV and a very long Au-S distance of 3.45 Å. Optimisation of the bridge configuration leads to a structure where the DHBT sulfur is nearly at a top position. In summary, we find very little conformational flexibility. In contrast to the more common thiol anchor groups, DHBT features a sulfur lone pair with fixed orientation with respect to the molecular plane, and this reduces the available conformational space. As also proposed in other studies [64, 245] this feature might explain the rather narrow conductance histograms seen above. Next, we investigated

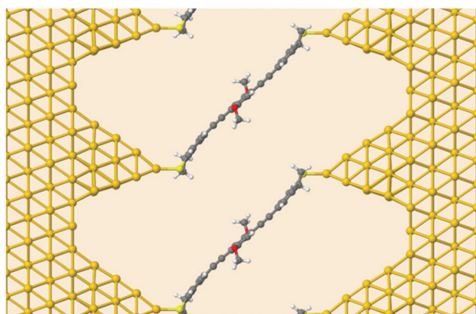


**Figure 4.10** Device geometry for DFTB transport simulations. Shown is OPE3-Ph(OMe)<sub>2</sub> connected to semi-infinite gold leads.

4

the transport properties of the various OPE3 derivatives by means of Non-Equilibrium Green's Function theory. Molecular Green's function, molecule-surface coupling and surface Green's function are all evaluated at the DFTB level, which is an approximate and numerically efficient DFT method. Similar to previous studies [68], the electrodes are modelled as multiple layers of the Au(111) surface connected to Au<sub>20</sub> clusters that are finally attached to the anchor groups (Fig. 4.10).

As detailed in the ESI, binding to the surface leaves the OPE3 backbone largely unchanged with respect to the experimentally determined X-ray crystal structure. The calculations provide the energy dependent transmission function  $t(E)$ , which is directly related to the electrical conductance  $G : G = t(E_F) \times G_0$ , where  $E_F$  denotes the Fermi energy of the junction and  $G_0$  is the quantum of conductance [63]. As Fig. 4.11 shows, the side groups at the central OPE3 ring have an important effect on the HOMO energy. The electron-donating OMe groups in OPE3-Ph(OMe)<sub>2</sub> lead to an upward shift of approximately 0.15 eV, while the extension of the  $\pi$ -system in OPE3-An has an even stronger effect with a shift of 0.75 eV with respect to OPE3-Ph. The LUMO energies exhibit a much weaker variation. Since conduction at low bias occurs through the tails of the frontier orbital that is situated closer to  $E_F$ , the small differences in conductance found for both experiment and theory (see Table 4.1) become understandable. While the LUMO transmission for OPE3-An reaches the maximal value of 1.0 (indicating perfect transmission), both OPE3-Ph(OMe)<sub>2</sub> and OPE3-Ph show reduced values below 0.04. This could be related to an asymmetric coupling to the left and right contacts, but since our models are symmetric, we attribute this fact to partial destructive interference of transmission paths through energetically close lying molecular orbitals. Similarly, the dip in transmission just below  $E_F$  could be of similar nature. The computed transmission can also be used to estimate the temperature dependent Seebeck coefficients  $S(T)$  for the OPE3 derivatives:

$$S = -\frac{\pi^2 \kappa_b^2 T}{3e} \frac{t'(E_F)}{t(E_F)} \quad (4.3)$$

The theoretical values obtained are reported in Table 4.1 and compared to the measured values. As mentioned above, the experimentally measured negative values for  $S$

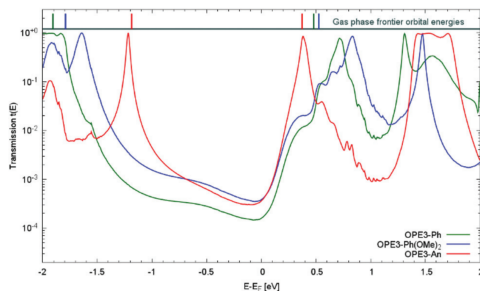


**Figure 4.11** DFTB transmission function  $t(E)$  for three OPE3 derivatives. For illustrative purposes the HOMO and LUMO energies of the isolated molecules in the gas phase are given at the top of the figure. To account for the Fermi level alignment upon contact formation, the gas phase energies have been shifted by  $\Delta = M_d - M_g$ , where  $M_d$  and  $M_g$  denote the HOMO/LUMO mid gap energies for the device and gas phase, respectively. We obtain  $\Delta_{\text{OPE3-Ph}} = -1.45$  eV,  $\Delta_{\text{OPE3-Ph(OMe)}_2} = -1.44$  eV and  $\Delta_{\text{OPE3-An}} = -1.00$  eV. The sign of these shifts is consistent with a charge transfer of electrons from the molecule to the electrode through formation of dative bonds.

	$G_{exp}$ [ $G_0$ ]	$G_{theo}$ [ $G_0$ ]	$S_{exp}$ [ $\mu\text{VK}^{-1}$ ]	$S_{theo}$ [ $\mu\text{VK}^{-1}$ ]
<b>OPE3-Ph</b>	$0.92 \times 10^{-4}$	$1.60 \times 10^{-4}$	$-11.4 \pm 0.5$	-25.6
<b>OPE3-Ph(OMe)<sub>2</sub></b>	$2.03 \times 10^{-4}$	$3.86 \times 10^{-4}$	$-7.9 \pm 1.3$	-27.0
<b>OPE3-An</b>	$1.82 \times 10^{-4}$	$3.642 \times 10^{-4}$	$-8.7 \pm 1.6$	-37.1

**Table 4.1** Experimental and theoretical values for the conductance  $G$  and Seebeck coefficients  $S$  at room temperature ( $T=295$  K) for different OPE3 derivatives obtained in this study. For each molecule,  $G_{exp}$  is the peak-value of the distribution used to build the 2D histogram (first column of Fig. 4.8). From the experimental value of  $S$ , the contribution of the copper leads ( $1.8 \mu\text{VK}^{-1}$ ) was subtracted (see ESI)

indicate a LUMO based transport mechanism, which is in agreement with the theoretical findings. Additional exploratory calculations for different plausible metal-molecule binding scenarios indicate that the Fermi level positioning is influenced by sulfur pyramidalisation and the bonding to undercoordinated Au atoms (see ESI), both factors favouring a negative Seebeck coefficient. In general, rather small variations for the different OPE3 derivatives are observed. Experimentally, OPE3-Ph has the largest conductance and the largest (in absolute value) Seebeck coefficient. Since the transmission derivative is usually dominating over the transmission in the denominator of Eq.(4.3), this is consistent with a LUMO position of OPE3-Ph that is slightly closer to  $E_F$  than for OPE3-Ph(OMe)<sub>2</sub> or OPE3-An. The theoretical simulations do not reproduce these subtle differences for the investigated junction models and generally overestimate the Seebeck coefficients. To a certain extent this might be related to known difficulties of DFT and DFTB to accurately predict the transport gap and level alignment [246, 247]. In addition, it would be desirable to sample a larger space of metal-molecule geometries to approach the experimental conditions, but already at this stage, the theoretical simulations confirm the main transport mechanism and small variability in the thermopower. In this context, we mention a recent review that highlights challenges in theory and experiment as well as the currently achievable agreement between the two [248].

4

## 4.2.5 Conclusion

Understanding and mastering the interplay of charge and heat transport in single-molecule junctions is of crucial importance for the development of modern molecular electronics technologies. From this perspective we have synthesised three new OPE3 derivatives possessing DHBT anchoring groups and different core units, and measured their single-molecule conductance and Seebeck coefficient by STM-BJ experiments using a custom-built temperature sensitive setup. The lateral substituents on the central ring have a negligible effect on the transport properties. The Seebeck coefficient was found to vary between -7.9 and -11.4  $\mu\text{V K}^{-1}$  and the negative sign is consistent with charge transport through the LUMO levels of the molecules. Thermoelectric transport through OPE3-backbone can be maintained despite the introduction of anchor points for side-group chemistry, and shows values in good consensus with the ones reported in literature for different anchoring groups [154, 249]. The results obtained from detailed simulations based on density functional theory were in good agreement with the experimental data. Both experimental and theoretical results suggest that the sulfur atom of the DHBT anchoring group coordinates to the electrode gold atoms in a very particular fashion. We conclude that the sharp break-junction histograms obtained in STM-BJ experiments and the very specific transmission function calculated for these molecules originate from that binding specificity. The molecules presented here are ideal candidates for nanoscale thermal conductivity studies. In the future, new lateral substituents on the OPE3 backbone will be implemented to influence the electrical conductance, the Seebeck coefficient and/or the thermal conductivity, and to enhance the overall thermoelectric efficiency in molecular junctions. On the theoretical side, future improvements are expected by enhanced conformational sampling as well as a more accurate determination of the transport gap at the DFTB level [246, 250].

### 4.3 Complete thermoelectric characterization of OPE3-Anthracene

Given the proven ability of the system to measure the electrical, thermal and thermoelectric properties of a single molecule, we carried out a full thermoelectric characterization of a single oligo(phenyleneethynylene)derivative with 9,10-anthracenyl group as core substituent (OPE3-An). By combining the measured electrical conductance ( $G_{el}$ ), thermal conductance ( $G_{th}$ ) and the Seebeck coefficient (S), in fact, it is possible to obtain the experimental thermoelectric *figure-of-merit*, i.e.:

$$ZT = \frac{S^2 \cdot G_{el}}{G_{th}} \quad (4.4)$$

The figure of merit describes how a system is close to the theoretical maximum efficiency represented by a Carnot machine working between the same temperature difference. The optimum condition for maximum efficiency is indeed [251]:

$$\eta_{max} = \frac{T_H - T_C}{T_H} \cdot \frac{\sqrt{1 + ZT} - 1}{\sqrt{1 + ZT} + \frac{T_C}{T_H}} \quad (4.5)$$

where  $T_H$  and  $T_C$  are the hot- and cold-side temperatures, respectively. The thermoelectric conversion efficiency in 4.5 is the product of the Carnot efficiency ( $\frac{T_H - T_C}{T_H}$ ) and a reduction factor as a function of the material's figure of merit ZT, taken at  $T = T_{avg} = T_{amb} + \frac{\Delta T}{2}$ , where  $\Delta T = T_H - T_C$

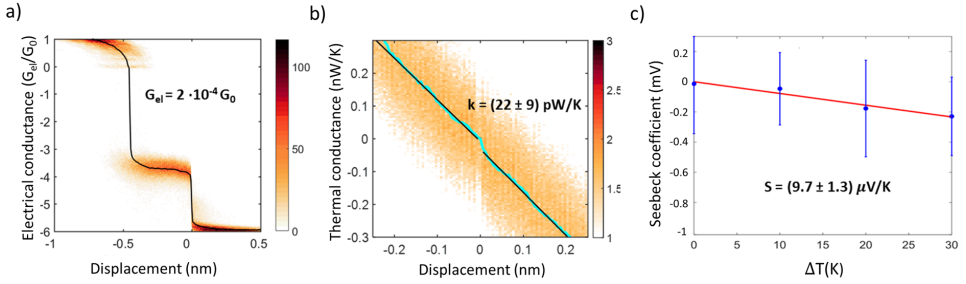


**Figure 4.12** Experimental thermoelectric value for a single OPE3-An obtained at room temperature. (a) Electrical conductance  $G_{el}$ . (b) Thermal conductance  $G_{th}$ , measured at room temperature with  $\Delta T = 20$  K. (c) Seebeck coefficient (also called thermopower).

Figure 4.12 shows, together with [252], the first ever complete measurement of the thermoelectric figure-of-merit for a single molecule. Break junction traces in the histograms have been aligned at the rupture point of the molecular plateau, in order to extract the thermal conductance of the single molecule as explained in Sec. 3.1.2.

Compared to [252] results here are obtained at room temperature. By feeding the measured experimental values into equation 4.5, we get:

$$ZT \simeq 1 \times 10^{-5} \quad (4.6)$$

that still falls short for what is actually needed to realize a viable molecular thermo-electric converter (compare [253, 254]). However, this result shows the capability of our method to characterize new chemically-engineered organic materials at the single molecule level, opening up the possibility for chemists to perform *data-driven* synthesis of new materials based on experimental evidence.

# 5 Machine learning tools for the analysis of single molecules

---

In this chapter, we present the use of new machine learning tools for the analysis of the thermoelectric properties of four selected molecules. The clustering algorithm employed in this study, was conceived by Dr. Mickael Perrin at EMPA, Dübendorf. Results have been obtained in collaboration with the MSc. student Elisa-Vidal Revel, from EPFL, during her master thesis project at IBM, under my supervision and of Dr. Bernd Gotsmann.

## 5.1 Clustering tool

### 5.1.1 Motivation

The 1D and 2D conductance histograms seen so far in chapters Ch. 3.6 and Ch. 4 are usually straightforward to interpret: a high conductance metallic contact, a tunnelling part and a molecular plateau. But this is not always the case. Depending on the kind of molecule, histograms can look like the ones in Fig. 5.1. In fact, some molecules are prone to stick together and form clusters of different conductance, they can move inside the junction adopting different configurations and leave solvent residues during their deposition. However, most of the times, a molecular footprint is hidden inside those *dirty* histograms. To just not throw away the entire dataset, traces containing apparent artefacts or with no molecular footprint are discarded from the dataset, which is then further analysed. The standard method to do this selection is, in our case, to embed in a MATLAB script filters that discard traces that don't show enough datapoints in a certain range of conductance where the molecular plateau is expected to be present (tunnelling traces), or without a clear breaking of the junction (dirty traces) or traces that show plateaus longer than at least 4x the length of the molecule (long traces). This will be referred as *standard method* for the rest of this chapter. Figure 5.2 shows, as an example, the histograms obtained after selecting only traces that contains enough points in the molecular range [ $1 \times 10^{-5}$ ,  $8 \times 10^{-4}$ ] $G_0$  and eliminating the ones that present excessive long plateaus ( $>4$  nm). Under those conditions, a clear molecular peak appears on the 1D histogram, together with a plateau on the 2D histogram (respectively figure 5.2 a) and b). However, this method, although effective, is not general and it needs an *a priori* knowledge of the molecular region. Additionally, different behaviours of the traces can be hidden inside a single peak/plateau, corresponding to different configurations of the molecule inside the junction. For these reasons, the implementation of a machine learning tool (*clustering method*) to analyse the conductance traces would be of great advantage: trace-selection would require less *a priori* knowledge and the tool will help

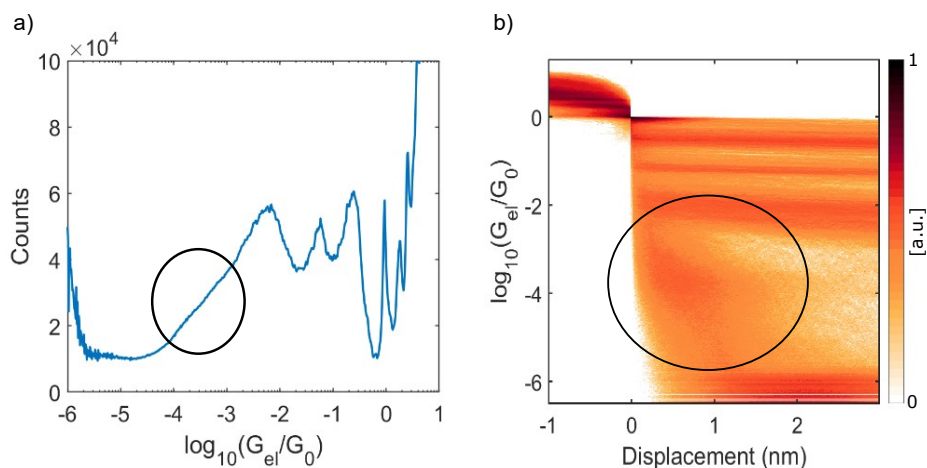


**Figure 5.1** Example of 1D and 2D histograms for the OPE3-dimer- $C_{10}$  obtained from an entire raw dataset with no trace selection. 1D histogram built from 10000 breaking traces a) and relative 2D histogram b). The black circles indicate the molecular footprint. Traces were recorded in vacuum, using two gold electrodes.

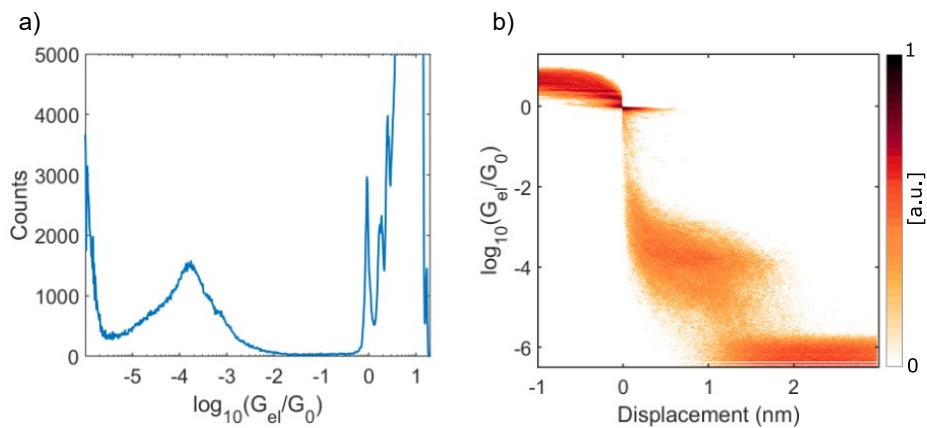


**Figure 5.2** Histograms built from Fig. 5.1 after eliminating spurious traces. a) 1D histograms built on 800 traces out of 10000. b) relative 2D histogram.

highlighting the different behaviours of molecular junctions. During this work, however, some previous knowledge about the value of conductance plateaus was still used. In fact, differently from the study this work is based on [255], we couldn't test different cross-validation indexes for assessing the suitability of the number of clusters used by the machine learning algorithm, but we flanked the Davies-Bouldin validation criterion, explained in the next section, by visual inspection and compared the results with the ones obtained through a our standard analysis method.

### 5.1.2 Clustering principles

Today, machine learning techniques and artificial intelligence are changing the way to process data and information coming from many different fields, from health care [256] to automotive [257], from pharmaceuticals [258] to information technology [259]. They can be used for several task including image and speech recognition, text understanding and autonomous driving [257, 260–265]. Their success is based on the ability to recognize patterns thanks to previous training/experience (supervised techniques) or without any prior knowledge of the system (unsupervised techniques). Clustering is part of the second category, i.e. a technique able to gather similar data together, without supervision and so effectively reducing issues linked to conformation bias. By clustering, it is possible to highlight features that usually are hidden among big datasets, which become apparent once only a sub-population is considered. The attribution of particular physical phenomena to the traces contained in a specific cluster, however, still requires a detailed understanding of the microscopic picture of the system under study.

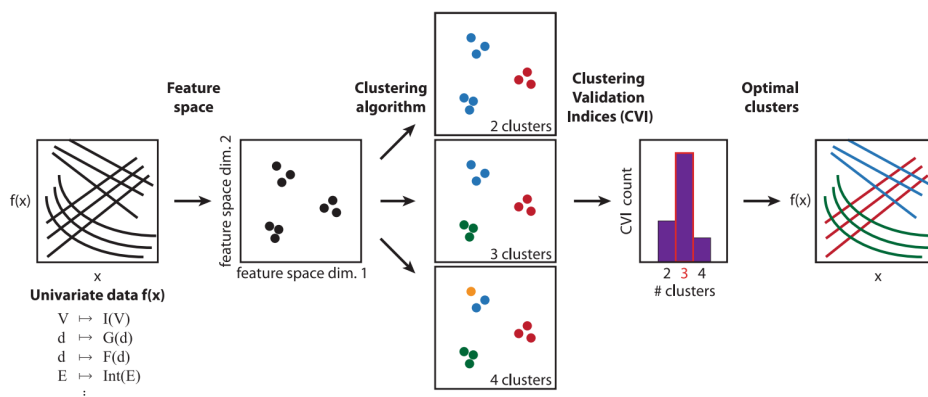


**Figure 5.3** Schematic representation of the working principle of the clustering technique developed by Dr. Mickael Perrin [266] to perform clustering on univariate data. Image from [255].

There are multiple ways to cluster data and a lot of different algorithms exist, based on different principles. Our study is based on the work of Dr. Mickael Perrin *Benchmark and application of unsupervised classification approaches for univariate data*, and on its clustering tool [255, 266]. A schematic representation of the working principle of Perrin's code is given in Fig. 5.3. Briefly, before applying the clustering algorithm, a feature

space is created starting from the raw data. Starting from a dataset consisting of  $N$  univariate and discrete measurement curves  $f_i(x)$ , with  $i \in [1, N]$ , each measurement is transformed into an  $M$ -dimensional feature vector  $f_i(x_m)$ ,  $m \in [1, M]$ , generating a feature space comprising  $M \times N$  data points. In case the feature space is too large, a dimensionality reduction technique is used to avoid the so called *curse of dimensionality* [267]. Then, the clustering algorithm is finally applied to the feature space for a different range of clusters. The most suitable number of clusters for the given algorithm is then selected by means of clustering validation indices, as explained in [255]. In this study, all the algorithms proposed by Dr. Perrin were tested on several real datasets, with the number of clusters ranging from 2 to 10, when the whole feature space was taken into consideration, and extended to 15 when the feature space was restricted to a region-of-interest (ROI) of  $G < 1 \times 10^{-3} G_0$ . The suitability of the number of clusters has been checked by visual inspection and by means of the MATLAB built-in Davies-Bouldin evaluation criterion. The criterion is based on an evaluation index called Davies-Bouldin index, whose minimization indicates the optimal number of natural partitions for a given datasets. The index does not depend on either the method used for the partition of the data, nor the number of clusters analysed, and thus it can be used to guide a cluster seeking algorithm [268]. An example is shown in Figure 5.4 for the analysis of the OPE3-tetramethyl molecule.

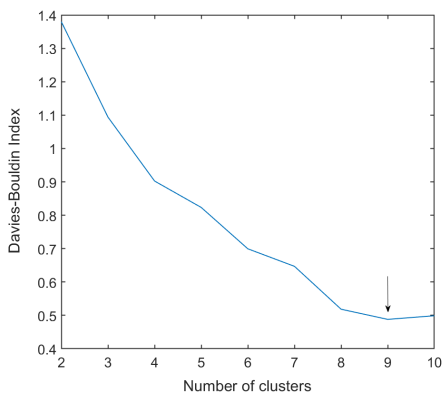


**Figure 5.4** Results of the Davies-Bouldin criterion applied to the feature space built with the  $28 \times 28 + T - SNE$  method to check the suitability of the number of clusters for the analysis of an OPE3-tetramethyl molecule with the clustering method developed by Perrin. The black arrow indicates the minimum of the Davies-Bouldin index, occurring for 9 clusters.

In order to have consistency throughout this work, the  $28 \times 28 + T - SNE$  feature space method, and the OPTICS algorithm for data clustering were selected among the best methods cited in [255]. For more details about all the other feature space methods, the different possible validation indices ( $\sim 30$ ) and the several clustering algorithms included in Perrin's code, please refer to the reference [255]. Here, a preliminary beta-version of the aforesaid code was used by Elisa Vidal-Revel during her Master thesis project, under

the supervision of Dr. Gotsmann and me, to perform the clustering analysis of some selected molecular data. A MATLAB GUI of the code is shown in figure 5.5, while results are discussed in the following section. We note that this work doesn't aim to validate and benchmark different algorithms for molecular data clustering, as in [255], but it wants to offer a two-folded perspective on previously measured conductance traces, where the typical standard method for data analysis is flanked by a clustering tool to possibly get new insights on the electrical and thermoelectric properties of some selected molecules.

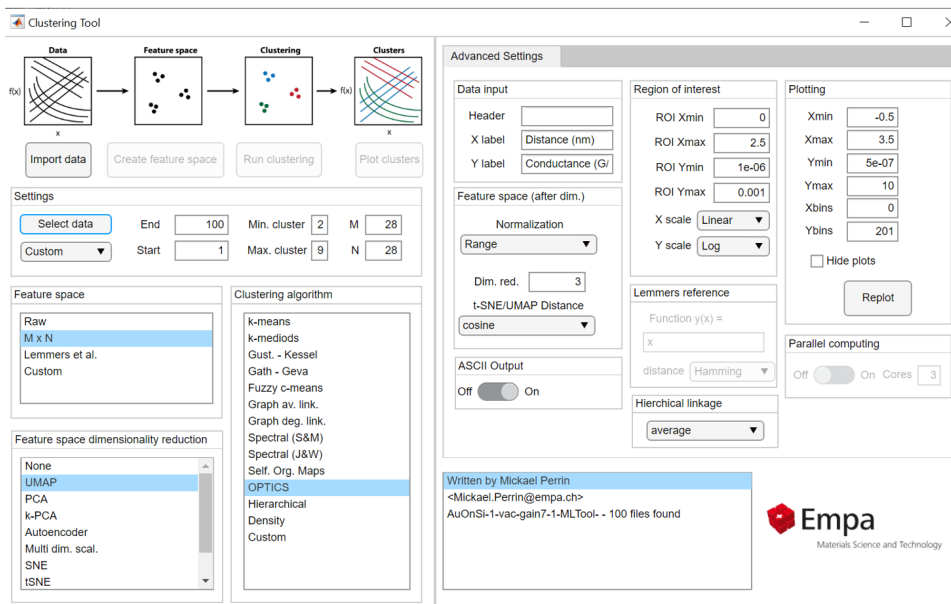


**Figure 5.5** Screenshot of the GUI developed by Dr. Mickael Perrin [255, 266] to perform clustering on univariate data

## 5.2 Results

Along this study, the electrical and thermoelectric properties of four different molecules, three derivatives of oligo-phenyleneethynylene (OPE3) and one based on the paracyclophane (pcp) compound, are investigated at the single molecule level. All the molecules possess interesting features from a technological point of view. The first three molecules are OPE3-derivatives, i.e. molecules derived from the same pristine OPE3, but featuring different side groups attached to the central molecular backbone as a strategy to both enhance cross-linkability and thermoelectric performance. The para-pcp3 molecule, instead, features a mechanosensitive  $\pi$ -stack at its core, that could allow for the decrease of phononic thermal transport along the molecule, hence increasing its thermoelectric performance. The results are analysed both with a MATLAB script (*standard method*)

and with the machine learning tools developed by Dr. Perrin (*clustering method*).

### 5.2.1 OPE3-tetramethyl

The first studied molecule is the OPE3-tetramethyl (OPE3-4Met), synthesized by Dr. Dekkiche in the group of Prof. Bryce at Durham University. Figure 5.6 shows the structural formula of the molecule.

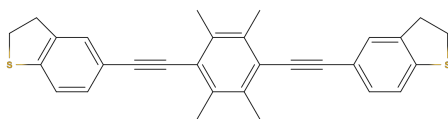


**Figure 5.6** Structural formula for the OPE3-Tetramethyl molecule with thiophene ending groups.

5

Compared to the standard OPE3, the OPE3-4Met presents four -methyl groups added to the central ring of the backbone.

**Sample preparation.** The sample was prepared as described in section 3.5, by immersing the device in a molecular solution with a concentration of 0.3 mM/L for 30 min, rinsed in the same solvent, for 1 min, to wash away eventual residues, and then blow-dried under nitrogen flow.

**Conductance measurement.** To compute the conductance of the OPE3-4Met, 10000 breaking traces were recorded using a constant bias of 90 mV over a 100 k $\Omega$  series resistor, and a gain of  $1 \times 10^7$  V/A. Figure 5.7 shows the results obtained with the standard approach. Out of 10000 traces, 800 were actually selected containing a molecular signature. Two different molecular conductance plateaus are visible. The first one is a plateau with high molecular conductance  $G_{high} = (1.3 \pm 0.8) \cdot 10^{-4} G_0$ , while the second one has a lower conductance of  $G_{low} = (3.5 \pm 2.5) \cdot 10^{-6} G_0$ .

The same dataset was further investigated with the clustering method. In Fig 5.8 it is possible to observe three different representative clusters obtained from the same measurement. The first cluster is shown in Fig 5.8a) containing a large amount of tunnelling traces (i.e. no molecular signature). The other clusters, not presented in 5.8, show also different variations of tunnelling traces but with a reduced statistics. In Fig 5.8b) instead, the low conductance plateau is presented, while c) displays the high conductance plateau. To analyse in a more quantitative way the level of the low conductance plateau, the 1D histogram is presented in Fig. 5.8d). The value obtained from the fitting curve is  $G_{low} = (4.4 \pm 2.8) \cdot 10^{-6} G_0$ , close to the one attained with the standard approach. In Fig. 5.8e) the 1D histogram of the high conductance cluster is shown. The peak value for the cluster is  $G_{high} = (1.3 \pm 0.5) \cdot 10^{-4} G_0$  same as the one from the standard approach, but with a slightly narrower distribution. Interestingly, this value corresponds, within the distribution limits, to the one of a standard OPE3 with the same anchoring group (see OPE3-Ph in table 4.1), suggesting that the methyl groups do not affect substantially the electrical properties of the molecule. The interpretation of

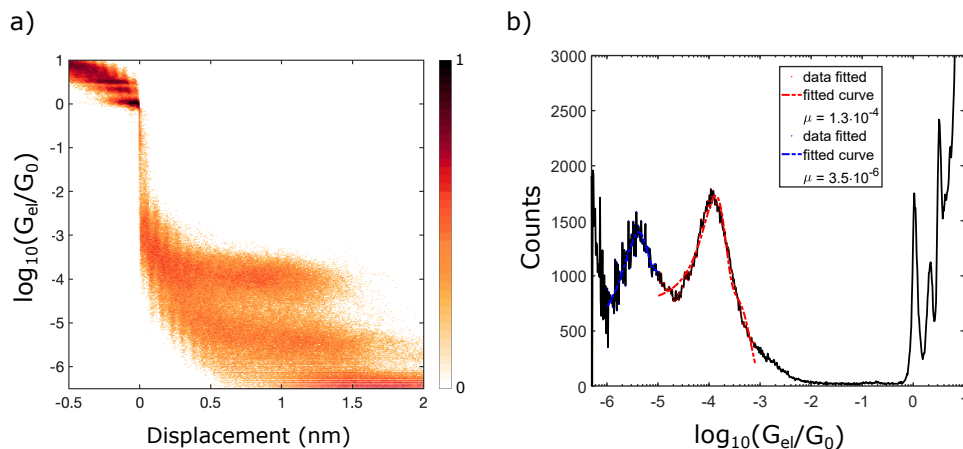


**Figure 5.7** Results obtained with the standard analysis method for the OPE3-4Met molecule. Both in the 2D histogram a) and in the 1D histogram b) two distinctive molecular signatures are present. Values for the scale bar in the 2D histogram were normalized to the maximum number of counts.

the low conductance plateau is less straightforward, given the proximity of the signal to the noise level ( $\sim 1 \times 10^{-6} G_0$ ). A first possible explanation is that the junction captures two or more molecules that are stuck together through the central  $\pi - \pi$  stacking. Tunnelling through such a stuck has a lower conductance compared to a single molecule. A second possibility could be that at least one of the two electrodes is not connected to the sulphur ending group, but rather to the central benzene ring. This forms a tunnelling barrier that has a larger resistance than through the gold-sulphur bond. In this case, if one of the electrode was attached to the central ring instead of the sulphur bond, the connection would be weaker and the link would break sooner. However, by looking at Fig. 5.8, it is possible to notice that the low conductance plateau is a bit longer than the high conductance plateau, endorsing the  $\pi - \pi$  stacking hypothesis.

**Seebeck measurement.** The Seebeck coefficient for the OPE3-4Met has been measured using a bias voltage of 90 mV over a 100 k $\Omega$  series resistor, and a gain of  $1 \times 10^7$  V/A. Following the same protocol as described in Sec. 3.1.4, the Seebeck voltage has been recorded for  $\Delta T = 0, 5, 15, 20$  K. For each measurement the median of the Seebeck voltage distribution is plotted versus the temperature difference, as shown in Fig. 5.9. The Seebeck coefficient is then extracted from the linear fit of the curve, and is equal to  $S_{fit} = -3.7 \pm 0.7 \mu\text{V/K}$ . As described in Sec. 3.1.4, a correction factor that takes into account the uncompensated thermoelectric voltage arising across the copper lead connecting the Au-tip must be subtracted from the the fit coefficient, leading to a value of  $S = -5.5 \pm 0.7 \mu\text{V/K}$ .

Each datapoint in Fig. 5.9 represents the mean of the Seebeck voltage distribution obtained at that temperature, unless otherwise stated. An example is shown in Fig. 5.10 for the OPE3-4Met at  $\Delta T = 20$  K.

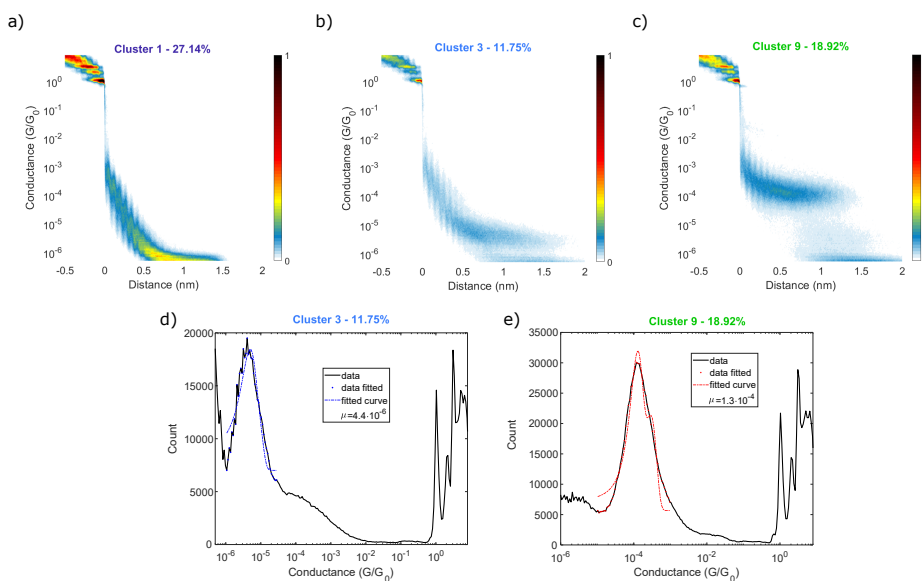


**Figure 5.8** Results obtained using the clustering tool (ML method) for the conductance of the OPE3-4Met molecule. a) 2D histogram of cluster 1 showing pure tunnelling traces. b) 2D histogram of cluster 3 showing the low conductance molecular plateau. c) 2D histogram of cluster 9 showing the high conductance plateau. d) 1D histogram of cluster 3 showing a peak at  $G_{low} = (4.4 \pm 2.8) \cdot 10^{-6} G_0$  and e) 1D histogram of cluster 9 showing a peak at  $G_{high} = (1.3 \pm 0.5) \cdot 10^{-4} G_0$ . Values for the scale bar in the 2D histogram were normalized to the maximum number of counts. Adapted from [269].

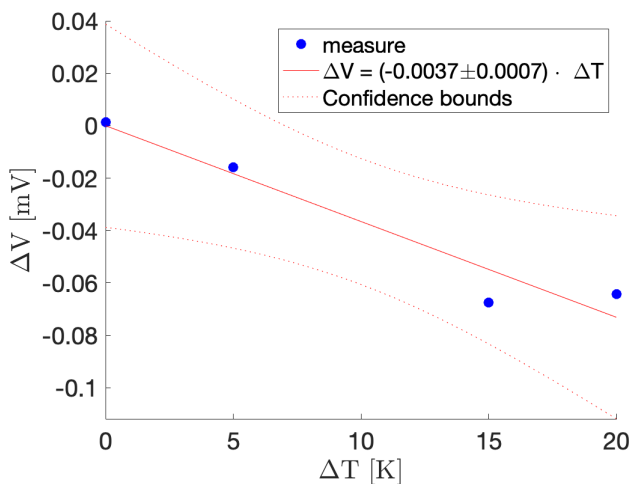


**Figure 5.9** Seebeck voltage versus temperature difference for four different applied temperatures for the OPE3-4Met molecule. The coefficient from the fit is  $S_{fit} = -3.7 \pm 0.7 \mu\text{V}/\text{K}$ .

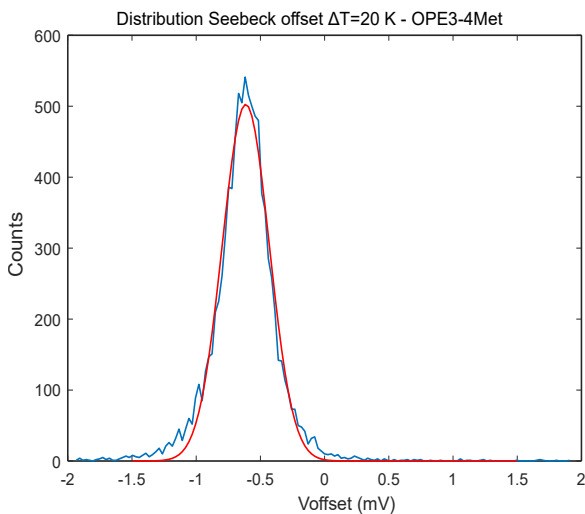


**Figure 5.10** Seebeck voltage distribution for the setpoint  $\Delta T = 20$  K, recorded over 4000 traces. The peak is at  $\Delta V_{secb} = (-0.62 \pm 0.26) \text{mV}$

The comparison between the Seebeck coefficient of the OPE3-4Met with the reference molecule OPE3-Ph ( $S = -11.4 \pm 0.5 \mu\text{V}/\text{K}$ , table 4.1) indicates that the addition of methyl groups decreases roughly by two the thermopower of the molecule.

### 5.2.2 OPE3-dimer- $C_1$ & OPE3-dimer- $C_{10}$

The second and third molecule under study are two OPE3-derived dimers: OPE3-dimer- $C_1$  and OPE3-dimer- $C_{10}$ . The first one, depicted in Fig. 5.11 a), has only one carbon atom connecting the two OPE3 branches, while the second one features ten carbon atoms in the linking chain, Fig. 5.11 b). The two dimers represent a first step towards the fabrication of engineered cross-linked molecular films, which constitute one of the strategies envisioned by the molecular electronics community to build functional molecular device (see Sec. 6.1 and [253]). The two molecules have been synthesized by

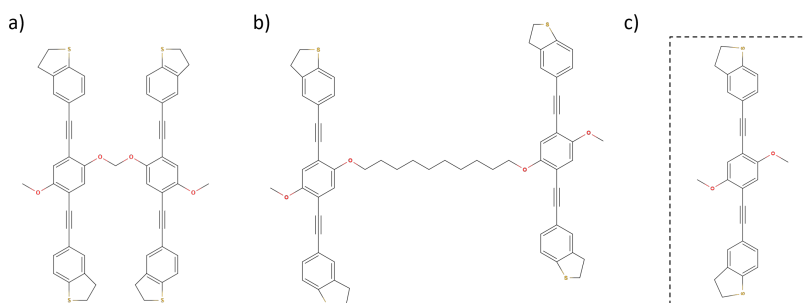


**Figure 5.11** a) OPE3-dimer- $C_1$  molecule featuring a single carbon atom linking the two molecular branches. b) OPE3-dimer- $C_{10}$  molecule possessing ten carbon atoms in the linking chain. c) Basic unit for the dimers: OPE3-dimethoxy molecule with thiophene ending groups and two methoxy groups attached to the central ring.

Dr. Herve Dekkiche and Prof. Martin Bryce, and posses the same thiophene ending groups as the OPE3-4Met. The different length in the connecting chains make the two dimers completely different from a mechanical point of view, with the dimer- $C_1$  being much stiffer thanks to the shorter distance between the two branches. Besides, each branch of the two dimers is not a standard OPE3, featuring two methoxy groups attached to the central benzene ring. For this reason, the reference molecule in this case will be the OPE3-dimethoxy (OPE3-Ph(OMe) $_2$ ) already described in Sec. 4.2 and visible in Fig. 5.11 c). Measurements of conductance and Seebeck coefficient for the OPE3-Ph(OMe) $_2$  are given in table 4.1.

**Sample preparation.** To study the properties of the OPE3-dimer- $C_1$  a solution with a concentration of 0.25 mM was prepared. Samples were immersed for 7 min in the molecular solution and then rinsed for 2 min in pure solvent. For the OPE3-dimer- $C_{10}$  instead, a solution with a concentration of 0.3 mM was used, with samples immersed for only 2.5 min and then rinsed for 45 sec in pure solvent and finally dried.

**OPE3-dimer-C<sub>1</sub>: conductance measurement.** In order to evaluate the conductance of the OPE3-dimer-C<sub>1</sub>, 10000 breaking traces were recorded using a constant bias of 90 mV over a 100 kΩ series resistor, and a gain of  $1 \times 10^7$  V/A. Results obtained with the standard method are shown in Fig. 5.12. The 2D histogram of Fig. 5.12 a) highlights a

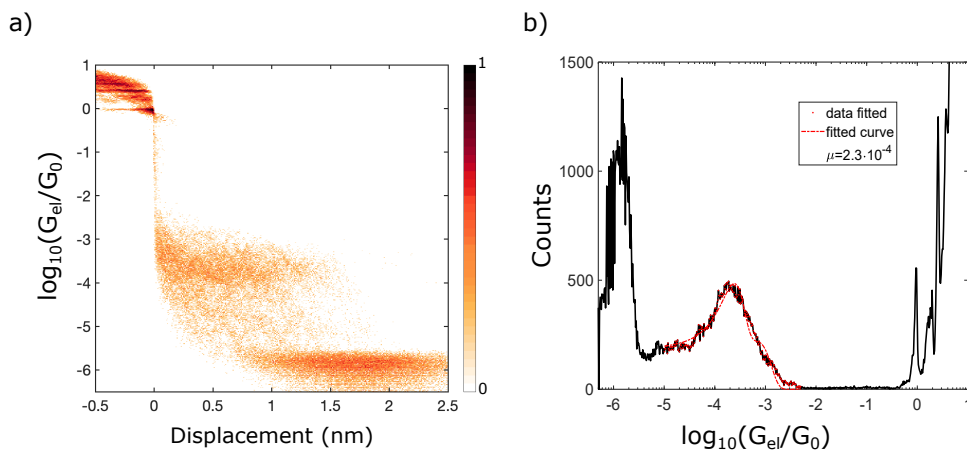


**Figure 5.12** Results obtained with the standard analysis method for the OPE3-dimer-C<sub>1</sub> molecule. Values for the scale bar in the 2D histogram were normalized to the maximum number of counts

molecular plateau between 1 and 1.5 nm, with a conductance of  $G = (2.3 \pm 1.5) \cdot 10^{-4} G_0$ .

By using the clustering GUI, we obtain, out of nine clusters, the 2D histogram in Fig 5.13. An additional behaviour, previously not visible in Fig. 5.12 emerges. Hidden among the other traces there is a plateau of  $\sim 0.5$  nm with a slope. The corresponding 1D histogram in Fig. 5.13b) points out a value for the conductance of this cluster of  $G = (1.9 \pm 1.2) \cdot 10^{-4} G_0$ .

The 2D histogram of Fig. 5.13 seems to contain different types of traces. To further investigate that, a region-of-interest (ROI) of  $G < 1 \times 10^{-3}$  was applied to the feature space and a larger number of clusters was created. Three selected new sub-clusters, out of fifteen, can be seen in Figure 5.14.

Cluster 4 (figure 5.14a)) features a short plateau ( $< 0.5$  nm) at  $1 \times 10^{-4} G_0$ , with a relative large slope and no clear breaking of the junction. The conductance reaches the noise level after 0.75 nm. The 1D histogram indicates a peak for the conductance at  $G = (1.7 \pm 1.3) \cdot 10^{-4} G_0$ . Cluster number 6, figure 5.14b), exhibits a similar behaviour but on a longer distance. The plateau extends for about 0.5 nm and then it falls into the noise level at 1 nm. From the 1D histogram, the conductance is equal to  $G = (1.9 \pm 0.9) \cdot 10^{-4} G_0$ . Finally, traces in cluster 7 (figure 5.14c)) show a more standard molecular plateau, with a clear break of the junction at  $\sim 1$  nm. The peak conductance, as visible in the 1D histogram of Fig. 5.14c), is  $G = (2.5 \pm 1.5) \cdot 10^{-4} G_0$ . The value is a bit larger than the one for the reference OPE3-Ph(OMe)<sub>2</sub>, but still in the uncertainty range.

The different conductance behaviours expressed by this molecule are not easy to

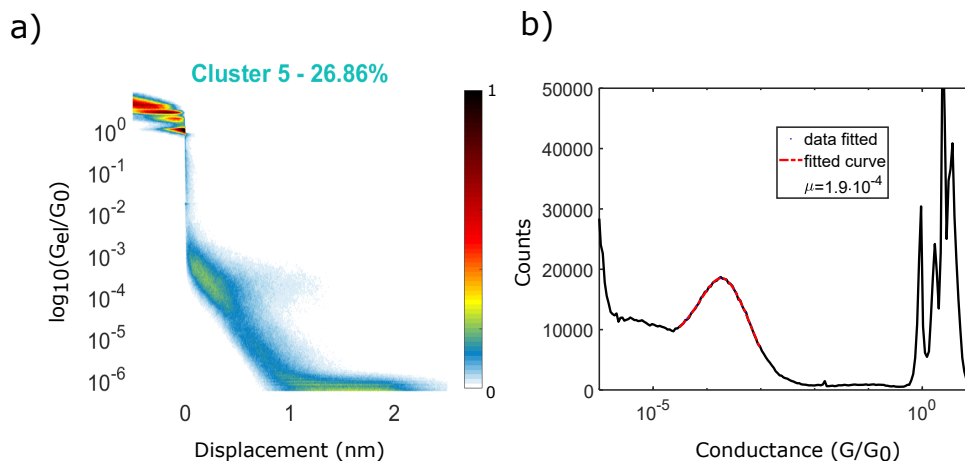


**Figure 5.13** Results for a selected cluster, out of nine, obtained using the clustering method for the OPE3-dimer- $C_1$  molecule. Values for the scale bar in the 2D histogram were normalized to the maximum number of counts. Adapted from [269].

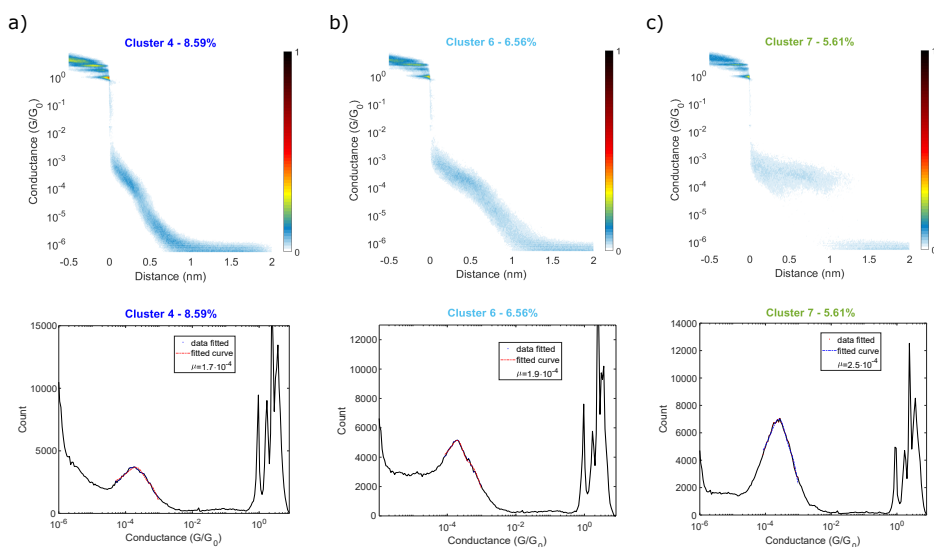


**Figure 5.14** Results obtained for the conductance of OPE3-dimer- $C_1$  using the clustering tool as in fig. 5.13, but restricting the feature space to a ROI  $G < 1 \times 10^{-3}$ . a) 2D and 1D histogram of cluster 4 featuring a short plateau with a slope in the conductance. b) 2D and 1D histogram of cluster 6 featuring a longer plateau and the same type of slope in the conductance. c) 2D and 1D histogram of cluster 7 showing a standard molecular plateau. Values for the scale bar in the 2D histogram were normalized to the maximum number of counts. Adapted from [269].

interpret, due to the large uncertainties and the many configurations the two branches can assume inside the junction. For example, due to the close distance between the two sides of the dimer, it would be easy to imagine a configuration where the two branches are contacted by the electrodes at the same time. This would translate into a conductance that is double the one of a single OPE3-Ph(OMe)<sub>2</sub>. This value has not been observed during any of the experiments, indicating that likely the two branches don't remain parallel inside the junction. A second imaginable configuration considers each of the electrode attaching singularly to a different branch of the dimer. It is difficult to predict the conductance for such a configuration, except that the value must be lower than the OPE3-Ph(OMe)<sub>2</sub>, due to the increased path length for the charges. Additionally, if this kind of connection occurs, pulling on different branches of the dimer can create instabilities inside the junction, that would explain the broadening of the conductance peak and the slope in the plateau.

**OPE3-dimer-C<sub>1</sub>: Seebeck measurement.** To measure the Seebeck coefficient of the OPE3-dimer-C<sub>1</sub>, a bias voltage of 9 mV over a 100 kΩ series resistor, and a gain of  $1 \times 10^8$  V/A has been used. The Seebeck voltage has been recorded at  $\Delta T = 0, 2, 10, 15, 20$  K. For each temperature two measurements of 4000 traces were performed. For the two measurements, the median of the corresponding distribution was extracted and averaged to get a single datapoint for each  $\Delta T$ . Results are plotted in Fig. 5.15.

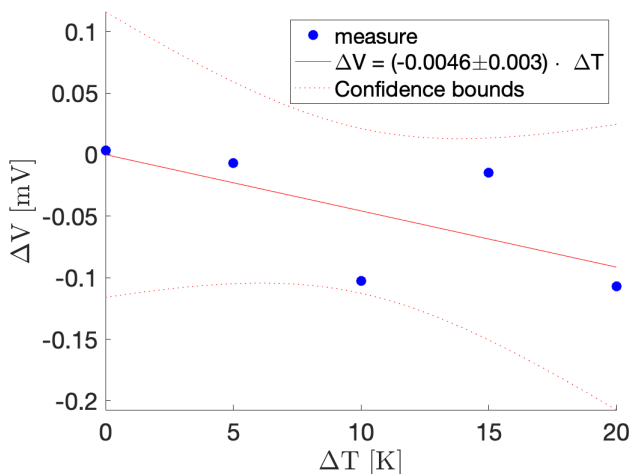


**Figure 5.15** Seebeck voltage versus temperature difference for four different applied temperatures. The coefficient from the fit is  $S_{fit} = -4.6 \pm 3.0 \mu\text{V}/\text{K}$ .

The Seebeck coefficient extracted from the fit is  $S_{fit} = -4.6 \pm 3.0 \mu\text{V}/\text{K}$ . As before, the correction factor for the copper lead has to be subtracted, giving a final Seebeck coefficient of  $S = -6.4 \pm 3.0 \mu\text{V}/\text{K}$ .

The dimerization of the molecule appears to affect negatively the thermoelectric performance, since the Seebeck coefficient for the OPE3-dimer-C<sub>1</sub> is lower than the one

of the reference molecule ( $S = -7.9 \pm 1.3 \mu\text{V/K}$ ). Also, by looking at Fig. 5.16, the Seebeck voltage as function of temperature difference does not follow exactly the linear trend, and this is visible in the large error in the calculation of the Seebeck coefficient. It is possible to speculate that the stiff, non-contacted, branch of the molecule dangling aside the one being measured might have a huge impact on the junction mechanics, yielding to a not univocal coefficient.

**OPE3-dimer- $C_{10}$ : conductance measurement.** In order to compute the conductance of the OPE3-dimer- $C_{10}$  molecule, 10000 break junction traces have been collected using a bias of 90 mV over a  $100 \text{ k}\Omega$  series resistor, and a gain of  $1 \times 10^7 \text{ V/A}$ . Results obtained with the standard method are plotted in Fig. 5.16.

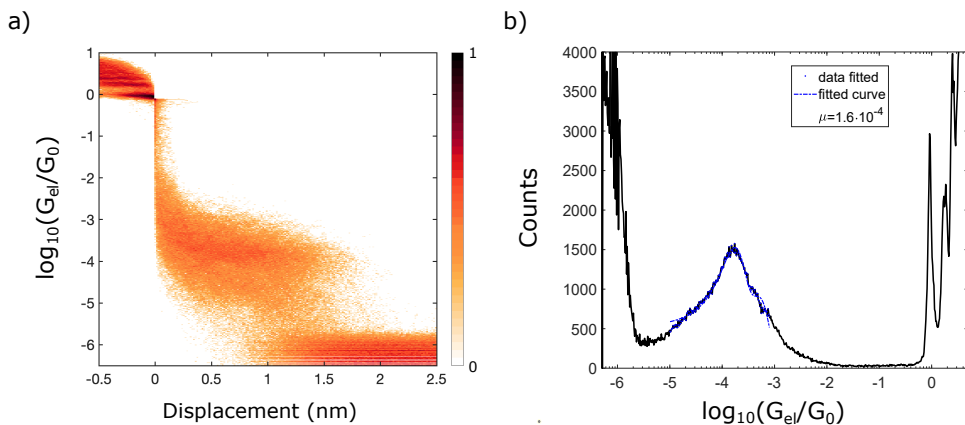


**Figure 5.16** Results obtained with the standard analysis method for the OPE3-dimer- $C_{10}$  molecule. Values for the scale bar in the 2D histogram were normalized to the maximum number of counts.

On the 2D histogram one can observe a wide molecular plateau around  $1 \times 10^{-4} G_0$  of about 1.5 nm. From the fit in the 1D histogram the conductance peak has a value of  $G = (1.6 \pm 1.2) \cdot 10^{-4} G_0$ . In figure 5.17, instead, the main cluster, out of four, obtained with the machine learning tool is shown.

The plateau in Fig. 5.17a) now seems to contain a lot of different kind of traces, with different length and slope. To extract more details about the different configurations inside the plateau, a region-of-interest (ROI) of  $G < 1 \times 10^{-3} G_0$  was selected and the number of clusters has been increased to 15. Three non-trivial selected clusters are shown in Figure 5.18.

Cluster 1 shows a clear molecular plateau with a length between 1.5 and 2 nm. The value for the plateau conductance is  $G = (2.1 \pm 1.1) \cdot 10^{-4} G_0$ . The longer molecular plateau compared to the one of the OPE3-dimer- $C_1$  suggests that the junction is more stable with this dimer. On the other hand, in Fig. 5.18b) the 2D histogram shows, similarly to the OPE3-dimer- $C_1$  molecule, a tilted plateau that reaches the noise level at 1.5 nm. The 1D histogram indicates a conductance of  $G = (1.1 \pm 1.0) \cdot 10^{-4} G_0$ . Finally, cluster 8 is observable in Fig. 5.18c). A 2D histogram featuring a tilted and

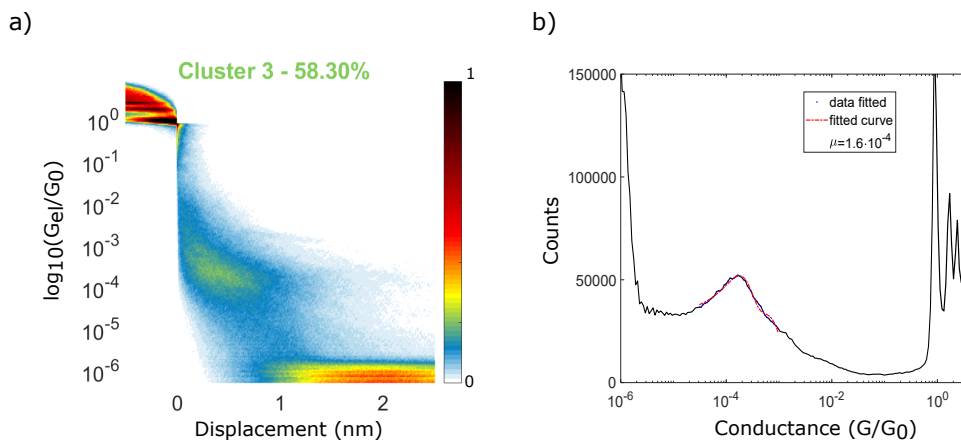


**Figure 5.17** Results for a selected cluster, out of four, obtained using the machine learning tool for the OPE3-dimer- $C_{10}$  molecule. Values for the scale bar in the 2D histogram were normalized to the maximum number of counts. Adapted from [269].

shorter plateau breaks between 1 and 1.5 nm. Superimposed to a flat plateau, there are some parasitic traces that the algorithm couldn't decouple. Those traces widen the peak in the 1D histogram, which has a peak value of  $G = (1.7 \pm 1.8) \cdot 10^{-4} G_0$ .

Similar to the case of the OPE3-dimer- $C_1$ , cluster 1, showing a clear and stable plateau, can be interpreted as related to a molecular configuration where one of the OPE3-branch is firmly trapped between the two electrodes. The length of the plateau indicates that the second OPE3-branch, now almost ten times further away compared to the case of the OPE3-dimer- $C_1$ , has a negligible influence on the stability of the junction.

**OPE3-dimer- $C_{10}$ : Seebeck measurement.** The coefficient for the OPE3-dimer- $C_{10}$  has been measured using a bias voltage of 9 mV over a 100 k $\Omega$  series resistor, and a gain of  $1 \times 10^8$  V/A. The Seebeck voltage has been recorded for  $\Delta T = 0, 10, 20, 30$  K. Two measurements of 5000 traces were collected for each temperature and then averaged to get a single value for each  $\Delta T$ . The Seebeck result for the  $C_{10}$ -dimer is plotted in Figure 5.19. The value of the coefficient extracted from the fit is equal to  $S_{fit} = -8.5 \pm 1.3 \mu\text{V/K}$ . When corrected for the uncompensated copper lead it gives  $S = -10.3 \pm 1.3 \mu\text{V/K}$ . This value is larger than the one of the  $C_1$ -dimer and the spread in the data is lower, suggesting once more the higher mechanical stability of the longer  $C_{10}$ -dimer.

### 5.2.3 para-*pcp3*

The last molecule in this study is the para- connected version of a paracyclophane compound, para-*pcp3*. The structural formula of the molecule can be observed in Figure 5.20.

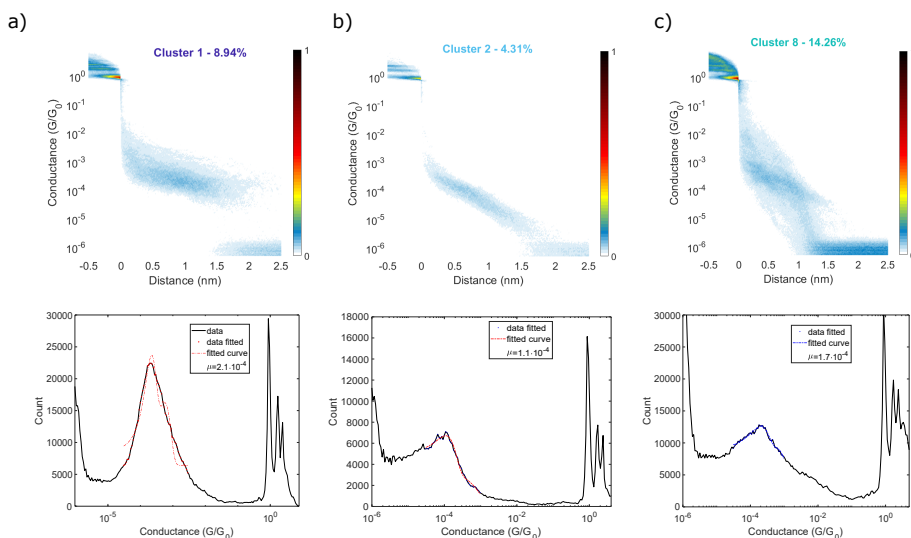


**Figure 5.18** Results obtained for the conductance of OPE3-dimer-C<sub>10</sub> using the clustering tool as in 5.17 but restricting the feature space to a ROI  $G < 1 \times 10^{-3}$ . a) 2D and 1D histogram of cluster 1 featuring a long plateau and a clear break of the junction. b) 2D and 1D histogram of cluster 2 featuring a long plateau and at the same time a slope in the conductance. c) 2D and 1D histogram of cluster 8 showing the superposition of a standard molecular plateau and some spurious traces. Adapted from [269].

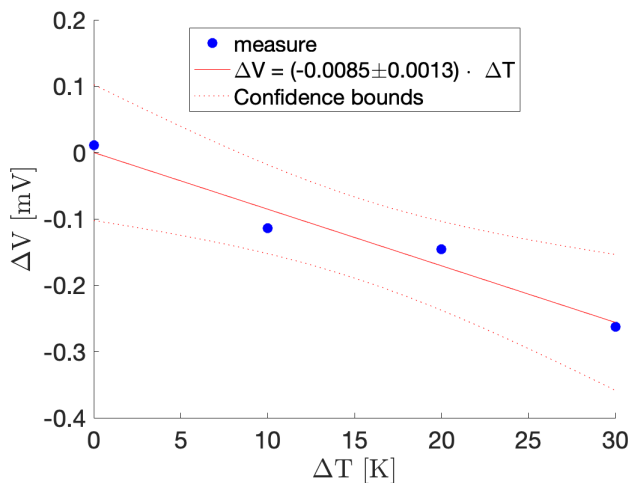


**Figure 5.19** Seebeck voltage versus temperature difference for the OPE3-dimer-C<sub>10</sub> molecule for four different applied temperatures. The coefficient from the fit is  $S_{fit} = -8.5 \pm 1.3 \mu\text{V}/\text{K}$ .

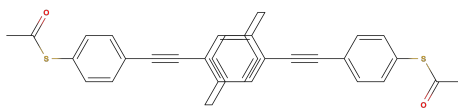


**Figure 5.20** Structural formula for the para-ppc3 molecule with a  $\pi$ -stack in the middle of the backbone.

The para-ppc3 consists of two branches featuring two benzene rings linked by a carbon triple bond. The two branches are connected by the  $\pi$ -stacking of the two central benzene rings. The molecule, synthesized by the group of Prof. Marcel Mayor in Basel, possesses acetyl-protected thiol ending groups. The  $\pi$ -stacking configuration is particularly interesting to study in vision of thermoelectric applications. Indeed, in order to fabricate efficient thermoelectric devices, it is necessary to maximize the  $ZT$  coefficient, also called *thermoelectric figure of merit*<sup>1</sup>:

$$ZT = \frac{S^2GT}{\kappa} \quad (5.1)$$

where  $S$  is the Seebeck coefficient,  $G$  is the electric conductance,  $T$  the absolute temperature, and  $\kappa = \kappa_e + \kappa_{ph}$  is the thermal conductance with both the contribution of electrons ( $\kappa_e$ ) and phonons ( $\kappa_{ph}$ ). One way to increase  $ZT$  is to lower the thermal conductance by reducing the phononic term  $\kappa_{ph}$ . A study of *Li et al.* has shown that, in various molecular junctions, the introduction of  $\pi$ -stacking bonds could result in a significant decrease of phonon transport [270].

A second interesting aspect of the para-ppc3 molecule is its mechanosensitivity. In fact, the strength of the  $\pi$ -stacking between the two stems of the molecule can be modulated by applying a force on it. For this reason, the molecule and its electrical properties have already been studied by Stefani *et al.* [271]. They measured a main conductance value for the molecular plateau of  $G = 3.7 \times 10^{-6} G_0$ . They also observed oscillations in the conductance when pulling and compressing the molecule back and forth between the two gold electrodes of a mechanical-controllable break junction (MCBJ) setup [271]. Their observations are reported in Fig. 5.21.

**Sample preparation.** Para-ppc3 samples were deposited from a solution with a concentration of 0.3 mM. Samples were immersed for 15 min in the molecular solution, for 1 min in the pure solvent, and then dried under the flow of a nitrogen gun.

**Conductance measurement.** In our study, to perform the conductance measurements on the para-ppc3 molecule, 2 amplifiers were used in a cascade-configuration: the first with a gain of  $1 \times 10^7$  V/A and the second with a gain of 10. The bias voltage was equal to 90 mV over a 100 k $\Omega$  series resistor. The measurement included over 20000 traces. Traces showing at least 50 points in the range  $[1 \times 10^{-6}, 8 \times 10^{-4}]$  were selected to form the histogram in Fig. 5.21. The 2D histogram (Fig. 5.21 a)) shows a high conductance

<sup>1</sup>Here with  $ZT$  we refer to the *material-ZT* (also called  $zT$ ). For more details about different definitions of  $ZT$  please refer to the footnote linked to equation 3.17 or [157].

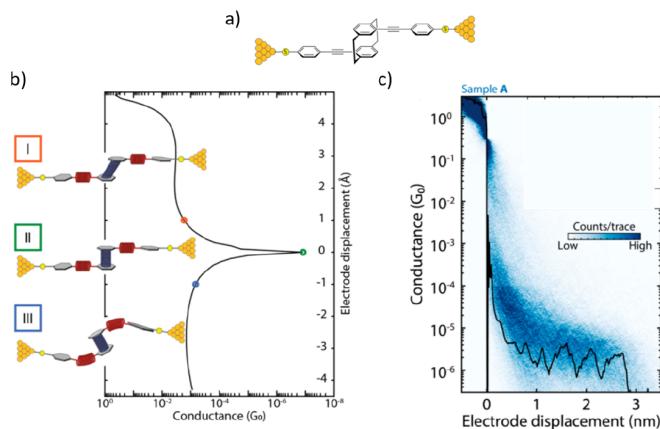


**Figure 5.21** a) Para-ppc3 molecule trapped between two gold electrodes. b) Predicted electrical response of the para-ppc3 molecule under applied tensile/compressive stress, obtained by DFT calculations. c) 2D histogram of the electrical conductance traces collected using the the MCBJ technique; a single trace is depicted in black. Figures adapted from [271].

plateau with few traces and a more crowded low conductance plateau. This behaviour is confirmed by the 1D histogram in Fig. 5.21 b), where it is possible to observe a smaller peak at  $G = (1.1 \pm 1.1) \cdot 10^{-4} G_0$  and a taller one at  $G = (4.7 \pm 2.7) \cdot 10^{-4} G_0$ . The low conductance peak is close to the one obtained by Stefani *et al.* ( $G = 3.7 \cdot 10^{-6} G_0$ ).

The same measurement was then further analysed using the clustering method. Results are shown in Figure 5.23. In Fig. 5.23 a), cluster 1 displays a tilted molecular plateau until  $\sim 0.5$  nm. The conductance drops quickly from above  $1 \times 10^{-3}$  down to the noise level ( $\sim 1 \times 10^{-6}$ ) at  $\sim 0.75$  nm. Those traces are not pure tunnelling traces, as highlighted by the 1D histogram showing a peak at  $G = (3.2 \pm 2.7) \cdot 10^{-4} G_0$ . In Fig. 5.23 b), cluster 3 shows a high conductance plateau of ca. 1 nm. The conductance value provided by the fit of the 1D histogram is  $G = (1.1 \pm 0.7) \cdot 10^{-4} G_0$ , same as without the clustering tool. Finally, in cluster 4 of Fig. 5.23 c) a low conductance plateau, in the range [0.5,1.25] nm is visible. The cut-off between the molecular footprint and the noise level is not very prominent in the 2D histogram, but a distinct peak in the 1D histogram gives a value of conductance of  $G = (4.1 \pm 1.7) \cdot 10^{-4} G_0$ , a bit smaller than the one obtained with the standard analysis method, but closer to the one reported by Stefani *et al.* [271].

**Seebeck measurement.** The Seebeck coefficient of the para-ppc3 was measured using the same cascade amplifiers configuration as for the conductance measurements. A 90 mV bias was applied to the junction with in series a 100 k $\Omega$  resistor. The Seebeck voltage was recorded at  $\Delta T = 0, 10, 20, 30$  K. Results are presented in Fig. 5.24. The Seebeck coefficient extracted from the fit is  $S_{fit} = -19.6 \pm 5.7 \mu\text{V/K}$ , that becomes  $S_{fit} = -21.4 \pm 5.7 \mu\text{V/K}$  by subtracting the correction factor for the copper lead. We

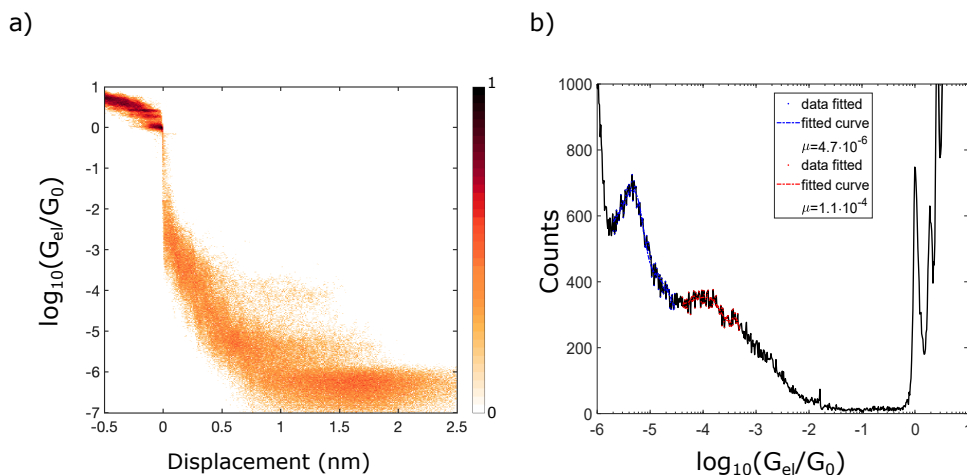


**Figure 5.22** a) 2D histogram for the measurement of para-ppc3 conductance traces using the standard method for the analysis. b) relative 1D histogram. Values for the scale bar in the 2D histogram were normalized to the maximum number of counts. Adapted from [269].

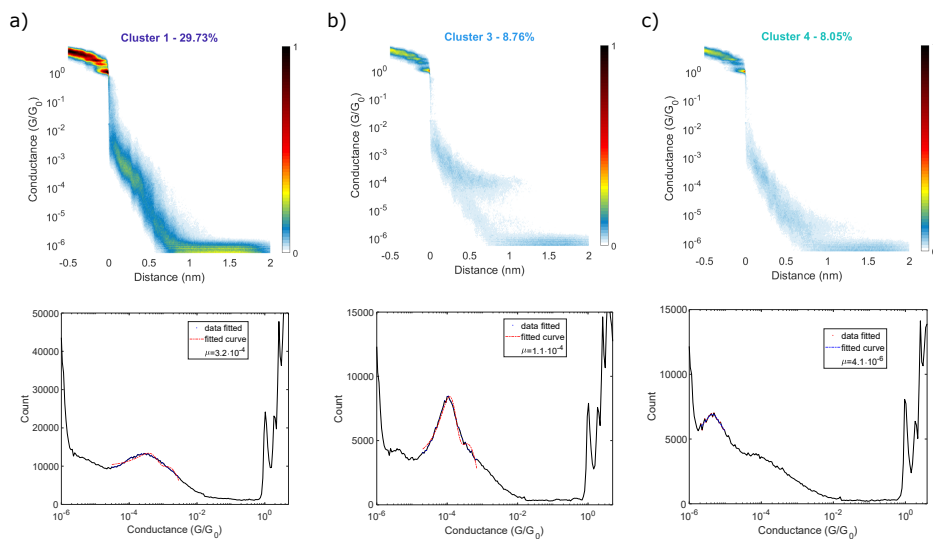


**Figure 5.23** Results obtained for the parapa-ppc3 molecule analysed with the clustering method. a) 2D and 1D histogram for cluster 1, featuring a high conductance plateau with a relative steep slope. b) 2D and 1D histogram for cluster 3, showing a high conductance plateau superimposed onto some left spurious traces. c) 2D and 1D histogram for cluster 4 showing the low conductance plateau. Values for the scale bar in the 2D histogram were normalized to the maximum number of counts. Adapted from [269].

note that the Seebeck coefficient for the para-pcp3 was only measured relatively to the high conductance plateau. Due to the close proximity of the noise level to the low conductance molecular plateau, in fact, it proved impossible to carry out reliable measurements for the Seebeck coefficient on the low conductance configuration.

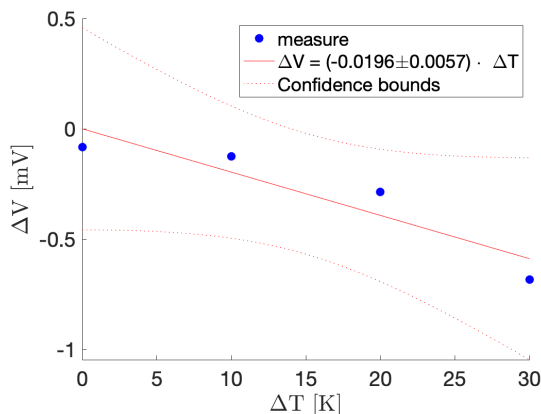


**Figure 5.24** Seebeck voltage versus temperature difference for four different applied temperatures for the para-pcp3 molecule. The coefficient from the fit is  $S_{fit} = -19.6 \pm 5.7 \mu\text{V}/\text{K}$ .

**Mechanosensitivity.** As in the work of Stefani *et al.*, also in this study conductance oscillations were observed. Two single traces for the para-pcp3 molecule can be seen in Fig. 5.25. In figure 5.25 a) the low conductance plateau is highlighted in green and, as for Stefani *et al.*, it features large oscillations in the electrical conductance of more than one order of magnitude. A slightly different behaviour is instead observed in figure 5.25 b). This trace shows first a high conductance plateau, followed by a low conductance plateau (highlighted in green) before reaching the noise level. The oscillations in the second plateau are similar in amplitude and periodicity to the ones present in Fig. 5.25 a), but interestingly the high conductance plateau observed in this trace doesn't display any oscillation. This corroborates the hypothesis that the high conductance plateau doesn't involve the  $\pi$ -stacking connection inside the molecule, and thus does not show any mechanosensitive behaviour.

## 5.2.4 Conclusions & Outlook

The results obtained in this study are summarized in the table 5.1.

All the molecules in this study show a conductance value that is close to the one of the molecule of origin, suggesting that the addition of side groups to the central electrical backbone doesn't affect largely the electrical properties of the molecules, for which the electrical conductance stays in the range around  $G = (1 - 2) \cdot 10^{-4} G_0$ .

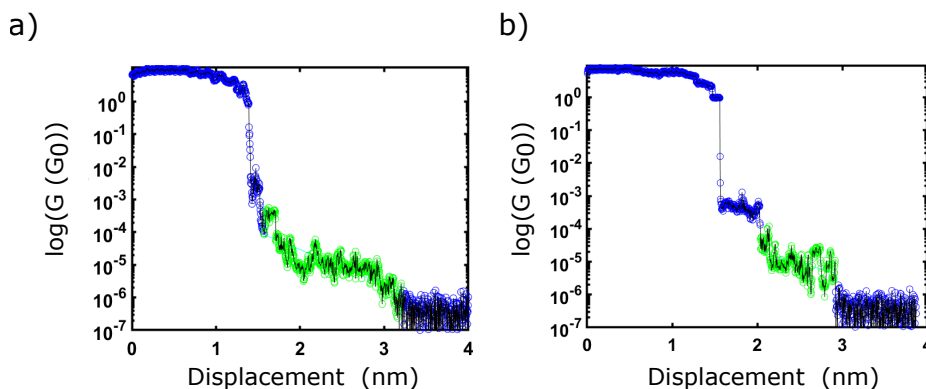


**Figure 5.25** Conductance vs. displacement traces for the para-ppc3 molecule. a) Single break junction trace showing oscillations (green) in the electrical conductance. b) Single break junction trace showing a high conductance plateau, and a lower molecular footprint with oscillation in the electrical conductance (green).

5

Furthermore, the study of the two dimers provides interesting insights in the mechanical stability of two closely coupled OPE3 molecules. As the results from the OPE3-dimer- $C_1$  suggests, a too short link between the two branches might create instability inside the junction, leading to precarious molecular configurations, whose electrical conductance depends on the electrodes separation (molecular plateaus with a slope). For those kind of configurations the thermoelectric properties are also not well defined (see OPE3-dimer- $C_1$ ). This issue is mitigated when a longer link is present between the two stems of a dimer, like in the case of the OPE3-dimer- $C_{10}$ . We the dimer- $C_{10}$ , in fact, we observed more stable junctions, with a higher yield of formation, that reflects on smaller variations in the Seebeck data. Those information are fundamental from a technological point of view, since dimers represent one of the strategies, currently under study, to form stable molecular carpets in vision of commercial molecular devices [253].

From a thermoelectric point of view is also interesting to notice that all the molecules featuring side-groups attached to the central backbone show, in general, a lower Seebeck coefficient compared to the straight OPE3 with the same anchoring group (compare OPE3-Ph and OPE3-An in Table 4.1). This will provide useful indication to chemists for the design and synthesis of new, improved molecules for thermoelectric applications.

Another useful outcome of this study is also the measurement of the Seebeck coefficient for the para-ppc3 molecule. Indeed, this molecule possess the highest Seebeck coefficient among all the molecules in this study, with its coefficient being at least double compared to the one of the OPE3-derivatives. The relative high Seebeck value, together with the hope for a reduced phononic thermal conductance provided by the internal  $\pi$ -stacking bond, puts this molecule on the list of good prospects for molecular thermoelectricity, and definitely makes it one of the most fascinating candidate for thermal conductance measurements at the single molecule level.

Molecule	$G_{classic}$ ( $G_0$ )	$G_{cluster}$ ( $G_0$ )	$S$ ( $\mu\text{VK}^{-1}$ )
<b>OPE3-4Met</b>	$(1.3 \pm 0.8) \cdot 10^{-4}$	$(1.3 \pm 0.5) \cdot 10^{-4}$	$-5.5 \pm 0.7$
	$(3.5 \pm 2.5) \cdot 10^{-6}$	$(4.4 \pm 2.8) \cdot 10^{-6}$	
<b>OPE3-dimer-C<sub>1</sub></b>	$(2.3 \pm 1.5) \cdot 10^{-4}$	$(1.9 \pm 1.2) \cdot 10^{-4}$	$-6.4 \pm 3.0$
		$(2.5 \pm 1.5) \cdot 10^{-4}$	
<b>OPE3-dimer-C<sub>10</sub></b>	$(1.6 \pm 1.2) \cdot 10^{-4}$	$(1.6 \pm 1.5) \cdot 10^{-4}$	$-10.3 \pm 1.3$
		$(2.1 \pm 1.1) \cdot 10^{-4}$	
<b>Para-pcp3</b>	$(1.1 \pm 1.1) \cdot 10^{-4}$	$(1.1 \pm 0.7) \cdot 10^{-4}$	$-21.4 \pm 5.7$
		$(3.2 \pm 2.7) \cdot 10^{-4}$	
	$(4.7 \pm 2.7) \cdot 10^{-6}$	$(4.1 \pm 1.7) \cdot 10^{-6}$	

**Table 5.1** Table summarizing the experimental results obtained in this study.  $G_{classic}$  is the conductance calculated with the standard analysis method,  $G_{cluster}$  the one obtained through the clustering algorithm and  $S$  the Seebeck coefficient. Distinct molecular plateaus are separated by a larger vertical space.

# 6 Towards applications

---

## 6.1 A roadmap for molecular thermoelectricity<sup>1</sup>

This chapter has been reviewed and submitted for publication in June 2021 to Nature Nanotechnology, and will be in press for the issue of October 2021. The text, figures and references have been re-formatted in the style of this thesis.

### A roadmap for molecular thermoelectricity

Andrea Gemma and Bernd Gotsmann  
IBM Research Europe – Zurich

#### 6.1.1 Abstract

Molecules have the potential to act as sharp energy filters for electrical currents and could thereby outperform other materials considered for thermoelectric energy conversion. Based on this vision, a considerable amount of research is being performed worldwide. However, there is a large discrepancy between predictions and actual demonstrations in the literature, and a research roadmap is needed to highlight necessary steps to transition from fundamental research into a viable technology. Considering both scientific and technological challenges, we propose eight milestones on the way yet to go for technological applications. The multi-disciplinary knowledge, generated while addressing the technological challenges, can yield to novel applications and answer unresolved fundamental science questions, which are of interest far beyond mere energy conversion.

---

<sup>1</sup>This document reflects the opinion of the authors and not necessarily the opinion of the IBM corporation, the EU commission or the QuIET and EFINEE consortium members.

## 6.1.2 Introduction

A molecular junction is a device, in which one or several molecules are contacted individually by conducting electrodes. Typically, one employs small organic molecules with delocalized  $\pi$ -electron system along the molecular backbone, into which and out of which charge carriers tunnel to and from metallic electrodes. The electrodes also act as thermal reservoirs, see Fig.6.1.

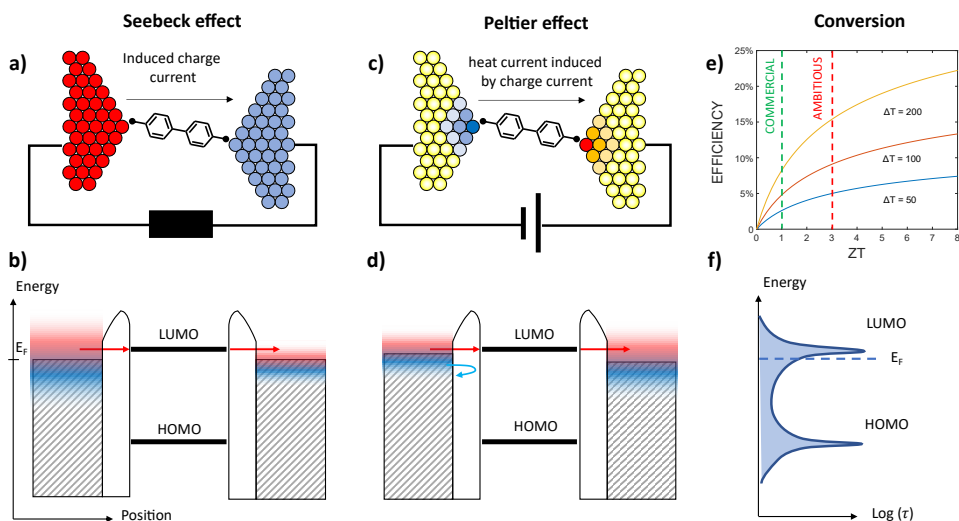


**Figure 6.1** (a) Schematic of a molecular junction acting as energy harvester using the Seebeck effect. A temperature difference applied to the junction results in a charge current through a temperature-dependent Fermi energy (or chemical potential). (b) The reason for a high efficiency is the occurrence of the sharp energy levels in molecular junctions denoted here as HOMO and LUMO. (c) In cooling circuit using the Peltier effect an applied charge current induces a heat current between the electrodes. (d) Again, the sharp molecular energy levels lead to a highly efficient process due to energy filtering. In this example only the hot electrons can pass the junction (through LUMO) while cold electrons are reflected. (e) Efficiency vs. temperature difference for different figure of merit ( $ZT$ ). (f) The energy band diagram for the transmission coefficient as a function of energy, exhibit sharp, energy-filtering capabilities. The challenge is to place the energy level at a steep part of the Energy-transmission diagram.

After the first claimed single-molecule transport measurements in the 1990s [272], the field rapidly grew, focusing initially on logic applications [273, 274]. Today, molecules are only rarely mentioned any more as replacement technology for highly-scaled semiconductor electronics. New research directions have emerged to study both the fundamental physics characterizing them, especially for transport phenomena, and possible commercial applications, among which energy conversion appears to be particularly popular. The energy filtering properties of molecular energy levels motivate their use in thermoelectric energy conversion, as shown and explained in Fig.6.1.

### The Molecular expectation for thermoelectricity

Several recent and ongoing research projects receiving significant government funding are based on the notion that molecular junctions are potentially good energy converters with high thermoelectric conversion efficiency near equilibrium, as expressed using the figure of merit  $ZT = G \cdot S^2 \cdot T/k$ , through thermal conductance  $k$ , electrical conductance  $G$  and Seebeck coefficient  $S$ . A value of  $ZT \sim 1$  can be achieved with solid materials such as  $\text{BiTe}_x$ ,  $\text{SnSe}$  or Heusler alloys, at room temperature, but the energy conversion efficiency stays well below 20% even at large temperature differences. The highest up-to-date laboratory reported values are around  $ZT = 3$  [275], with  $ZT=2.5$  for optimized  $\text{Bi}_2\text{Te}_3$  nanowires [276], a predicted  $ZT=4.6$  for “star-like” nanotubes of  $\text{SnSe}$  [277] and  $ZT=4.8$  for the carbon allotrope Graphdiyne [278]. However, most of the materials showing the highest  $ZT$  values are measured at high temperatures ( $>500$  K), and they are often doped with expensive metals or toxic elements. The ambition is that molecular junctions can reach similar or higher values of  $ZT$ , for novel and more efficient thermoelectric devices. Experimental demonstrations of thermoelectric efficiency of molecular junctions are typically difficult to achieve, because of the challenges in measuring their thermal properties. So far, the only demonstration of  $ZT \sim 0.7$  required 2 K absolute temperature and the external gating of a planar configuration [252]. Therefore, it is fair to wonder where this expectation comes from, and what it would take to turn it into reality. This commentary seeks, in the first part, to shed light on the necessary milestones to possibly push molecules out from research labs and turn them into a viable technology. In the second part, potential use and viability in some popular areas of application are discussed. For exhaustive information on the materials and methods, we refer to exhaustive reviews of molecular systems [211] and other candidate materials including composites and polymers [275]. Furthermore, we stress that the basic research involved, even if not successful in producing a viable technology has been giving and will continue to give us insight into understanding and even controlling molecular systems in unprecedented manner.

#### 6.1.3 The Roadmap: 8 technological milestones

**M1. Competitive cooling power:** demonstrate a molecular junction with a power factor of  $GS^2 > 1 \times 10^{-14}$  W/K<sup>2</sup>.

Both Seebeck coefficient and electrical conductance play a role in thermoelectric applications in an interrelated manner. Therefore, it is useful to consider the power factor  $GS^2$ . In cooling applications where the maximum power is more important than efficiency, the power factor is an equally relevant quantity to  $ZT$  [279, 280]. Our first Milestone is set by the competition, the technological reference material Bismuth Telluride. Milestone 1, reaching  $1 \times 10^{-13}$  W/K<sup>2</sup>, translates, for example, to a molecular junction with a Seebeck coefficient of  $360 \mu\text{V/K}$  at low bias and an electrical conductance of  $1 \times 10^{-3} G_0$ . Best reported power factors in junctions are  $\sim 3 \times 10^{-15}$  W/K<sup>2</sup> for C60 molecules [211]. To compare with  $\text{BiTe}_x$  bulk materials, which have a power factor  $\sigma S^2 \sim 30$  mW/(K<sup>2</sup>m) [281] a molecule would have to reach  $GS^2 = 6 \times 10^{-13}$  W/K<sup>2</sup> for a molecular length of 3 nm and an area of  $5 \times 10^{-19}$  m<sup>2</sup>. Milestone 1, although ambitious in combining

high  $S$  and high  $G$ , does not yet compete with existing technology for cooling power, but would place molecules on the map.

**M2. Minimized intrinsic thermal losses:** achieve phonon thermal conductance below 10 pW/K with electrical conductance of at least  $1 \times 10^{-3} G_0$ .

In molecular systems the thermal conductance  $K$  is typically dominated by phonons as heat carriers. For a single molecule,  $K$ , is typically on the order of a few 10s of pW/K [186, 282], the electrical thermal conductance, in contrast, is expected to contribute sub-pW/K. This is rather problematic in view of reaching a high  $ZT$ , especially when comparing to good bulk thermoelectric materials in which the phonon thermal conduction can be avoided or reduced. There are several strategies to reduce thermal conductivity in molecular junctions to reach Milestone M2. First, the molecule may comprise side-groups that are electrically inactive but reducing phonon conduction [43, 123]. In fact, the interaction of those side chains with the molecule, generates Fano-like resonances in the phononic spectrum, reducing the number of modes available for transport. Secondly, intra-molecular interference effects may be exploited [119, 121]. Variations of the position of substituents might induce destructive interference effects and decrease the thermal conductance compared to the unaltered molecules. Thirdly, a variation of vibration frequencies along the molecular backbone may be achieved for lower phonon transmission [125]. Similar to guitar strings, where waves with specific frequencies are suppressed by pressing the string, modifying the mass of substituents can suppress phonons with certain frequencies. The needed control over thermal phonon transport along molecules would also be welcome in other domains, such as quantum sensing and thermal management.

**M3. Competitive efficiency:** experimentally demonstrate a figure of merit  $ZT > 3$ .

Milestones 1 and 2 combined would correspond to a  $ZT$  of 0.3 at ambient temperatures, which would be encouraging although still falling short of the state of the art. To estimate an attainable  $ZT$  value for a material class, it is dangerous to combine individual best values for  $S$ ,  $G$  and  $K$ . Indeed, not only  $G$  and  $S$  are highly interdependent, also  $K$  and  $S$  are. Maybe due to the lack of experiments and predictions of  $K$ , it has become a custom in the molecular electronics community literature to report an “electronic  $ZT$ ”, or  $ZT_e$ . For  $ZT_e$ , only the thermal conductance through charge carriers is considered and the phonon contribution neglected. In this way very large efficiencies can be implied. Furthermore, the validity of the Wiedemann Franz relationship is often assumed, which may not be valid in all molecular junctions, even if phonon transport would be neglected. In this context it is interesting to note that assuming the Wiedemann Franz law ( $K = L_0 \cdot T \cdot G$ ), the efficiency only depends on the Seebeck coefficient,  $ZT = S^2/L_0$ , which would reach 0.4 for  $S = 100 \mu\text{V/K}$ . Here  $L_0$  is the Sommerfeld value. It is safe to conclude, that there is still a huge discrepancy between predictions for molecular efficiency and what has been demonstrated. However, in order for a molecular prototype to enter the industrial market, a demonstration is required of at least on the order of 10% energy conversion efficiency for waste heat, which translates to  $ZT > 3$  (M3).

**M4. Arrays and defects:** measure charge and thermoelectric transport across arrays of molecular junctions, maintaining or improving thermoelectric properties of single molecule junctions.

An application based on a single molecule is currently not realistic. However, a device using an ensemble of molecular junctions in an array to allow integration into solid-state electronics is clearly envisioned, using molecular monolayer films. From regarding single molecule junctions, however, it is not obvious that films of molecular junctions will maintain the advantageous properties of single-molecule junctions. The conformational and vibrational freedom of molecules can be influenced by neighbours and various film defects [134], that could take influence on both phonon and charge transport [207]. These correlation effects are scientifically highly interesting and are already under study in the scientific community, with research groups trying for example to add side groups to the molecular backbone as anchor points to promote ordered crosslinking without altering the thermoelectric properties and preserve quantum features [249].

**M5. Thermal radiation:** quantify the role of radiative thermal transport in the presence of organic molecules for nanometric electrode gaps.

Currently, thermal radiation in the so-called extreme near-field across gaps of only few nanometers is highly debated in the community [193, 194]. Experimental data suggests that the presence of molecular systems may have significant influence and could reach similar orders of magnitude as the phonon conduction across the molecules ( $\sim$ nW/K for a sharp tip a few nanometers far from a surface)[193]. Fundamental studies are required to address this (M5), so that we can consider engineering the near field through patterning or layering electrodes. This may open doors to other technologies, such as solar energy conversion, electronic device integration, or radiation sensors [283, 284].

**M6. Contacts to molecular junctions:** engineer electrodes for thin film / monolayer.

In quest for improved efficiency, it is worth mentioning the already existing efforts on replacing the rather resistive coupling of the molecules via the gold-thiol bond. Quite interesting appears to be the use of graphene electrodes with pi-stacked anchor groups [285]. The planar geometry requiring a carrying substrate, however, is not suited for harvesting applications and limits cooling application scenarios. The research on these and other alternative anchor groups [9], as well as contact geometries, can be leveraged to reach milestone M6 and solve the thin film issue (M8, see below).

**M7. Endurance:** determine and predict the endurance and cyclability in view of a 10-year operation.

The next step after a successful thermoelectric demonstration of power factor or ZT in a molecular film will be to measure and understand endurance issues. A film will need to be temperature-cycled many times during an anticipated ten-year lifetime. Numerous methods for predictive testing of materials for life-time analysis are ready to be applied to molecular junctions [286, 287]. Typically, at the stage of evaluating device endurance,

physicists and chemists pass the ball on to engineers and materials scientists to solve these “remaining details”. This creates a gap and ignores the fact that the endurance mechanisms often reach deep into the fundamental sciences and needs to be addressed using basic science methods (M7). For example, accelerated testing may require operation at elevated temperature or increased current, which, in turn, pose interesting fundamental questions.

**M8. Contact resistance in molecular monolayers:** demonstrate basic concepts of thermal impedance matching of molecular systems.

Having discussed the development of functional prototypes above, we now turn to engineering aspects of molecular films. The most pressing issue foreseen by the authors is related to the augmented influence that contact resistances have for molecularly thin layers. Even if bulk materials are used, roughly half of the efficiency given by ZT is lost in the functional thermoelectric converters due electrical and thermal impedance matching issues. First, for electrical impedance matching, one uses a series of miniature Seebeck (or Peltier) elements operated electrically in series and thermally in parallel. Both p- and n-type materials are used, requiring a certain complexity of contacts and wiring. Secondly, the thermal contacts between active materials and the thermal reservoirs induce a temperature drop across the contacts, which is lost to energy conversion. The thinner the thermoelectric layer, the more relative weight is carried by series thermal resistances. We can obtain a rough estimation of the effect considering a typical thermal conductance of 30 pW/K per molecule. This would translate to  $\sim 1 \times 10^7$  W/K/m<sup>2</sup> (assuming a packing density of 0.21 nm<sup>-2</sup>), which is a typical value for (good) thermal interfaces. This needs to be compared to the other thermal resistances involved, namely across the electrodes contacting the molecules  $R_{contact}$ , at the electrical isolation layer  $R_{isolation}$  and the thermal interface  $R_{interface}$  to the thermal reservoirs. A metal contact of 100 nm thickness has a negligible value of about  $R_{contact} = 5 \times 10^{-10}$  Km<sup>2</sup>/W. However, a 100 nm silicon oxide insulator already has  $R_{isolation} = 7 \times 10^{-8}$  Km<sup>2</sup>/W, and we need to consider at least four thermal interfaces (between electrical contacts and insulator and between insulator and electrical reservoirs), all of which are at best on the order of  $1 \times 10^{-8}$  to  $1 \times 10^{-7}$  Km<sup>2</sup>/W. Consequently, the temperature drop across the molecular layer will therefore be only few % to a few 10s % compared to the one originally available between the thermal reservoirs. To address this issue, one could reduce the packing density of the molecular film, which would require exploring ways to stabilize two closely separated electrodes. A second important approach is to use literally or effectively a multilayer of molecular junction carpets. Another beautiful approach is the use of nanoparticle assembly [288, 289]. Being able to engineer molecular films in such ways will enable other technologies as well, such as drug delivery from implants or integrated sensing elements.

#### 6.1.4 Technological use cases: It is not only about the figure of merit ZT

Assuming we have reached these milestones, what would be possible thermoelectric applications? We will turn to a list of candidate applications for thermoelectric energy conversion, mainly focused on thermoelectric generators (TEG). While it is important

to be frank about the limited promise in certain technological areas, we find several applications with significant potential. For thermoelectric converters, as well as solar cells and many others, there are several parameters governing the technological viability of a product besides efficiency. These include the cost of fabrication, the lifetime, the robustness, the weight of the module, and many more. A decisive factor is always the availability of other competing technological solutions. While lower cost is a motivation to introduce solution-processable organic thermoelectrics and other inexpensive materials, molecular junctions may be more promising for high performance, which justifies higher cost.

### Mass energy production from primary heat sources

The potential of thermoelectrics as replacement technology of gas turbines in large power plants or in solar energy (either photovoltaics or solar thermal) have been controversially discussed already [254, 290]. In any case, the existing technology is well-established and, so far, thermoelectrics have not been implemented. In addition to not yet demonstrated efficiency, organic or molecular thermoelectrics will not stand the high temperatures of the hot reservoir. A possible workaround for such large temperature differences, could be to cascade thermoelectric converters, such that a certain temperature range is seen by a particular material. In such a scenario, organics could play the role of a near-room temperature component of such a stack.

### Automotive

Automotive waste heat recovery is a popular special case of waste heat recovery. An engine burning fossil fuel has a large exhaust temperature and a comfortable 20 to 200 kW engine power. In a car the usable electricity can be on the order of 600 W. A relevant metric here is the Watt per kilogram of installation. The additional power needed to accelerate the additional weight of a thermoelectric converter can be estimated to be about 60 W per kg. A second important aspect is that the heat needs to be removed relatively quickly with the exhaust gas from the engine. This necessitates a heat exchanger of significant weight. If we assume 10 kg for a heat exchanger, then the first 600 W of conversion power is lost to the additional need to accelerate weight. Additionally, the industry has a focus in developing electric cars, in which not sufficient waste heat will be produced. It appears this application is not particularly promising, and molecular systems may not be applicable.

### Mobile devices

Another popular vision for thermoelectric conversion is the direct use of body heat to charge mobile devices such as sensors or even smartphones. To give a reference, the stand-by power of a smartphone is on the order of 70 mW, which is an interesting target [291]. A human body dissipates roughly 50 mW per 10 cm<sup>2</sup> of the body surface (up to a point the person feels cold). With an efficiency of 1.6 % ( $ZT = 3$  and  $\Delta T = 15$  K) this would translate into about 1 mW of power. However, this assumes that the full temperature difference between body and ambient of about 15 K can be used. But, considering the cascade of thermal resistances in series (Milestone 8) and the thermal

interface to the cold reservoir, i.e. the ambient air, which couples by convection about  $20 \text{ W/K/m}^2$ , the situation is even worse. Without dedicated and bulky cooling structures [292], there will be a more realistic temperature drop over the thermoelectric around  $0.1 - 1 \text{ K}$ . Considering that a  $ZT = 3$  is hard to achieve outside the laboratory, even for a basic optimized design, results are not much better, with a temperature drop of  $\sim 5 \text{ K}$  and an output power of  $\sim 1 \mu\text{W}$  [293]. It appears, the energy harvesting application from body-heat is not realistic.

### Sensing nodes for the IoT

Turning to more promising use cases, a new interesting possible domain of application for thermoelectric materials, used as generators, could arise from the field of distributed, intercommunicating sensing networks (the so-called internet of things, IoT). Albeit from a theoretical point-of-view the amount of power converted by thermoelectric devices could be adequate to replace or at least flank ordinary storage solutions (e.g. batteries) for small sensing nodes (SNs), some more practical reason can explain the inertia of the industry to exploit and further develop thermoelectric solutions for the IoT. In case of a thermoelectric power supply, the overall sensor design must be re-optimized in order to improve the heat uptake and, considerably increasing production time and final price. Also, the overall price of a SN network is, in the first place, fixed by the capital cost (electronics, installation...). Thus, the impact of TEGs can be from both an energetic point-of-view and for reduced servicing cost [294]. Already today, thermoelectric generators represent a convenient solution in case of forbidding locations, or when parts substitution/repair plays a major role.

### Chip or device cooling

Although there is little motivation to propose thermoelectrics as an alternative for household refrigeration for food or air conditioning, a more interesting application involves solid-state refrigeration for device cooling. Today an increasing amount of electronics and sensors are operated at cryogenic temperatures, in particular with the emerge of quantum computers. To reach these, one typically uses liquid cryogens, which implies a certain minimum size and price of installation. A solid-state solution, even with low overall efficiency would enable additional applications. As a target, consider, for example, a cooling device of 1 liter volume, operated using 1 A, that can cool a  $1 \text{ cm}^3$  body to 10 K in a room temperature environment. Such a cooler may be of interest in various context. For comparison, cascades of Peltier coolers today have been shown to exceed 100 K below an ambient environment. This constitutes a possible sweet spot for molecular devices, with a clear collocation in the market, that although represents a niche lacks the presence of already well-established solutions and ferocious competitors.

## 6.1.5 Conclusions

Figure 6.2 summarizes applications discussed here. For both energy harvesting and cooling applications, there are different possible implementations and constraints, here simplified to temperature range and power output (or scalability), which pose the clearest limitations of molecular systems, namely limited thermal stability and strong com-

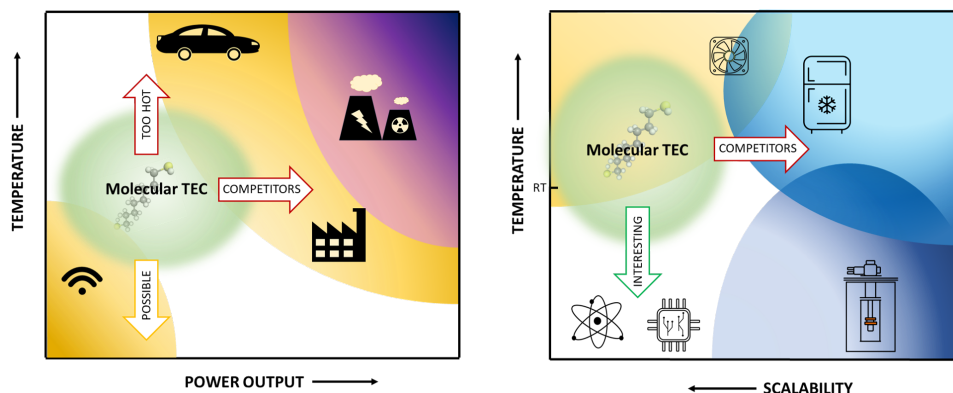


**Figure 6.2** Simple depiction of the use areas and challenges for harvesting (left) and cooling (right) applications.

petition, respectively. Therefore, we are less enthusiastic for applications for large scale conversion (MW). However, energy harvesting at moderate power (mW to kW) and temperature (ambient to few hundred degrees C) is potentially interesting, especially in cases where maintenance and repair play a major role or for remote sensing. We consider the cooling space even more exciting. There is potential for device cooling near or below ambient temperatures. Despite the large amount of research done in the area, significant break-through still needs to come. Reaching a prototype in few years would necessitate dedicated engineering research efforts after the current focus on physics and chemistry. It is therefore likely that the milestones which are still interesting for academic research (Milestones 1 to 6) will have to yield results, before integration issues (Milestones 7 to 8) will be seriously started. The resulting long time scales from science to technology is a known dilemma [295]. On the other hand, from an academic point of view (that falls outside the scope of this roadmap) there are key advantages to keep investigating molecular junctions. For example, charge transport in molecules can be precisely tuned, and various quantum-mechanical transport effects are directly accessible and testable at room temperature, with first experimental studies reporting evidence that quantum interference does exist in single molecules [296, 297]. Also, the knowledge produced while addressing the different Milestones can yield to other applications, such as solar energy conversion (M5) or novel engineered thermal paste (M2).



# 7 Conclusion and Outlook

---

The thesis describes the design, development and validation of a novel experimental setup for the variable temperature measurement of the electrical and thermal transport properties of single atom and single molecule junctions. The new setup, familiarly known as Hibernum, is, to our knowledge, the first tool combining the STM-Break Junction technique, notably requiring high level of stability (below 1 Å), with the use of a pulse-tube cryocooler (featuring a vibration level of tens of microns). The extraordinary mechanical stability of the setup, with a relative vibration level as low as 11.8 pm, enables a very long junction lifetime at different temperatures, as confirmed by the recording of electrical quantization steps at room and low temperatures (Sec. 3.3) and by the verification of the Wiedemann-Franz law (Sec. 3.6). Besides, the use of a pulse-tube cooler avoids wasting of cryogenic fluids, making break-junction experiments at variable temperature more affordable in terms of costs and impact on the environment.

The setup allows using the same measurement technique already used at room temperature. The technique is based on the highly sensitive measurement of tiny heat fluxes flowing through the tip of a modified STM microscope, to record simultaneously the thermal and electrical conductance of quantum scale contacts. This is made possible by the use of MEMS devices which are suspended to guarantee high thermal insulation, and which feature an integrated heater/thermometer as sensing element. The design of the MEMS structure posed rather extreme trade-offs. The first trade-off was between thermal sensitivity and mechanical stiffness. In fact, a good decoupling from the environment, i.e. a large thermal resistance ( $R_{th} \sim 1 \times 10^8$  K/W), is required for high thermal sensitivity, but makes the suspended sensor floppy and fragile, and so not suitable for break junction measurements, requiring a mechanical stiffness larger than the one needed to break the mechanical contacts (an atomic contact of gold has about 1 N/m stiffness [47]). To solve this trade-off a new fabrication process has been developed. Starting from a non-planar carrier layer, u-shaped suspending beams have been designed for an increased stiffness via a larger effective thickness, while at the same time the cross-section was maintained rather small to maximize the thermal resistance. The second trade off instead, involved the response time and optical access to the sensor. Indeed, a fast thermal sensor ( $\tau \sim$  ms) requires a low thermal capacitance, hence reduced area ( $< 400 \mu\text{m}^2$ ). This is in contrast with the requirement of minimum visibility from a large working distance ( $> 100$  mm), given by the optical arrangement.

Thanks to the quietness of the instrument, the high sensitivity of the MEMS device and the low noise laboratory environment, it was possible to measure the charge transport properties of atomic gold contacts at reduced temperature (Sec. 3.3), to validate at ambient temperature the measurement of the Wiedemann-Franz law for single atom contacts (Sec. 3.6), and to measure the thermal transport properties of a single ODT

molecule. This measurement, together with the one of a single OPE3 molecule, represents the first ever room-temperature measurement of thermal conductance at the single molecule level (Sec. 4.1). Through the quantitative agreement between the experimental conductance results and the theory, it was possible to verify the phase-coherent nature of thermal transport across such molecular junctions.

The measurement protocol was then further optimized and developed to characterize the thermoelectric power (or Seebeck coefficient) of three OPE3 derivatives and study the role of substituents in the cross-linking of the same three molecules (Sec. 4.2). The tiny signals involved in the measurements required an accurate data analysis, a comprehensive statistical averaging, and a careful compensation of the electronic noise. Indeed, different noise sources were present at the same time. Among those, first 50 Hz noise from the power line was mitigated by accurate shielding and grounding of all the metallic parts in the setup. Second, amplifiers offsets were adjusted and then kept constant by continuously monitoring the temperature and humidity in the lab. And third, the mechanical stability of the setup was kept to a level such that a bias voltage could be switched on/off for several times, while keeping a molecule firmly in the junction. By combining measurements of electrical conductance, thermal conductance and Seebeck coefficient, it was possible to obtain, to our knowledge, the first complete experimental measurement of the  $ZT$  of a single molecule at room temperature (Sec. 4.3).

Furthermore, new machine learning tools for the analysis of single molecule data were tested and implemented in our data-analysis code (Ch. 5).

In the end, thanks to the knowledge acquired in the field, it was possible to write a critical technological roadmap, towards applications of molecular thermoelectricity (Ch. 6). In fact, after an initial period when the molecular-electronics community focused mainly on logic applications for the replacement of silicon electronics, today the big hope is that molecules could outperform other materials considered for thermoelectric energy conversion. This is due to their potential to act as sharp energy filters for electrical currents. However, there is still a large discrepancy between predictions and actual demonstrations in the literature, for this reason the aim of the roadmap is to highlight necessary steps to actually transition molecules from fundamental research into a viable technology.

**Outlook** Given the new possibilities opened by the novel Hibernum setup, I believe that the first natural follow-up of the work done so far would be continuing the investigation on the quantization of phononic thermal conductance in quantum point contacts and on the validity of Wiedemann-Franz law at reduced temperature. This will give the chance to understand better the role and amount of the phononic contribution to the thermal conductance in metals and so definitely proving (or disproving) Wiedemann-Franz law at low temperature. Eventual violations of such a law, in fact, could provide a handle for understanding how to decouple the electrical and thermal properties in engineered materials, in view of higher thermoelectric efficiencies. Due to the extreme sensitivity required for such an experiment, a new generation of suspended MEMS structures with improved performance at low temperature needs to be developed, together with new measurement protocols. So far only once the measurement of the phononic thermal conductance quantum has been claimed [89], but still remain controversial [93], and it is

---

not clear if it represents a universal value or just an upper limit for perfect conduction through 1D channels. The research in this field would therefore contribute to a bottom-up picture of the phonon scattering processes happening in atomic-scale conductors. An immediate consequence could be in the field of neuromorphic computing, for which most of the hardware solutions investigated today rely on the formation of current-carrying filaments with atomic diameters, or in the thermal-driven phase change of nano-domains in memristive materials.

Another valuable experiment would be the screening of the thermal properties of molecules at low and intermediate temperatures. In this way it could be possible to not only observe quantum interference effects, but also to validate theory models for phonon-transport that usually fail at intermediate ranges of temperature. Indeed, in thermal experiments, temperature plays the same role as voltage bias for electrical measurements. For this reason, it is often necessary to let the temperature of an experiment span over a wide range, from above room temperature to the cryogenic regime, in order to clearly separate all the different contributions and mechanism arising in thermal transport.

This experiment could also be flanked by measurements of the Seebeck coefficient of such molecules, allowing for their classification in terms of thermoelectric efficiency ( $ZT$ ), putting in numbers the expectation on their use as thermoelectric generators. In this context, the roadmap in Ch. 6 can already provide technological guidance.

Even though I see little hope for single molecules, to revolutionize soon the energy conversion sector, I believe that the knowledge we can gather from their study will shape a new path for the scientific research at the nanoscale, where the boundaries between different disciplines, like biology, chemistry and physics, become blurry. In the future, an even more pronounced integration between different research areas will be required to understand the founding principles necessary to develop novel molecule-based technologies. For this to happen, research efforts should focus not only on measuring the conductance properties of single molecules, but especially on the stability of molecular devices. New paradigms have to be found to couple (multiple) molecules to the electrodes, directly or by means of nanosized intermediates. Single molecules will clearly remain important from a fundamental point-of-view, but most likely, future devices will be multi-molecular. Only after having achieved basic, reliable device functionality, molecules will unlock their true potential. Not as mere *beyond-silicon* technology, but as main actors in a realm where their unique properties (e.g. chemical tunability, self-assembling, intrinsic quantum nature) can be crucial. In this context, the first molecular devices I foresee are hybrid sensors (CMOS + molecules), with custom sensing properties and improved efficiency, able to react in an unprecedented manner to external physical stimuli.

In a longer term, I think that the knowledge acquired through the study of thermal transport in molecules and QPCs should be used by researchers to advance in observing, controlling and eventually fabricating structures that could support anisotropic heat flow, i.e. a diode-like behaviour against energy transport. This has represented so far one of the most desired goal for the entire thermal community, and has the potential to truly unlock countless applications based on the control and rectification of energy flows. One example of those applications, would be the realization of solid-state cooling devices operating at cryogenic temperature, which will impact all those emerging technologies operating at low temperatures, such as the recent quantum computers.



# Bibliography

- [1] P. Maunz, T. Puppe, I. Schuster, N. Syassen, P. W. Pinkse, and G. Rempe, *OSA Trends in Optics and Photonics Series* **97**, 289 (2004).
- [2] W. Paul, *Reviews of Modern Physics* **62**, 531 (1990).
- [3] M. Vogel, *Contemporary Physics*, Vol. 52 (2011) pp. 604–605.
- [4] M. Brune, F. Schmidt-Kaler, A. Maali, J. Dreyer, E. Hagley, J. M. Raimond, and S. Haroche, *Physical Review Letters* **76**, 1800 (1996).
- [5] B. D. Josephson, *Physics Letters* **1**, 251 (1962).
- [6] Y. Makhlin, G. Schön, and A. Shnirman, *Reviews of Modern Physics* **73**, 357 (2001).
- [7] H. Van Houten and C. Beenakker, *Physics Today* **49**, 22 (1996).
- [8] B. J. Van Wees, H. Van Houten, C. W. Beenakker, J. G. Williamson, L. P. Kouwenhoven, D. Van Der Marel, and C. T. Foxon, *Physical Review Letters* **60**, 848 (1988).
- [9] N. Xin, J. Guan, C. Zhou, X. Chen, C. Gu, Y. Li, M. A. Ratner, A. Nitzan, J. F. Stoddart, and X. Guo, *Nature Reviews Physics* **1**, 211 (2019).
- [10] S. V. Aradhya and L. Venkataraman, *Nature Nanotechnology* **8**, 399 (2013).
- [11] J. J. Parks, A. R. Champagne, G. R. Hutchison, S. Flores-Torres, H. D. Abruña, and D. C. Ralph, *Physical Review Letters* **99**, 1 (2007).
- [12] M. A. Kastner, *Reviews of Modern Physics* **64**, 849 (1992).
- [13] M. D. Eisaman, J. Fan, A. Migdall, and S. V. Polyakov, *Review of Scientific Instruments* **82** (2011), 10.1063/1.3610677.
- [14] T. J. Bukowski and J. H. Simmons, *Critical Reviews in Solid State and Materials Sciences* **27**, 119 (2002).
- [15] J. C. Norman, D. Jung, Z. Zhang, Y. Wan, S. Liu, C. Shang, R. W. Herrick, W. W. Chow, A. C. Gossard, and J. E. Bowers, *IEEE Journal of Quantum Electronics* **55**, 1 (2019).
- [16] J. Gambetta, “IBM’s roadmap for scaling quantum technology,” (2020).
- [17] F. Arute, K. Arya, R. Babbush, D. Bacon, J. C. Bardin, R. Barends, R. Biswas, S. Boixo, F. G. Brandao, D. A. Buell, B. Burkett, Y. Chen, Z. Chen, B. Chiaro, R. Collins, W. Courtney, A. Dunsworth, E. Farhi, B. Foxen, A. Fowler, C. Gidney, M. Giustina, R. Graff, K. Guerin, S. Habegger, M. P. Harrigan, M. J. Hartmann, A. Ho, M. Hoffmann, T. Huang, T. S. Humble, S. V. Isakov, E. Jeffrey, Z. Jiang, D. Kafri, K. Kechedzhi, J. Kelly, P. V. Klimov, S. Knysh, A. Korotkov, F. Kostritsa, D. Landhuis, M. Lindmark,

- E. Lucero, D. Lyakh, S. Mandrà, J. R. McClean, M. McEwen, A. Megrant, X. Mi, K. Michielsen, M. Mohseni, J. Mutus, O. Naaman, M. Neeley, C. Neill, M. Y. Niu, E. Ostby, A. Petukhov, J. C. Platt, C. Quintana, E. G. Rieffel, P. Roushan, N. C. Rubin, D. Sank, K. J. Satzinger, V. Smelyanskiy, K. J. Sung, M. D. Trevithick, A. Vainsencher, B. Villalonga, T. White, Z. J. Yao, P. Yeh, A. Zalcman, H. Neven, and J. M. Martinis, *Nature* **574**, 505 (2019).
- [18] J. M. Gambetta, J. M. Chow, and M. Steffen, *npj Quantum Information* **3**, 0 (2017).
- [19] N. Friis, O. Marty, C. Maier, C. Hempel, M. Holzäpfel, P. Jurcevic, M. B. Plenio, M. Huber, C. Roos, R. Blatt, and B. Lanyon, *Physical Review X* **8**, 21012 (2018).
- [20] N. J. Tao, *Nature Nanotechnology* **1**, 173 (2006).
- [21] C. J. Lambert, *Chemical Society Reviews* **44**, 875 (2015).
- [22] N. Mosso, U. Drechsler, F. Menges, P. Nirmalraj, S. Karg, H. Riel, and B. Gotsmann, *Nature Nanotechnology* **12**, 430 (2017).
- [23] N. Mosso, H. Sadeghi, A. Gemma, S. Sangtarash, U. Drechsler, C. Lambert, and B. Gotsmann, (2019), 10.1021/acs.nanolett.9b02089.
- [24] R. Viskanta, *Energetika* **59**, 175 (2014).
- [25] A. L. Moore and L. Shi, *Materials Today* **17**, 163 (2014).
- [26] E. Pop, *Nano Research* **3**, 147 (2010).
- [27] G. E. Childs, L. J. Ericks, and R. L. Powell, (1973).
- [28] S. S. Kumar, S. M. Ranjan, W. K., T. T., B. Sumilan, and D. Anindya, *Science Advances* **5**, eaaw5798 (2021).
- [29] K. Schwab, J. L. Arlett, J. M. Worlock, and M. L. Roukes, *Physica E: Low-Dimensional Systems and Nanostructures* **9**, 60 (2001).
- [30] M. Partanen, K. Y. Tan, J. Govenius, R. E. Lake, M. K. Mäkelä, T. Tanttu, and M. Möttönen, *Nature Physics* **12**, 460 (2016).
- [31] J. S. Wang, J. Wang, and J. T. Lü, *European Physical Journal B* **62**, 381 (2008).
- [32] R. E. Peierls, *Quantum theory of solids* (Clarendon Press, 1996).
- [33] H. Spohn, *Journal of statistical physics* **124**, 1041 (2006).
- [34] D. G. Cahill, W. K. Ford, K. E. Goodson, G. D. Mahan, A. Majumdar, H. J. Maris, R. Merlin, and S. R. Phillpot, *Journal of Applied Physics* **93**, 793 (2003).
- [35] M. Galperin, M. A. Ratner, and A. Nitzan, *Journal of Physics Condensed Matter* **19** (2007), 10.1088/0953-8984/19/10/103201.
- [36] Y. Dubi and M. Di Ventra, *Reviews of Modern Physics* **83**, 131 (2011).
- [37] A. Dhar, *Advances in Physics* **57**, 457 (2008).
- [38] S. Lepri, R. Livi, and A. Politi, *Physics Reports* **377**, 1 (2003).

- [39] P. F. Meier (Springer Berlin Heidelberg, Berlin, Heidelberg, 1974) pp. 17–36.
- [40] G. D. Mahan, *Physics Reports* **145**, 251 (1987).
- [41] A. J. McGaughey and M. Kaviani, *Advances in Heat Transfer* **39**, 169 (2006).
- [42] P. Heino, *Journal of Computational and Theoretical Nanoscience* **4**, 896 (2007).
- [43] M. Famili, I. Grace, H. Sadeghi, and C. J. Lambert, *ChemPhysChem* **18**, 1234 (2017).
- [44] T. Markussen, *Journal of Chemical Physics* **139** (2013), 10.1063/1.4849178.
- [45] D. Segal and A. Nitzan, *Journal of Chemical Physics* **122** (2005), 10.1063/1.1900063.
- [46] H. Sadeghi, S. Sangtarash, and C. J. Lambert, *Nano Letters* **15**, 7467 (2015).
- [47] N. Agraït, A. L. Yeyati, and J. M. van Ruitenbeek, *Physics Reports* **377**, 81 (2003).
- [48] A. Jain and A. J. McGaughey, *Physical Review B* **93**, 1 (2016).
- [49] R. Landauer, *IBM Journal of Research and Development* **44**, 251 (1957).
- [50] M. Büttiker, Y. Imry, R. Landauer, and S. Pinhas, *Physical Review B* **31**, 6207 (1985).
- [51] N. W. Ashcroft and N. D. Mermin, *Solid State Physics* (Holt-Saunders, 1976).
- [52] H. Sadeghi, “Theory of Electron, Phonon and Spin Transport in Nanoscale Quantum Devices,” (2018).
- [53] J. Gooth, M. Borg, H. Schmid, V. Schaller, S. Wirths, K. Moselund, M. Luisier, S. Karg, and H. Riel, *Nano Letters* **17**, 2596 (2017).
- [54] L. Olesen, E. Laegsgaard, I. Stensgaard, F. Besenbacher, J. Schio/tz, P. Stoltze, K. W. Jacobsen, and J. K. No/rskov, *Physical Review Letters* **72**, 2251 (1994).
- [55] C. J. Muller, J. M. Krans, T. N. Todorov, and M. A. Reed, *Physical Review B* **53**, 1022 (1996).
- [56] M. Teresa González, S. Wu, R. Huber, S. J. Van Der Molen, C. Schönenberger, and M. Calame, *Nano Letters* **6**, 2238 (2006).
- [57] F. Schwarz and E. Lörtscher, *Journal of Physics Condensed Matter* **26** (2014), 10.1088/0953-8984/26/47/474201.
- [58] N. Agraït, J. G. Rodrigo, and S. Vieira, *Physical Review B* **47**, 12345 (1993).
- [59] A. Gemma, A. Zulji, F. Hurtak, S. Fatayer, A. Kittel, M. Calame, and B. Gotsmann, *Review of Scientific Instruments* (2021).
- [60] A. I. Yanson, G. Rubio Bollinger, H. E. Van Den Brom, N. Agraït, and J. M. Van Ruitenbeek, *Nature* **395**, 783 (1998).
- [61] H. Ohnishi, Y. Kondo, and K. Takayanagi, *Nature* **395**, 780 (1998).
- [62] M. Brandbyge, M. R. Sørensen, and K. W. Jacobsen, *Physical Review B - Condensed Matter and Materials Physics* **56**, 14956 (1997).

- [63] J. C. Cuevas and E. Scheer, *Molecular Electronics: An introduction to Theory and Experiment* (World Scientific, Singapore, 2010).
- [64] T. A. Su, M. Neupane, M. L. Steigerwald, L. Venkataraman, and C. Nuckolls, *Nature Reviews Materials* **1** (2016), 10.1038/natrevmats.2016.2.
- [65] A. Vilan, D. Aswal, and D. Cahen, *Chemical Reviews* **117**, 4248 (2017).
- [66] Q. Lu, K. Liu, H. Zhang, Z. Du, X. Wang, and F. Wang, *ACS Nano* **3**, 3861 (2009).
- [67] R. Frisenda, S. Tarkuç, E. Galán, M. L. Perrin, R. Eelkema, F. C. Grozema, and H. S. van der Zant, *Beilstein Journal of Nanotechnology* **6**, 1558 (2015).
- [68] P. Moreno-García, M. Gulcur, D. Z. Manrique, T. Pope, W. Hong, V. Kaliginedi, C. Huang, A. S. Batsanov, M. R. Bryce, C. Lambert, and T. Wandlowski, *Journal of the American Chemical Society* **135**, 12228 (2013).
- [69] V. Kaliginedi, P. Moreno-García, H. Valkenier, W. Hong, V. M. García-Suárez, P. Buitter, J. L. H. Otten, J. C. Hummelen, C. J. Lambert, and T. Wandlowski, *Journal of the American Chemical Society* **134**, 5262 (2012).
- [70] T. Böhler, A. Edtbauer, and E. Scheer, *Physical Review B - Condensed Matter and Materials Physics* **76**, 1 (2007).
- [71] C. Huang, A. V. Rudnev, W. Hong, and T. Wandlowski, *Chemical Society Reviews* **44**, 889 (2015).
- [72] P. N. Butcher, *Journal of Physics: Condensed Matter* **2**, 4869 (1990).
- [73] H. Van Houten, L. W. Molenkamp, C. W. Beenakker, and C. T. Foxon, *Semiconductor Science and Technology* **7** (1992), 10.1088/0268-1242/7/3B/052.
- [74] L. G. Rego and G. Kirczenow, *Physical Review Letters* **81**, 232 (1998).
- [75] J. B. Pendry, *J. Phys. A: Math. Gen.* **16**, 2161 (1983).
- [76] S. Ciraci, A. Buldum, and I. P. Batra, *Journal of Physics Condensed Matter* **13**, 537 (2001).
- [77] S. Majumdar, J. A. Sierra-Suarez, S. N. Schiffres, W. L. Ong, C. F. Higgs, A. J. McGaughey, and J. A. Malen, *Nano Letters* **15**, 2985 (2015).
- [78] T. Luo and J. R. Lloyd, *Journal of Heat Transfer* **132**, 32401 (2009).
- [79] T. Luo and J. R. Lloyd, *International Journal of Heat and Mass Transfer* **53**, 1 (2010).
- [80] S. Majumdar, J. A. Malen, and A. J. H. McGaughey, *Nano Letters* **17**, 220 (2016).
- [81] L. Cui, S. Hur, Z. A. Akbar, J. C. Klöckner, W. Jeong, F. Pauly, S.-Y. Jang, P. Reddy, and E. Meyhofer, *Nature* (2019), 10.1038/s41586-019-1420-z.
- [82] E. T. Swartz and R. O. Pohl, *Reviews of Modern Physics* **61**, 605 (1989).
- [83] K. R. Patton and M. R. Geller, *Physical Review B - Condensed Matter and Materials Physics* **64**, 1 (2001).
- [84] R. Prasher, *Nano Letters* **5**, 2155 (2005).

- [85] P.-O. Chapuis, J.-J. Greffet, K. Joulain, and S. Volz, *Nanotechnology* **17**, 2978 (2006).
- [86] J. Zhou and B. Xu, *Applied Physics Letters* **99** (2011), 10.1063/1.3615803.
- [87] K. T. Regner, D. P. Sellan, Z. Su, C. H. Amon, A. J. McGaughey, and J. A. Malen, *Nature Communications* **4**, 1 (2013).
- [88] D. G. Cahill, P. V. Braun, G. Chen, D. R. Clarke, S. Fan, K. E. Goodson, P. Koblinski, W. P. King, G. D. Mahan, A. Majumdar, H. J. Maris, S. R. Phillpot, E. Pop, and L. Shi, *Applied Physics Reviews* **1** (2014), 10.1063/1.4832615.
- [89] K. Schwab, E. A. Henriksen, J. M. Worlock, and M. L. Roukes, *Nature* **404**, 974 (2000).
- [90] B. Gotsmann and M. A. Lantz, *Nature Materials* **12**, 59 (2013).
- [91] M. Thompson Pettes and L. Shi, *Journal of Heat Transfer* **136** (2013), 10.1115/1.4025643.
- [92] L. Cui, W. Jeong, S. Hur, M. Matt, J. C. Klöckner, F. Pauly, P. Nielaba, J. C. Cuevas, E. Meyhofer, and P. Reddy, *Science* **355**, 1192 (2017).
- [93] A. Tavakoli, K. Lulla, T. Crozes, N. Mingo, E. Collin, and O. Bourgeois, *Nature Communications* **9** (2018), 10.1038/s41467-018-06791-0.
- [94] Y. Tanaka, F. Yoshida, and S. Tamura, *physica status solidi (c)* **1**, 2625 (2004).
- [95] E. G. Haanappel and D. van der Marel, *Physical Review B* **39**, 5484 (1989).
- [96] H. van Houten, L. W. Molenkamp, C. W. J. Beenakker, and C. T. Foxon, *Semiconductor Science and Technology* **7**, B215 (1992).
- [97] N. Mosso, A. Prasmusinto, A. Gemma, U. Drechsler, L. Novotny, and B. Gotsmann, *Applied Physics Letters* **114** (2019), 10.1063/1.5086483.
- [98] M. Bürkle and Y. Asai, *Nano Letters* **18**, 7358 (2018).
- [99] X. Zhao, J. Li, T. C. Au Yeung, C. H. Kam, Q. H. Chen, and C. Q. Sun, *Journal of Applied Physics* **107**, 2 (2010).
- [100] M. A. Panzer and K. E. Goodson, *Journal of Applied Physics* **103**, 1 (2008).
- [101] D. O. Möhrle, F. Müller, M. Matt, P. Nielaba, and F. Pauly, *Physical Review B* **100**, 1 (2019).
- [102] X. Xu, J. Chen, J. Zhou, and B. Li, *Advanced Materials* **30**, 1705544 (2018).
- [103] D. Schwarzer, P. Kutne, C. Schröder, and J. Troe, *Journal of Chemical Physics* **121**, 1754 (2004).
- [104] S. Shen, A. Henry, J. Tong, R. Zheng, and G. Chen, *Nature Nanotechnology* **5**, 251 (2010).
- [105] D. Segal, A. Nitzan, and P. Hänggi, *Journal of Chemical Physics* **119**, 6840 (2003).
- [106] M. D. Losego, M. E. Grady, N. R. Sottos, D. G. Cahill, and P. V. Braun, *Nature Materials* **11**, 502 (2012).

- [107] G. J. Ashwell, B. Urasinska, C. Wang, M. R. Bryce, I. Grace, and C. J. Lambert, *Chemical Communications*, 4706 (2006).
- [108] P. J. O'Brien, S. Shenogin, J. Liu, P. K. Chow, D. Laurencin, P. H. Mutin, M. Yamaguchi, P. Keblinski, and G. Ramanath, *Nature Materials* **12**, 118 (2013).
- [109] Z. Ge, D. G. Cahill, and P. V. Braun, *Physical Review Letters* **96**, 186101 (2006).
- [110] Z. Tian, A. Marconnet, and G. Chen, *Applied Physics Letters* **106**, 211602 (2015).
- [111] T. Meier, F. Menges, P. Nirmalraj, H. Hölscher, H. Riel, and B. Gotsmann, *Physical Review Letters* **113**, 1 (2014).
- [112] J. C. Klöckner, M. Bürkle, J. C. Cuevas, and F. Pauly, *Physical Review B* **94**, 1 (2016).
- [113] L. Hu, L. Zhang, M. Hu, J. S. Wang, B. Li, and P. Keblinski, *Physical Review B* **81**, 1 (2010).
- [114] F. Sun, T. Zhang, M. M. Jobbins, Z. Guo, X. Zhang, Z. Zheng, D. Tang, S. Ptasinska, and T. Luo, *Advanced Materials* **26**, 6093 (2014).
- [115] N. Mingo, *Physical Review B* **74**, 125402 (2006).
- [116] P. E. Hopkins, P. M. Norris, M. S. Tsegaye, and A. W. Ghosh, *Journal of Applied Physics* **106**, 1 (2009).
- [117] J. C. Duda, C. B. Saltonstall, P. M. Norris, and P. E. Hopkins, *Journal of Chemical Physics* **134**, 094704 (2011).
- [118] E. Díaz, R. Gutierrez, and G. Cuniberti, *Physical Review B* **84**, 144302 (2011).
- [119] T. Markussen, *The Journal of chemical physics* **139**, 244101 (2013).
- [120] R. Moghaddasi Fereidani and D. Segal, *Journal of Chemical Physics* **150** (2019), 10.1063/1.5075620.
- [121] J. C. Klöckner, J. C. Cuevas, and F. Pauly, *Physical Review B* **96**, 1 (2017).
- [122] L. Yang, Y. Tao, Y. Zhu, M. Akter, K. Wang, Z. Pan, Y. Zhao, Q. Zhang, Y.-Q. Xu, R. Chen, T. T. Xu, Y. Chen, Z. Mao, and D. Li, *Nature Nanotechnology*, in revision to address the second round review comments., 0 (2021).
- [123] S. Sangtarash and H. Sadeghi, *Nanoscale Advances* **2**, 1031 (2020).
- [124] M. Famili, I. M. Grace, Q. Al-Galiby, H. Sadeghi, and C. J. Lambert, *Advanced Functional Materials* **28**, 1703135 (2018).
- [125] H. Sadeghi, *Journal of Physical Chemistry C* **123**, 12556 (2019).
- [126] D. Segal, *Physical Review B* **73**, 205415 (2006).
- [127] D. M. Leitner, *The Journal of Physical Chemistry B* **117**, 12820 (2013).
- [128] C. Chang, D. Okawa, A. Majumdar, and A. Zettl, *Science* **314**, 1121 (2006).
- [129] M. Schmotz, J. Maier, E. Scheer, and P. Leiderer, *New Journal of Physics* **13** (2011), 10.1088/1367-2630/13/11/113027.

- [130] B. Li, L. Wang, and G. Casati, *Physical Review Letters* **93**, 184301 (2004).
- [131] J. Zhu, K. Hippalgaonkar, S. Shen, K. Wang, Y. Abate, S. Lee, J. Wu, X. Yin, A. Majumdar, and X. Zhang, *Nano Letters* **14**, 4867 (2014).
- [132] C. Dames, *Journal of Heat Transfer* **131** (2009), 10.1115/1.3089552.
- [133] N. A. Roberts and D. G. Walker, *International Journal of Thermal Sciences* **50**, 648 (2011).
- [134] J. C. Love, L. A. Estroff, J. K. Kriebel, R. G. Nuzzo, and G. M. Whitesides, *Chemical Reviews* **105**, 1103 (2005).
- [135] J.-T. Lü, R. B. Christensen, J.-S. Wang, P. Hedegård, and M. Brandbyge, *Physical Review Letters* **114**, 96801 (2015).
- [136] Y. Mo, K. T. Turner, and I. Szlufarska, *Nature* **457**, 1116 (2009).
- [137] B. Gotsmann, *Nature Materials* **10**, 87 (2011).
- [138] J. Senior, A. Gubaydullin, B. Karimi, J. T. Peltonen, J. Ankerhold, and J. P. Pekola, *Communications Physics* **3**, 1 (2020).
- [139] M. Aspelmeyer, T. J. Kippenberg, and F. Marquardt, *Reviews of Modern Physics* **86**, 1391 (2014).
- [140] J. P. Pekola, *Nature Physics* **11**, 118 (2015).
- [141] A. I. Yanson, G. Rubio Bollinger, H. E. Van Den Brom, N. Agraït, and J. M. Van Ruitenbeek, *Nature* **395**, 783 (1998).
- [142] N. J. Tao, *Nanoscience and Technology: A Collection of Reviews from Nature Journals*, 185 (2009).
- [143] H. Dekkiche, A. Gemma, F. Tabatabaei, A. S. Batsanov, T. Niehaus, B. Gotsmann, and M. R. Bryce, *Nanoscale*, 18908 (2020).
- [144] P. Gehring, J. K. Sowa, C. Hsu, J. de Bruijckere, M. van der Star, J. J. Le Roy, L. Bogani, E. M. Gauger, and H. S. van der Zant, *Nature Nanotechnology* (2021), 10.1038/s41565-021-00859-7.
- [145] G. Binnig and H. Rohrer, *Surface Science* **126**, 236 (1983).
- [146] E. DM and S. EK, *Nature* **344**, 524 (1990).
- [147] F. E. Kalf, M. P. Rebergen, E. Fahrenfort, J. Girovsky, R. Toskovic, J. L. Lado, J. Fernández-Rossier, and A. F. Otte, *Nature Nanotechnology* **11**, 926 (2016).
- [148] R. Pawlak, S. Kawai, T. Meier, T. Glatzel, A. Baratoff, and E. Meyer, *Journal of Physics D: Applied Physics* **50** (2017), 10.1088/1361-6463/aa599d.
- [149] B. Xu and N. J. Tao, *Science* **301**, 1221 LP (2003).
- [150] N. Mosso, *Thermal Transport across Atomic and Molecular Junctions*, Ph.D. thesis, University of Regensburg (2018).
- [151] E. Lörtscher, D. Widmer, and B. Gotsmann, *Nanoscale* **5**, 10542 (2013).

- [152] C. Li, I. Pobelov, T. Wandlowski, A. Bagrets, A. Arnold, and F. Evers, *Journal of the American Chemical Society* **130**, 318 (2008).
- [153] Keithley, Book , vi, I (2016).
- [154] W. Lee, K. Kim, W. Jeong, L. A. Zotti, F. Pauly, J. C. Cuevas, and P. Reddy, *Nature* **498**, 209 (2013).
- [155] L. A. Zotti, M. Bürkle, F. Pauly, W. Lee, K. Kim, W. Jeong, Y. Asai, P. Reddy, and J. C. Cuevas, *New Journal of Physics* **16** (2014), 10.1088/1367-2630/16/1/015004.
- [156] M. Tsutsui, T. Kawai, and M. Taniguchi, *Scientific Reports* **2**, 1 (2012).
- [157] G. J. Snyder and A. H. Snyder, *Energy and Environmental Science* **10**, 2280 (2017).
- [158] D. Stefani, K. J. Weiland, M. Skripnik, C. Hsu, M. L. Perrin, M. Mayor, F. Pauly, and H. S. Van Der Zant, *Nano Letters* **18**, 5981 (2018).
- [159] Y. Ikushima, R. Li, T. Tomaru, N. Sato, T. Suzuki, T. Haruyama, T. Shintomi, and A. Yamamoto, *Cryogenics* **48**, 406 (2008).
- [160] R. Radebaugh, *Journal of Physics Condensed Matter* **21** (2009), 10.1088/0953-8984/21/16/164219.
- [161] M. Pelliccione, A. Sciambi, J. Bartel, A. J. Keller, and D. Goldhaber-Gordon, *Review of Scientific Instruments* **84** (2013), 10.1063/1.4794767.
- [162] F. P. Quacquarelli, J. Puebla, T. Scheler, D. Andres, C. Bödefeld, B. Sipos, C. Dal Savio, A. Bauer, C. Pfeleiderer, A. Erb, and K. Karrai, *Microscopy Today* **23**, 12 (2015).
- [163] A. M. Den Haan, G. H. Wijts, F. Galli, O. Usenko, G. J. Van Baarle, D. J. Van Der Zalm, and T. H. Oosterkamp, *Review of Scientific Instruments* **85** (2014), 10.1063/1.4868684.
- [164] T. Suzuki, T. Tomaru, T. Haruyama, N. Sato, A. Yamamoto, T. Shintomi, Y. Ikushima, and R. Li, , 4 (2006).
- [165] S. Caparrelli, E. Majorana, V. Moscatelli, E. Pascucci, M. Perciballi, P. Puppo, P. Rappagnani, and F. Ricci, *Review of Scientific Instruments* **77** (2006), 10.1063/1.2349609.
- [166] E. Majorana, M. Perciballi, P. Puppo, P. Rappagnani, and F. Ricci, *Journal of Physics: Conference Series* **32**, 374 (2006).
- [167] J. C. Slater, *The Journal of Chemical Physics* **41**, 3199 (1964).
- [168] E. Clementi, D. L. Raimondi, and W. P. Reinhardt, *The Journal of Chemical Physics* **47**, 1300 (1967).
- [169] B. Cordero, V. Gómez, A. E. Platero-Prats, M. Revés, J. Echeverría, E. Cremades, F. Barragán, and S. Alvarez, *Journal of the Chemical Society. Dalton Transactions* , 2832 (2008).
- [170] F. Menges, P. Mensch, H. Schmid, H. Riel, A. Stemmer, and B. Gotsmann, *Nature Communications* **7**, 1 (2016).
- [171] QMC Instruments Ltd., “<http://www.qmcinstruments.co.uk/>,” .
- [172] Infrared Laboratories, “<https://www.irlabs.com/products/bolometers/>,” .

- [173] LYNRED, “<https://www.lynred.com/>,” .
- [174] S. F. Karg, V. Troncale, U. Drechsler, P. Mensch, P. Das Kanungo, H. Schmid, V. Schmidt, L. Gignac, H. Riel, and B. Gotsmann, *Nanotechnology* **25** (2014), 10.1088/0957-4484/25/30/305702.
- [175] C. Yu, S. Saha, J. Zhou, L. Shi, A. M. Cassell, B. A. Cruden, Q. Ngo, and J. Li, *Journal of Heat Transfer* **128**, 234 (2006).
- [176] A. I. Boukai, Y. Bunimovich, J. Tahir-Kheli, J. K. Yu, W. A. Goddard, and J. R. Heath, *Nature* **451**, 168 (2008).
- [177] M. C. Wingert, Z. C. Chen, E. Dechaumphai, J. Moon, J. H. Kim, J. Xiang, and R. Chen, *Nano Letters* **11**, 5507 (2011).
- [178] B. Song, A. Fiorino, E. Meyhofer, and P. Reddy, *AIP Advances* **5** (2015), 10.1063/1.4919048.
- [179] F. Hurtak, *Master Thesis: Quantum Heat Transport in Atomic and Molecular Junctions*, Master thesis, ETH (2021).
- [180] W. E. Lawrence and J. W. Wilkins, *Physical Review B* **6**, 4466 (1972).
- [181] L. L. Patera, X. Liu, N. Mosso, S. Decurtins, S. X. Liu, and J. Repp, *Angewandte Chemie - International Edition* **56**, 10786 (2017).
- [182] L. Gross, Z. L. Wang, D. Ugarte, F. Mohn, N. Moll, W. a. Heer, P. Vincent, P. Liljeroth, C. Journet, G. Meyer, V. T. Binh, M. Poot, H. S. J. V. D. Zant, a. Aguasca, a. Bachtold, K. Kim, a. Zettl, P. Hung, H. W. C. Postma, M. Bockrath, X. Blase, and S. Roche, *Science* **325**, 1110 (2009).
- [183] M. G. Boyle, L. Feng, and P. Dawson, *Ultramicroscopy* **108**, 558 (2008).
- [184] C. A. Martin, R. H. Smit, R. V. Egmond, H. S. Van Der Zant, and J. M. Van Ruitenbeek, *Review of Scientific Instruments* **82** (2011), 10.1063/1.3593100.
- [185] D. Segal and B. K. Agarwalla, *Annual Review of Physical Chemistry* **67**, 185 (2016).
- [186] H. Sadeghi, S. Sangtarash, and C. J. Lambert, *Nano Letters* **15**, 7467 (2015).
- [187] S. Wu, M. T. González, R. Huber, S. Grunder, M. Mayor, C. Schönenberger, and M. Calame, *Nature Nanotechnology* **3**, 569 (2008).
- [188] M. T. González, E. Leary, R. García, P. Verma, M. Á. Herranz, G. Rubio-Bollinger, N. Martín, and N. Agrait, *Journal of Physical Chemistry C* **115**, 17973 (2011).
- [189] V. Kaliginedi, P. Moreno-García, H. Valkenier, W. Hong, V. M. García-Suárez, P. Buitter, J. L. Otten, J. C. Hummelen, C. J. Lambert, and T. Wandlowski, *Journal of the American Chemical Society* **134**, 5262 (2012).
- [190] S. Y. Jang, P. Reddy, A. Majumdar, and R. A. Segalman, *Nano Letters* **6**, 2362 (2006).
- [191] M. Lemmer, M. S. Inkpen, K. Kornysheva, N. J. Long, and T. Albrecht, *Nature Communications* **7**, 1 (2016).
- [192] L. Cui, R. Miao, K. Wang, D. Thompson, L. A. Zotti, J. C. Cuevas, E. Meyhofer, and P. Reddy, *Nature Nanotechnology* **13**, 1 (2017).

- [193] K. Klopstech, N. Köne, S. A. Biehs, A. W. Rodriguez, L. Worbes, D. Hellmann, and A. Kittel, *Nature Communications* **8**, 14475 (2017).
- [194] L. Cui, W. Jeong, V. Fernández-Hurtado, J. Feist, F. J. García-Vidal, J. C. Cuevas, E. Meyhofer, and P. Reddy, *Nature Communications* **8** (2017), 10.1038/ncomms14479.
- [195] R. Frisenda, V. A. Janssen, F. C. Grozema, H. S. Van Der Zant, and N. Renaud, *Nature Chemistry* **8**, 1099 (2016).
- [196] H. Lissau, R. Frisenda, S. T. Olsen, M. Jevric, C. R. Parker, A. Kadziola, T. Hansen, H. S. Van Der Zant, M. Brøndsted Nielsen, and K. V. Mikkelsen, *Nature Communications* **6**, 1 (2015).
- [197] W. Haiss, S. Martín, E. Leary, H. van Zalinge, S. J. Higgins, L. Bouffier, and R. J. Nichols, *The Journal of Physical Chemistry C* **113**, 5823 (2009).
- [198] M. Suzuki, S. Fujii, and M. Fujihira, *Japanese Journal of Applied Physics* **45**, 2041 (2006).
- [199] X. Li, J. He, J. Hihath, B. Xu, S. M. Lindsay, and N. Tao, *Journal of the American Chemical Society* **128**, 2135 (2006).
- [200] Z. Huang, F. Chen, R. D'Agosta, P. A. Bennett, M. Di Ventra, and N. Tao, *Nature Nanotechnology* **2**, 698 (2007).
- [201] C. Nef, P. L. T. M. Frederix, J. Brunner, C. Schönenberger, and M. Calame, *Nanotechnology* **23**, 365201 (2012).
- [202] M. Frei, S. V. Aradhya, M. S. Hybertsen, and L. Venkataraman, *Journal of the American Chemical Society* **134**, 4003 (2012).
- [203] B. Xu, X. Xiao, and N. J. Tao, *Journal of the American Chemical Society* **125**, 16164 (2003).
- [204] C. A. Martin, R. H. Smit, R. V. Egmond, H. S. Van Der Zant, and J. M. Van Ruitenbeek, *Review of Scientific Instruments* **82** (2011), 10.1063/1.3593100.
- [205] T. Markussen, , 1 (2018).
- [206] Z. Wang, J. A. Carter, A. Lagutchev, K. K. Yee, N. H. Seong, D. G. Cahill, and D. D. Dlott, *Science (New York, N.Y.)* **317**, 787 (2007).
- [207] R. Y. Wang, R. A. Segalman, and A. Majumdar, *Applied Physics Letters* **89**, 2004 (2006).
- [208] D. Xiang, X. Wang, C. Jia, T. Lee, and X. Guo, *Chemical Reviews* **116**, 4318 (2016).
- [209] L. Rincón-García, C. Evangeli, G. Rubio-Bollinger, and N. Agrait, *Chemical Society Reviews* **45**, 4285 (2016).
- [210] W. B. Chang, C. K. Mai, M. Kotiuga, J. B. Neaton, G. C. Bazan, and R. A. Segalman, *Chemistry of Materials* **26**, 7229 (2014).
- [211] L. Cui, R. Miao, C. Jiang, E. Meyhofer, and P. Reddy, *The Journal of Chemical Physics* **146**, 092201 (2017).

- [212] V. Tayari, B. V. Senkovskiy, D. Rybkovskiy, N. Ehlen, A. Fedorov, C. Y. Chen, J. Avila, M. Asensio, A. Perucchi, P. Di Pietro, L. Yashina, I. Fakih, N. Hemsworth, M. Petrescu, G. Gervais, A. Grüneis, and T. Szkopek, *Physical Review B* **97**, 1 (2018).
- [213] M. Zebarjadi, K. Esfarjani, M. S. Dresselhaus, Z. F. Ren, and G. Chen, *Energy and Environmental Science* **5**, 5147 (2012).
- [214] W. Liu, X. Yan, G. Chen, and Z. Ren, *Nano Energy* **1**, 42 (2012).
- [215] A. Harzheim, *Materials Science and Technology (United Kingdom)* **34**, 1275 (2018).
- [216] N. Almutlaq, Q. Al-Galiby, S. Bailey, and C. J. Lambert, *Nanoscale* **8**, 13597 (2016).
- [217] Q. H. Al-Galiby, H. Sadeghi, L. A. Algharagholy, I. Grace, and C. Lambert, *Nanoscale* **8**, 2428 (2016).
- [218] M. Tsutsui, T. Morikawa, Y. He, A. Arima, and M. Taniguchi, *Scientific Reports* **5**, 1 (2015).
- [219] F. Chen, J. Hihath, Z. Huang, X. Li, and N. J. Tao, *Annual Review of Physical Chemistry* **58**, 535 (2007).
- [220] S. Park, H. Kang, and H. J. Yoon, *Journal of Materials Chemistry A* **7**, 14419 (2019).
- [221] U. H. F. Bunz, *Chemical Reviews* **100**, 1605 (2000).
- [222] N. M. Jenny, M. Mayor, and T. R. Eaton, *European Journal of Organic Chemistry*, 4965 (2011).
- [223] J. M. Tour, A. M. Rawlett, M. Kozaki, Y. Yao, R. C. Jagessar, S. M. Dirk, D. W. Price, M. A. Reed, C. W. Zhou, J. Chen, W. Wang, and I. Campbell, *Chemistry - A European Journal* **7**, 5118 (2001).
- [224] R. Huber, M. T. González, S. Wu, M. Langer, S. Grunder, V. Horhoiu, M. Mayor, M. R. Bryce, C. Wang, R. Jitchati, C. Schönenberger, and M. Calame, *Journal of the American Chemical Society* **130**, 1080 (2008).
- [225] B. Huang, X. Liu, Y. Yuan, Z. W. Hong, J. F. Zheng, L. Q. Pei, Y. Shao, J. F. Li, X. S. Zhou, J. Z. Chen, S. Jin, and B. W. Mao, *Journal of the American Chemical Society* **140**, 17685 (2018).
- [226] H. Ozawa, M. Baghernejad, O. A. Al-Owaedi, V. Kaliginedi, T. Nagashima, J. Ferrer, T. Wandlowski, V. M. García-Suárez, P. Broekmann, C. J. Lambert, and M. A. Haga, *Chemistry - A European Journal* **22**, 12732 (2016).
- [227] E. Leary, L. A. Zotti, D. Miguel, I. R. Márquez, L. Palomino-Ruiz, J. M. Cuerva, G. Rubio-Bollinger, M. T. González, and N. Agrait, *Journal of Physical Chemistry C* **122**, 3211 (2018).
- [228] E. W. C. Chan, P. Baek, D. Barker, and J. Travas-Sejdic, *Polymer Chemistry* **6**, 7618 (2015).
- [229] V. S. Pavlovich, D. T. Kozhich, and T. A. Pavich, *Journal of Applied Spectroscopy* **66**, 208 (1999).

- [230] P. Giannozzi, S. Baroni, N. Bonini, M. Calandra, R. Car, C. Cavazzoni, D. Ceresoli, G. L. Chiarotti, M. Cococcioni, I. Dabo, A. Dal Corso, S. De Gironcoli, S. Fabris, G. Fratesi, R. Gebauer, U. Gerstmann, C. Gougoussis, A. Kokalj, M. Lazzeri, L. Martin-Samos, N. Marzari, F. Mauri, R. Mazzarello, S. Paolini, A. Pasquarello, L. Paulatto, C. Sbraccia, S. Scandolo, G. Sclauzero, A. P. Seitsonen, A. Smogunov, P. Umari, and R. M. Wentzcovitch, *Journal of Physics Condensed Matter* **21** (2009), 10.1088/0953-8984/21/39/395502.
- [231] P. Giannozzi, O. Andreussi, T. Brumme, O. Bunau, M. Buongiorno Nardelli, M. Calandra, R. Car, C. Cavazzoni, D. Ceresoli, M. Cococcioni, N. Colonna, I. Carnimeo, A. Dal Corso, S. De Gironcoli, P. Delugas, R. A. Distasio, A. Ferretti, A. Floris, G. Fratesi, G. Fugallo, R. Gebauer, U. Gerstmann, F. Giustino, T. Gorni, J. Jia, M. Kawamura, H. Y. Ko, A. Kokalj, E. Küçükbenli, M. Lazzeri, M. Marsili, N. Marzari, F. Mauri, N. L. Nguyen, H. V. Nguyen, A. Otero-De-La-Roza, L. Paulatto, S. Poncé, D. Rocca, R. Sabatini, B. Santra, M. Schlipf, A. P. Seitsonen, A. Smogunov, I. Timrov, T. Thonhauser, P. Umari, N. Vast, X. Wu, and S. Baroni, *Journal of Physics Condensed Matter* **29** (2017), 10.1088/1361-648X/aa8f79.
- [232] J. P. Perdew, K. Burke, and M. Ernzerhof, *Physical Review Letters* **77**, 3865 (1996).
- [233] A. Dal Corso, *Computational Materials Science* **95**, 337 (2014).
- [234] A. Pecchia, G. Penazzi, L. Salvucci, and A. Di Carlo, *New Journal of Physics* **10** (2008), 10.1088/1367-2630/10/6/065022.
- [235] M. Elstner, D. Porezag, G. Jungnickel, J. Elsner, M. Haugk, T. Frauenheim, S. Suhai, and G. Seifert, *Computer Security in the 21st Century* **58**, 25 (1998).
- [236] T. Frauenheim, G. Seifert, M. Elstner, T. Niehaus, C. Köhler, M. Amkreutz, M. Sternberg, Z. Hajnal, A. Di Carlo, and S. Suhai, *Journal of Physics Condensed Matter* **14**, 3015 (2002).
- [237] B. Hourahine, B. Aradi, V. Blum, F. Bonafé, A. Buccheri, C. Camacho, C. Cevallos, M. Y. Deshayé, T. Dumitric, A. Dominguez, S. Ehlert, M. Elstner, T. Van Der Heide, J. Hermann, S. Irle, J. J. Kranz, C. Köhler, T. Kowalczyk, T. Kubař, I. S. Lee, V. Lutsker, R. J. Maurer, S. K. Min, I. Mitchell, C. Negre, T. A. Niehaus, A. M. Niklasson, A. J. Page, A. Pecchia, G. Penazzi, M. P. Persson, J. Åkerman, C. G. Sánchez, M. Sternberg, M. Stöhr, F. Stuckenberg, A. Tkatchenko, V. W. Yu, and T. Frauenheim, *Journal of Chemical Physics* **152** (2020), 10.1063/1.5143190.
- [238] A. Gagliardi, G. Romano, A. Pecchia, A. Di Carlo, T. Frauenheim, and T. A. Niehaus, *New Journal of Physics* **10** (2008), 10.1088/1367-2630/10/6/065020.
- [239] D. Martinez Gutierrez, A. Di Pierro, A. Pecchia, L. M. Sandonas, R. Gutierrez, M. Bernal, B. Mortazavi, G. Cuniberti, G. Saracco, and A. Fina, *Nano Research* **12**, 791 (2019).
- [240] G. Schulze, K. J. Franke, A. Gagliardi, G. Romano, C. S. Lin, A. L. Rosa, T. A. Niehaus, T. Frauenheim, A. Di Carlo, A. Pecchia, and J. I. Pascual, *Physical Review Letters* **100**, 1 (2008).
- [241] T. A. Niehaus, M. Elstner, T. Frauenheim, and S. Suhai, *Journal of Molecular Structure: THEOCHEM* **541**, 185 (2001).

- [242] A. Fihey, C. Hettich, J. Touzeau, F. Maurel, A. Perrier, C. Köhler, B. Aradi, and T. Frauenheim, *Journal of Computational Chemistry* **36**, 2075 (2015).
- [243] M. Valiev, E. J. Bylaska, N. Govind, K. Kowalski, T. P. Straatsma, H. J. Van Dam, D. Wang, J. Nieplocha, E. Apra, T. L. Windus, and W. A. De Jong, *Computer Physics Communications* **181**, 1477 (2010).
- [244] A. Hjorth Larsen, J. Jørgen Mortensen, J. Blomqvist, I. E. Castelli, R. Christensen, M. Dułak, J. Friis, M. N. Groves, B. Hammer, C. Hargus, E. D. Hermes, P. C. Jennings, P. Bjerre Jensen, J. Kermode, J. R. Kitchin, E. Leonhard Kolsbjerg, J. Kubal, K. Kaasbjerg, S. Lysgaard, J. Bergmann Maronsson, T. Maxson, T. Olsen, L. Pastewka, A. Peterson, C. Rostgaard, J. Schiøtz, O. Schütt, M. Strange, K. S. Thygesen, T. Vegge, L. Vilhelmsen, M. Walter, Z. Zeng, and K. W. Jacobsen, *Journal of Physics Condensed Matter* **29** (2017), 10.1088/1361-648X/aa680e.
- [245] A. Batra, P. Darancet, Q. Chen, J. S. Meisner, J. R. Widawsky, J. B. Neaton, C. Nuckolls, and L. Venkataraman, *Nano Letters* **13**, 6233 (2013).
- [246] A. Gagliardi, T. A. Niehaus, T. Frauenheim, A. Pecchia, and A. Di Carlo, *Journal of Computational Electronics* **6**, 345 (2007).
- [247] J. B. Neaton, M. S. Hybertsen, and S. G. Louie, *Physical Review Letters* **97**, 1 (2006).
- [248] F. Evers, R. Korytár, S. Tewari, and J. M. Van Ruitenbeek, *Reviews of Modern Physics* **92**, 35001 (2020).
- [249] X. Wang, T. L. Bennett, A. Ismael, L. A. Wilkinson, J. Hamill, A. J. White, I. M. Grace, O. V. Kolosov, T. Albrecht, B. J. Robinson, N. J. Long, L. F. Cohen, and C. J. Lambert, *Journal of the American Chemical Society* **142**, 8555 (2020).
- [250] V. Lutsker, B. Aradi, and T. A. Niehaus, *Journal of Chemical Physics* **143** (2015), 10.1063/1.4935095.
- [251] A. F. Ioffe, *Physics Today* **12**, 42 (1959).
- [252] P. Gehring, J. K. Sowa, C. Hsu, J. de Bruijckere, M. van der Star, J. J. Le Roy, L. Bogani, E. M. Gauger, and H. S. van der Zant, *Nature Nanotechnology* **16**, 426 (2021).
- [253] A. Gemma and B. Gotsmann, *Nature Nanotechnology* (2021).
- [254] C. B. Vining, *Nature Materials* , 83 (2009).
- [255] M. E. Abbassi, J. Overbeck, O. Braun, M. Calame, H. S. J. V. D. Zant, and M. L. Perrin, *Communications Physics* **4** (2021), 10.1038/s42005-021-00549-9.
- [256] K. Kourou, T. P. Exarchos, K. P. Exarchos, M. V. Karamouzis, and D. I. Fotiadis, *Computational and structural biotechnology journal* **13**, 8 (2015).
- [257] M. Bojarski, D. Del Testa, D. Dworakowski, B. Firner, B. Flepp, P. Goyal, L. D. Jackel, M. Monfort, U. Muller, and J. Zhang, *arXiv preprint arXiv:1604.07316* (2016).
- [258] J. Vamathevan, D. Clark, P. Czodrowski, I. Dunham, E. Ferran, G. Lee, B. Li, A. Madabhushi, P. Shah, and M. Spitzer, *Nature Reviews Drug Discovery* **18**, 463 (2019).

- [259] C. Hutto and E. Gilbert, in *Proceedings of the International AAAI Conference on Web and Social Media*, Vol. 8 (2014).
- [260] Y. Sun, X. Wang, and X. Tang, in *Proceedings of the IEEE conference on computer vision and pattern recognition* (2014) pp. 1891–1898.
- [261] Z. Liu, P. Luo, X. Wang, and X. Tang, in *Proceedings of the IEEE international conference on computer vision* (2015) pp. 3730–3738.
- [262] T. Mikolov, M. Karafát, L. Burget, J. Cernocký, and S. Khudanpur, in *Interspeech*, Vol. 2 (Makuhari, 2010) pp. 1045–1048.
- [263] G. Hinton, L. Deng, D. Yu, G. E. Dahl, A.-r. Mohamed, N. Jaitly, A. Senior, V. Vanhoucke, P. Nguyen, and T. N. Sainath, *IEEE Signal processing magazine* **29**, 82 (2012).
- [264] X. Zhang, J. Zhao, and Y. LeCun, *Advances in neural information processing systems* **28**, 649 (2015).
- [265] V. Tshitoyan, J. Dagdelen, L. Weston, A. Dunn, Z. Rong, O. Kononova, K. A. Persson, G. Ceder, and A. Jain, *Nature* **571**, 95 (2019).
- [266] M. L. Perrin, “Data Clustering Tool,” (2020).
- [267] R. Bellman, *Press Princeton, New Jersey*, 2010th ed. (Princeton University Press, 1957).
- [268] D. L. Davies and D. W. Bouldin, *IEEE Transactions on Pattern Analysis and Machine Intelligence* **PAMI-1**, 224 (1979).
- [269] E. Vidal-Revel, *Quantized thermoelectric transport in single molecule junction (MSc. Thesis)* (2020).
- [270] Q. Li, M. Strange, I. Duchemin, D. Donadio, and G. C. Solomon, *The Journal of Physical Chemistry C* **121**, 7175 (2017).
- [271] D. Stefani, K. J. Weiland, M. Skripnik, C. Hsu, M. L. Perrin, M. Mayor, F. Pauly, and H. S. Van Der Zant, *Nano Letters* **18**, 5981 (2018).
- [272] A. Aviram, C. Joachim, and M. Pomerantz, *Chemical Physics Letters* **146**, 490 (1988).
- [273] A. Aviram, *Journal of the American Chemical Society* **110**, 5687 (1988).
- [274] S. Woitellier, J. Launay, and C. Joachim, *Chemical Physics* **131**, 481 (1989).
- [275] J. Wei, L. Yang, Z. Ma, P. Song, M. Zhang, J. Ma, F. Yang, and X. Wang, *Journal of Materials Science* **55**, 12642 (2020).
- [276] H. Y. Lv, H. J. Liu, J. Shi, X. F. Tang, and C. Uher, *Journal of Materials Chemistry A* **1**, 6831 (2013).
- [277] C. Lin, W. Cheng, Z. Guo, G. Chai, and H. Zhang, *Physical Chemistry Chemical Physics* **19**, 23247 (2017).
- [278] L. Sun, P. H. Jiang, H. J. Liu, D. D. Fan, J. H. Liang, J. Wei, L. Cheng, J. Zhang, and J. Shi, *Carbon* **90**, 255 (2015).
- [279] F. L. Curzon and B. Ahlborn, *American Journal of Physics* **43**, 22 (1975).

- 
- [280] W. Liu, H. S. Kim, Q. Jie, and Z. Ren, *Scripta Materialia* **111**, 3 (2016).
- [281] A. Nozariasbmarz, B. Poudel, W. Li, H. B. Kang, H. Zhu, and S. Priya, *iScience* **23**, 101340 (2020).
- [282] J. C. Klöckner and F. Pauly, arXiv preprint , 1 (2019).
- [283] R. Zhou, Z. Jiang, C. Yang, J. Yu, J. Feng, M. A. Adil, D. Deng, W. Zou, J. Zhang, K. Lu, W. Ma, F. Gao, and Z. Wei, *Nature Communications* **10**, 1 (2019).
- [284] K. Pushpavanam, E. Narayanan, and K. Rege, *ChemNanoMat* **2**, 385 (2016).
- [285] M. E. Abbassi, J. Overbeck, O. Braun, M. Calame, H. S. J. van der Zant, and M. L. Perrin, , 1 (2020).
- [286] W. R. Broughton, A. S. Maxwell, and G. D. Sims, *NPL REPORT MAT* **99**, 6 (2021).
- [287] A. Plota and A. Masek, *Materials* **13**, 1 (2020).
- [288] J. Liao, L. Bernard, M. Langer, C. Schönenberger, and M. Calame, *Advanced Materials* **18**, 2444 (2006).
- [289] J. Liao, S. Blok, S. J. van der Molen, S. Diefenbach, A. W. Holleitner, C. Schönenberger, A. Vladyka, and M. Calame, *Chem. Soc. Rev.* **44**, 999 (2015).
- [290] L. Liu, *New Journal of Physics* **16** (2014), 10.1088/1367-2630/16/12/123019.
- [291] A. Carroll and G. Heiser, in *USENIX annual technical conference*, Vol. 14 (2010) pp. 21–21.
- [292] M. Thielen, L. Sigrist, M. Magno, C. Hierold, and L. Benini, *Energy Conversion and Management* **131**, 44 (2017).
- [293] J. Weber, K. Potje-Kamloth, F. Haase, P. Detemple, F. Völklein, and T. Doll, *Sensors and Actuators, A: Physical* **132**, 325 (2006).
- [294] D. Narducci, *Journal of Physics: Energy* **1**, 024001 (2019).
- [295] L. E. Bell, *Journal of Electronic Materials* **38**, 1344 (2009).
- [296] R. Miao, H. Xu, M. Skripnik, L. Cui, K. Wang, K. G. Pedersen, M. Leijnse, F. Pauly, K. Wärnmark, E. Meyhofer, P. Reddy, and H. Linke, *Nano Letters* **18**, 5666 (2018).
- [297] M. Gantenbein, L. Wang, A. A. Al-Jobory, A. K. Ismael, C. J. Lambert, W. Hong, and M. R. Bryce, *Scientific Reports* **7**, 1 (2017).



# Author Contributions

In this section, I would like to highlight the main scientific contributions to this work. First of all, I would like to thank once more Dr. Bernd Gotsmann for his keen scientific guidance and help throughout the whole PhD project. He actively contributed in many different ways to the several stages of this project. Second, I would like to give credit to all the other colleagues and collaborators who contributed to this work:

- **Section 3.1.3.** The EPFL master student Elisa Vidal-Revel created the GUI for the temperature controller during her master thesis project at IBM.
- **Section 3.3.** The mechanical parts and vacuum components were machined by Anel Zulji in the mechanical modelshop at IBM.
- **Section 3.4.** The MEMS devices were fabricated by Ute Drechsler in the BRNC cleanroom at IBM.
- **Section 3.4.3.** The thermometer calibration was performed by the ETH master student Femke Hurtak, during her master thesis project at IBM.
- **Section 3.5.4.** The recipes for preparing STM tips by electrochemical etching were developed by the ETH master student Alissa Prasmusinto, during her master thesis project at IBM.
- **Section 3.6.1.** Femke Hurtak also adapted the MATLAB script for analysing the Wiedemann-Franz data at low temperature.
- **Section 5.1.** Dr. Mickael Perrin from EMPA developed the clustering tools used for the machine learning analysis.
- **Section 5.2.** Elisa Vidal-Revel also analysed the data with the GUI provided by Dr. Mickael Perrin and compared them to the data analysed with a standard statistical method.
- **Section 5.2.** Dr. Herve Dekkiche from Durham University synthesized the molecules used in this study.

Co-authors of all the papers included in this thesis are acknowledged at the beginning of the respective sections.



# Acknowledgements

Looking back on my time as PhD student at IBM, I must thank all the people who helped, assisted and shared with me both ups and downs of a journey lasted almost four years. Without their help and continuous support I could have not achieved what I have achieved today. For this reason, the first and special thanks go to my supervisor at IBM, Dr. Bernd Gotsmann: he was a mentor, a scientific guidance and a perfect sparring partner for all the adventures (and misadventures) we faced in the lab. It has been a pleasure for me to work under his bright supervision. Second, my sincere thanks go to Prof. Michel Calame, for the time he devoted in supervising me, the useful suggestions and his scientifically sound criticism. I would also like to thank Prof. András Halbritter and Prof. Mika Prunilla for taking part in my doctoral committee and their keen review of my thesis. Among all the people which shared this journey with me, I would like to thank:

- The *Thermal group*, for the inspiring scientific discussions, the collaborations and the availability in always helping each other out. Thanks Siegi, Nele, Elisabetta, Fabian, Olivier, Elisa and Femke. In particular I would like to thank Nico Mosso, because thanks to his expertise I could start my PhD in the best way possible.
- The W222, for being the best office ever. You guys always gifted me with a laugh whenever I needed it the most! Thanks Markus, Daniel, Nele, Alan, Philipp, Enrico and Pengyan.
- Special thanks go to Preksha and Markus with whom I shared this adventure since the beginning.
- The MIND group for all the stimulating discussions, countless coffees, lunch breaks and exciting group events. Particular thanks to Kirsten Moselund, for being such a good manager, and her ability to keep an entire group close-knit and motivated during a worldwide pandemic.
- The BRNC team for their availability and technical support. Especially thanks to Ute for her commitment and incessant effort in fabricating perfect devices that made all the experimental work possible.
- Heike Riel for their managerial support and willingness in helping young generations of PhD students, and the entire Science and Technology Department at IBM.
- The untamed IBM Football Team, for being such good friends and for the tough battles on the pitch, in Tenero and at Lili's terrace. Special nominations for Fabio, Davide, Luca, Federico and all the *Si-dice-Dazoon* squad.

## *Acknowledgements*

---

- The old colleagues from *Più ansia del solito*, for the thousands adventures that brought me here. Thanks Paolo, Edo, Filippo, Michele e Matteo.
- I would also like to thank all my friends from Sicily, and in particular the A.TO.MI.CA. group, for always being there. Thanks Ciccio, Pietro, Placido, Peppe, Flavio, Erika.

The most passionate thanks go to my family, for their unconditional love and help. They always allowed me to feel secure, understood and appreciated. Grazie Mamma, Papà e Luca! Last but definitely not the least, I would like to thank my girlfriend Carla, for her infinite patience, love and support throughout the whole PhD adventure and beyond.

Thank you!

